

MATER. TEHNOL.	LETNIK VOLUME	50	ŠTEV. NO.	2	STR. P.	163–286	LJUBLJANA SLOVENIJA	MAR.–APR. 2016
-------------------	------------------	----	--------------	---	------------	---------	------------------------	-------------------

VSEBINA – CONTENTS

IZVIRNI ZNANSTVENI ČLANKI – ORIGINAL SCIENTIFIC ARTICLES

Corrosion behavior and the weak-magnetic-field effect of aluminum packaging paper Vpliv šibkega magnetnega polja na korozijo aluminijeve embalažne folije N. Zazi, J.-P. Chopart, A. Bilek	165
Characteristics of the AlTiCrN+DLC coating deposited with a cathodic arc and the PACVD process Značilnosti AlTiCrN+DLC prevleke, nanešene s katodnim oblokom in PACVD postopkom K. Lukaszewicz, E. Jonda, J. Sondor, K. Balin, J. Kubacki	175
Implicit numerical multidimensional heat-conduction algorithm parallelization and acceleration on a graphics card Paralelizacija in pospešitev implicitnega numeričnega večdimenzijskega algoritma prevajanja toplote na grafični kartici M. Pohanka, J. Ondroušková	183
Magnetic properties and microstructure of a bulk amorphous Fe₆₁Co₁₀Ti₃Y₆B₂₀ alloy, fabricated as rods and tubes Magnetne lastnosti in mikrostruktura masivne amorfnе zlitine Fe ₆₁ Co ₁₀ Ti ₃ Y ₆ B ₂₀ v obliki palic in cevi M. Nabiałek, K. Bloch, K. Szlązak, M. Szota	189
Effect of the skin-core morphology on the mechanical properties of injection-moulded parts Vpliv morfologije skorja-jedro na mehanske lastnosti vbrizganih delov E. Hnatkova, Z. Dvorak	195
Recrystallization behaviour of a nickel-based superalloy Obnašanje superzlitine na osnovi niklja pri rekristalizaciji P. Podany, Z. Novy, J. Dlouhy	199
Estimation of the number of forward time steps for the sequential Beck approach used for solving inverse heat-conduction problems Ugotavljanje števila vnaprejšnjih časovnih korakov za sekvenčni Beckov približek pri reševanju problemov inverzne toplotne prevodnosti J. Komínek, M. Pohanka	207
Enhanced stability and electrochemical performance of a BaTiO₃/PbO₂ electrode via a layer obtained with layer electrodeposition Izboljšana stabilnost in elektrokemijska zmogljivost elektrode BaTiO ₃ /PbO ₂ , izdelane z elektrodepozicijo plast na plast G. Muthuraman, K. Karunakaran, I. S. Moon	211
Deformation behaviour of amorphous Fe-Ni-W/Ni bilayer-confined bulk metallic glasses Obnašanje deformiranega, amorfnega, na dve plasti omejenega kovinskega stekla Fe-Ni-W/Ni H. K. Lau, N. Yip, S. H. Chen, W. Chen, K. C. Chan	217
Synergistic effect of organic- and ceramic-based ingredients on the tribological characteristics of brake friction materials Sinergističen vpliv sestavin z organsko in keramično osnovo na tribološke značilnosti materialov za torne zavore R. Ertan	223
Optimization of the parameters for the surfactant-added EDM of a Ti–6Al–4V alloy using the GRA-Taguchi method Optimizacija površinsko aktivnih mešanih EDM parametrov na Ti-6Al-4V zlitini z uporabo GRA-Taguchi metode M. Kolli, K. Adepu	229
Determination of the cutting-tool performance of high-alloyed white cast iron (Ni-Hard 4) using the Taguchi method Določanje zmogljivosti rezalnih orodij na močno legiranem belem litem železu (Ni-Hard 4) z uporabo Taguchi metode D. Kir, H. Öktem, M. Çöl, F. Gül Koç, F. Erzincanlı	239
Use of the ABI technique to measure the mechanical properties of aluminium alloys: effect of chemical composition on the mechanical properties of the alloys Uporaba tehnike ABI za merjenje mehanskih lastnosti aluminijevih zlitin: vpliv kemijske sestave na mehanske lastnosti zlitin M. Puchnin, O. Trudonoshyn, O. Prach	247
Fe-Zn intermetallic phases prepared by diffusion annealing and spark-plasma sintering Fe-Zn intermetalne faze, pripravljene z difuzijskim žarjenjem in s sintranjem v iskreči plazmi P. Pokorný, J. Cinert, Z. Pala	253
High-temperature oxidation of silicide-aluminide layer on the TiAl6V4 alloy prepared by liquid-phase siliconizing Visokotemperaturna oksidacija plasti silicid-aluminid, pripravljene s silikoniziranjem s tekočo fazo zlitine TiAl6V4 T. F. Kubatfk	257

Characterization and kinetics of plasma-paste-borided AISI 316 steel

Karakterizacija in kinetika plazma boriranja s pasto jekla AISI 316

R. Chegroune, M. Keddou, Z. Nait Abdellah, S. Ulker, S. Taktak, I. Gunes 263

Investigation of the adhesion and wear properties of borided AISI H10 steel

Preiskava adhezije in obrabnih lastnosti boriranega jekla AISI H10

I. Gunes, M. Ozcatal 269

The effects of cutting conditions on the cutting torque and tool life in the tapping process for AISI 304 stainless steel

Vpliv pogojev rezanja na moment pri rezanju in zdržljivost navojnega vreznika pri vrezovanju notranjih navojev v nerjavno jeklo AISI 304

G. Uzun, I. Korkut 275

STROKOVNI ČLANKI – PROFESSIONAL ARTICLES

Chemical synthesis and densification behavior of Ag/ZnO metal-matrix composites

Obnašanje Ag/ZnO kompozita s kovinsko osnovo pri kemijski sintezi in zgoščevanju

M. Ardestani 281

CORROSION BEHAVIOR AND THE WEAK-MAGNETIC-FIELD EFFECT OF ALUMINUM PACKAGING PAPER

VPLIV ŠIBKEGA MAGNETNEGA POLJA NA KOROZIJO ALUMINIJEVE EMBALAŽNE FOLIJE

Nacer Zazi¹, Jean-Paul Chopart², Ali Bilek¹

¹University Mouloud Mammeri of Tizi-Ouzou, Faculty of Construction Engineering, Department of Mechanical Engineering (LMSE),
B.P.17 RP Tizi-Ouzou, Algeria

²Université de Reims Champagne Ardenne, LISM EA 4695 UFR SEN, BP1039, Moulin de la Housse, 51687 Reims, Cedex, France
zazinacer@yahoo.fr

Prejem rokopisa – received: 2014-05-21; sprejem za objavo – accepted for publication: 2015-04-13

doi:10.17222/mit.2014.083

Aluminum can be absorbed through the digestive system from water and drinks and the food that contains natural traces and processed food or the food cooked in aluminum cookware. Some studies show that the people exposed to high levels of aluminum may develop kidney, bone and brain diseases. Aluminum foil (AlFeSi) is daily used as packaging for food and drugs stored in the refrigerator where an electric motor induces a magnetic field of a few microteslas. The purpose of this work is to study the corrosion behavior of various aluminum packaging foils and the effect of a weak magnetic field on the morphology and the corrosion kinetics in the 0.3 % and 3 % of mass fractions of NaCl solutions. The mean results for various aluminum packaging foils show that localized corrosion is controlled by the electrochemical potentials of different phases constituting the aluminum foil and the concentration of the precipitates from the other phases. The morphology and the corrosion kinetics of aluminum packaging foil in the 0.3 % and 3 % of mass fractions of NaCl solutions are different with and without an application of a weak magnetic field. Electrochemical tests applied to cheese packaging paper show that the introduction of a magnetic field decreases the polarization resistance, the potential of passivation and the value of the open-circuit potential at the beginning of the corrosion; however, its passivation-current density increases at the beginning of the corrosion. The values of the open-circuit potential with and without a weak magnetic field are the same after thirty days of corrosion.

Keywords: aluminum packaging foil, weak magnetic field, aluminum alloys, corrosion, passivation

Aluminij se lahko absorbira v prebavni sistem iz vode in pijač in iz hrane, ki vsebuje naravne sledi ter obdelane hrane ali hrane, kuhane v aluminijasti posodi. Nekatere študije kažejo, da ljudje izpostavljeni visokemu nivoju aluminija, lahko zbolijo na ledvicah, kosteh in možganih. Aluminijeva folija (AlFeSi), ki se dnevno uporablja kot embalaža za hrano in zdravila, se hrani v hladilniku, kjer elektromotor inducira magnetno polje jakosti nekaj mikroteslov. Namen študije je predstavitev korozijskega obnašanja različnih aluminijevih embalažnih folij in vpliv šibkega magnetnega polja na morfologijo in kinetiko korozije v 0,3 % in 3 % raztopini NaCl. Rezultati kažejo, da je pri različnih aluminijevih folijah lokalna korozija kontrolirana z elektrokemijskim potencialom različnih faz, ki sestavljajo aluminijevo folijo in s koncentracijo izločkov drugih faz. Morfologija in kinetika korozije aluminijevih embalažnih folij v 0,3 % in 3 % raztopini NaCl, sta različni pri prisotnosti ali odsotnosti šibkega magnetnega polja. Elektrokemijski preizkusi, izvršeni na ovojni foliji za sir, so pokazali, da prisotnost magnetnega polja na začetku korozije zmanjša polarizacijsko odpornost, potencial pasivacije in vrednost potenciala odprtega kroga, vendar pa gostota pasivacijskega toka narašča. Vrednost potenciala odprtega kroga je po tridesetih dneh enaka, ob prisotnosti ali odsotnosti šibkega magnetnega polja.

Ključne besede: aluminijeva embalažna folija, šibko magnetno polje, aluminijeve zlitine, korozija, pasivacija

1 INTRODUCTION

Aluminums, when combined with various elements and subjected to various thermomechanical treatments, exhibit considerable advantages, such as good mechanical properties. However, the use of these alloys does not remove any disadvantage; for example, various types of corrosion can appear. These alloys are used as packaging for foodstuffs, drugs, and in the kitchen utensils for short, average or long durations because of their low density, good formability and excellent corrosion resistance in the air environment.¹⁻³ The corrosion resistance of aluminum is directly related to the formation of an alumina oxide or hydroxide on the material surface, inducing a relative passivation of these alloys. This resistance is limited to the environments where these oxides are slightly soluble at the pH values of 4–9.¹

Aluminum alloys are sensitive to localized corrosion in aggressive environments containing chlorides such as food and drugs. Several theories on localized corrosion were closely connected to the passive oxide-film rupture. In aluminums, localized corrosion appears when aggressive ions such as chlorides break the protection by locally attacking the passive layer. The chlorides generate the corrosion surrounding the defect oxide film in surface heterogeneities, such as crevices, precipitates and intermetallic particles.⁴⁻⁸ These heterogeneities create a distribution of cathodic and anodic areas across the alloy surface and then various forms of localized corrosion take place.⁵

Aluminum of the first fusion contains 0.1 % iron, which is higher than the limit solubility of iron in aluminum at room temperature. Moreover, only few products are elaborated from aluminum of the first

fusion, while great quantities of recycled-aluminum alloys are used in the manufactured products. This increases the iron content in aluminum alloys, so iron phases are formed.⁹

An iron phase is cathodic and nobler than aluminum; its presence in an aluminum alloy affects the kinetics of the aluminum anodic dissolution and makes it a significant factor of the localized aluminum-alloy corrosion.⁹ The richer the phases are in iron, the more they become favorable sites for cathodic reactions and their surroundings are adequate positions for anodic reactions and localized corrosion.

Others impurities are soluble in aluminum because their solubility limits are higher than their concentrations in aluminum.

The presence of different intermetallic precipitates in aluminum-matrix alloys increases the mechanical properties and their susceptibility to corrosion.¹⁰

Aluminum alloys used for kitchen utensils come from recycled worn parts of cars, aircraft, gutters, wires, drink cans, etc. Their chemical analysis revealed the presence of heavy elements such as Cd, Co, Cr, Pb, Ni and Zn. These utensils can contaminate man's food chain and lead to a bio-accumulation of heavy metals in the vital parts of the human body such as liver, kidneys, spleen.¹¹⁻¹² When the concentration of these elements is higher than their solubility limit, they modify the electrochemical potential of the material surface by generating new intermetallic particles or joining the chemical compositions of the existing intermetallic particles.

Magnetic fields are powerful scientific tools for metal-deposition or dissolution studies. The presence of a magnetic field improves the mass transfer of an electrochemical system, the quality of the deposit and the influence of the corrosion phenomena.¹³

Aluminum foil is daily used as packaging for food and drugs stored in a refrigerator where an electric motor induces a magnetic field of a few microteslas.¹⁴

The purpose of this study is to examine the corrosion phenomena of various aluminum foils intended for food and drug packaging and aluminum kinetic dissolution. The effect of a week permanent magnetic field on the morphology and corrosion kinetics of an aluminum foil in a NaCl solution is also examined.

2 MATERIALS AND METHODS

Various aluminum packaging foils were tested in our experiments using light microscopy, scanning electronic microscopy, X-ray diffraction and corrosion tests. Batches of aluminum foil intended for cheese, chocolate, drug and foodstuff packaging in rolls were used as samples.

The nominal chemical composition of different aluminum packaging paper is given in **Table 1**.

The corrosion measurements were undertaken at room temperature. Samples of 1 cm² ($\varnothing = 11.28$ mm) were immersed in chloride sodium solutions of the 0.3 % and 3 % of mass fractions of NaCl. The four-electrode method was used. A saturated calomel electrode (SCE) was used as the reference electrode. The two auxiliary electrodes were in graphite.

Open-circuit potential and current potential were obtained by means of an EGG-Princeton 263 potentiostat. Before determining the layout of the polarization curves, the working electrode was polarized at -0.8 V. To obtain the polarization curves, we applied a potential that evolved to ascending values, passing from the cathodic domain towards the anodic domain. The samples intended for electrochemical tests, microscopic examination and X-ray diffraction were not polished in order to keep the surface of the aluminum foil appropriate for its daily use.

The microstructures and surface morphologies of corroded and non-corroded samples were characterized with light microscopy and scanning electron microscopy (Philips Esem-XL30, tungsten filament). Prior to microscopic characterization, the corroded samples were rinsed with distilled water and dried in desiccators.

The chemical composition of the aluminum foil surface was characterized with a JEOL JSM 6460LA microscope coupled with an EDS JEL 1300 microprobe.

The corrosion tests were carried out by immersing the aluminum packaging-foil samples in the 0.3 % and 3 % of mass fractions of NaCl solutions at pH = 7 with and without a week permanent magnetic field (42 mT). A magnet with a ring shape was positioned near the sample surfaces. The same distance was kept between the working electrodes and the magnet for all samples.

Micro-hardness measurements were taken with a Zwick Roell ZHV 1M tester. The HV scale, under a load of 5 g was chosen for this testing. Five measurements were taken for each sample.

Table 1: Chemical compositions of various packaging foils

Tabela 1: Kemijska sestava različnih embalažnih folij

Elements/Aluminum packaging foil for:	Al	Si	Fe	Mg	Cu	Mn	V	Cr	Ti	Zn	Other
domestic use	99.344	0.208	0.253	0.040	0.038	0.035	0.020	0.012	0.006	0.004	0.040
drug	98.100	0.700	0.820	0.050	0.095	0.014	0.020	0.022	0.050	0.086	0.043
chocolate	99.271	0.300	0.150	0.035	0.025	0.022	0.033	0.005	0.040	0.026	0.093
cheese	98.300	0.630	0.575	0.083	0.072	0.026	0.011	0.016	0.042	0.076	0.169

The X-ray spectrum was obtained with a Bruker AXS D8 Advance diffractometer.

3 RESULTS AND DISCUSSION

The Vickers micro-hardness results obtained for several batches of aluminum packaging foil for cheese (Table 2) show the changes between the batches. This means that the mechanical and chemical properties of the aluminum foil surface change from one batch to another.^{7,15} Consequently, the morphology and corrosion kinetics are expected to differ from one batch to another.^{7,15}

Table 2: Hardness measurements of aluminum packaging foils

Tabela 2: Meritve trdote aluminijevih embalažnih folij

Sample of the cheese aluminum packaging foil	1	2	3
Vickers micro-hardness (25 °C)	16.2	19.4	14.8

The aluminum packaging foil under light and scanning electron microscopy reveals an aluminum solid-solution matrix, intermetallic particles and or precipitates (Figures 1 to 3). The microstructure of a non-polished aluminum drug-packaging foil shows the presence of furrows oriented in one direction (Figure 1d). Except for certain batches of aluminum cheese-packaging foil, no furrows were observed (Figures 1a to 1c). This is probably due to the wear of the rolling mills during the manufacture of aluminum cheese-packaging foil. The furrows on the surface constitute corrosive-solution storage zones that induce differential aeration. This phenomenon causes changes in the morphology and the kinetics of corrosion and increases the dissolution of aluminum and other anodic metals. Several precipitates were seen in the aluminum drug-packaging foil (Figure 2).

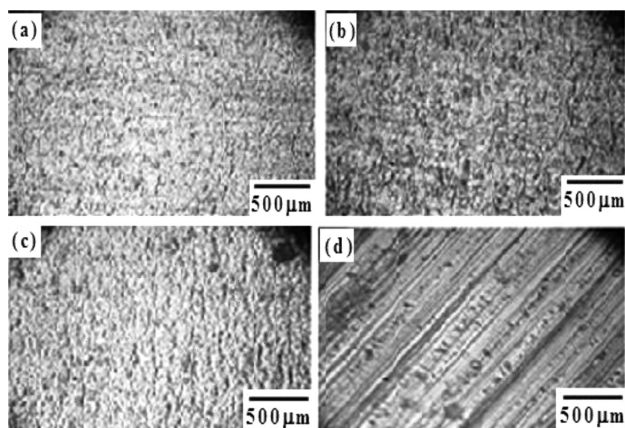


Figure 1: Microstructure of the aluminum packaging foil: a) for domestic use, b) for chocolate, c) for cheese, d) for drugs

Slika 1: Mikrostruktura aluminijevje folije: a) za gospodinjstvo, b) za čokolado, c) za sir, d) za zdravila

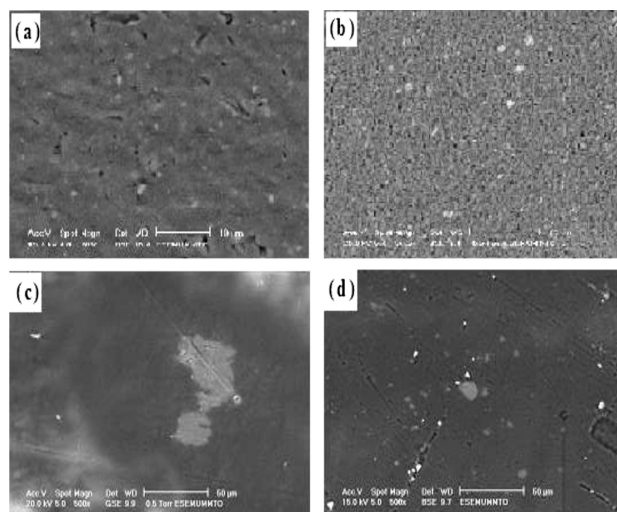


Figure 2: Micrographs of scanning electron microscopy (SEM) showing the structure of aluminum: a) for domestic use, b) for chocolate, c) for cheese, d) for drugs

Slika 2: SEM-posnetki z vrstičnim elektronskim mikroskopom (SEM), ki kaže strukturo aluminija: a) za gospodinjstvo, b) za čokolado, c) za sir, d) za zdravila

The thermomechanical history varies between different aluminum foils. On the surface perpendicular to a rolled surface, the grains appear to be small for all the aluminum foils (Figure 3). The aluminum packaging foils do not have the same thickness and the same grain size (Figure 3). The X-ray spectrum of the aluminum packaging foil intended for drugs (Figure 4) and the texture-calculating method of Muresan et al.¹⁶ show the presence of a pseudo-texture because the rates of the (220 and 311) plans exceed 50 %. This is probably due to the mechanical treatments (cold rolling) during its elaboration. This can influence the corrosion phenomena and support an oriented corrosion with privileged plans.

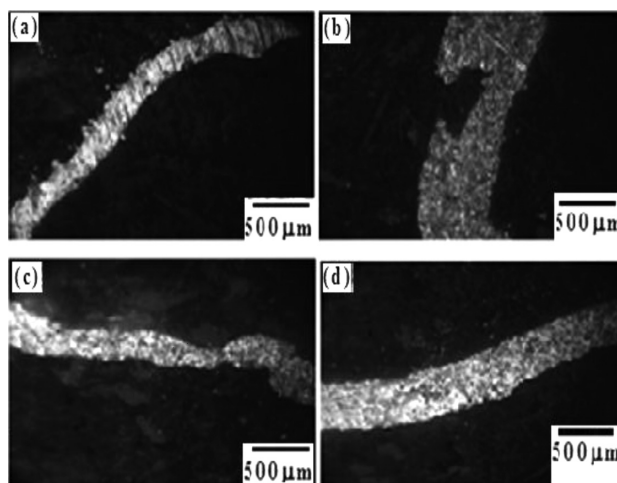


Figure 3: Perpendicular face of rolled aluminum foil for: a) domestic use, b) chocolate, c) cheese and d) drugs

Slika 3: Prečni presek valjane aluminijevje embalažne folije za: a) gospodinjstvo, b) čokolado, c) sir in d) zdravila

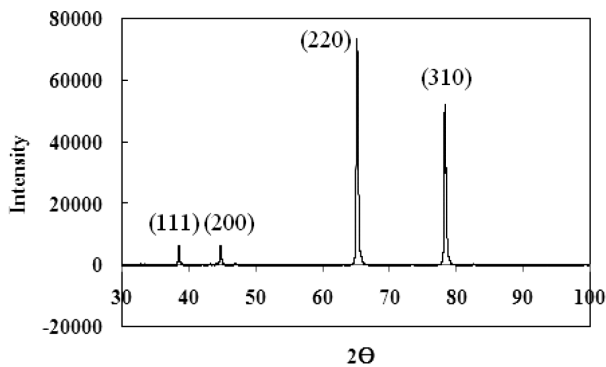


Figure 4: X-ray spectrum of the aluminum packaging foil for drugs
Slika 4: Rentgenogram aluminijeve embalažne folije za zdravila

The corrosion investigation has been studied in the presence and absence of magnetic field (Table 3, Figure 5 and 6).

3.1 Corrosion morphology of aluminum packaging foil

In order to correlate the accelerated electrochemical tests with the real corrosion phenomena of aluminum packaging foil, long-term tests involving an immersion in the 0.3 % of mass fractions of NaCl solution were realized. Figure 5 shows the corroded surfaces of various aluminum packaging foils intended for domestic use, chocolate, cheese and drugs under an light microscope after 30 d of the immersion in 0.3 % of mass fractions of NaCl at room temperature. On various aluminum packaging foils, a local destruction of the passive film was observed, having a localized-corrosion appearance. No apparent corrosion was observed on

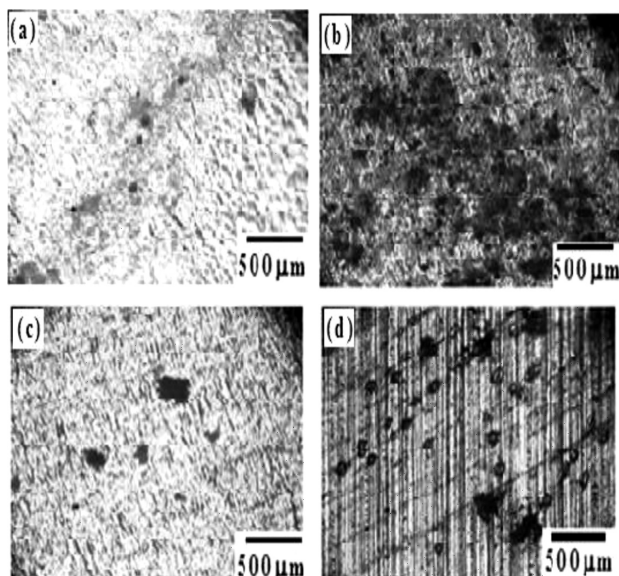


Figure 5: Microstructures of various aluminum packaging foils for: a) domestic use, b) chocolate, c) cheese and d) drugs, after 30 d of immersion in a 0.3 % NaCl solution in the absence of the magnetic field

Slika 5: Mikrostruktura različnih aluminijevih embalažnih folij za: a) gospodinjstvo, b) čokolado, c) sir in d) zdravila, po 30 dneh namakanja v raztopini 0,3 % NaCl v odsotnosti magnetnega polja

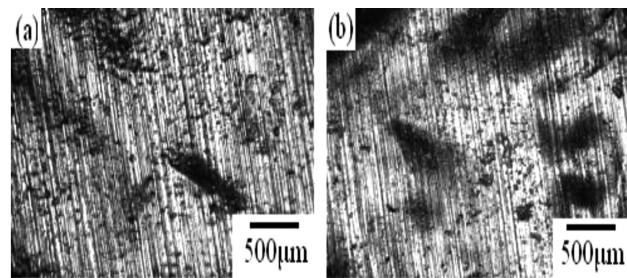


Figure 6: Microstructures of other batches of aluminum packaging after 8 d of immersion in a 3 % of mass fraction of NaCl solution: a) in the absence of the magnetic field, b) in the presence of a weak magnetic field

Slika 6: Mikrostrukturi drugih serij aluminijevih folij po 8 dneh namakanja v 3 % raztopini NaCl: a) v odsotnosti magnetnega polja, b) ob prisotnosti šibkega magnetnega polja

domestic aluminum packaging foil (Figure 5a). The surfaces of the aluminum packaging foils intended for chocolate and drugs appear to be more corroded (Figures 5b and 5d). The corrosion of the packaging foil for drugs is oriented according to the privileged direction (Figure 5d). The corrosion on the aluminum packaging foils seems to be more controlled by the precipitate and intermetallic-particle densities (Figures 1, 2 and 5).

The electrochemical responses of these alloys are related to the precipitates and intermetallic particles distributed heterogeneously on the surface, to the impurities in the aluminum packaging foils and to the chloride ions in the solution (Figures 5 and 6).

Table 3: Corrosion potential and polarization resistance of the aluminum packaging foil for cheese in the presence and absence of the magnetic field for a sample area of 1 cm² in a 0.3 % of mass fractions of NaCl medium

Tabela 3: Korozijski potencial in polarizacijska upornost aluminijeve embalažne folije za sir ob prisotnosti in odsotnosti magnetnega polja za vzorec s površino 1 cm² v 0,3 % raztopini NaCl

Sample	Corrosion potential (mV)	Polarization resistance (kΩ)
Presence of a weak magnetic field after 1 h of immersion	-560	4
Presence of a weak magnetic field after 30 d of immersion	-220	20
Absence of the magnetic field after 1 h of immersion	-645	20
Absence of the magnetic field after 30 d of immersion	-135	33

Other authors observed the presence of the AlSiFe, AlFe, AlFeMn, and AlSi phases in alloys with the compositions similar to the alloys presented in this study.¹⁷⁻¹⁹ Okeoma Kelechukwu et al.¹⁸ observed the AlFeMn and MnFe particles in the AA8011 aluminum alloy containing 0.1 % of Mn used as a packaging foil. They noticed that the presence of the Fe and Si elements in the material support the precipitation of the dispersoids and decreases the solubility of Mn in a solid solution. They also noticed that the precipitation of Mn and other inter-

metallic particles definitely causes changes in the morphology and electrochemical stability of the material system. Sanders Jr. et al.¹⁷ noticed that AA8xxx foils containing manganese in the order of 0.5 % promote the formation of (Fe, Mn)Al₆ intermetallic particles with the average diameter of 0.1–1.5 μm. Paes et al.²⁰ observed the formation of (Fe, Mn)Al_n and (Fe, Mn, Si)Al_n in the AA8006 material. Mondolfo²¹ reported the presence of the Al₃Fe and AlFeSi phases in the AA1050 aluminum. Allen et al.²² reported three phases in 1xxx-series aluminum foils such as FeAl₃, β-FeSiAl₅ and α(AlFeSi).

After immersing the aluminum material in a corrosive environment, nobler phases in the aluminum matrix such as AlSiFe, AlFe, and AlSi²³ promote the dissolution of aluminum in the matrix and the elements less noble than aluminum. However, Al_xFe_yMn_z phases can promote the dissolution of aluminum in the matrix if the iron concentration in a phase is much higher than the manganese concentration, while on the contrary Al_xFe_yMn_z is dissolved if the iron is nobler than the aluminum matrix and manganese is less noble than the matrix.^{23–25} In such cases the behavior of intermetallic particles depends principally on the potential difference between the intermetallic-particle phase and the matrix.²⁵

During cold working, precipitates and intermetallic particles are fractured and redistributed in bands along the rolling direction.²⁶ The particles that contain copper and iron represent cathodic particles compared to the matrix, supporting the matrix dissolution and the ones that contain magnesium or/and manganese represent anodic particles compared to the matrix, which dissolve preferentially.²⁶ The presence of the cathodic particles increases the susceptibility to a localized corrosion.¹⁰ Iron- and copper-rich phases are catalytic sites for cathodic reactions and the sites for pits nucleation.

Using scanning electron microscopy after 30 d of immersion, localized attacks were observed on the surfaces of several aluminum foils (**Figures 7a to 7d**), together with the destruction of the oxide-protective film,

probably due to the pitting and dissolution of aluminum due to the chloride adsorption to the surfaces, thus facilitating an aluminum oxidation of the Al³⁺ ions.²⁷ We observed the traces of aluminum oxide Al₂O₃ on the packaging foil for domestic use after the immersion (**Table 4**). All the aluminums made from the primary or recycled aluminum contain iron. Ambat et al.⁹ showed that the presence of a small concentration of iron in aluminum alloys leads to a localized corrosion due to pitting. Our results (**Figure 7**) are in good agreement with Ambat et al.⁹ The presence of chloride ions has a harmful effect on the passive-layer formation. It leads to an instability of passivation causing a localized corrosion. The material structure, composition and defects, and the oxide structure, composition and thickness have very significant influences on the aluminum-packaging-foil corrosion.

Table 4: EDS analysis of a foodstuff foil in a roll (aluminum for domestic use)

Tabela 4: EDS-analiza navite folije za živila (aluminij za domačo uporabo)

Before corrosion		Element	Energy (keV)	Concentration in mass fractions (w/%)	Concentration in amount fractions (x/%)	Error (%)
		Al	1.486	100.00	100.00	0.38
		O	–	0	0	–
After 3 months of corrosion	Zone 1	Al	1.486	95.96	93.68	1.97
		O	0.525	4.04	6.62	5.60
	Zone 2	Al	1.486	93.79	89.96	1.93
		O	0.525	6.21	10.4	5.30

The corrosion microstructures of the cheese aluminum packaging foil in the 3 % of mass fractions of NaCl solution after 8 d of immersion with or without a weak magnetic field are compared. The effect of a weak magnetic field on the morphology corrosion was observed. In the case of the absence of the magnetic field, the corrosion is located only in certain areas on the

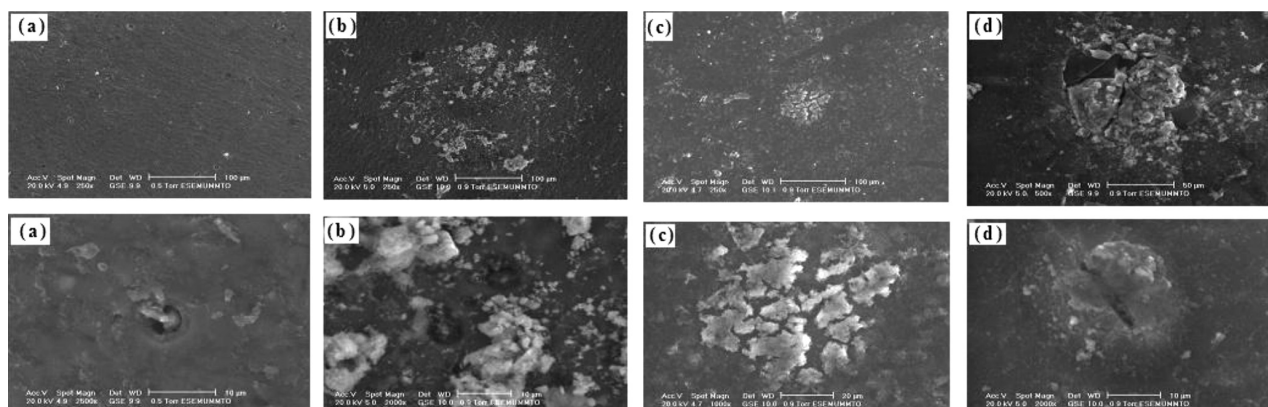
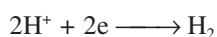


Figure 7: Morphologies of the corrosion of various aluminum packaging foils after 30 d of corrosion in a solution of 0.3 % of mass fractions of NaCl in the absence of the magnetic field: a) for domestic use, b) for chocolate, c) for cheese, d) for drugs

Slika 7: Morfologija korozije različnih aluminijevih embalažnih folij po 30-dnevni koroziji v raztopini 0,3 % NaCl in ob odsotnosti magnetnega polja: a) za gospodinjstvo, b) za čokolado, c) za sir, d) za zdravila

corroded-material surface, but with the samples corroded under a weak magnetic field, the corrosion affected a more significant area (**Figure 6**). At room temperature, iron is ferromagnetic; this characteristic can explain some changes in the morphology and the corrosion kinetics under a weak permanent magnetic field. Several authors: Devos et al.²⁸ and Nikolić²⁹ showed that an imposed magnetic field equal to or more than 0.3 T in the study of Devos et al.²⁸, and equal to 39788 A/m in the study of Nikolić²⁹ causes various effects, in particular, on the morphologies and structures of deposited metals or alloys. However, the magnetic field used was not permanent and the intensity of the field was not weak. The authors attribute these effects to the Lorentz force of electrolytic processes; this force affects the migration of ions and induces a convective flow of the electrolyte close to the electrode surface. This idea can also explain the obtained results and the difference between the corruptions with and without a weak magnetic field because the ion migration and the convective flow affect the corrosion phenomena.

Aluminum-packaging-foil environment (food and drugs) is rich in oxygen, acid and salt. Localized corrosion attacks occur due to galvanic coupling between the nobler particles and the more active aluminum-alloy matrix, and between the less noble particles and the other nobler phases (the aluminum matrix and nobler particles). A cathodic reaction of the oxygen and hydrogen reduction occurs on the cathodic precipitate surface:^{10,30}



The main anodic process, which happens in parallel with the cathodic reaction, is the dissolution of the aluminum matrix:¹⁰



In the concave environment, we observed the pitting of some aluminum packaging foil; the dissolution of intermetallic particles with a round shape can explain this observation that was also well discussed by Seri³⁰. If the less noble intermetallic particles are dissolved, they enter the corrosion solution. If this solution is food or a drug, it becomes toxic.

The investigation of the surface composition of the aluminum packaging foil before and after three months of corrosion in the 0.3 % of mass fractions of NaCl solution, using an EDS analysis, revealed that the surface of the aluminum foil for domestic use (foodstuff packaging in a roll) was not varnished because the concentration of aluminum was 100 % before the corrosion (**Table 4**). After three months of the packaging-foil corrosion, an aluminum oxide film was developed because the oxygen concentration was increased (**Table 4**). The EDS analysis of the foils intended for drugs, cheese and chocolate show that the foils were varnished, but the varnish film did not completely cover the aluminum

surface because the analysis before the corrosion showed the presence of aluminum on the surface (**Tables 5 to 7**). Part of the varnish dissolved after three months of the corrosion in the 0.3 % of mass fractions of NaCl solution as the analysis also showed an increase in the aluminum concentration on the surface (**Tables 5 to 7**). Thus, the aluminum surface became partially naked. This situation is almost the same as in the case of the aluminum for domestic use (**Table 4**).

Table 5: EDS analysis of a foil for drugs

Tabela 5: EDS-analiza folije za zdravila

	Element	Energy (keV)	Concentration in mass fractions (w/%)	Concentration in amount fractions (x/%)	Error (%)
Aluminum foil before corrosion	Al	1.486	15.05	7.86	0.31
	O	0.525	25.33	22.30	0.70
	C	0.277	59.54	69.81	0.17
	Cl	2.621	0.08	0.03	0.42
Aluminum foil after 3 months of corrosion	Al	1.486	31.60	17.64	0.68
	O	0.525	10.81	10.18	3.11
	C	0.277	57.58	72.19	1.25

Table 6: EDS analysis of a foil for cheese

Tabela 6: EDS-analiza folije za sir

	Element	Energy (keV)	Concentration in mass fractions (w/%)	Concentration in amount fractions (x/%)	Error (%)
Aluminum foil before corrosion	Al	1.486	0.68	0.37	0.13
	O	0.525	43.98	40.73	0.24
	C	0.277	43.85	54.09	0.11
	Cl	2.621	11.49	4.80	0.16
Aluminum foil after 3 months of corrosion	Al	1.486	52.61	17.64	3.61
	O	0.525	13.38	10.18	3.94
	C	0.277	34.01	72.19	1.10

Table 7: EDS analysis of a foil for chocolate

Tabela 7: EDS-analiza folije za čokolado

	Element	Energy (keV)	Concentration in mass fractions (w/%)	Concentration in amount fractions (x/%)	Error (%)
Aluminum foil before corrosion	Al	1.486	23.96	18.20	0.16
	O	0.525	04.96	6.36	0.46
	C	0.277	30.43	51.93	0.58
	Cl	2.621	40.65	23.50	0.23
Aluminum foil after 3 months of corrosion	Al	1.486	81.44	69.53	1.62
	O	0.525	1071	15.42	4.57
	C	0.277	7.87	15.06	9.06

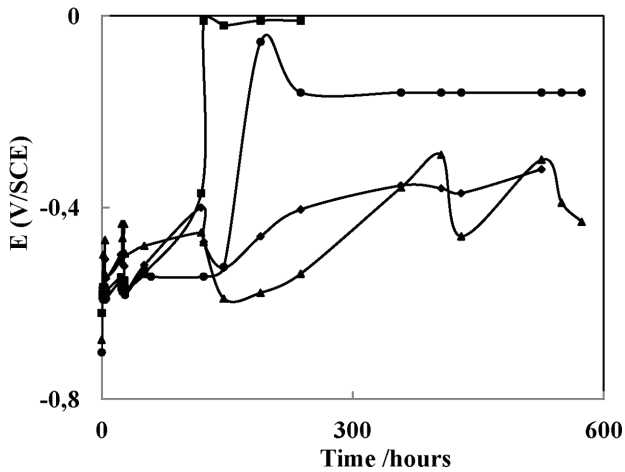


Figure 8: Open-circuit potential in the absence of the magnetic field for aluminum packaging foils for: ● drugs, ▲ domestic use, ◆ chocolate, ■ cheese

Slika 8: Potencial odprtega kroga ob odsotnosti magnetnega polja pri aluminijevi embalažni foliji za: ● zdravila, ▲ gospodinjstvo, ◆ čokolado, ■ sir

3.2 Kinetics of the corrosion and the dissolution of the aluminum packaging foil

The results considered (Figure 8) show differences between the corrosion kinetics for different aluminum packaging foils. For an open-circuit potential, the taken measurements present a high degree of dispersion of values. The initial open-circuit potential, the passivation open-circuit potential and the passivation time are different for different aluminum packaging foils. The differences are due to the chemical compositions of the matrices and the presence of different kinds of precipitates and intermetallic particles in the alloy matrices, and the differences between the chemical compositions of different foils and the thermomechanical-treatment histories of the samples.

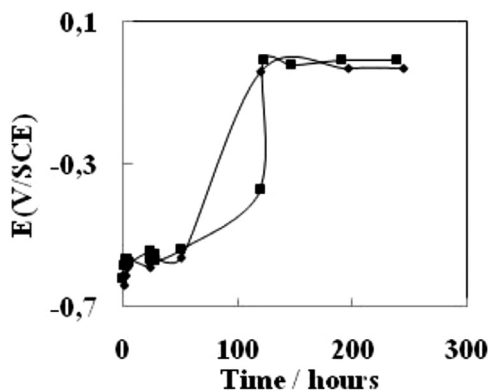


Figure 9: Corrosion-free potential of the aluminum packaging foil for cheese in a 0.3 % of mass fractions of NaCl solution: ■ absence of the magnetic field, ◆ presence of a weak magnetic field

Slika 9: Korozijski prosti potencial aluminijeve embalažne folije za sir v raztopini 0,3 % NaCl: ■ odsotnost magnetnega polja, ◆ prisotnost šibkega magnetnega polja

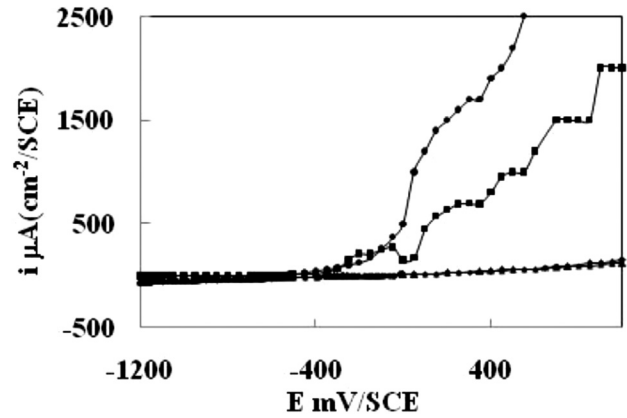


Figure 10: Polarization curves of the aluminum packaging foil for cheese in a 0.3 % of mass fractions of NaCl solution: ● presence of a weak magnetic field 1 h after the immersion, ■ absence of the magnetic field 1 h after the immersion, ◆ absence of the magnetic field 30 d after the immersion, ▲ presence of a weak magnetic field 30 d after the immersion

Slika 10: Polarizacijske krivulje aluminijeve embalažne folije za sir v raztopini 0,3 % NaCl: ● prisotnost šibkega magnetnega polja 1 h po potopitvi, ■ odsotnost magnetnega polja 1 h po potopitvi, ◆ odsotnost magnetnega polja po 30-dnevnem namakanju, ▲ prisotnost šibkega magnetnega polja po 30-dnevnem namakanju

A complete electrochemical study of the aluminum packaging foil with and without a weak magnetic field was carried out only for the aluminum packaging foil intended for cheese, because cheese has to be preserved in a refrigerator. The open-circuit potential at the immersion time of the aluminum packaging foil for cheese is -0.62 V in the absence of the magnetic field and -0.638 V in the presence of a weak magnetic field (Figure 9). The presence of a weak magnetic field seems to influence the corrosion kinetics in the first moments of

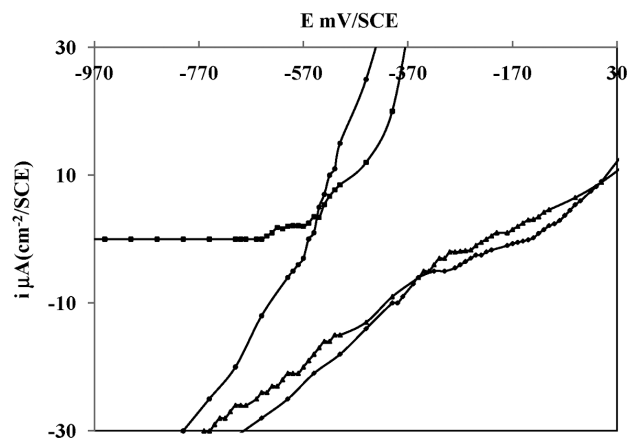


Figure 11: Magnifying-glass effect of polarization curves of the aluminum packaging foil for cheese in a 0.3 % of mass fractions of NaCl solution: ● presence of a weak magnetic field 1 h after immersion, ■ absence of the magnetic field 1 h after immersion, ◆ absence of magnetic field 30 d after immersion, ▲ presence of weak magnetic field 30 d after immersion

Slika 11: Povečan izsek polarizacijske krivulje aluminijeve embalažne folije za sir v 0,3 % raztopini NaCl: ● prisotnost šibkega magnetnega polja 1 h po namočitvi, ■ odsotnost magnetnega polja 1 h po namočitvi, ◆ odsotnost magnetnega polja 30 dni po namočitvi, ▲ prisotnost šibkega magnetnega polja 30 dni po namočitvi

immersion. The magnetic-field effect appears more visible later. The open-circuit potentials of the aluminum packaging foil for cheese with and without a magnetic field converge towards the same potential value of -0.03 V at the stationary regime and after 122 h of immersion (Figure 9).

Figure 10 represents polarization curves of the aluminum packaging foil intended for cheese and Figure 11 represents the magnifying-glass effect of the polarizations curves in the absence and presence of a weak magnetic field after 1 h and after 30 d of immersion. The presence of a weak magnetic field seems to increase the potential of corrosion at the beginning of corrosion and decrease it after 30 d of immersion (Figures 10 and 11; Table 3), but the passivation-current density seems to be increased at the beginning of corrosion in the presence of a magnetic field (Figures 9 and 10). We also observed that the presence of a weak magnetic field decreases the polarization resistance at the beginning and after 30 d of corrosion (Table 3), and decreases the passivation potential at the beginning (Figures 10 and 11). Thus, a weak magnetic field modifies the corrosion kinetics and aluminum-packaging-foil dissolution as soon as the corrosion starts. This result is in good agreement with the work of Devos et al.³¹, except that the minimum magnetic field applied by Devos et al.³¹ was a few hundreds of mT.

The corrosion kinetics of aluminum packaging foils in the 0.3 % of mass fractions of NaCl solution (Figures 8 to 10) compared to the work of Seri³⁰ who studied the Al1.4%Fe aluminum alloy, is different. This dissimilarity is due to the difference between the chemical compositions of the alloys or to the disparity between the surface residual stresses.⁷

4 CONCLUSION

Based on the study combining microscopy, X-ray diffraction, electrochemistry tests of aluminum packaging foil and the EDS results, the following conclusions were made:

- Various aluminum packaging foils underwent a localized corrosion in a 0.3 % of mass fractions of NaCl solution, showing that the morphologies and the corrosion kinetics are different for different foils, depending on the chemical composition of the surface.
- The application of a weak magnetic field modifies the morphology and the kinetics of corrosion, decreasing the polarization resistance, the passivation potential and the corrosion potential at the beginning of corrosion. However, it increases the density of passivation current 1 h after the immersion of the cheese aluminum packaging foil, increases the corrosion potential after 1 h of corrosion and decreases the corrosion potential after 30 d of corrosion.

- X-ray diffraction results show the presence of a textured structure with a preferential orientation.
- The passivation of the aluminum packaging foil intended for cheese takes place after 122 h of corrosion in the absence and the presence of a weak magnetic field.
- The food packed in aluminum packaging foil can be contaminated by the aluminum metal.
- The EDS results show the presence of aluminum oxide on the surface after three months of corrosion.

5 REFERENCES

- ¹ M. Elboudjani, E. Ghali, A. Galibois, Corrosion par piqûre des alliages d'aluminium 5083-H321 et 6061-T651, *Journal of Applied Electrochemistry*, 18 (1988) 2, 257–267, doi:10.1007/BF01009273
- ² S. W. Dean, W. H. Anthony, Atmospheric corrosion of wrought aluminum alloys during a ten-year period, In: S. W. Dean, T. S. Lee (Eds.), *Degradation of Metals in the Atmosphere*, ASTM STP 965, American Society for Testing and Materials, Philadelphia 1988, 191–205
- ³ F. L. McGeary, T. J. Summerson, W. H. Ailor, Atmospheric Exposure of Nonferrous Metals and Alloys-Aluminium: Seven-Year Data, *Metal Corrosion in the Atmosphere*, ASTM STP 435, American Society for Testing and Materials, Philadelphia 1968, 141–174
- ⁴ I. T. E. Fonseca, N. Lima, J. A. Rodrigues, M. I. S. Pereira, J. C. S. Salvador, M. G. S. Ferreira, Passivity breakdown of Al 2024-T3 alloy in chloride solutions: attest of the point defect model, *Electrochemistry Communications*, 4 (2002) 5, 353–357, doi:10.1016/S1388-2481(02)00273-4
- ⁵ A. Aballe, M. Bethencourt, F. J. Botana, M. J. Cano, M. Marcos, Influence of the cathodic intermetallics distribution on the reproducibility of the electrochemical measurements on AA5083 alloy in NaCl solutions, *Corrosion Science*, 45 (2003) 1, 161–180, doi:10.1016/S0010-938X(02)00067-7
- ⁶ E. J. Lee, S. I. Pyun, The effect of oxide chemistry on the passivity of aluminium surfaces, *Corrosion Science*, 37 (1995) 1, 157–168, doi:10.1016/0010-938X(94)00127-R
- ⁷ N. Zazi, A. Bouabdallah, O. Aaboubi, J. P. Chopart, Pretreatment effects on the electrochemical responses for aluminium-magnesium alloy AA5083 corrosion behavior, *Journal of Solid State Electrochemistry*, 14 (2010) 9, 1705–1711, doi:10.1007/s10008-010-1021-0
- ⁸ H. Ezuber, A. El-Houd, F. El-Shawesh, A Study on the corrosion behavior of aluminum alloys in seawater, *Materials and Design*, 29 (2008) 4, 801–805, doi:10.1016/j.matdes.2007.01.021
- ⁹ R. Ambat, A. J. Davenport, G. M. Scamans, A. Afseth, Effect of iron-containing intermetallic particles on the corrosion behavior of aluminium, *Corrosion Science*, 48 (2006) 11, 3455–3471, doi:10.1016/j.corsci.2006.01.005
- ¹⁰ K. A. Yasaku, M. L. Zheludkevich, S. V. Lamaka, M. G. S. Ferreira, Role of intermetallic phases in localized corrosion of AA5083, *Electrochimica Acta*, 52 (2007) 27, 7651–7659, doi:10.1016/j.electacta.2006.12.072
- ¹¹ H. H. P. Fang, L. C. Xu, K. Y. Chan, Effects of toxic metals and chemicals on biofilm and biocorrosion, *Water Research*, 36 (2002) 19, 4709–4716, doi:10.1016/S0043-1354(02)00207-5
- ¹² T. Ramdé, L. Bonou, B. Guel, J. B. Legma, Comportement à la corrosion des alliages d'aluminium recyclés pour la confection de marmites, *Journal de la Société Ouest-Africaine de Chimie*, 026 (2008), 113–121
- ¹³ R. A. Tacke, L. J. J. Janssen, Applications of magneto-electrolysis, reviews of applied electrochemistry, *Journal of Applied Electrochemistry*, 25 (1995) 1, 1–5, doi:10.1007/BF00251257
- ¹⁴ Federal Office for Radiation Safety, World Health Organisation, Germany 1999

- ¹⁵ M. Marciszko, A. Baczanski, K. Wierzbowski, M. Wróbel, C. Braham, J. P. Chopart, A. Lodini, J. Bonarski, L. Tarkowski, N. Zazi, Application of multireflection grazing incidence method for stress measurements in polished Al–Mg alloy and CrN coating, *Applied Surface Science*, 266 (2013) 1, 256–267, doi:10.1016/j.apsusc.2012.12.005
- ¹⁶ L. Muresan, L. Oniciu, M. Froment, G. Murin, Inhabitation of lead electrocrystallization by organic additives, *Electrochimica Acta*, 37 (1992) 12, 2249–2254, doi:10.1016/0013-4686(92)85119-6
- ¹⁷ R. E. Sanders Jr., P. A. Hollinshead, E. A. Simielli, Industrial Development of Non-Heat Treatable Aluminum Alloys, *Materials Forum*, 28 (2004), 53–64
- ¹⁸ B. Okeoma Kelechukwu, O. Owate Israel, E. Oguzie Emeka, M. Mejehe Ihebrodike, Effects of Heat Treatment on the Electrochemical Corrosion Behaviour of Aluminum Alloy AA8011 in 0.1M H₂SO₄ Aqueous Acid Media, *International Journal of Materials and Chemistry*, 2 (2012) 4, 178–184, doi:10.5923/j.ijmc.20120204.11
- ¹⁹ O. Keles, M. Dunder, Aluminum foil: Its typical quality problems and their causes, *Journal of Materials Processing Technology*, 186 (2007) 1, 125–137, doi:10.1016/j.jmatprotec.2006.12.027
- ²⁰ M. Paes, W. Gonçalves, E. J. Zoqui, Effect of grain refining and homogenizing treatment on Al-Fe-Mn-Si cast alloys, 18th International Congress of Mechanical Engineering, Ouro Preto, MG, Brazil, 2005
- ²¹ L. F. Mondolfo, *Aluminium Alloys: Structure and Properties*, Butterworths, London 1976
- ²² C. M. Allen, K. A. Q. O'Reilly, B. Cantor, P. V. Evans, Intermetallic phase selection in lxxx Al alloys, *Progress in Materials Science*, 43 (1998) 2, 89–170, doi:10.1016/S0079-6425(98)00003-6
- ²³ N. Birbilis, R. G. Buchheit, Electrochemical Characteristics of Intermetallic Phases in Aluminum Alloys, *Journal of The Electrochemical Society*, 152 (2005) 4, 140–151, doi:10.1149/1.1869984
- ²⁴ A. J. Bard, R. Parsons, J. Jordan, *Standard Potentials in Aqueous Solutions*, IUPAC, Marcel Dekker, New York USA 1985
- ²⁵ Z. Szklarska-Smialowska, Pitting corrosion of aluminum, *Corrosion Science*, 41 (1999) 9, 1743–1767, doi:10.1016/S0010-938X(99)00012-8
- ²⁶ F. Andreatta, M. M. Lohrengel, H. Terryn, J. H. W. de Wit, Electrochemical characterisation of aluminium AA7075-T6 and solution heat treated AA7075 using a micro-capillary cell, *Electrochimica Acta*, 48 (2003) 20, 3229–3247, doi:10.1016/S0013-4686(03)00379-7
- ²⁷ S. Berrada, M. Elboudjaini, E. Ghali, Comportement électrochimique des alliages d'aluminium 2024 ET 7075 dans un milieu salin, *Journal of Applied Electrochemistry*, 22 (1992) 11, 1065–1071, doi:10.1007/BF01029586
- ²⁸ O. Devos, A. Olivier, J. P. Chopart, O. Aaboubi, G. Maurin, Magnetic Field Effects on Nickel Electrodeposition, *Journal of The Electrochemical Society*, 145 (1998) 2, 401–405, doi:10.1149/1.1838276
- ²⁹ N. D. Nikolić, Some aspects of nickel electrodeposition in the presence of a magnetic field, *Journal of the Serbian Chemical Society*, 70 (2005) 10, 1213–1217, doi:10.2298/JSC0510213N
- ³⁰ O. Seri, The effect of NaCl concentration on the corrosion behavior of aluminum-containing iron, *Corrosion Science*, 36 (1994) 10, 1789–1803, doi:10.1016/0010-938X(94)90132-5
- ³¹ O. Devos, O. Aaboubi, J. P. Chopart, E. Merienne, A. Olivier, J. Amblard, Magnetic Field Effects on Nickel Electrodeposition II. A Steady-State and Dynamic Electrochemical Study, *Journal of The Electrochemical Society*, 145 (1998) 12, 4135–4139, doi:10.1149/1.1838927

CHARACTERISTICS OF THE AlTiCrN+DLC COATING DEPOSITED WITH A CATHODIC ARC AND THE PACVD PROCESS

ZNAČILNOSTI AlTiCrN+DLC PREVLEKE, NANEŠENE S KATODNIM OBLOKOM IN PACVD POSTOPKOM

Krzysztof Lukaszewicz¹, Ewa Jonda¹, Jozef Sondor^{2,3,4}, Katarzyna Balin^{3,4}, Jerzy Kubacki^{3,4}

¹Institute of Engineering Materials and Biomaterials, Silesian University of Technology, Konarskiego St. 18A, 44-100 Gliwice, Poland

²LISS, Dopravni 2603, 756 61 Rožnov p.R., Czech Republic

³A. Chelkowski Institute of Physics, University of Silesia, Uniwersytecka 4, 40-007 Katowice, Poland

⁴Silesian Center for Education and Interdisciplinary Research, University of Silesia, 75 Pulku Piechoty 1A, 41-500 Chorzów, Poland
krzysztof.lukaszewicz@polsl.pl

Prejem rokopisa – received: 2014-07-13; sprejem za objavo – accepted for publication: 2015-03-23

doi:10.17222/mit.2014.104

A coating system composed of the AlTiCrN film covered with diamond-like carbon (DLC)-based lubricant, deposited on a hot-work tool-steel substrate was the subject of the research. The AlTiCrN and DLC layers were deposited with a cathodic arc and the PACVD technology on the X40CrMoV5-1.

A HRTEM investigation showed an amorphous character of the DLC layer. It was found that the tested AlTiCrN layer has a columnar character with fine crystallites. Based on the XRD analysis, the fcc type of the crystal structure was proposed for this layer. Combined studies including SEM, AES and ToF-SIMS confirmed the chemical composition and layered structure of the coating. The chemical distributions of the elements inside the layers and at the interfaces were analyzed with the SEM and AES methods. It was shown that an additional layer of Cr and AlTiN is present between the substrate and the AlTiCrN coating. In sliding dry-friction conditions, the friction coefficient for the investigated elements is set in the range of 0.02–0.03. The investigated coating revealed a high wear resistance. The coating demonstrated a good adhesion to the substrate.

Keywords: AlTiCrN film, DLC film, TEM, SEM, AES, ToF-SIMS, chemical composition, tribological properties

Predmet preiskave je bil sestavljen sistem AlTiCrN plasti, pokritih z diamantu podobnim ogljikom (DLC)- kot mazivom, ki je bil nanešen na podlago iz orodnega jekla, za delo v vročem. AlTiCrN in DLC plasti so bile nanešene s tehnologijo katodnega ARC in PACVD na X40CrMoV5-1.

HRTEM-preiskava je pokazala amorfne značilnosti DLC plasti. Ugotovljeno je bilo, da ima preiskovana plast AlTiCrN stebrasta drobna kristalna zrna. Na osnovi XRD analize je za to plast predlagana ploskovno centrirana kubična (fcc) kristalna zgradba. Kombinirane SEM, AES in ToF-SIMS študije so potrdile kemijsko sestavo in plasti v zgradbi nanosa. Razporeditev kemijskih elementov v plasteh in na stiku je bila analizirana s SEM in AES metodami. Ugotovljeno je, da je dodatna plast Cr in AlTiN prisotna med podlago in AlTiCrN nanosom. Pri pogojih suhega drsenja je bil koeficient trenja postavljen v območje med 0,02–0,03. Preiskovan nanos je pokazal veliko odpornost na obrabo in dobro oprijemljivost na podlago.

Ključne besede: plast AlTiCrN, plast DLC, TEM, SEM, AES, ToF-SIMS, kemijska sestava, tribološke lastnosti

1 INTRODUCTION

Rapid advancements in modern industries, including plastic fabrication, mostly depend on the capabilities of the surface engineering.^{1,2} A wide range of the currently available types of coatings and deposition technologies is a result of a growing demand, in the recent years, for modern-material surface-modification and protection methods. Currently, from among a myriad of the techniques enhancing the tool life, the CVD (chemical vapour deposition) and PVD (physical vapour deposition) methods are playing an important role in industrial practice.³ An innovative approach in the surface treatment is the application of hybrid technologies providing a broad range of the types of the associated processes, allowing the fabrication of a whole array of materials with unique properties for precisely defined applications,

unachievable with the standard surface-treatment methods.^{4,5}

The coatings produced with the PVD technique are recognised as one of the very interesting premium technologies for modifying and protecting tool surfaces, due to the possibility to synthesize the materials with unique chemical and physical properties. One of the most effective and universal coatings of this type is the AlTiCrN hard coating. AlTiCrN coatings were developed for wet and dry machining, as well as forming due to the stability of their mechanical characteristics at elevated temperatures.^{6,7} Diamond-like carbon (DLC) films showed a considerable potential for wear-resistant coatings due their low friction coefficients and a good wear resistance, particularly under dry-friction conditions. Their beneficial tribological properties come from smooth surfaces and good tribochemistry, leading to the

formation of graphite-rich layers acting as a solid lubricant.^{8–10} DLC films have been produced with various deposition techniques such as PACVD (plasma-assisted chemical vapour deposition), magnetron sputtering, PLD (pulsed-laser deposition) etc.

The aim of this work is to examine the microstructure, mechanical and tribological properties of the AlTiCrN+DLC coating system.

2 EXPERIMENTAL DETAILS

The examinations were made on the X40CrMoV5-1 hot-work tool steel covered with the AlTiCrN+DLC coating. The AlTiCrN film was deposited with the cathodic-arc technology (coating machine PLATIT PL1000). Coating depositions were carried out in an Ar and N₂ atmosphere. Cathodes containing pure Cr and the AlTi alloy (67:33 amount fractions) were used for the coating deposition. To improve the adhesion of the coatings, the Cr and AlTi cathodes were started to burn and form the Cr and AlTiN adhesion layer. The DLC topcoat was deposited using acetylene (C₂H₂) as the gas precursor in a PLATIT π 300+DLC unit. The DLC layer was produced with the PACVD. The deposition conditions are summarized in **Table 1**.

The cross-sections of the deposited coatings were mapped with a SUPRA 35 scanning electron microscope (SEM). Detection of secondary electrons was used for generating fracture images with a 4 kV bias voltage.

Table 1: Coating-deposition parameters

Tabela 1: Parametri nanašanja plasti

Parameter	AlTiCrN	DLC
Working pressure (Pa)	2.5	2.0
Substrate bias voltage (V)	-50	-500
Target current (A)	Cr – 140 AlTi – 120	–
Process temperature (°C)	430	220

The diffraction and thin-film microstructures were tested with a TITAN 80-300 ultrahigh-resolution scanning/transmission electron microscope. The thin cross-section lamellas for TEM observations were prepared with the focused-ion-beam (FIB) technique using a Quanta 200i instrument with gallium ions.

Raman spectroscopy was used to identify the sp^3/sp^2 bond ratio and the chemical bond of the DLC film. Raman measurements were performed at room temperature with an inVia-Raman microscope (Renishaw) with a 514.5 nm Ar⁺ laser and a resolution of 1 cm⁻¹.

X-ray diffraction studies of the analyzed coatings were carried out on an X'Pert PRO system made by the Panalytical Company using the filter radiation of a cobalt anode lamp. The phase identification of the investigated coatings was carried out in the Bragg-Brentano geometry (XRD) and in the grazing-incidence geometry (GIXRD).

The measurements of the stresses of the analyzed coatings were made with $\sin^2\psi$ on the basis of the X'Pert Stress Plus program. In the method of $\sin^2\psi$ based on the displacement effect of diffraction lines for different ψ angles, appearing in the stress conditions of the materials with a crystalline structure, a silicon strip detector was used at the side of the diffracted beam. The sample inclination angle ψ towards the primary beam was changed in the range of 0°–75°.

The layered structure of the coating was tested with a depth-profile measurement performed with the ToF-SIMS method. Time-of-flight secondary-ion mass spectrometry (ToF-SIMS) experiments were performed using a TOF.SIMS 5 (ION-TOF GmbH, Munster, Germany) reflection-type spectrometer equipped with a bismuth-liquid metal-ion gun. A focused high-energy primary-ion beam (pulsed 30 keV Bi⁺ ions at an ion current of ~1 pA) was aimed at the sample surface at an angle of 45° relative to the surface normal causing the emission of secondary ions. Secondary-ion spectra and distribution maps were collected by rastering the ion beam across areas of 300 $\mu\text{m}^2 \times 300 \mu\text{m}^2$ in a m/z range of 1–800 u. For the depth profiling, an etching Cs gun (2 kV, 100 nA) was also used in the alternating mode with the analysis bismuth gun. The raster of the analysis beam (300 $\mu\text{m}^2 \times 300 \mu\text{m}^2$) was centred inside the etching one (500 $\mu\text{m}^2 \times 500 \mu\text{m}^2$).

The chemical composition of the cross-section of the coating was tested with the Auger electron spectroscopy (AES) method. The measurements were carried out with a PHI 5700/660 Physical Electronics spectrometer. A Xe⁺ ion gun was used to create a crater through all the layers of the sample. Then, the obtained crater was analyzed with scanning electron microscopy (SEM) and Auger electrons (AES). The chemical distributions of particular elements in the coating were tested along the selected line across the crater using Auger electrons. The atomic concentration of the main elements of the coating was calculated from the Al, Ti, Cr, N, Fe, O and C Auger lines using the MULTIPAK software (version 9.5.0.8, Ulvac-phi, Inc.).

The adhesion of the coating to the substrate material was verified with a scratch test on a CSM REVETEST device, by moving the diamond indenter along the examined specimen surface with a gradually increasing load. The tests were made using the following parameters: a load range of 0–100 N, a load-increase rate (dL/dt) of 100 N/min, the indenter sliding speed (dx/dt) of 10 mm/min, and the acoustic-emission detector sensitivity (AE) of 1. The critical load L_{C2} , causing a loss in the coating adhesion to the material, was determined on the basis of the values of the acoustic emission (AE) and the recorded friction force (F_i) as well as the observations of the damage developed during the scratch test on a LEICA MEF4A light microscope.

The friction coefficient and the wear rate of the coating were determined with a ball-on-disc test. The

tests were carried out on a T-01M (ITE) device with the following parameters: a sliding speed of 0.2 m/s, a normal load of 20 N, an Al₂O₃ counterpart of a 10 mm diameter, a sliding distance of 1000 m, a temperature of 22 °C (± 1 °C) and a relative humidity of 30 % (± 5 %). To determine the wear rate of the coating (k_{vc}) and the wear rate of the counterpart (k_{vb}), the procedure proposed by Wänstrand et al.¹¹ was used.

3 RESULTS AND DISCUSSION

3.1 Surface and structural studies of the coating

The cross-section of the investigated coating is presented in **Figure 1**. The coating presents a compact structure; there is no trace of any coating delamination. The morphology of the DLC layer is characterized by a dense microstructure. A columnar structure is noticed only for the AlTiCrN layer. A clear boundary line is visible between the AlTiCrN and DLC layers. The adhesion layer between AlTiCrN and the steel substrate is not as well defined but still visible on the SEM image. The measured thickness values of the DLC and AlTiCrN layers and the adhesion layer are approximately 1.9, 1.2 and 120 nm, respectively.

Subsequently, for the coating structure characterization, TEM and HRTEM microscopes were used. The images, presented in **Figure 2**, were obtained from selected regions. The bright-field images (**Figure 2a**) and the HRTEM micrograph (**Figure 2b**) show an amorphous character of the DLC films. As expected, the electron-diffraction patterns obtained show a considerable broadening of diffraction rings (the inset image in **Figure 2a**).

A structural study of the DLC coating was carried out with the Raman spectroscopy. **Figure 2c** shows a Raman spectrum, decomposed into two Gaussian line shapes. In the current study, the Raman spectra of the DLC layer reveal two broad bands, located at 1403 cm⁻¹ and 1572

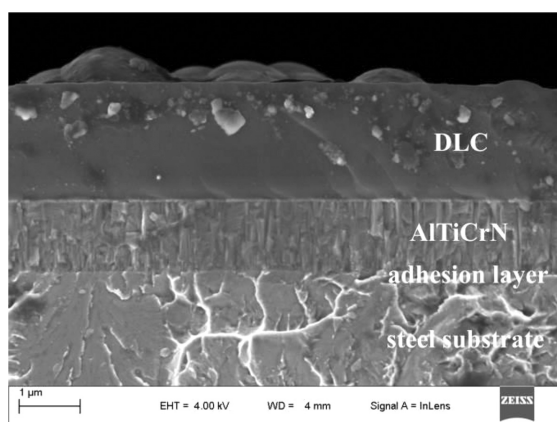


Figure 1: SEM fracture image of the AlTiCrN+DLC coating deposited on the steel substrate

Slika 1: SEM-posnetek preloma AlTiCrN+DLC nanosa na podlagi iz jekla

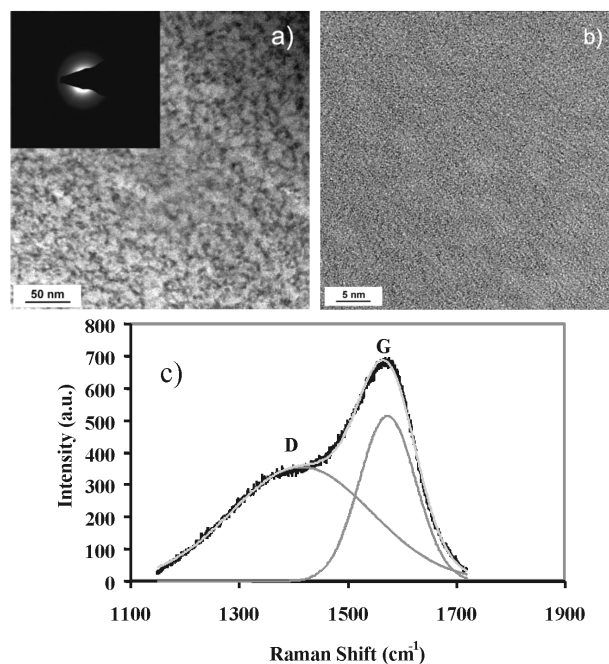


Figure 2: DLC top layer: a) TEM bright-field image and electron-diffraction pattern, b) HRTEM micrograph, c) Raman spectra of DLC layer

Slika 2: DLC vrhnja plast: a) TEM-posnetek svetlega polja in uklon elektronov, b) HRTEM-posnetek, c) Ramanski spektri DLC plasti

cm⁻¹, designated as the D and G peaks, respectively, typically observed in diamond-like carbon coatings.¹²

A columnar structure of the AlTiCrN layer was observed (**Figure 3a**). In addition, it was also found that the

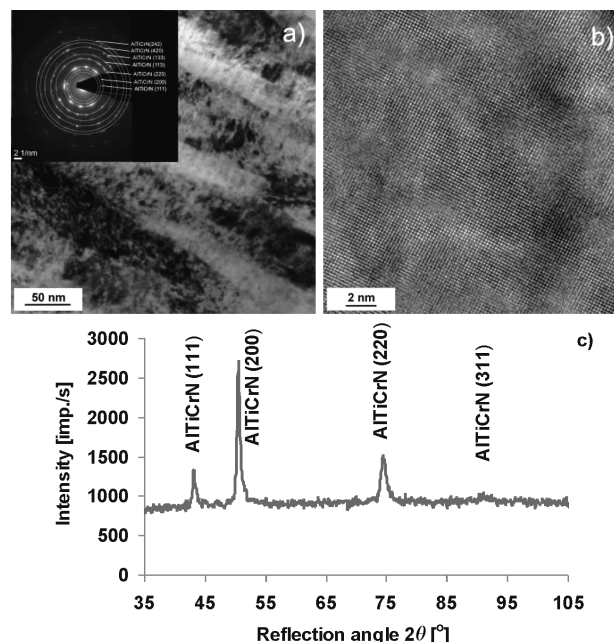


Figure 3: AlTiCrN film: a) TEM bright-field image and electron-diffraction pattern, b) HRTEM micrograph, c) GIXRD spectra at an incidence angle of $\alpha = 3^\circ$

Slika 3: AlTiCrN nanos: a) TEM-posnetek svetlega polja in uklon elektronov, b) HRTEM-posnetek, c) GIXRD-spektri pri vpadnem kotu $\alpha = 3^\circ$

layer features a compact structure with a high homogeneity (**Figure 3b**). Fine grains were observed in the big columnar grains of this film, and within one column, the grains are similarly oriented.

On the basis of the results of the GIXRD pattern for the AlTiCrN film, presented in **Figure 3c**, four reflexes (111), (200), (220) and (311) are shown, corresponding to interplanar spacings of (0.239, 0.207, 0.146, 0.125) nm, respectively, which are characteristic of the CrN cubic phase. The rate of the intensity of the detected reflexes indicates the presence of the fcc-type crystal structure for the AlCrTiN layer.

Two subzones – Cr and AlTiN (**Figure 4a**) – can be differentiated for the transition zone between the hard AlTiCrN layer and the substrate material. **Figure 4b** presents the electron-diffraction pattern and HRTEM micrograph obtained for the AlTiN film deposited between the substrate and the AlTiCrN layer.

3.2 Chemical composition of the coating

The chemical composition of the coating can be recognized from **Figure 5**, where the result of the ToF-SIMS depth profile is presented. The distribution of the intensity for H⁺, O⁺, N⁺, C⁺, Ti⁺, Cr⁺, Al⁺ and Fe⁺ ions confirmed a layered structure of the test sample. Three different uniform layers can be distinguished. An analysis of the molecular signals of carbon and hydrogen ions indicates that the first layer can be linked with the outermost hydrogenated DLC layer of the coating. The molecular signals of C⁺ and H⁺ drop rapidly when the second layer containing Al, Ti, Cr and N is exposed. The second layer corresponds to the PVD-grown AlTiCrN film. The molecular signals of the Al⁺, Ti⁺, Cr⁺ and N⁺ ions are roughly constant throughout the width of this layer although, at the interfaces of DLC/AlTiCrN and AlTiCrN/substrate, some changes can be observed in the depth profiles of the selected Al⁺, Ti⁺, Cr⁺ ions.

Additionally, at the interface of DLC/AlTiCrN a small signal from the oxygen ions was detected. An increase in the counts of Ti⁺, Cr⁺ and Al⁺ in the transition

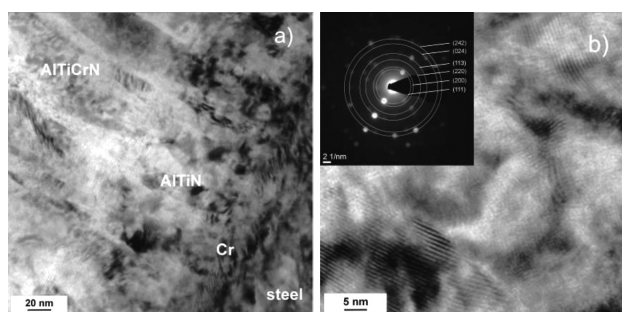


Figure 4: a) Structure of the transition zone between the AlTiCrN layer and substrate material, b) TEM bright-field image and electron-diffraction pattern of the AlTiN interlayer

Slika 4: a) Struktura prehodnega področja med AlTiCrN plastjo in podlago, b) TEM-posnetek svetlega polja in uklona elektronov v AlTiN vmesni plasti

zone of DLC is associated with the border-exposure values of the elements at the start of the deposition, suggesting the presence of an additional layer composed of the Al, Ti and Cr atoms. However, the increase in the counts in the transition zone may also be related with the specific conditions of the deposition process. The observed increase in the Cr counts in the transition region between AlTiCrN and the substrate confirmed the presence of the adhesion layer. However, a clear depth profile of the Cr signal observed before the visible maximum and the increase in the Al and Ti counts suggested the presence of another additional layer, detected in **Figure 4a**.

In the region of the substrate, the signals of Fe and Cr were detected at a stable level. A small signal of carbon was also detected for this part of the tested coating. The small counts observed in the case of the nitrogen ions are a result of a small cross-section of the positive ionization process for the nitrogen ions. The presented analysis of the ToF-SIMS measurement is compared with the AES results in the next section of this article. It is noted that the distribution of the particular elements in the structure of the sample was obtained during the Cs sputtering process in ultra-high vacuum conditions. Hence, it is the real composition of the coating without the presence of adsorbates.

In order to obtain the information about the chemical distribution and atomic concentration of the coating, a study combining SEM and AES was performed. At the beginning, a crater area was obtained using the sputtering method (the sputtering process was described in detail in the experimental-detail section) on all the layers of the coating. The size of the crater was about two millimeters. Next, particular surface parts of the crater area were analyzed with Auger electron spectroscopy (AES).

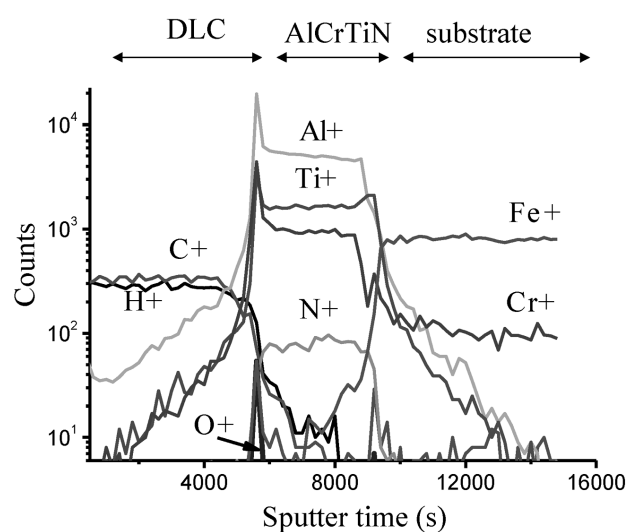


Figure 5: ToF-SIMS depth profile of the tested coating obtained for positive ions

Slika 5: ToF-SIMS globinski profil preiskovanega nanosa s pozitivnimi ioni

In **Figure 6a**, a SEM image of the coating interface, obtained with the sputtering process, is presented. Auger differentiation spectra (**Figure 6b**) were obtained from the marked points of the SEM photography. The top spectrum containing only a C KLL signal was detected from the outermost DLC layer. The middle spectrum contains the signals corresponding to the Al KLL, Cr LMM, Ti LMM and N KLL Auger transitions. A small signal of carbon contamination occurred at a kinetic energy of 279 eV. The obtained results are in agreement with the ToF-SIMS study, where carbon was also detected in the AlTiCrN layer (**Figure 5**). The spectrum recorded for the substrate area consists of groups corresponding to the oxygen and iron Auger transitions. The presence of oxygen in the substrate of the coating is a result of the adsorption process involving the residual gases of the tested sample, taking place during the long measurement. The adsorption process is discussed together with the analysis of the line-profile results.

In **Figures 7a** and **7b** the results of the chemical distribution of particular elements, detected along the marked line on the attached SEM picture are presented. It should be noted that the x -axis on the SEM image and the line-profile curves represent the dimensions in the lateral plane, not in the depth of the coating. Three different areas can be distinguished on the top images in **Figures 7a** and **7b**. The first, dark region between 0 μm

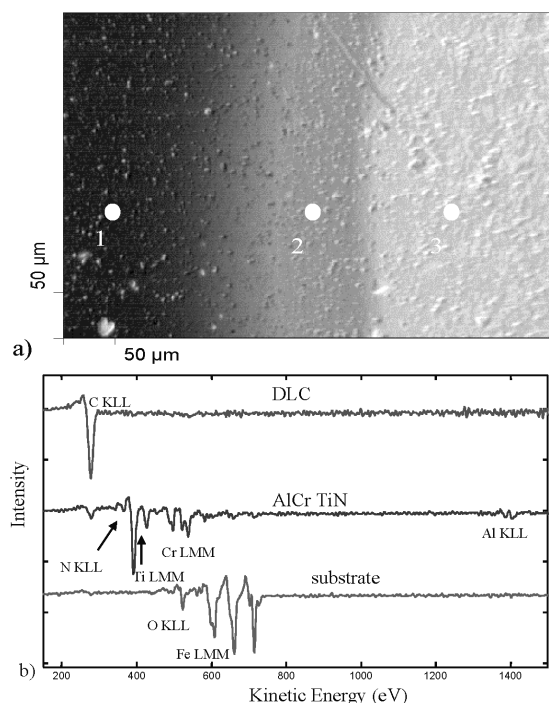


Figure 6: SEM image of the cross-section of the test coating: obtained with the argon-sputtering process. The Auger differentiation spectra, recorded for various parts of the area, are marked as points 1, 2 and 3.

Slika 6: SEM-posnetek prečnega prereza preizkušane nanosa: pridobljen z jedkanjem z argonom. Augerjevi diferencirani spektri zapsani iz različnih področij so označeni kot točke 1, 2 in 3.

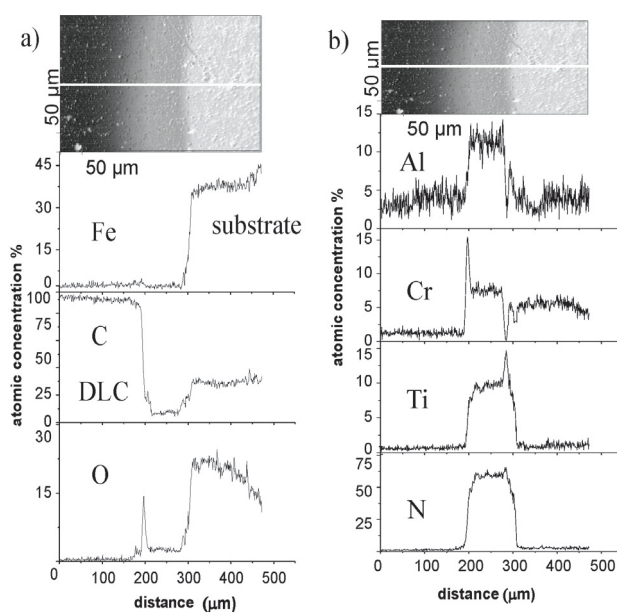


Figure 7: SEM images and chemical distributions of: a) iron, carbon oxygen, b) aluminum, chromium, titanium and nitrogen, at the DLC – AlCrTiN – substrate interface

Slika 7: SEM-posnetka in porazdelitev vsebnosti: a) železa, ogljika in kisika ter b) aluminija, kroma, titana in dušika, na stiku med DLC – AlCrTiN – podlago

– 200 μm represents the DLC film. The next, light-gray area corresponds to the AlTiCrN layer between 200 μm – 300 μm . The last, light region corresponds to the substrate.

The chemical distributions of carbon, oxygen and iron obtained along the marked line are presented in **Figure 7a**. The concentrations of carbon and oxygen in the DLC region are about 98 % and below 2 %, rapidly decreasing to 5 % and 2 % in the AlTiCrN layer, respectively. However, an increase in the oxygen signal to about 15 % is clearly visible at the DLC/AlTiCrN interface. A similar result was obtained with the ToF-SIMS method (**Figure 5**). The presence of small amounts of carbon and oxygen in the AlTiCrN layer and the steel substrate can be explained as the presence of a thin adsorbate layer on the analyzed surface. This layer was created due to the adsorption of the residual gases from the analysis chamber. The amount of the adsorbate layer increased during the measurement and different parts of the coating had various adhesion coefficients. Hence, the chemical distributions of carbon and oxygen in the substrate area, i.e., the increases in the concentrations observed for these elements are due to the increase in the adsorbate layer and it is not related with the real chemical structure of the substrate.

The distributions of the concentrations of Al, Ti, N and Cr in the AlTiCrN area are presented in **Figure 7b**. The levels of atomic concentrations of aluminum, chromium, titanium and nitrogen are almost stable and are about 12 %, 8 %, 10 % and 60 %, respectively. An increase in the atomic concentration of Cr to a value of

15 % is observed in the transition zone between DLC and AlTiCrN. This suggests that an additional layer of chromium exists in the interface area, i.e., CrN. Increases in the atomic concentrations to 15 % for titanium, to 8 % for aluminum and to 64 % for nitrogen are visible in the transition zone between AlTiCrN and the substrate.

On the other hand, the atomic concentration of chromium in this area rapidly drops to nearly zero. This may be due to the presence of additional layer AlTiN in the interface. Further, the concentration of chromium rapidly jumps from zero to about 5 % in the transition zone, which may suggest the presence of the second additional layer of chromium. Both of these layers may constitute an adhesion layer presented in **Figures 1** and **4a**. In the substrate area, the atomic concentrations of Al, Ti and N decreased to zero; only a small signal of chromium was detected. These results are in agreement with the data from **Figure 5** (ToF-SIMS) where, apart from iron, chromium ions were also recorded on the substrate.

3.3 Mechanical properties

The measurements of the stresses within the analysed layers were performed with the $\sin^2\psi$ method. The values of the stresses could only be determined for the AlTiCrN layer due to an amorphous character of the DLC layer. The "negative" slope of the line acquired during the measurements of the stresses indicates that internal compressive stresses exist in the AlTiCrN coating (**Figure 8**). Depending on their values, the internal stresses may positively or negatively influence the coating/substrate material system, which directly relates to the service life of the tools coated with protective layers. The compressive stresses produced for the analysed layers improve the cracking resistance and enhance the coating adhesion to the substrate. The tensile stresses, though, accelerate the coating-destruction process with an externally load applied.

Critical load values L_{C1} and L_{C2} were determined using the scratch-test method with a linearly increasing load, characterizing the adhesion of the investigated coatings to the steel substrate. The load at which the first

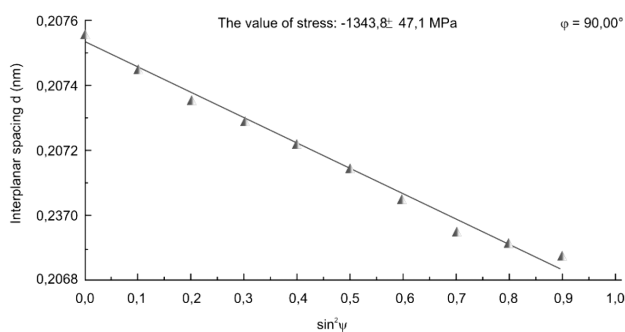


Figure 8: Changes in interplanar-spacing value d of reflex (200) of the AlTiCrN layer in the function of $\sin^2\psi$

Slika 8: Sprememba vrednosti razdalje d odboja (200) plasti AlTiCrN v odvisnosti od $\sin^2\psi$

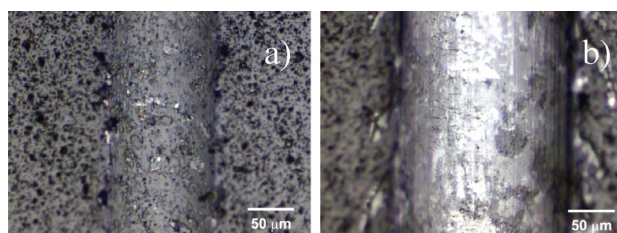


Figure 9: Scratch-failure images of the AlTiCrN+DLC coating at: a) L_{C1} , b) L_{C2}

Slika 9: Posnetka raze v AlTiCrN+DLC nanosu pri: a) L_{C1} , b) L_{C2}

coating defects appear is known as the first critical load, L_{C1} . The first critical load, L_{C1} , corresponds to the point, at which the first damage is observed (**Figure 9a**); the first appearance of microcracking, surface flaking outside or inside the track without any exposure of the substrate material – the first cohesion – indicates a failure event. The second critical load, L_{C2} , is the point, at which a complete delamination of the coating starts; the first appearance of cracking, chipping, spallation and delamination outside or inside the track with an exposure of the substrate material – the first adhesion – indicates a failure event (**Figure 9b**). The investigated coating shows relatively high values of the critical load. The first failure occurs at a value of ~ 28 N. The second critical load, L_{C2} , occurs at 67 N.

To determine the tribological properties of the AlTiCrN+DLC coating, an abrasion test under dry-sliding friction conditions was carried out using the ball-on-disk method. **Figure 10** presents a graph of friction coefficient μ including its changes obtained during the wear tests in relation to the Al_2O_3 counterpart. The friction curve is in the initial transitional state of an unstabilized course, during which the friction coefficient is reduced along with the growth of the sliding distance until it obtains the stabilized state, which normally occurs after a distance of about 150 m. Under dry-friction conditions, after the wearing-in period, the friction coefficient recorded for the associations tested is sta-

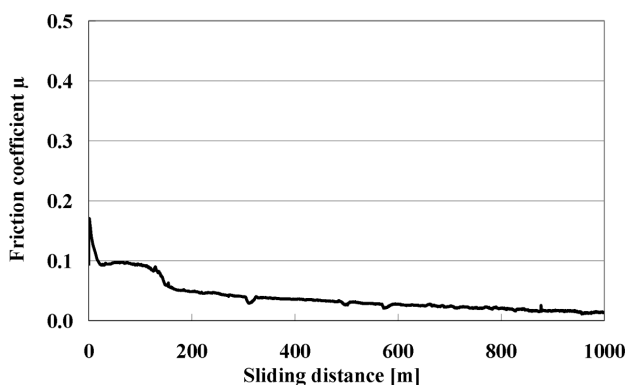


Figure 10: Dependence of the friction coefficient on the sliding distance during the wear test for the AlTiCrN+DLC coating

Slika 10: Odvisnost koeficienta trenja od dolžine poti drsenja med preizkusom obrabe AlTiCrN+DLC nanosa

bilized in a range of 0.02–0.03. No case of a complete coating wear-through occurred because the maximum wear-in depths were below the thickness values. The coating and the counterpart examined show a low wear. The values of the wear rate of the coating k_{vc} and the counterpart k_{vb} were recorded to be $3.30 \times 10^{-7} \text{ mm}^3/\text{N m}$ and $4.53 \times 10^{-9} \text{ mm}^3/\text{N m}$, respectively. The microhardness of the AlTiCrN film is 3400 HV and the one of the DLC is 1650 HV.

4 CONCLUSION

The AlTiCrN+DLC coating was successfully deposited on the X40CrMoV5-1 hot-work tool-steel substrate. A columnar microstructure of the coating, without any visible delamination, was observed with the scanning electron microscope. The investigation indicates the occurrence of a transition zone between the substrate material and the coating, which improves the adhesion. This is evidenced by the high values of the critical load L_{C2} of the coatings analysed. It was observed that the AlTiCrN film has a nanostructure with fine crystallites. The tests using TEM confirmed an amorphous character of a low-friction DLC layer. A phase-composition analysis of the DLC layer with the Raman-spectroscopy method showed the presence of bonds distinctive for diamond (sp^3) and graphite (sp^2), typically observed in diamond-like carbon coatings. Under dry-friction conditions, the friction coefficient for the associations tested is within a range of 0.02–0.03 for the investigated coating. According to the XRD pattern of AlTiCrN, fcc phases only occurred in the coating. Negative (compressive) internal stresses exist in the tested coating, substantially influencing the growth of tribological and strength properties, including the coating adhesion to the substrate. A chemical-composition analysis carried out with the AES method revealed an equilibrium concentration of nitride and metallic elements forming the AlTiCrN layer. The DLC film is composed of carbon and hydrogen.

5 REFERENCES

- ¹ T. W. Scharf, S. V. Prasad, Solid lubricants: a review, *Journal of Materials Science*, 48 (2013), 511–531, doi:10.1007/s10853-012-7038-2
- ² P. Jurči, J. Bohovičová, M. Hudáková, P. Bílek, Characterization and wear performance of CrAgN thin films deposited on Cr-V ledeburitic tool steel, *Mater. Tehnol.*, 48 (2014) 2, 159–170
- ³ S. Veprek, M. J. G. Veprek-Heijman, Industrial applications of super-hard nanocomposite coatings, *Surface & Coatings Technology*, 202 (2008), 5063–5073, doi:10.1016/j.surfcoat.2008.05.038
- ⁴ A. A. Voevodin, J. S. Zabinski, Nanocomposite and nanostructured tribological materials for space applications, *Composites Science and Technology*, 65 (2005), 741–748, doi:10.1016/j.compscitech.2004.10.008
- ⁵ D. Yu, C. Wang, X. Cheng, F. Zhang, Microstructure and properties of TiAlSiN coatings prepared by hybrid PVD technology, *Thin Solid Films*, 517 (2009), 4950–4955, doi:10.1016/j.tsf.2009.03.091
- ⁶ D. V. Shtansky, P. V. Kiryukhantsev-Korneev, I. A. Bashkova, A. N. Sheveiko, E. A. Levashov, Multicomponent nanostructured films for various tribological applications, *International Journal of Refractory Metals & Hard Materials*, 28 (2010), 32–39, doi:10.1016/j.ijrmhm.2009.07.014
- ⁷ A. Alberdi, M. Marin, B. Diaz, O. Sanchez, R. Escobar Galindo, Wear resistance of titanium-aluminium-chromium-nitride nanocomposite thin films, *Vacuum*, 81 (2007), 1453–1456, doi:10.1016/j.vacuum.2007.04.024
- ⁸ S. Zhang, X. L. Bui, Y. Fu, H. Du, Development of carbon-based coating of extremely high toughness with good hardness, *International Journal of Nanoscience*, 3 (2004), 571–578, doi:10.1142/S0219581X04002395
- ⁹ K. W. Weng, S. Han, Y. C. Chen, D. Y. Wang, Characteristics of diamond-like carbon film deposited by filter arc deposition, *Journal of Materials Processing Technology*, 203 (2008), 117–120, doi:10.1016/j.jmatprotec.2007.09.061
- ¹⁰ K. Lukaszowicz, A. Czyzniewski, W. Kwasny, M. Pancielejko, Structure and mechanical properties of PVD coatings deposited onto the X40CrMoV5-1 hot work tool steel substrate, *Vacuum*, 86 (2012), 1186–1194, doi:10.1016/j.vacuum.2011.10.031
- ¹¹ O. Wänstrand, M. Larsson, P. Hedenqvist, Mechanical and tribological evaluation of PVD WC/C coatings, *Surface and Coatings Technology*, 111 (1999), 247–254, doi:10.1016/S0257-8972(98)00821-4
- ¹² J. Robertson, Diamond-like amorphous carbon, *Materials Science and Engineering R*, 37 (2002), 129–281, doi:10.1016/S0927-796X(02)00005-0

IMPLICIT NUMERICAL MULTIDIMENSIONAL HEAT-CONDUCTION ALGORITHM PARALLELIZATION AND ACCELERATION ON A GRAPHICS CARD

PARALELIZACIJA IN POSPEŠITEV IMPLICITNEGA NUMERIČNEGA VEČDIMENZIJSKEGA ALGORITMA PREVAJANJA TOPLOTE NA GRAFIČNI KARTICI

Michal Pohanka, Jana Ondroušková

Heat Transfer and Fluid Flow Laboratory, Faculty of Mechanical Engineering, Brno University of Technology, Technická 2,
616 69 Brno, Czech Republic
pohanka@fme.vutbr.cz

Prejem rokopisa – received: 2014-07-29; sprejem za objavo – accepted for publication: 2015-03-30

doi:10.17222/mit.2014.128

Analytical solutions are much less computationally intensive than numerical ones, and moreover, they are more accurate because they do not contain numerical errors; however, they can only describe a small group of simple heat-conduction problems. A numerical simulation of heat conduction is often used as it is able to describe complex problems, but its computational time is much longer, especially for unsteady multidimensional models with temperature-dependent material properties. After a discretization using the implicit scheme, the heat-conduction problem can be described with N non-linear equations, where N is the large number of the elements of the discretized model. This set of equations can be efficiently solved with an iteration of the line-by-line method, based on the heat-flux superposition, although the computational procedure is strictly serial. This means that no parallel computation can be done, which is strictly required when a graphics card is used to accelerate the computation. This paper describes a multidimensional numerical model of unsteady heat conduction solved with the line-by-line method and a modification of this method for a highly parallel computation. An enormous increase in the speed is demonstrated for the modified line-by-line method accelerated on the graphics card, and the durations of the computations for various mesh sizes are compared with the original line-by-line method.

Keywords: heat conduction, numerical simulation, multidimensional numerical model algorithm, acceleration, parallelization, graphics card

Analične rešitve so mnogo manj računsko intenzivne kot numerične, poleg tega pa so bolj natančne, ker ne vsebujejo numeričnih napak, vendar pa lahko opisujejo samo majhno skupino enostavnih problemov prevajanja toplote. Numerična simulacija prevajanja toplote se pogosto uporablja, ker je sposobna opisati kompleksne probleme, vendar pa je čas izračuna mnogo daljši, še posebno pri nestabilnih večdimenzijskih modelih, z lastnostmi materiala, odvisnimi od temperature. Po diskretizaciji z uporabo implicitne sheme je mogoče problem prevajanja toplote opisati z N nelinearnimi enačbami, kjer je N veliko število elementov diskretiziranega modela. Ta sklop enačb je mogoče učinkovito rešiti s približkom metode vrsta za vrsto, ki temelji na predpostavki toka toplote, čeprav izračun poteka serijsko. To pomeni, da ni mogoč vzporedni izračun, kar je striktna zahteva, kadar se uporablja grafično kartico za pohitritev izračuna. Ta članek opisuje večdimenzijski numerični model nestabilnega prevajanja toplote, kar je bilo rešeno z metodo vrsta za vrsto in s pospešitvijo modifikacije te metode na grafični kartici. Trajanje izračuna je primerjano z osnovno metodo vrsta za vrsto pri različnih dimenzijah mreže.

Ključne besede: prevajanje toplote, numerična simulacija, večdimenzijski model algoritma, pospešitev, paralelizacija, grafična kartica

1 INTRODUCTION

Although the computational power of modern computers continues to rapidly increase year by year, numerical simulations can last several hours or days for detailed numerical models where high accuracy is required. The computational time becomes even longer when the models are used for inverse computations, where thousands of direct-heat-conduction computations can be required. Computations of the boundary conditions (such as the surface temperature, the heat flux, and the heat-transfer coefficient) for continuous casting¹⁻², heat treatment³, hot rolling⁴⁻⁶ and different types of spray cooling⁷ using ill-posed inverse methods^{8,9} are typical applications.

Many very fast algorithms have been developed, but they are often used strictly in a serial fashion^{10,11} and cannot be efficiently used by modern multicore processors, as they require parallel processing. It has been shown that a seemingly lesser algorithm can be much more efficient because it allows parallel processing¹²⁻¹⁵ that is absolutely necessary for the use of the maximum computational power of modern processors, where thousands of tasks can be computed at the same time. The time when a personal computer's central processing unit (CPU) was able to compute only one thread at a time is over. Today, CPUs often compute from 4 to 16 threads at the same time.^{16,17} New graphics processing units (GPUs)^{18,19} allow scientific computing in double precision, which is necessary for numerical heat-con-

duction computations and the GPUs can run more than 2800 threads at the same time. When looking at the computational power, a GPU has over 2500 Giga Floating-point Operations per Second (GFLOPS) in double precision, while a CPU has only 70 GFLOPS. However, to use all of the computational power of a GPU a highly parallel computational algorithm is required.

After the discretization of a heat-conduction problem (HCP) using the implicit scheme, the HCP can be described with a set of linear equations $A \cdot T = B$ for constant material properties where T is the unknown temperature in the model and A is a very large sparse square matrix for large models. The A matrix has dimensions of $N \cdot N$ where N is the number of the nodes in the entire model. For example, a 3D model with 100 nodes in each dimension has an A matrix of 10^6 times 10^6 consisting of 10^{12} values. It is necessary to compute the huge inverse matrix A^{-1} and store this inverse matrix in the computer memory to compute the T vector. Furthermore, for a temperature-dependent model, the computation must be iterated because matrix A and vector B change with a better estimate of the final T vector. However, there is a different approach, often called the line-by-line method, which requires much less computer memory, although the computation procedure is strictly serial¹⁰ and does not allow for parallel processing.

2 LINE-BY-LINE METHOD FOR HCP

A two-dimensional (2D) problem can be discretized into an orthogonal mesh.²⁰ One equation is necessary for each control volume represented by one temperature. An explicit, implicit, or Crank-Nicholson differencing scheme for the time domain can be used. The focus here is on the implicit scheme because the explicit one is conditionally stable. When writing the heat-flux equation for each control volume, all the equations can be rearranged into the matrix form of $A \cdot T = B$ where T is the vector of nodal temperatures. The inverse matrix A^{-1} must be computed to solve this set of equations.²¹ This approach is very inefficient and unstable for the models with many control volumes. The stability problem arises from the rounding of the values during a large number of operations because the computers use only a limited number of decimal places to store these values.

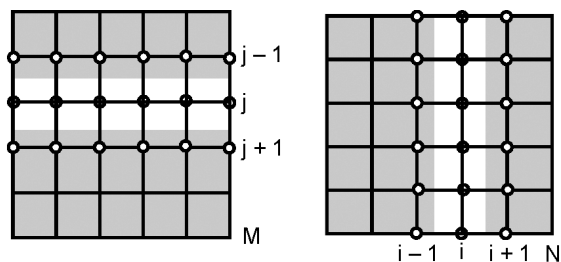


Figure 1: Line-by-line method for a 2D problem
Slika 1: Metoda vrsta za vrsto za 2D problem

Patankar¹⁰ described an approach called the line-by-line method to overcome the problem with an inverse matrix. This method uses the principle of the heat-flux superposition. The domain is solved by iterating two steps for a 2D model and by iterating three steps for a 3D model. The 2D model is partitioned into lines in the first step and into columns in the second step (Figure 1). The first line is solved separately, then the second one and so on until all the lines are finished. Each line j (where $j = 1..M$) is solved using an implicit scheme and the most up-to-date temperatures for lines $j-1$ and $j+1$ are used to include vertical heat fluxes for line j to ensure the fastest convergence to the final solution. This means that the temperatures for line $j-1$ are those only computed for this line and the temperatures for line $j+1$ are those computed during the previous iteration. A similar process is performed with columns in the second step. This approach leads to M matrices $C_j T_j = D_j$ and N matrices $E_i T_i = F_i$ where C_j and E_i are tridiagonal matrices. This set of equations can be solved very fast using the direct TDMA method.¹¹ These two steps (computations of rows and columns) are repeated until the desired accuracy of the computed temperature field is attained.

The problem with the original line-by-line method is that line j can only be computed when line $j-1$ has already been finished. Neither does the TDMA method¹¹ allow parallel processing, which is strictly required by a GPU. However, parallel processing can be enabled with a simple modification. The temperatures from the previous iterations for both line $j-1$ and $j+1$ can be used

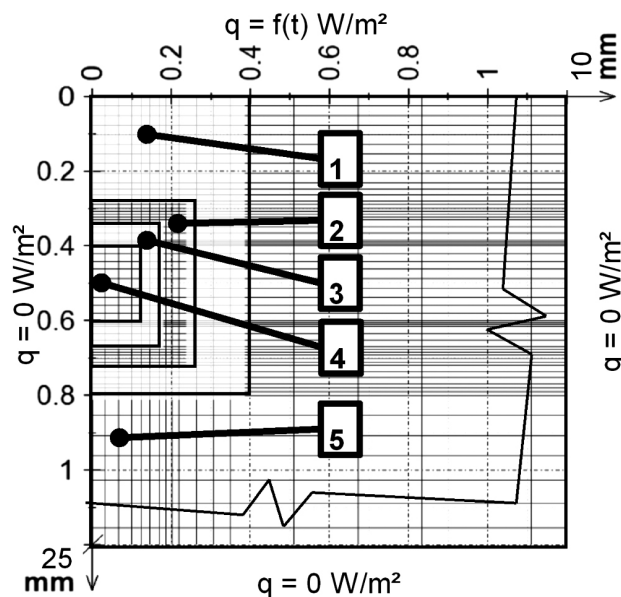


Figure 2: Structure of the 2D model used for testing and non-uniform discretization: 1) silver solder Ag40, 2) thermocouple shield Inconel 600, 3) electrical insulation MgO, 4) K-thermocouple, 5) stainless steel 1.4301

Slika 2: Zgradba 2D modela, uporabljenega za preizkus in spremenljiva diskretizacija: 1) srebrova spajka Ag40, 2) termoelement Inconel 600, 3) električna izolacija MgO, 4) K-termoelement, 5) nerjavno jeklo 1.4301

when line j is being computed. However, this modification significantly slows down the speed of convergence.

3 EXAMPLE OF PARALLEL PROCESSING

GPU acceleration was tested on a 2D computational model (Figure 2) which is often used for the inverse computation of boundary conditions (the cooling intensity of a spraying header on a work roll during hot rolling).⁶ This represents a cut of a shielded K-thermocouple soldered with a silver solder in a slot made on the surface of stainless steel. The actual circular geometry of the shielded thermocouple is simplified in this example to the equivalent square geometry so that the model can be easily refined by dividing the control volumes. Because the geometry is symmetrical, only one half is used for the model. All sides are insulated except for the upper one, where a time-dependent heat flux is applied (Figure 3). The applied heat flux represents the heat flux from the real cooling measurement during one rotation of a heated roll. The roll is hollow with an outer perimeter of 2 m and a wall thickness of 25 mm. The velocity of the outer surface of the roll during the rotation is 2 m/s. One rotation lasts for 1 s. The sampling frequency is 300 Hz. The starting temperature is 400 °C. The temperatures computed on the surface and in the center of the thermocouple are shown in Figure 3.

When the computation is accelerated, the GPU is used as a co-processor. Only the most computationally intensive sections that can be processed in parallel are run on the GPU, rather than the whole program. The main program is run on the CPU and the most computationally intensive tasks are sent to the GPU using Open Computing Language (OpenCL).²² In this case, three procedures are accelerated on the GPU: 1) the computing-material properties for the actual temperature; 2) the TDMA method for solving a set of equations; 3) the

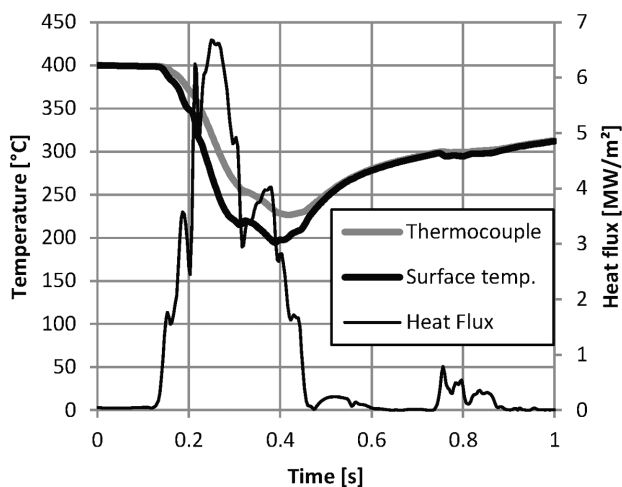


Figure 3: Computed temperature history for the thermocouple, for the surface above the thermocouple (corner (0;0)) and the used heat flux
Slika 3: Izračunana zgodovina temperature v termoelementu, na površini nad termoelementom (vogal (0;0)) in uporabljeni tok toplote

estimation of the attained accuracy of the computed temperature field. The first and the third functions are well suited for parallelization. Each node can be computed in a separate thread. This means that the total number of nodes determines the maximum number of parallel threads. Function 2 is not as well suited for parallelization. The maximum number of parallel threads is the number of rows M in the first stage and the number of columns N in the second stage.

The durations of the computations for functions 1 and 2 are listed in Table 1 for different numbers of nodes. These are the net values without the time required for preparing the tasks, data, and for launching. Table 2 includes the results from the entire simulation of one rotation during the roll cooling. The values for the CPU were obtained using the original line-by-line method, computed in one thread, while the values for the GPU were obtained using the modified line-by-line method, accelerated on the GPU. The desired accuracy was 1 °C for the whole simulation in all the nodes. An Intel Core i5-2500K²³ was used for the CPU and an AMD Radeon HD 7970²⁴ was used for the GPU.

Table 1: Computations on CPU and GPU for one iteration

Tabela 1: Izračunana CPU in GPU za eno ponovitev

Nodes		Mat. properties (μ s)		TDMA $M+N$ (ms)	
X	Y	CPU	GPU	CPU	GPU
32	107	51	19	5	1.1
92	107	147	20	17	1.5
182	212	605	24	72	3.1
362	422	2532	57	293	6.4
722	842	10220	191	1152	12.3
1442	1682	41479	726	4611	16.0

4 DISCUSSION

The test example showed that the GPU acceleration makes sense for the models with many nodes (the more nodes the better). For a very fine mesh (800 rows and 800 columns), results can be obtained almost 11 times faster when using the GPU acceleration. For a very small number of nodes, the original method used only by the CPU can be even faster. This is caused by a relatively slow communication between the CPU and GPU, which is necessary for the acceleration on the GPU. An explicit scheme was also tested because it is more suitable for parallel processing. However, it was found that it is 164 times slower on the CPU than an implicit scheme due to its conditional stability, which requires a 6000 \times higher sampling frequency.

The numbers of iterations for steps 1 and 2 of the line-by-line method for 2D are listed in Table 2. It is clear that the original method (the CPU column) needs approximately half the number of iterations required by the modified method (the GPU column) to reach the same 1 °C accuracy. However, the model introduced here has a very slow convergence rate because the silver

Table 2: Computing times on CPU and with GPU acceleration for the increasing number of nodes. M is the number of rows and N is the number of columns.**Tabela 2:** Časi izračunov na CPU in z GPU pospešitvijo pri naraščajočem številu vozlišč. M je število vrst in N je število stolpcev.

Nodes		Iterations		Time (s)		Speed-up	Time/ (Iter.* $(M+N)$) (μ s)		Time/ (Iter.* $M*N$) (μ s)	
Rows	Col.	CPU	GPU	CPU	GPU		CPU	GPU	CPU	GPU
107	32	33596	101445	22	53	0.4	4.71	3.76	0.19	0.15
107	92	128624	241864	253	175	1.4	9.88	3.64	0.20	0.07
212	182	492610	970922	3873	1451	2.7	19.95	3.79	0.20	0.04
422	362	1928762	3804033	61256	11826	5.2	40.51	3.97	0.21	0.02
842	722	7664187	14338003	988219	90617	10.9	82.44	4.04	0.21	0.01

solder used has an approximately five-time higher thermal conductivity than stainless steel. In the models where materials with similar thermal conductivities are used, the number of the necessary iterations is much smaller.

The computational time required for one node in one iteration for the CPU is almost independent of the number of nodes and lasts for about 0.2 μ s. The situation is completely different for the acceleration using the GPU (it decreases). However, the total time divided by the product of the number of iterations and the sum of lines and columns is almost constant (3.8 μ s). A similar situation exists for the TDMA $M+N$ function in **Table 1** because this function is the longest during the computation. The time/(iter.* $(M+N)$) is almost constant because there are not enough parallel threads to fully utilize the GPU. There are only about 800 threads and the GPU can process over 2000 threads. The increase in TDMA $M+N$ for a higher number of nodes is caused by a larger tridiagonal matrix to be solved but not by a higher number of tridiagonal matrices to be solved.

5 CONCLUSION

It was found that for the models with a high number of computational elements the acceleration on a GPU card can speed up 2D heat-conduction calculations by almost eleven times. For a model with a small number of nodes, it is better to use a CPU and the original line-by-line method. The AMD 7970 starts to be fully utilized when there are more than 32,000 threads. The GPU acceleration will be even more useful for 3D models where there may be more parallel threads for the TDMA function.

Acknowledgement

This work is an output of the research and scientific activities of the NETME Centre, regional R&D centre built with the financial support from Operational Programme Research and Development for Innovations within the NETME Centre project (New Technologies for Mechanical Engineering), Reg. No. CZ.1.05/2.1.00/

01.0002 and, in the follow-up sustainability stage, supported through NETME CENTRE PLUS (LO1202) with the financial means from the Ministry of Education, Youth and Sports under the National Sustainability Programme.

6 REFERENCES

- M. Pohanka, K. A. Woodbury, A downhill simplex method for computation of interfacial heat transfer coefficients in alloy casting, *Inverse Problems in Engineering*, 11 (2003) 5, 409–424, doi:10.1080/1068276031000109899
- J. Horský, M. Raudenský, M. Pohanka, Experimental study of heat transfer in hot rolling and continuous casting, *Materials Science Forum*, 473–474 (2005), 347–354, doi:10.4028/www.scientific.net/MSF.473-474.347
- M. Raudenský, J. Horský, P. Kotrbáček, M. Hnízdil, M. Pohanka, In-Line Heat Treatment and Hot Rolling, *Proc. of the International Conference on Advances in Materials and Processing Technologies (AMPT2010)*, 1315 (2011), 563–568, doi:10.1063/1.3552506
- M. Pohanka, M. Raudenský, J. Horský, Attainment of more precise parameters of a mathematical model for cooling flat and cylindrical hot surfaces by nozzles, In: C. A. Brebbia, B. Suncten (Ed.), *Advanced Computational Methods in Heat Transfer VI*, WIT Press, 2000, 627–635
- M. Raudenský, M. Pohanka, J. Horský, Combined inverse heat conduction method for highly transient processes, *WIT Transactions on Engineering Sciences, Advanced Computational Methods in Heat Transfer VII*, 35 (2002), 35–42, doi:10.2495/HT020041
- J. Ondroušková, M. Pohanka, B. Vervae, Heat-Flux Computation from Measured-Temperature Histories during Hot Rolling, *Mater. Tehnol.*, 47 (2013) 1, 85–87
- A. A. Tseng, H. Bellerová, M. Pohanka, M. Raudenský, Effects of titania nanoparticles on heat transfer performance of spray cooling with full cone nozzle, *Applied Thermal Engineering*, 62 (2013) 1, 20–27, doi:10.1016/j.applthermaleng.2013.07.023
- J. V. Beck, B. Blackwell, C. R. St. Clair, *Inverse Heat Conduction: Ill-posed Problems*, Wiley, New York 1985, 308
- M. Pohanka, P. Kotrbáček, Design of Cooling Units for Heat Treatment, *Heat Treatment Conventional and Novel Applications*, InTech, 2012, 1–20, doi:10.5772/50492
- S. V. Patankar, *Numerical Heat Transfer and Fluid Flow*, Hemisphere Publishing Corporation, New York 1980, 214
- H. P. William, A. T. Saul, T. V. William, P. F. Brian, *Numerical Recipes in C*, 2nd ed., Cambridge University Press, New York 1992, 994
- J. Lee, J. C. Wright, A block-tridiagonal solver with two-level parallelization for finite element-spectral codes, *Computer Physics Communication*, 185 (2014) 10, 2598–2608, doi:10.1016/j.cpc.2014.06.006

- ¹³ E. S. Quintana, G. Quintana, X. Sun, R. Van de Geijn, A note on parallel matrix inversion, *SIAM J. Sci. Comput.*, 22 (2001) 5, 1762–1771, doi:10.1137/S1064827598345679
- ¹⁴ L. Karlsson, B. Kågström, Parallel two-stage reduction to Hessenberg form using dynamic scheduling on shared-memory architectures, *Parallel Computing*, 37 (2011) 12, 771–782, doi:10.1016/j.parco.2011.05.001
- ¹⁵ R. Zheng, Q. Zhang, H. Jin, Z. Shao, X. Feng, A GPU-based parallel method for evolutionary tree construction, *Computers & Electrical Engineering*, 40 (2014) 5, 1580–1591, doi:10.1016/j.compeleceng.2014.04.013
- ¹⁶ AMD Opteron™ 6300 Series Processors, <http://www.amd.com/en-us/products/server/opteron/6000/6300#>
- ¹⁷ Intel® Xeon® Processor E7 v2 Family, <http://ark.intel.com/products/family/78584/Intel-Xeon-Processor-E7-v2-Family#@Server>
- ¹⁸ AMD FirePro™ S9150 Server GPU, <http://www.amd.com/en-us/products/graphics/server/s9150#>
- ¹⁹ Tesla Server GPUs, <http://www.nvidia.co.uk/object/tesla-server-gpus-uk.html>
- ²⁰ M. Pohanka, Ph.D. Thesis: Technical Experiment Based Inverse Tasks in Mechanics, Brno 2006, 202, <http://lab4.fme.vutbr.cz/Pohanka/PDF/PhDThesisPohankaM.pdf>
- ²¹ F. P. Incropera, D. P. DeWitt, *Fundamentals of Heat and Mass Transfer*, 4th ed., Wiley, New York 1996, 912
- ²² OpenCL – The open standard for parallel programming of heterogeneous systems, <https://www.khronos.org/opencl/>
- ²³ Intel® Core™ i5-2500K Processor, http://ark.intel.com/products/52210/Intel-Core-i5-2500K-Processor-6M-Cache-up-to-3_70-GHz
- ²⁴ AMD Radeon™ HD 7900 Series Graphics Cards, <http://www.amd.com/en-us/products/graphics/desktop/7000/7900#>

MAGNETIC PROPERTIES AND MICROSTRUCTURE OF A BULK AMORPHOUS $\text{Fe}_{61}\text{Co}_{10}\text{Ti}_3\text{Y}_6\text{B}_{20}$ ALLOY, FABRICATED AS RODS AND TUBES

MAGNETNE LASTNOSTI IN MIKROSTRUKTURA MASIVNE AMORFNE ZLITINE $\text{Fe}_{61}\text{Co}_{10}\text{Ti}_3\text{Y}_6\text{B}_{20}$ V OBLIKI PALIC IN CEVI

Marcin Nabialek¹, Katarzyna Bloch¹, Karol Szlązak², Michał Szota¹

¹Czestochowa University of Technology, Institute of Physics, Faculty of Production Engineering and Materials Technology, 19 Armii Krajowej Av., 42-200 Czestochowa, Poland

²Warsaw University of Technology, Faculty of Materials Science and Engineering, 141 Woloska, 02-507 Warsaw, Poland
23kasial@wp.pl

Prejem rokopisa – received: 2014-07-31; sprejem za objavo – accepted for publication: 2015-03-10

doi:10.17222/mit.2014.144

In this paper, studies are presented that characterize a bulk amorphous $\text{Fe}_{61}\text{Co}_{10}\text{Ti}_3\text{Y}_6\text{B}_{20}$ alloy. Samples were fabricated in two forms: as a rod of 1 mm in diameter and as a tube of 1 mm in the outer diameter. The investigated material was obtained using the injection method, whereby the liquid alloy was injected into a copper mould. Using an X-ray diffractometer, a scanning electron microscope and computer tomography, the microstructures of these rapidly cooled samples were studied. Based on the obtained results, it was found that both the rod and the tube were fully amorphous. The cross-sections of the broken rod and tube were characterized by a mixed rupture consisting of smooth chevron and river patterns. This shows that there are regions of different ductility distributed throughout the volume of a sample. Three-dimensional images of the investigated materials, obtained with computer tomography, allowed the determination of the contribution of the pores (and their size) to the total volumes of the samples. The investigated alloy is a ferromagnetic material exhibiting good soft-magnetic properties such as a high saturation magnetization, a high magnetic permeability and a low value of the coercive field. The technique of injecting the liquid alloy into a copper mould, combined with the suction-casting method, can be used to produce toroidal cores that exhibit highly promising properties for a successful application in the construction of electric motors.

Keywords: bulk amorphous alloys, X-ray diffractometry, electron scanning microscopy, computer tomography, saturation magnetization, coercivity

Članek prikazuje študijo značilnosti masivne amorfne zlitine $\text{Fe}_{61}\text{Co}_{10}\text{Ti}_3\text{Y}_6\text{B}_{20}$, katere vzorci so bili izdelani na dva načina: kot palica premera 1 mm in kot cev z zunanjim premerom 1 mm. Preiskovani material je bil izdelan z vbrzgvanjem, saj je bila talina vbrzgvana v bakreno kokilo. Mikrostrukture hitro strjenih zlitin so bile proučevane s pomočjo rentgenskega difraktometra, z vrstičnim elektronskim mikroskopom in z računalniško tomografijo. Na podlagi dobljenih rezultatov je bilo ugotovljeno, da sta palica in cev popolnoma amorfni. Presek prelomljene palice in cevi ima mešan prelom, ki sestoji iz gladkih površin in stopnic v obliki rečic. To pomeni, da so različna področja duktilnosti razporejena po volumnu vzorca. Trodimenzionalne slike preiskovanih materialov, dobljenih s pomočjo računalniške tomografije, omogočajo določitev deleža por (in njihovih velikosti) v celotnem volumnu vzorcev. Preiskovana zlitina je feromagnetna in ima dobre mehko magnetne lastnosti, kot so: visoko nasičenje pri magnetizaciji, visoka magnetna permeabilnost in majhna vrednost koercitivnega polja. Tehniko vbrzgvanja tekoče litine v bakreno kokilo, v kombinaciji z livno metodo z vsesavanjem, se lahko uporabi za izdelavo toroidnih jeder, ki imajo dobre lastnosti za uspešno uporabo pri konstrukciji elektromotorjev.

Ključne besede: masivne amorfne zlitine, rentgenski difraktometer, vrstični elektronski mikroskop, računalniška tomografija, nasičena magnetizacija, koercitivnost

1 INTRODUCTION

The 21st century could be called the 'age of miniaturization and proliferation of the cutting-edge technology'. Currently, the rapid development of subassemblies for electronic devices is on the increase, featuring increasingly compact physical dimensions. Of particular importance are the component parts for miniature motors, targeted at specialist applications. The magnetic material used in micro-motors should have a good coefficient of fulfilment and, of course, excellent magnetic and mechanical properties.¹⁻⁶ Bulk amorphous alloys include highly promising materials for electrical-engineering applications.⁷⁻¹⁰ Conventional amorphous alloys, manufactured in the form of a strip (ribbon), cannot be

used for the construction of micro-motors because the strip shape is not suitable for the application.

Through the selection of the right chemical composition for an alloy, the amorphous state can be obtained using a relatively slow cooling rate (10^2 K/s – 10^0 K/s).¹¹ This feature has been utilized in the production of the so-called bulk amorphous alloys. The bulk amorphous alloys consist of many components (more than three chemical elements). In order to obtain a high value of the glass-forming ability (GFA) the atomic radii of the main alloy components must vary by more than 12 % and these components should be characterized by the negative mixing heat.¹¹ Moreover, the bulk amorphous alloys are characterized by a wide range of the so-called super-cooled liquid region, $\Delta T_x (= T_x - T_g)$, where T_x is

the crystallization-onset temperature and T_g is the glass-transition temperature.¹² Due to the facts that the bulk amorphous alloys consist of many components of various atomic radii and are obtained using a slow cooling rate, their density is higher than that typical of the classical amorphous alloys. The relatively slow cooling rate, used in the manufacture of the bulk amorphous alloys, yields a more relaxed structure in the resulting as-cast state.

This paper presents the results of the studies of the microstructure and magnetic properties of the $\text{Fe}_{61}\text{Co}_{10}\text{Ti}_3\text{Y}_6\text{B}_{20}$ bulk amorphous alloy in the forms of a rod and a tube.

2 METHOD

The samples used in the investigations were produced of high-purity elements (greater than 99.95 % of amount fraction), using a combination of the injection- and suction-casting methods. The molten liquid was sucked into a water-cooled, copper die. The initial material was melted by arc melting (current range: 240–300 A; voltage: 80 V) under a protective atmosphere of inert gas. In addition, immediately prior to the suction process, pure titanium was re-melted in order to avoid a sample oxidation.

The structure and microstructure of the resulting material were investigated by means of an X-ray diffractometer (Bruker Advanced D8), scanning electron microscope (SEM – Zeiss, Supra 35) and computer tomograph (Bruker, SkyScan 1172 Micro-CT). X-ray diffraction patterns ($\text{Cu-K}\alpha$) were taken in a 2-theta range from 30° to 120° , with a measurement step of 0.05° and time per step of 2 s. Images of the surfaces of the samples were obtained using the SEM, with a constant electron-acceleration voltage of 25 kV and the maximum magnification of 12×10^3 . A three-dimensional visualization of the scanned samples was performed using the SkyScan software (Bruker). This kind of equipment is commonly used in amorphous and nanocrystalline materials investigations.¹³ The X-ray parameters such as the voltage, the type of filter, the exposure time and the pixel size were optimized in order to obtain the best image contrast. The X-ray tube voltage was 100 kV and the current was 100 μA . The X-ray

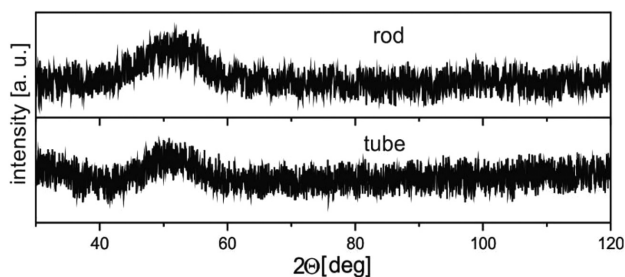


Figure 1: X-ray diffraction patterns for the $\text{Fe}_{61}\text{Co}_{10}\text{Ti}_3\text{Y}_6\text{B}_{20}$ alloy
Slika 1: Rentgenogram zlitine $\text{Fe}_{61}\text{Co}_{10}\text{Ti}_3\text{Y}_6\text{B}_{20}$

projections were obtained at 0.3° intervals with a scanning angular rotation of 360° and 6 frames were averaged for each rotation. The obtained resolution yielded a pixel size of $2.38 \mu\text{m}$. In addition, ring artefacts were reduced through the selection of the random-movement amplitude of 50. The exposure time was 1200 ms. The images were reconstructed and analysed using the Bruker NRecon and CTAn software. DataViewer (Bruker) and CTVol (Bruker) were used to reveal the microstructural features of the samples. Static hysteresis loops were taken by means of a Lake Shore 7301 vibrating-sample magnetometer (VSM), using a magnetic field of up to 2 T.

3 RESULTS AND DISCUSSIONS

In **Figure 1**, X-ray diffraction patterns, obtained from the powdered alloy samples, are presented. A wide maximum, typical for the amorphous materials, can be observed on the X-ray diffraction patterns at $2\Theta \approx 50^\circ$. **Figure 2** shows SEM images of the investigated samples. Images showing the cross-sectional structures of the investigated samples are presented in **Figure 3**.

Figure 3a corresponds to the rod sample and reveals a visible mixed rupture, consisting of a smooth cleavage, a poorly developed chevron and river patterns. This is a sign of a varying degree of the structural relaxation of

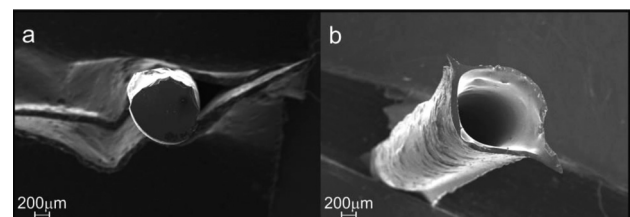


Figure 2: SEM images for the investigated samples: a) rod of a 1 mm diameter, b) tube of a 1 mm diameter

Slika 2: SEM-posnetka preiskovanih vzorcev: a) palica premera 1 mm, b) cev premera 1 mm

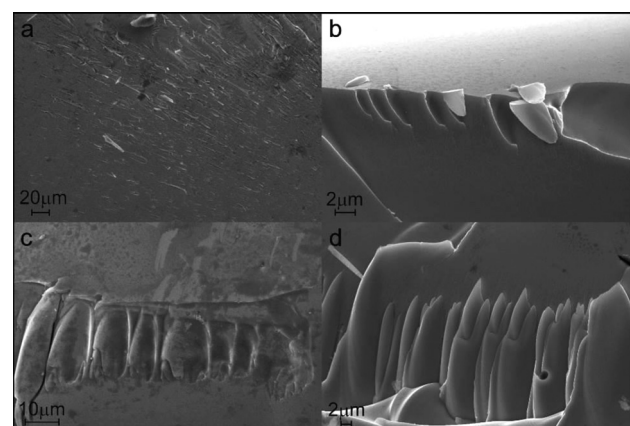


Figure 3: SEM images of the surfaces of the: a) rod and b), c), d) tube for the $\text{Fe}_{61}\text{Co}_{10}\text{Ti}_3\text{Y}_6\text{B}_{20}$ alloy

Slika 3: SEM-posnetki površine palice: a) palica in b), c), d) cevka iz $\text{Fe}_{61}\text{Co}_{10}\text{Ti}_3\text{Y}_6\text{B}_{20}$

the rod-shaped sample. Similar patterns were observed across the whole of the surface of the rod sample (**Figure 3a**). The cross-sectional images obtained for the tube-shaped sample (**Figures 3b to 3d**) were more inhomogeneous and different characters of the ruptures were observed for different sections of the tube. In **Figure 3b**, a well-developed band can be observed, dividing the regions of smooth and scale-like breakthroughs. At the top of this band, and situated perpendicularly to it, fine and poorly developed scales are visible. In another area of the investigated tube-like sample (**Figure 3c**), a band separating the regions of the smooth cleavage was also observed, with well-developed scales that are parallel to each other. In the lower part of the band determining the border of the scales, numerous breakthroughs appeared, indicating the direction of the created scale-like structure. In **Figure 3d**, the cross-section of the tube (with the parallel band of well-developed scales) can be seen. However, the character of this breakthrough is not typical. A further expansion of the scale-like structure is limited by the areas that feature different degrees of stress, and, as a result, double-graded scales can be observed.

On the basis of the SEM investigations, it can be stated that the quenching time (and, related with this, the cooling speed) has a significant influence on the structures of the breakthroughs featured in the investigated samples. The microstructures of the investigated rod- and tube-shaped samples are shown, with a 3-D visualisation, in **Figures 4 to 6**. On the basis of computed-tomography investigations of the rod-shaped sample of $\text{Fe}_{61}\text{Co}_{10}\text{Ti}_3\text{Y}_6\text{B}_{20}$ alloy, it was found that its structure is uniform and free from defects in the form of pores; this is in agreement with the results of the SEM investigations (**Figure 3a**).

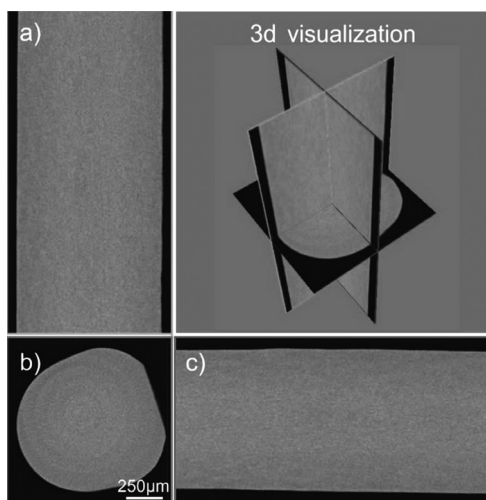


Figure 4: Three different cross-sectional views of the rod microstructure: a) coronal, b) transaxial, c) sagittal

Slika 4: Trije različni prikazi mikrostrukture preseka palice: a) koronalni, b) transaksialni, c) sagitalni

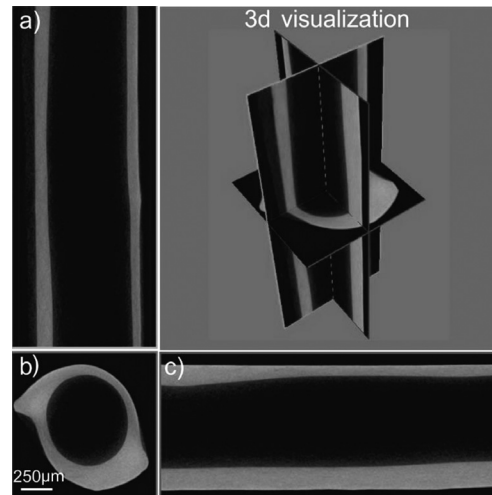


Figure 5: Three different cross-sectional views of the tube microstructure: a) coronal, b) transaxial, c) sagittal

Slika 5: Trije različni prikazi mikrostrukture preseka cevi: a) koronalni, b) transaksialni, c) sagitalni

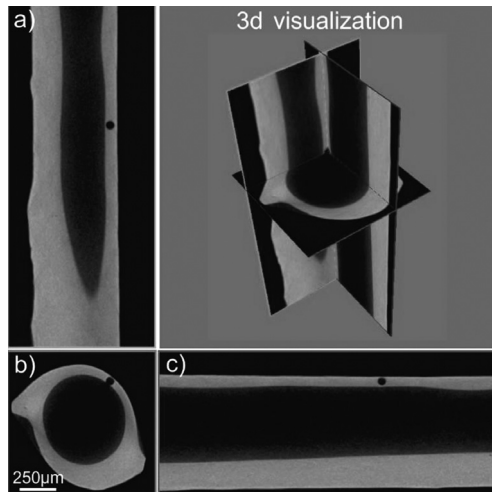


Figure 6: Three different cross-sectional views of the tube microstructure with open pores: a) coronal, b) transaxial, c) sagittal

Slika 6: Trije različni prikazi mikrostrukture preseka cevi z odprtimi porami: a) koronalni, b) transaksialni, c) sagitalni

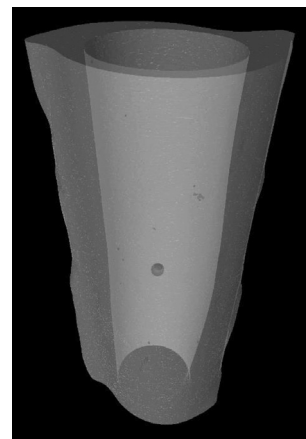


Figure 7: 3-D microstructure of the tube (in grey) with pores
Slika 7: 3-D mikrostruktura cevi (siva barva) s porami

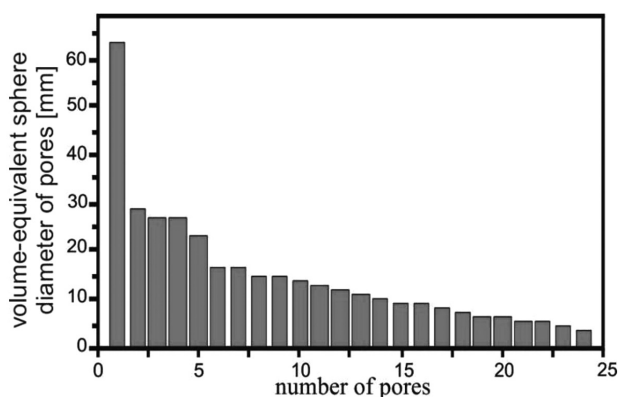


Figure 8: Volume-equivalent sphere diameter of the pores
Slika 8: Volumenski ekvivalent kroglastega premera por

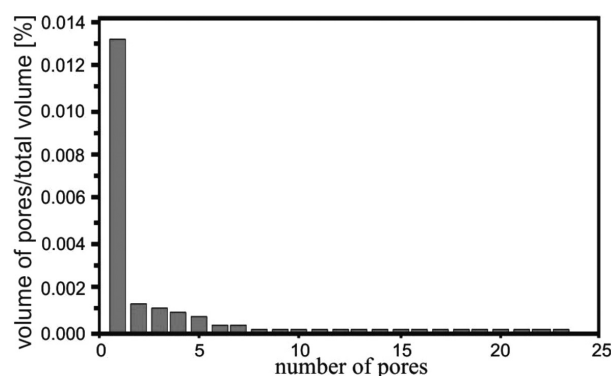


Figure 9: Ratio of the volume of the pores to the total volume
Slika 9: Razmerje volumna por glede na celotni volumen

The microstructure of the tube was found to be mostly continuous (Figure 5) but there were some open and closed pores (Figure 6) that were visualized in 3-D (Figure 7). The volume-equivalent sphere diameter of the pores (Figure 8) revealed that there were only five pores of a volume of 0.0170 % in the range of 23 μm – 63.7 μm (Figure 9). The largest quantity of the pores (19) was in the range of 3.8 μm to 17 μm , but the volume was only 0.0014 % (Figure 9). In addition, various breakthrough structures, related with the varying thickness of the tube, can be observed in the SEM images (Figure 6).

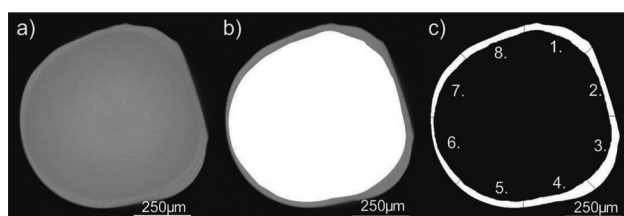


Figure 10: Microstructure of the rod: a) maximum intensity projection, b) differences for the main diameter (in white) and their distribution (in grey), c) thickness distribution divided into 8 parts
Slika 10: Mikrostruktura palice: a) projekcija največje intenzivnosti, b) razlika med glavnim premerom (bela barva) in njihova razporeditev (siva barva), c) razporeditev debeline, razdeljene na 8 delov

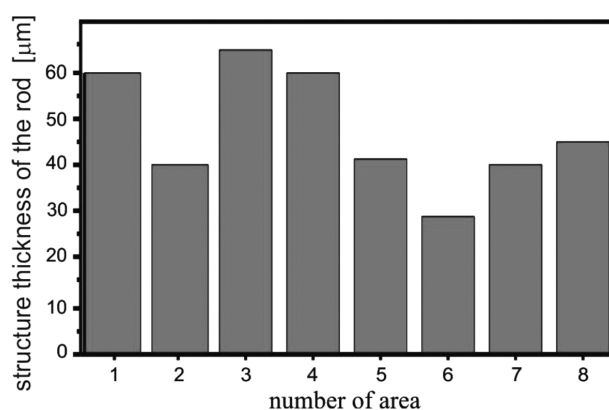


Figure 11: Rod thickness distribution divided into 8 parts (Figure 7c)
Slika 11: Razporeditev debeline palice, razdeljene na 8 delov (Slika 7c)

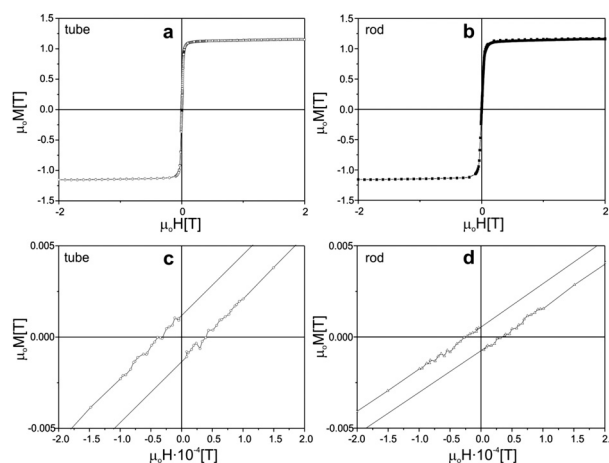


Figure 12: a), b) Static hysteresis loops, c), d) inserts with the origin of M-H system

Slika 12: a), b) Statične histerezne zanke ter c), d) vložki iz M-H sistema

The microstructure of the rod was continuous. To analyse the rod thickness, the distribution of maximum intensity projection (MIP) was used (Figure 10a). The differences, related to the main diameter (1082.2 μm), and their distribution are shown in Figure 10b. To calculate the thickness distribution of the rod, this area was divided into eight parts (Figure 10c) and analysed (Figure 11). The average shell thickness was found to be 47.4 μm .

The measurements of the ‘magnetization versus magnetic field’ were performed on the rod- and tube-shaped samples of the $\text{Fe}_{61}\text{Co}_{10}\text{Ti}_3\text{Y}_6\text{B}_{20}$ amorphous alloy (Figure 12). The static hysteresis loops were found to have the shapes typical for the ferromagnetic materials that exhibit soft-magnetic properties. The saturation-magnetization values for the rod- and tube-shaped samples of the investigated alloy were found to be almost identical, both being approximately 1.17 T. Moreover, the investigated alloys are characterized by low values of coercivity: $0.37 \cdot 10^{-4}$ T and $0.25 \cdot 10^{-4}$ T for the tube- and rod-shaped samples, respectively.

4 CONCLUSIONS

The utilization of the combined injection-casting method, which features the suction casting of a molten alloy into a copper die, facilitated the fabrication of a bulk amorphous $\text{Fe}_{61}\text{Co}_{10}\text{Ti}_3\text{Y}_6\text{B}_{20}$ alloy. In the case of the investigated alloy, the most important application parameters are the good soft-magnetic properties, attained whilst preserving the amorphous structure. Elements Ti and Y were used as the components facilitating the amorphicity of the alloy. It is commonly known that the addition of a small quantity of titanium (up to 5 % of amount fraction), or a similar addition of yttrium, to the Fe-based alloys improve their glass-forming ability (an increase in ΔT_x); however, usually this has a negative impact on the soft-magnetic properties. As demonstrated in this work, despite the addition of these components (3 % of amount fraction of Ti and 6 % of amount fraction of Y), the bulk amorphous $\text{Fe}_{61}\text{Co}_{10}\text{Ti}_3\text{Y}_6\text{B}_{20}$ alloy is characterized by good soft-magnetic properties; i.e., a high value of the saturation magnetization (1.17 T) and low values of coercivity ($0.37 \cdot 10^{-4}$ T and $0.25 \cdot 10^{-4}$ T for the tube and rod samples, respectively).

When carrying out a computer-tomography investigation of the rod-shaped sample of the $\text{Fe}_{61}\text{Co}_{10}\text{Ti}_3\text{Y}_6\text{B}_{20}$ alloy, no pores were observed in the structure. However, during the production of the tube-shaped sample, pores were found in the volume of the sample. The volume-equivalent sphere diameter of the pores indicated that there were only five pores within a range of 23–63.7 μm with a volume of 0.0170 %. The largest quantity of the pores was within a range of 3.8 μm to 17 μm , but their volume comprised only 0.0014 %. The presence of the pores within the volume of the tube-shaped sample caused only a minor deterioration of the magnetic properties in comparison with the rod-shaped sample (an increase in the coercivity). Despite this, the material can be used for the magnetic cores in micromotors, for applications involving miniature devices.

By regulating the technical parameters of the production process, it was possible for the rod- or tube-shaped samples to be obtained. On the basis of the performed investigations, it can be stated that a variation in the quenching speed of the molten alloy has a substantial influence on the structure, the microstructure and some of the magnetic properties of the investigated material. Hitherto, the bulk amorphous alloys have been produced mainly in the forms of rods and plates. The creation of bulk samples in the form of closed rings is a major technological step. During the production process, an additional problem was the appearance of the pores in the volume of the tube, which had deleterious effects on the durability and soft-magnetic properties of the investigated alloy. Given an appropriate chemical composition, these rings could be used in the construction of the magnetic cores in electronic and electric microdevices.

The results of the investigations presented in this paper demonstrate that changes in the structural stresses and quenching speed of the molten alloy have a major

influence on the value of the coercivity, which is a measure of the energy required for demagnetizing the material. Despite a minor increase in the value of the coercivity for the tube-shaped sample, the material formed in this shape can be used for the magnetic cores of micromotors in miniaturized devices.

5 REFERENCES

- A. Inoue, Bulk amorphous alloys with soft and hard magnetic properties, *Materials Science and Engineering*, 226–228 (1997), 357–363, doi:10.1016/S0921-5093(97)80049-4
- M. Nabiałek, J. Zbrozarczyk, J. Olszewski, M. Hasiak, W. Ciużyńska, K. Sobczyk, J. Świerczek, J. Kaleta, A. Łukiewska, Microstructure and magnetic properties of bulk amorphous and nanocrystalline $\text{Fe}_{61}\text{Co}_{10}\text{Zr}_{2.5}\text{Hf}_{2.5}\text{Nb}_2\text{W}_2\text{B}_{20}$ alloy, *Journal of Magnetism and Magnetic Materials*, 320 (2008), 787–791, doi:10.1016/j.jmmm.2008.04.046
- T. Kozieł, J. Latuch, S. Kąc, Structure of melt-spun Fe–Cu–Si–B–Nb alloy, *Journal of Alloys and Compounds*, 586 (2014) S121–S125, doi:10.1016/j.jallcom.2012.11.169
- J. Gondro, J. Świerczek, J. Olszewski, J. Zbrozarczyk, K. Sobczyk, W. Ciużyńska, J. Rzącki, M. Nabiałek, Microstructure and some magnetic properties of bulk amorphous $(\text{Fe}_{0.61}\text{Co}_{0.10}\text{Zr}_{0.025}\text{Hf}_{0.025}\text{Ti}_{0.02}\text{W}_{0.02}\text{B}_{0.20})_{100-x}\text{Y}_x$ ($x = 0, 2, 3$ or 4) alloys, *Journal of Magnetism and Magnetic Materials*, 324 (2012), 1360–1364, doi:10.1016/j.jmmm.2011.11.038
- R. Hasegawa, Soft magnetic properties of metallic glasses, *Journal of Magnetism and Magnetic Materials*, 41 (1984), 79–85, doi:10.1016/0304-8853(84)90142-2
- H. Jian, W. Luo, S. Tao, M. Yan, Mechanical and magnetic properties of $(\text{Fe}_{72}\text{Mo}_4\text{B}_{24})_{100-x}\text{Tb}_x$ ($x = 4, 5, 6, 7$ at.%) bulk glassy alloys, *Journal of Alloys and Compounds*, 505 (2010), 315–318, doi:10.1016/j.jallcom.2010.06.061
- T. Kozieł, J. Latuch, A. Zielińska-Lipiec, Structure of the amorphous-crystalline $\text{Fe}_{66}\text{Cu}_6\text{B}_{19}\text{Si}_5\text{Nb}_4$ alloy obtained by the melt-spinning process, *Archives of Metallurgy and Materials*, 58 (2013) 601–605, doi: 10.2478/amm-2013-0044
- M. Hasiak, K. Sobczyk, J. Zbrozarczyk, W. Ciużyńska, J. Olszewski, M. Nabiałek, J. Kaleta, J. Świerczek, A. Łukiewska, Some Magnetic Properties of Bulk Amorphous Fe–Co–Zr–Hf–Ti–W–B–(Y) Alloys, *IEEE Transactions on Magnetics*, 44 (2008), 3879–3882, doi:10.1109/TMAG.2008.2002248
- K. Błoch, J. Gondro, P. Pietrusiewicz, M. Dośpiał, M. Nabiałek, M. Szota, K. Gruszka, Time and thermal stability of magnetic properties in $\text{Fe}_{61}\text{Co}_{10}\text{Y}_8\text{Nb}_1\text{B}_{20}$ bulk amorphous alloys, *Acta Physica Polonica A*, 126 (2014), 108–109, doi:10.12693/APhysPolA.126.108
- H. Chirac, N. Lupu, Design and preparation of new soft magnetic bulk amorphous alloys for applications, *Materials Science and Engineering A*, 375–377 (2004), 255–259, doi:10.1016/j.msea.2003.10.007
- K. Sobczyk, J. Świerczek, J. Gondro, J. Zbrozarczyk, W. Ciużyńska, J. Olszewski, P. Brągiel, A. Łukiewska, J. Rzącki, M. Nabiałek, Microstructure and some magnetic properties of bulk amorphous $(\text{Fe}_{0.61}\text{Co}_{0.10}\text{Zr}_{0.025}\text{Hf}_{0.025}\text{Ti}_{0.02}\text{W}_{0.02}\text{B}_{0.20})_{100-x}\text{Y}_x$ ($x=0, 2, 3$ or 4) alloys, *Journal of Magnetism and Magnetic Materials*, 324 (2012), 540–549, doi:10.1016/j.jmmm.2011.08.038
- A. Inoue, W. Zhang, T. Zhang, K. Kurosaka, High-strength Cu-based bulk glassy alloys in Cu–Zr–Ti and Cu–Hf–Ti ternary systems, *Acta Materialia*, 49 (2001), 2645–2652, doi:10.1016/S1359-6454(01)00181-1
- K. Gruszka, M. Nabiałek, K. Błoch, S. Walters, Analysis of the structure (XRD) and microstructure (TEM, SEM, AFM) of bulk amorphous and nanocrystalline alloys based on FeCoB, *International Journal of Materials Research*, 106 (2015) 7, 689–696, doi: 10.3139/146.111226

EFFECT OF THE SKIN-CORE MORPHOLOGY ON THE MECHANICAL PROPERTIES OF INJECTION-MOULDED PARTS

VPLIV MORFOLOGIJE SKORJA-JEDRO NA MEHANSKE LASTNOSTI VBRIZGANIH DELOV

Eva Hnatkova^{1,2}, Zdenek Dvorak^{1,2}

¹Department of Production Engineering, Faculty of Technology, Tomas Bata University in Zlín, Vavreckova 275, 760 01 Zlín, Czech Republic

²Centre of Polymer Systems, University Institute, Tomas Bata University in Zlín, Trida T. Bati 5678, 760 01 Zlín, Czech Republic
ehnatkova@ft.utb.cz

Prejem rokopisa – received: 2014-07-31; sprejem za objavo – accepted for publication: 2015-04-13

doi:10.17222/mit.2014.151

The presented study deals with the effects of different processing parameters during injection moulding on the morphological structure through the thickness of the injection-moulded samples and, consequently, on their mechanical properties. In this work, tensile bars of an isotactic polypropylene were injected under different conditions such as the flow rate, the melt temperature and the mould temperature. The morphological structure of the samples was investigated with polarized light microscopy using thin cross-sections cut perpendicularly to the flow direction. The fountain flow in the mould cavity influenced the crystallization kinetics and the presence of three distinct crystalline zones was observed; namely, the highly oriented non-spherulitic skin, the shear-nucleated spherulitic intermediate layer and the inner core composed of spherulites with a low orientation. The results showed that the flow rate has the highest influence on the thickness of the oriented skin layer. The mechanical properties of the tensile samples demonstrated that the larger thickness of the two outer skins provides the higher tensile strength. The same effect was also confirmed with a microhardness test where the skin layer was harder than the inner spherulitic core.

Keywords: skin-core structure, polypropylene, morphology, tensile strength, microhardness

Predstavljena študija obravnava vpliv različnih procesnih parametrov pri vbrizgavanju na morfologijo strukture, zaradi debeline vbrizganih vzorcev, in posledično na njihove mehanske lastnosti. V tem delu so bile natezne palice izotaktičnega propilena vbrizgane pri različnih pogojih, kot so: hitrost tečenja, temperatura snovi in temperatura kokile. Morfološka struktura vzorcev je bila preiskovana z mikroskopijo s polarizirano svetlobo, z uporabo tankih rezin, odrezanih pravokotno na smer toka. Lijakasto litje v votlini orodja je vplivalo na kinetiko kristalizacije in opažena je bila prisotnost treh različnih kristalnih področij, in sicer: močno orientirana ne-sferulitna skorja, s striženjem nukleirana sferulitna vmesna plast in notranje jedro, sestavljeno iz sferulitov, brez orientacije. Rezultati so pokazali, da ima hitrost toka največji vpliv na debelino skorje. Mehanske lastnosti nateznih preizkušancev so pokazale, da večja debelina dveh zunanjih skorij zagotavlja višjo natezno trdnost. Enak učinek je bil potrjen tudi s preizkusom mikrotrote, kjer je bila plast skorje bolj trda kot pri notranjem sferulitnem jedru.

Ključne besede: struktura skorja-jedro, polipropilen, morfologija, natezna trdnost, mikrotrodota

1 INTRODUCTION

It is well known that the internal morphological structure of a semi-crystalline polymer is strongly dependent on the processing parameters during the injection moulding.¹⁻³

The injection of a molten polymer into a relatively cold mould immediately leads to a frozen layer of the polymer at the cavity wall. Then, the melt flow inside takes place between two frozen layers. This mechanism is called the fountain flow. The molecules at the flow front are elongated before their deposition on the cold cavity and, because of the rapid solidification, the surface layer shows a high degree of molecular orientation. In the centre of the flow, the material has more time to relax and crystallize, although even here the shear flow also generates orientation.⁴ The internal morphology displays a strong structural heterogeneity through the cross-section of a sample thickness. This structural deve-

lopment consequently affects the mechanical properties of the final components.⁵

Many studies about injection-moulded polypropylene (PP) have shown that at least two regions are noticeable through a specimen thickness.^{6,7} The first frozen surface layer is called "the skin", whereas the zone in the middle of the cavity is called "the core". Between them, there is an intermediate zone, sometimes called "the shear zone" due to the fountain flow, as can be seen in **Figure 1**.

Previous research was first focused on the effects of both the melt and mould temperatures or the holding pressure on the molecular structure; then, on the influence of the injection speed on the skin thickness and mechanical properties.⁸⁻¹⁰ However, only a few papers deal with the microhardness of the skin and the core structure in correlation with the tensile properties.

This paper describes the effects of different processing parameters during injection moulding such as the melt and mould temperatures and the injection speed on the thickness of the skin layer and the mechanical pro-

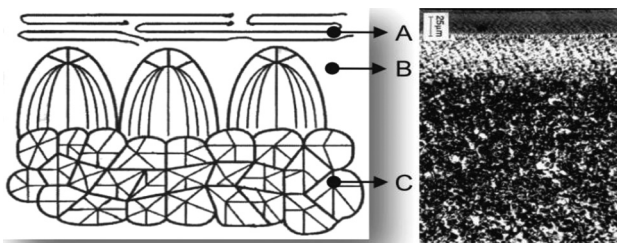


Figure 1: Morphological structure:⁷ A – non-spherulitic skin, B – intermediate zone, C – inner spherulitic core

Slika 1: Morfologija strukture:⁷ A – ne-sferulitna skorja, B – vmesno področje, C – notranje sferulitno jedro

properties of the samples with different morphological structures as well as the microhardness of the skin and core.

2 EXPERIMENTAL WORK

2.1 Material and sample preparation

Throughout this study, the isotactic polypropylene with the commercial name PP HD 601 CF, provided by Borealis, was used. This material is characterized by the melt flow index of 8.0 g/10 min (230 °C/2.16 kg, ISO 1133).

The tensile bars, shown in **Figure 2**, were injection moulded under different processing conditions (**Table 1**) from PP pellets using an Arburg Allrounder 370S injection-moulding machine (Germany) with a screw diameter of 20 mm.

Table 1: Processing conditions of injection moulding

Tabela 1: Pogoji procesiranja pri vbrizgavanju

Parameters	Value	Units
Melt temperature	190, 220	°C
Mould temperature	20, 90	°C
Injection speed	10, 60, 150	mm/s
Injection pressure	55	MPa
Holding pressure	45	MPa
Holding time	5	s

2.2 Morphological structure

The morphological structure of the injection-moulded specimens was characterized with an Olympus polarized light microscope at a 100× magnification. 30-µm micro-

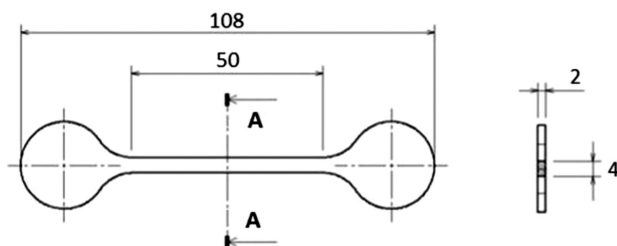


Figure 2: Dimensions of tensile specimens

Slika 2: Dimenzije nateznih preizkušancev

tome samples were cut with a Leica RM225 rotational microtome in the centre of the tensile bars, perpendicular to the flow direction.

2.3 Mechanical properties

The tensile properties of the specimens were determined using a ZWICK 1456 testing machine at 25 °C; the crosshead speed was 50 mm/min. A total of 10 specimens obtained under two different processing conditions were tested, and the average value was reported.

The microhardness of the core and skin was investigated with a CSM Micro-Combi Tester using a Vickers pyramidal indenter according to EN ISO 6507-1. The applied force was 0.5 N and it was maintained for 90 s; the loading and unloading rate was 1 N/min. All the samples were measured at 25 °C and the elastic modulus (E_{IT}) was calculated from the unloading curve using the Oliver and Pharr method.¹¹ For the measurement of the spherulitic core, tensile samples were cut, with a Buhler IsoMet 4000 cutter, to the thickness of 1 mm. Then, the samples were polished in several steps to ensure smooth surfaces.

3 RESULTS AND DISCUSSION

3.1 Skin-core morphology

Figures 3 and **4** illustrate cross-sectional views of different morphological structures on the surface and in the middle of an injection-moulded tensile sample.

As can be seen, the morphological structure changes through the thickness of the injected samples. On the surface, there is a highly oriented non-spherulitic skin layer, which changes into a micro-spherulitic structure at a certain depth from the surface. This means that in this intermediate transition area a large number of spherulites are nucleated. On the other hand, towards the centre of the sample, the spherulites have a larger size due to a different temperature profile in the cooling stage.

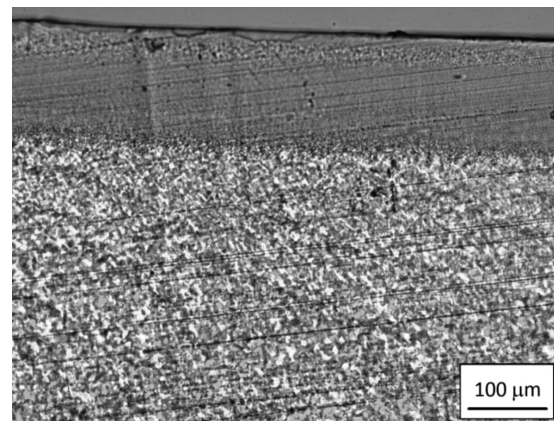


Figure 3: Non-spherulitic surface-layer "skin"

Slika 3: Ne-sferulitna površinska plast "skorja"

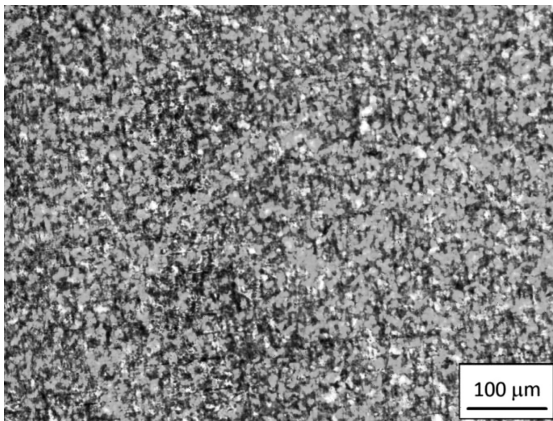


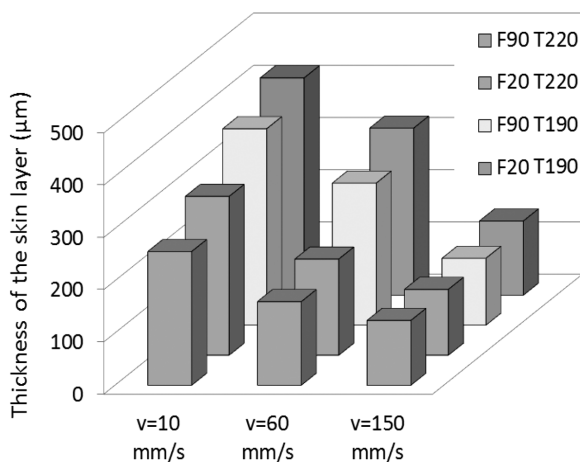
Figure 4: Spherulitic-core structure
Slika 4: Struktura sferulitnega jedra

Figure 5 shows the thickness of skin layers depending on the process parameters.

As can be seen, the thickness of the surface layers varies from 124 μm to 416 μm and is mostly influenced by the injection speed. With a lower speed, the thickness of the skin is higher because the melt front of the material has more time for relaxation and has a greater tendency to be cooled down. With lower mould or melt temperatures, the skin layer also becomes larger. In the case of the highest injection speed, when the mould is filled within 1 s, both the mould and melt temperatures have a negligible effect on the skin thickness.

In comparison with the tensile-bar thickness (2 mm), the largest skin layer, at both sides, occupies more than 40 % of the total sample thickness and this percentage can have an important influence on the mechanical properties, while the thickness of the skin layer of a thicker injection-moulded component has a minor effect.

The spherulite size in the core and the quantity of the intermediate phase, affected by the shear stress, also influence the total tensile strength and must be taken into consideration.



**F* – mould temperature, *T* – melt temperature, *v* – injection speed

Figure 5: Thickness of both skin layers of the samples
Slika 5: Debelina obeh površinskih plasti na vzorcih

3.2 Tensile properties

A tensile measurement was performed for two series of the samples injected under different processing conditions; sample A with a larger skin, where the thickness of both skin layers was approximately around 0.83 mm in the cross-section perpendicular to the flow direction and sample B with the total thickness of both skins of around 0.25 mm.

The process parameters for each series of the samples were as follows:

A: *F* = 20 °C, *T* = 190 °C, *v* = 10 mm/s

B: *F* = 90 °C, *T* = 220 °C, *v* = 150 mm/s

where *F* is the mould temperature, *T* is the melt temperature and *v* is the injection speed.

Figure 6 illustrates the difference in tensile-stress progress for samples A and B. The obtained results are listed in **Table 2**, where *E* is the Young’s modulus, σ_{max} is the maximum nominal stress and $\epsilon_{\sigma_{max}}$ is the strain at σ_{max} .

Table 2: Tensile properties

Tabela 2: Natezne lastnosti

Sample	<i>E</i> /MPa	<i>sd</i> /MPa	σ_{max} /MPa	<i>sd</i> /MPa	$\epsilon_{\sigma_{max}}$ /%	<i>sd</i> /%
A	1787	85.90	35.55	0.32	7.79	0.31
B	1476	22.21	34.67	0.38	9.52	0.19

As can be seen, sample A with the larger skin layers demonstrated the higher tensile strength and Young’s modulus, while the elongation at σ_{max} was a bit smaller than for sample B. This means, that highly oriented molecules of the surface layer have better mechanical properties in the flow direction, except for ductility.

The results indicate that the processing condition during injection moulding play an important role, particularly for the thin-walled products, where the thickness of the skin layer influences the final mechanical properties of the injected components.

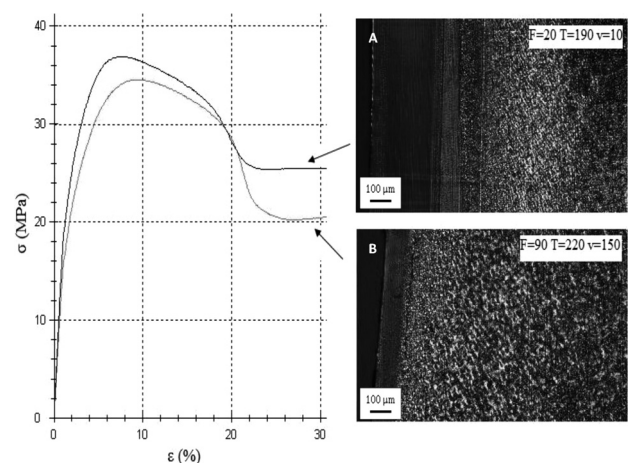


Figure 6: Stress versus strain curves of samples A and B
Slika 6: Krivulji napetost-raztezek vzorcev A in B

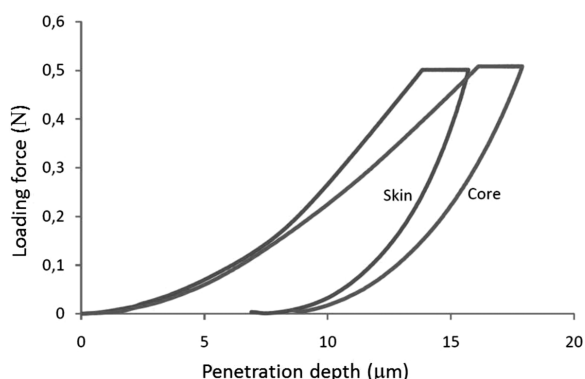


Figure 7: Indentation force versus indentation depth

Slika 7: Sila vtiskovanja v odvisnosti od globine vtiskovanja

3.3 Microhardness properties

A microhardness test for the skin and core was carried out on sample A and **Figure 7** demonstrates the correlation between the force and the penetration depth. The obtained results for the microhardness are shown in **Table 3**, where H_{IT} is the indentation hardness, E_{IT} is the indentation modulus and C_{IT} is the indentation creep.

Table 3: Microhardness values

Tabela 3: Vrednosti mikrotrdote

Sample	H_{IT}/MPa	sd/MPa	E_{IT}/GPa	sd/GPa	$C_{IT}/\%$	$sd/\%$
Skin	107.47	3.97	2.1527	0.47	13.36	0.275
Core	92.911	3.52	1.3083	0.51	10.31	0.314

As can be seen, the measured values in **Table 3** as well as the penetration depth showed a difference in the microhardness of the highly oriented skin layer and the spherulitic core.

The indentation hardness (H_{IT}) of the skin is higher than that of the core by about 14 MPa, the indentation modulus (E_{IT}) is higher by about 0.8 GPa and the creep (C_{IT}) is at approximately the same level. The same trend was confirmed with the tensile test, where a higher strength was demonstrated for the samples with larger skin layers.

4 CONCLUSION

In this study, it was confirmed that the injection-moulding process parameters influence the internal morphological skin-core structure of isotactic PP. In particular, due to a decrease in the injection velocity, the thickness of the surface-skin layer became larger.

Another significant effect was also exhibited by the mould and melt temperatures; but at a high injection rate, when the mould cavity was filled within 1 s, the influence of these parameters was not significant and the thickness of the skin layers remained substantially constant.

Mechanical testing showed that the samples with a larger skin-core effect had a higher tensile strength and Young's modulus, while the ductility of the samples was decreasing. The same results were obtained from the microhardness, where the skin structure was harder than the spherulites in the centre of the sample.

This influence on the mechanical properties is important especially for the thin-walled products. On the other hand, in the case of thicker samples, the skin-core effect has a negligible influence.

Acknowledgments

This work was supported by the Ministry of Education, Youth, and Sports of the Czech Republic – Program NPU I (LO1504). This study was also supported by the internal grant of TBU in Zlin IGA/FT/2016/002 funded from the resources of the specific university research. The authors would like also to thank Petra Pavelova for her help with mechanical testing.

5 REFERENCES

- A. E. Woodward, Understanding polymer morphology, Hansen/Gardner Publication, Ohio, USA 1995
- J. C. Viana, Development of the skin layer in injection moulding: phenomenological model, *Polymer*, 45 (2004) 3, 993–1005, doi:10.1016/j.polymer.2003.12.001
- M. R. Kantz, H. D. Newman, F. H. Stigale, The skin-core morphology and structure-property relationships in injection-moulded polypropylene, *J. Appl. Polym. Sci.*, 16 (1972), 1249–1260, doi:10.1002/app.1972.070160516
- G. Kumaraswamy et al., Shear-enhanced crystallization in isotactic polypropylene: Part 2, Analysis of the formation of the oriented "skin", *Polymer*, 41 (2000) 25, 8931–8940, doi:10.1016/S0032-3861(00)00236-6
- J. W. Housmans, M. Gahleitner, G. W. Peters, H. E. Meijer, Structure-property relations in molded, nucleated isotactic PP, *Polymer*, 50 (2009) 10, 2304–2319, doi:10.1016/j.polymer.2009.02.050
- T. Jaruga, E. Bociaga, Structure of polypropylene parts from multicavity injection mould, *Archives of Materials Science and Engineering*, 28 (2007) 7, 429–432
- F. Lednický, Microscopy and morphology of polymers, 1st ed., Technical university of Liberec, CZ 2009
- M. Obadal, R. Čermák, N. Baran, K. Stoklasa, J. Šimoník, Impact strength of β -nucleated polypropylene, *International Polymer Processing*, 19 (2004) 1, 35–39, doi:10.3139/217.1802
- M. Fujiyama, Structures and Properties of Injection Mouldings of β -Crystal Nucleator-Added Polypropylenes: Part 1, Effect of β -Crystal Nucleator Content, *Int. Polym. Proces.*, 10 (1995) 2, 172–178, doi:10.3139/217.950172
- R. Čermák, M. Obadal, P. Ponížil, M. Polášková, K. Stoklasa, A. Lengálová, Injection-moulded α - and β -polypropylenes: I. Structure vs. processing parameters, *Eur. Polym. J.*, 41 (2005) 8, 1838–1845, doi:10.1016/j.eurpolymj.2005.02.020
- W. C. Oliver, G. M. Pharr, An improved technique for determining hardness and elastic modulus using load and displacement sensing indentation experiments, *J. Mater. Res.*, 7 (1992) 6, 1564–1583, doi:10.1557/JMR.1992.1564

RECRYSTALLIZATION BEHAVIOUR OF A NICKEL-BASED SUPERALLOY

OBNAŠANJE SUPERZLITINE NA OSNOVI NIKLJA PRI REKRISTALIZACIJI

Pavel Podany, Zbysek Novy, Jaromir Dlouhy

COMTES FHT, Prumyslova 995, 334 41 Dobruška, Czech Republic
pavel.podany@comtesfht.cz

Prejem rokopisa – received: 2014-08-01; sprejem za objavo – accepted for publication: 2015-04-16

doi:10.17222/mit.2014.163

The thermomechanical processing of a nickel-based superalloy is the way to considerably influence the grain size. A uniform coarse-grain size increases the creep strength and the crack-growth resistance. In this work, the processing for achieving a uniform recrystallized-grain structure with a variation in the thermomechanical parameters is investigated.

The MoNiCr alloy is intended for modern designs of nuclear reactors, in which molten fluoride salts are used as the coolants in the primary and/or secondary circuit. It represents a material alternative with a high corrosion resistance in the area of fluoride salts and it has very good creep properties in the temperature range of 650–750 °C as well.

The manufacture of vessels and fittings from the MoNiCr alloy requires the mastering of the technology for forming this high-alloyed material. The key step seems to be the transition of the cast state of the material to the state of a cast recrystallized microstructure with homogenous fine grains. A particular stress condition is, besides the temperature, very important during hot forming. Nickel alloys are able to accept a significantly higher deformation level if the compressive stress prevails.

A forming process involving the compression state of stress increases the probability that the material will reach, without failure, a level of deformation that allows recovery and recrystallization processes. A particular deformation process was carried out on a physical simulator. The preceding cold deformation essentially accelerates the recrystallization process of a deformed cast structure.

Keywords: recrystallization, nickel alloys, physical simulation

Termomehanska obdelava superzlitine na osnovi niklja je način, s katerim lahko močno vplivamo na velikost kristalnih zrn. Enakomerna velikost velikih zrn povečuje odpornost na lezenje in ovira rast razpok. V tem delu je s spreminjanjem parametrov termomehanske predelave preiskovana predelava za doseganje enakomerne rekristalizirane mikrostrukture.

Zlitina MoNiCr je namenjena modernemu konceptu nuklearnih reaktorjev, v katerih se uporablja staljene fluoridne soli, kot sredstvo za hlajenje v primarnem in/ali sekundarnem tokokrogu. Predstavlja alternativni material z visoko korozijsko odpornostjo v področju fluoridnih soli in ima hkrati zelo dobro odpornost na lezenje v temperaturnem področju 650–750 °C.

Izdelava posod in prirobnic iz zlitine MoNiCr zahteva obvladovanje tehnologije preoblikovanja tega visoko legiranega materiala. Ključni moment izgleda je preoblikovanje litega stanja materiala do stanja rekristalizirane mikrostrukture s homogenimi, drobnimi zrn. Pri vročem preoblikovanju je poleg temperature pomembno tudi stanje napetosti. Nikljeve zlitine so sposobne veliko večje deformacije, če prevladujejo tlačne napetosti.

Preoblikovanje s tlačnimi napetostmi povečuje verjetnost, da bo material brez porušitve dosegel tak nivo deformacije, ki omogoča procese poprave in rekristalizacije. Proces deformacije je bil izvršen na fizikalnem simulatorju. Nadaljnja hladna deformacija občutno pospeši proces rekristalizacije deformirane lite strukture.

Ključne besede: rekristalizacija, nikljeve zlitine, fizikalna simulacija

1 INTRODUCTION

Superalloys are nickel-, iron-nickel-, and cobalt-based alloys generally used at temperatures above about 540 °C. The alloys that can be used even at higher temperatures are continuously investigated thanks to their excellent mechanical and corrosion properties.¹ The iron-nickel-based superalloys form an extension of the stainless-steel technology and are generally wrought. A large number of alloys were invented and studied; many were patented. However, many alloys were winnowed down over the years; only a few are extensively used.² Due to their excellent creep resistance, the nickel-based superalloys are used in the power industry, especially for power engineering. The current nuclear-power engineering is mostly represented by the light water nuclear reactor that uses low-enriched uranium in the form of

uranium dioxide as its fuel. However, the current use of the uranium raw material is low, in most cases it ranges between 3 % and 5 %. A limited number of reactors use mixed uranium-plutonium fuel that increases the primary use of the uranium raw material. The research of the fourth-generation reactor system deals with the way of how to prevent a non-economical use of uranium.³

The fourth generation of reactors is generally divided into two types: thermal and fast reactors. The thermal reactors use a moderator to slow down the neutrons emitted by fission, making them more likely to be captured by the fuel. A fast reactor directly uses the fast neutrons emitted by fission, without a moderation. These new reactors are designed with the following objectives in mind:^{3,4}

- Enhanced nuclear-reactor safety
- Increase in the nuclear-reactor energy efficiency

- Closure of the nuclear-reactor fuel cycle
- Reduction in the fuel-radioactivity level
- Disposal of the used fuel

It appears that the waste management is the major concern regarding the existing once-through cycle because of the limited availability of the repository space worldwide. Closed fuel cycles of recycling reactors allow some of the fuel to be reused. An improvement in the reactor performance can be achieved if the thermal and fast reactors are operated in a coupled mode. An increase in the fuel burnup of the thermal reactors can improve the management of the produced actinides by burning them in situ. With a transmutation, the relative toxicity of the radioactive waste decreases considerably (Figure 1).⁴

An increase in the nuclear-power-plant energy efficiency is possible by increasing the output coolant temperature in the reactor. This can be achieved if a coolant other than water is used. Sodium, lead, gases, supercritical water and other media are under consideration. One of the concepts of the fourth-generation reactors is a molten-salt reactor where molten fluoride salt is considered for the primary and also for the secondary circuit. The main advantage of this reactor is a high efficiency (a high level of the nuclear-fuel usage), but the main disadvantage is the environment of the molten fluoride salt with a temperature of 700–800 °C. A suitable material for fittings and vessels must have an extreme corrosive and creep resistance in this environment. It is, nevertheless, necessary to make moulded plates and pipes that must be bent and hermetically joined together – they must be welded to the shape of the final fittings. The formation of semi-finished products from cast ingot is one of the technologically most complicated operations during the manufacture of vessels and fittings.

Many studies stated that nickel-based superalloys with high Mo and low Cr contents are generally superior with respect to the high-temperature corrosion resistance in fluorine environments.⁵

The main microstructure parameter that affects the mechanical properties is the grain size. It greatly influences the strength, the creep, the fatigue-crack initiation

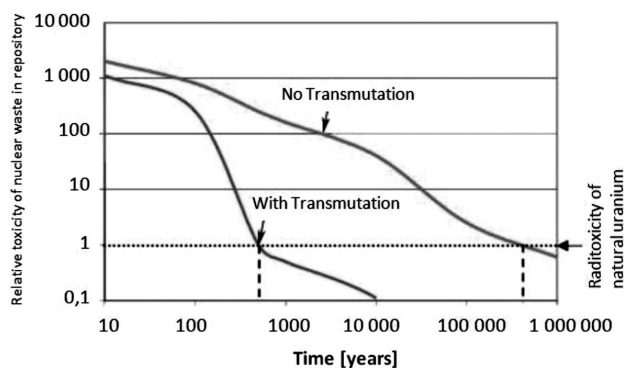


Figure 1: Relative toxicity of the nuclear waste in repository⁴
 Slika 1: Relativna toksičnost nuklearnih odpadkov na odlagališču⁴

and the growth rate. A uniform coarse-grain size increases the creep strength, the crack-growth resistance and the ductility. On the contrary, a uniform fine-grain size provides a high low-cycle fatigue life and high tensile and yield strengths.⁶

Usually the microstructure of a nickel superalloy after hot working consists of large and fine grains and is not uniform. Irrespective of whether the microstructure is coarse grained or fine grained it should be uniform for further annealing processing. Previous studies found that hot working followed by cold working and then by the annealing process is the best way to achieve a uniform recrystallized microstructure.⁷

The inability of the nickel-based superalloys to dynamically recrystallize during forging leads to difficulties during the forging at the highest temperatures close to the temperature of solidus. Even more, such high temperatures can lead to hot cracking on grain boundaries. This can be caused partially by the presence of low-melting impurities on the grain boundaries and also by the oxidation, which occurs much faster through the grain boundaries than within the grains. High-temperature oxidation is much promoted by the main solid-solution strengthening element – molybdenum. Therefore, the forging temperature has to be kept in the interval below the hot cracking and above the point that ensures dynamic recrystallization.

The strain rate is the second important parameter of forming. A high strain rate does not bring enough time for "self-healing" processes in the crystal lattice and usually strengthening takes place in the microstructure. This also leads to cracking during forming.

2 EXPERIMENT DESCRIPTION

An experiment was carried on the MoNiCr nickel superalloy, developed by COMTES FHT Inc. regarding its application in molten-salt reactor circuits. The chemical composition of this alloy is shown in Table 1.

Table 1: Chemical composition of the experimental alloy in mass fractions (w/%)

Tabela 1: Kemijska sestava preizkusnih zlitin v masnih deležih (w/%)

Element	Mo	Cr	Ti	Fe	Mn	Nb	Al	W	Ni
w/%	15.81	6.82	0.03	2.32	0.04	0.01	0.26	0.06	base

The experiment was focused on an evaluation of the influences of various thermomechanical processes on the behaviour of the processed samples and their microstructures. At first, an evaluation of the strain-deformation characteristics of the samples made from the material in the as-cast state was performed. A similar evaluation of the strain-deformation characteristics was also made on the samples in the as-cast state, with a preceding hot deformation (while alternating the strain) (Figure 2).

Further experiment consisted of the following steps:

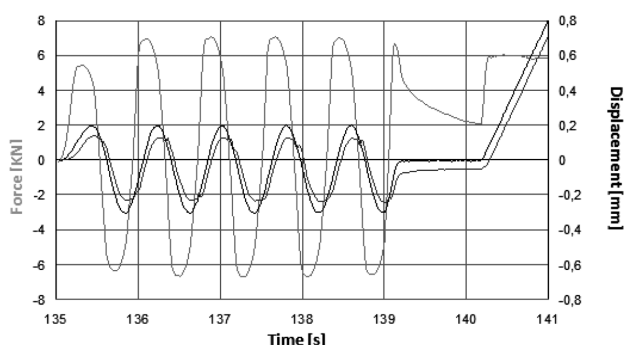


Figure 2: Example of cyclic heat deformation prior to the heat-tensile test – 10 °C/s at 1200 °C, 15 s, 10 mm × 0.5 mm, 1 mm/s

Slika 2: Primer ciklične toplotne deformacije pred vročim nateznim preizkusom – 10 °C/s pri 1200 °C, 15 s, 10 mm × 0,5 mm, 1 mm/s

- Evaluation of the influence of thermomechanical processing (heat deformation) on recrystallization
- Evaluation of the influence of cold deformation on recrystallization.

A strain-deformation characterisation and thermomechanical processing were carried out on the samples whose shape is represented on **Figure 3**. These samples were tested on a simulator of heat-deformation cycles (**Figure 3**). This simulator was used in the previous studies for similar purposes.⁸ In the device, the body of a sample is heated by resistance heating to the controlled temperature. In the case of the experimental focus on the evaluation of the thermomechanical processing, a sample is loaded with cycles of tensile and compression deformation. Each partial compressive deformation was higher than the preceding tensile deformation. The total logarithmic degree of deformation for a sample was approximately 0.5–2.5.

In the case of the experimental focus on the evaluation of cold forming, cold deformation preceded high-temperature deformation – upsetting. **Table 2** shows an overview of the performed ways of the treatment.

After the thermomechanical processing, all the samples were cut in the longitudinal direction and they

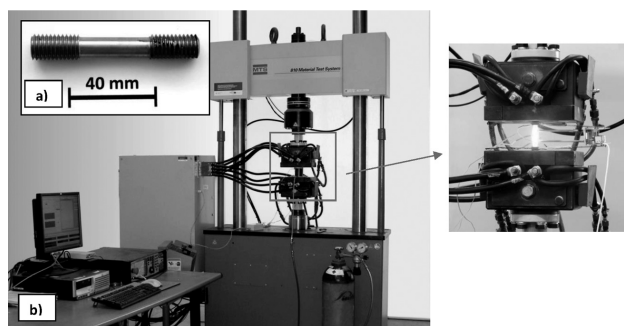


Figure 3: a) Shape of an experimental sample, b) simulator of heat-deformation cycles – servo-hydraulic mechanical testing system MTS complemented by resistance heating

Slika 3: a) Oblika preizkušanca, b) simulator toplotnih deformacijskih ciklov – servo hidravlični mehanski preizkusni sistem MTS, dopolnjen z uporovnim ogrevanjem

underwent the standard metallographic preparation (grinding and subsequent polishing). The microstructure was revealed by etching in Marble’s reagent and documented on a Nikon light microscope. An image analysis of the recrystallized-grain fraction was performed by means of the NIS-Elements software.

Table 2: Processing of the samples with cold deformation and the subsequent cyclic hot deformation

Tabela 2: Obdelava vzorcev s hladno deformacijo, ki ji je sledila vroča ciklična deformacija

Embedded deformation		Hot Deformation at 1200 °C		
		0.3	0.7	1.1
Cold Deformation (at room temperature)	0.05	CD0.05-HD0.3	CD0.05-HD0.7	CD0.05-HD1.1
	0.25	CD0.25-HD0.3	CD0.25-HD0.7	CD0.25-HD1.1

3 RESULTS AND DISCUSSION

3.1 Strain-deformation characteristics of the as-cast state

The tensile test was made on the samples in a temperature range of 1050–1250 °C. As they were in the cast state, the ductility was very low up to the breaking limit of Ag (**Figure 4**). Even with the cyclic deformation prior to the tensile test, it did not reach the value sufficient for the development of a massive recrystallization. **Figure 5** shows the microstructure near the fracture of a sample treated in this way at 1200 °C. Before the tensile test, the sample was loaded with the preceding hot deformation (by alternating the strain). The deformation was not sufficient for the development of a massive recrystallization. Recrystallization only takes place at the boundaries of the large grains of the cast structure.

3.2 Thermomechanical processing – cyclic loading and its influence on the microstructure

The samples were subjected to the loading with cycles of tensile and compression deformation. The amount of deformation was increased in steps. It is

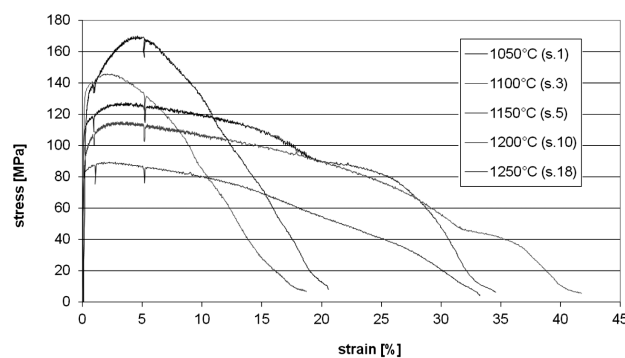


Figure 4: Stress-strain curves of the samples heated with resistance heating at 1050–1200 °C

Slika 4: Krivulje napetost-raztezek za vzorce, ogrevane z uporovnim gretnjem pri 1050–1200 °C

evident that the increase in deformation (see **Figure 6** for the applied deformation) led to an increase in the volume of recrystallized grains. At lower deformation, recrystallization occurs only at the boundaries of the grains, but with higher deformation, it extends into the grains (**Figures 7 to 11**).

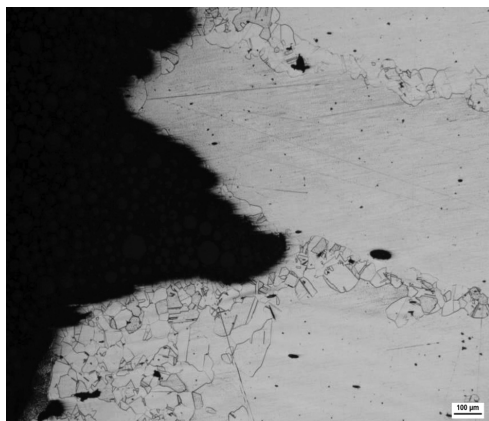


Figure 5: Microstructure of a sample near the fracture area after the tensile test performed at 1200 °C

Slika 5: Mikrostruktura vzorca blizu preloma po nateznem preizkusu, izvršenem na 1200 °C

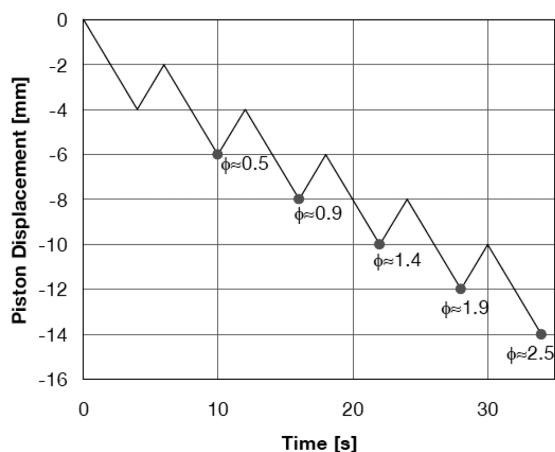


Figure 6: Deformation of particular samples

Slika 6: Deformacija posameznih vzorcev

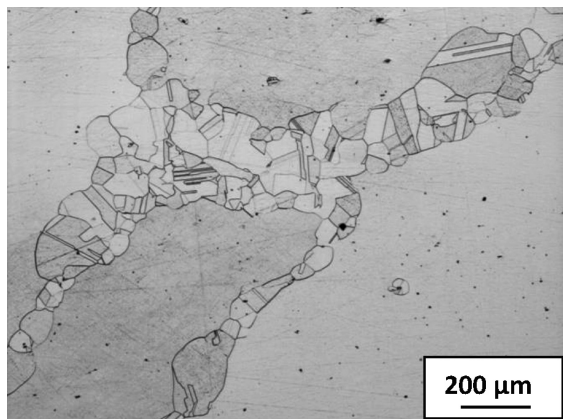


Figure 7: Microstructure after deformation $\Phi \approx 0.5$

Slika 7: Mikrostruktura po deformaciji $\Phi \approx 0,5$

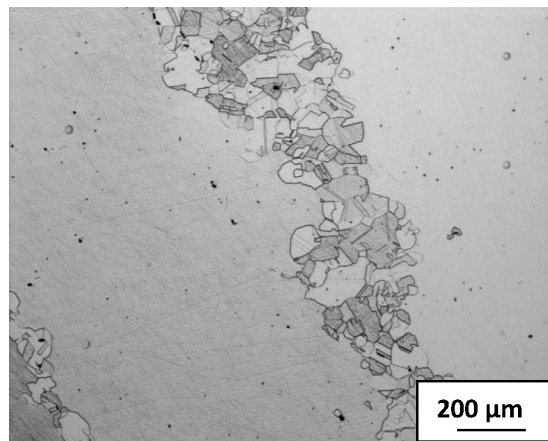


Figure 8: Microstructure after deformation $\Phi \approx 0.9$

Slika 8: Mikrostruktura po deformaciji $\Phi \approx 0,9$

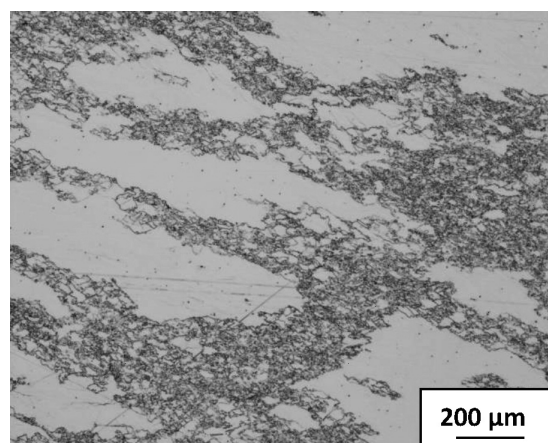


Figure 9: Microstructure after deformation $\Phi \approx 1.4$

Slika 9: Mikrostruktura po deformaciji $\Phi \approx 1,4$

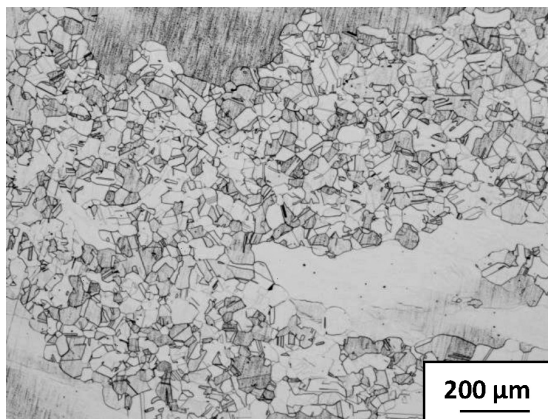


Figure 10: Microstructure after deformation $\Phi \approx 1.9$

Slika 10: Mikrostruktura po deformaciji $\Phi \approx 1,9$

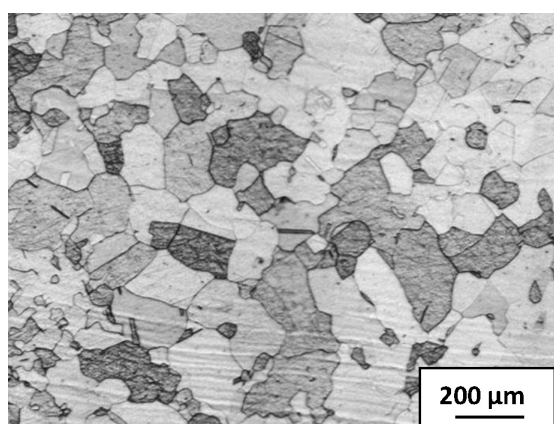


Figure 11: Microstructure after deformation $\Phi \approx 2.5$
Slika 11: Mikrostruktura po deformaciji $\Phi \approx 2,5$

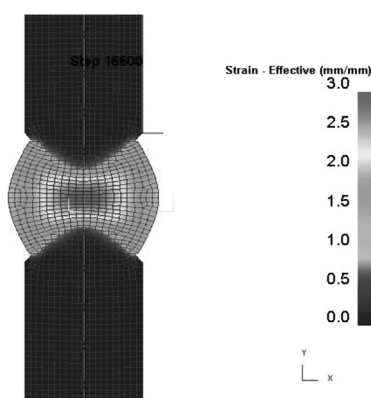


Figure 12: Effective-strain distribution in a sample after the last tensile-compression cycle. The calculated value of deformation is $\Phi \approx 2.5$.
Slika 12: Razporeditev efektivnega raztezka v vzorcu po zadnjem natezno-tlačnem ciklu. Izračunana stopnja deformacije je $\Phi \approx 2,5$.

3.3 Cold working of the samples prior to hot deformation

It was stated in the introduction that cold deformation of nickel superalloys promoted recrystallization during the following hot processing. An acceleration of the recrystallization process is obvious already in the case of a relatively small plastic deformation.

The volume fraction of the recrystallized microstructure with the highest cold deformation of a sample after the highest hot deformation is about 90 %.¹³

3.4 Experimental forging

Experimental forging was carried out on a rectangular-shaped piece made from ingot. The dimensions of the sample were 45 mm × 45 mm × 125 mm (**Figure 14a**). The sample was gradually heated (**Figure 14b**) to a forging temperature of 1170 °C.

Due to a rather quick natural cooling of the sample during the forging, only three reduction blows were applied in one forging step, immediately followed by

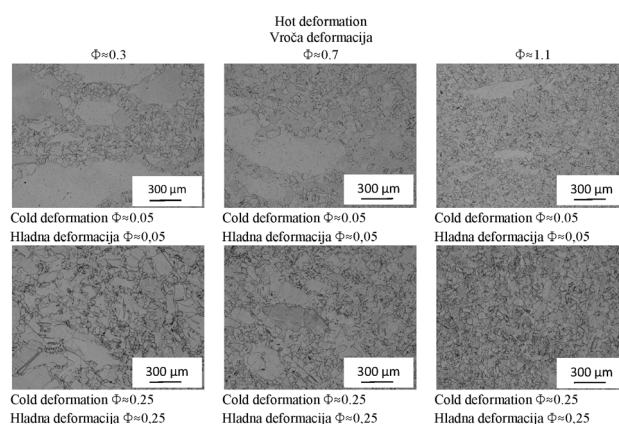


Figure 13: Influence of the size of cold and hot deformation on the share of the recrystallized structure
Slika 13: Vpliv stopnje hladne in vroče deformacije na delež rekristalizirane strukture

further reheating of the sample. The first forging operation before upsetting rounded the edges because sharp corners are usually the source of cracking. After that, the sample with dimensions of about 47 mm in diameter and about 150 mm in length was subjected to the upsetting to a height of about 90 mm and a diameter of about 60 mm. The last forging operation was drawing. The final shape of the forged sample was rectangular, with two differently reduced parts (**Figure 15**). These two parts were subjected to a microstructure examination.

The microstructure of both parts shows a uniform distribution of the grains with no traces of the as-cast structure (**Figures 16 and 17**). Sample A shows a presence of small recrystallized grains (5 μm – 10 μm) around the boundaries of larger grains (**Figure 17b**).

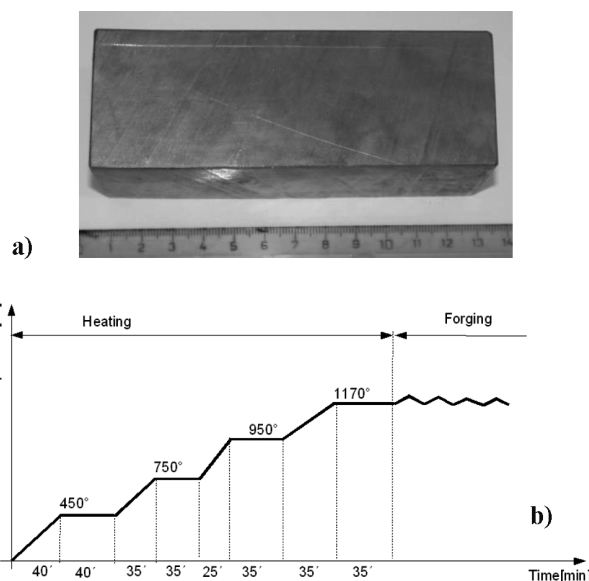


Figure 14: a) Sample for open-die forging on a hydraulic press, b) heating of the sample before forging
Slika 14: a) Vzorec za prsto kovanje na hidravlični preši, b) postopek ogrevanja vzorca pred kovanjem



Figure 15: Forged sample after the final forging operation
Slika 15: Kovani vzorec po končni operaciji kovanja

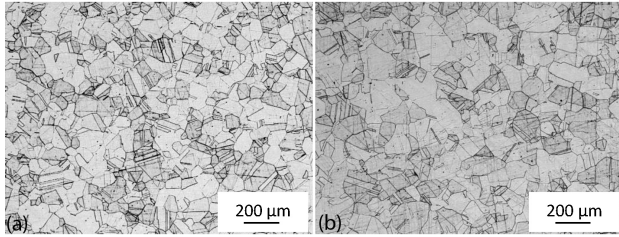


Figure 16: a) Microstructure of part B – near the surface, b) microstructure of part B – in the centre
Slika 16: a) Mikrostruktura v delu B – blizu površine, b) mikrostruktura v delu B – v sredini

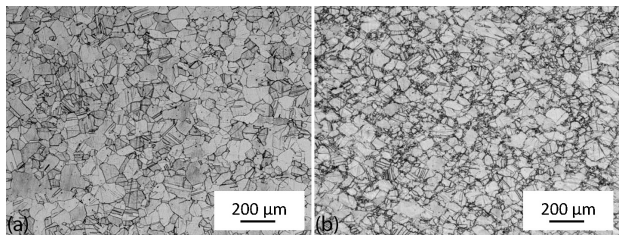


Figure 17: a) Microstructure of part A – near the surface, b) microstructure of part A – in the centre
Slika 17: a) Mikrostruktura v delu A – blizu površine, b) mikrostruktura v delu A – v sredini

The microstructure was also subjected to a grain-size measurement. The grain size was measured by means of image-analysis software NIS-Elements – module D.

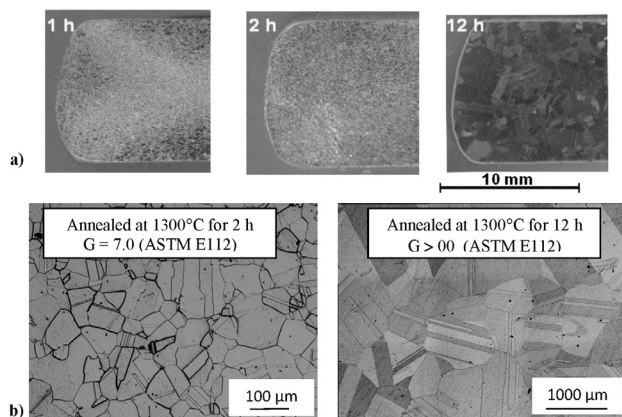


Figure 18: a) Grain growth after annealing at 1300 °C for 1 h, 2 h and 12 h, b) comparison of the microstructures of the samples after annealing for 2 h and 12 h at 1300 °C

Slika 18: a) Rast zrn po žarjenju na 1300 °C 1 h, 2 h in 12 h, b) primerjava mikrostrukture vzorcev po žarjenju 2 h in 12 h na 1300 °C

Table 3: Grain size according to ASTM E 112

Tabela 3: Velikost zrn po ASTM E 112

Sample	Near the surface – G (ASTM E 112)	Centre – G (ASTM E 112)
A	5.5	5.0
B	6.5	6.5

3.5 Further processing – annealing

The obtained uniform microstructure had to be further processed with high-temperature annealing. It is necessary to obtain a uniform coarse-grained microstructure for ensuring good creep strength and crack-growth resistance. **Figures 18a** and **18b** illustrate the grain growth after the annealing at 1300 °C. Particular grain size shows **Table 3**.

4 CONCLUSION

The following facts were found during the research of the nickel-based-superalloy recrystallization behaviour:

- The warm strength of the monitored alloy is very high. Even at 1200 °C it significantly exceeds 100 MPa. The ductility at the maximum stress is very low. After reaching the maximum stress, the material is further deformed but the first cracks start to arise. When the deformation continues a neck is not formed.
- It was found that the minimum deformation level for the start of the recrystallization during the hot working is $\Phi \approx 2.5$. Only such a high strain level ensures the recrystallization within the cast grains.
- The recrystallization process is significantly accelerated by the preceding cold forming. The structure was perfectly recrystallized after $\Phi \approx 0.25$ cold deformation followed by $\Phi \approx 1.1$ hot deformation.
- The microstructure examination after an intense experimental forging showed a good distribution of the recrystallized grains within the whole cross-section with respect to the compliance of the forging temperature.
- A coarse-grained microstructure for a good creep resistance can be obtained with the annealing at 1300 °C for 12 h.

Acknowledgments

These results were created under the project entitled Development of West-Bohemian Centre of Materials and Metallurgy No.: LO1412, financed by the Ministry of Education, Youth and Sports of the Czech Republic.

5 REFERENCES

- ¹ J. Malcharcziková et al., Influence of the hip process on the properties of as-cast Ni-based alloys, *Mater. Tehnol.*, 49 (2015) 1, 15–18

- ² M. J. Donachie, S. J. Donachie, *Superalloys, A Technical Guide*, The Materials Information Society, Materials Park, OH 2002
- ³ Z. Nový et al., *Recrystallization of Nickel Superalloys*, 1st International Conference about Recent Trends in Structural Materials – COMAT, Plzen 2010
- ⁴ <http://mragheb.com/NPRE%20402%20ME%20405%20Nuclear%20Power%20Engineering/Fourth%20Generation%20Reactor%20Concepts.pdf>
- ⁵ P. Wangyao et al., *Microstructure Development by Hot and Cold Working Processes in Nickel Based Alloy*, *Journal of Metals, Materials and Minerals*, 13 (2003) 2, 33–43
- ⁶ R. Jones, L. Jackmann, *The Structural Evolution of Superalloy Ingots during Hot Working*, *Journal of Metals*, 51 (1999) 1, 27–31
- ⁷ V. Vrchovinsky et al., *Effect of Final Cold Rolled Microstructure on Creep Deformation Behaviour on Nickel Base Alloy*, *Journal of Metals, Materials and Minerals*, 15 (2005) 2, 57–68
- ⁸ J. Džugan, Z. Nový, M. Sosnová, *Fatigue life optimization of steel by thermomechanical treatment with the use of physical simulator*, *Advanced Materials Research*, 264–265 (2011), 1725–1730, doi:10.4028/www.scientific.net/AMR.264-265.1725

ESTIMATION OF THE NUMBER OF FORWARD TIME STEPS FOR THE SEQUENTIAL BECK APPROACH USED FOR SOLVING INVERSE HEAT-CONDUCTION PROBLEMS

UGOTAVLJANJE ŠTEVILA VNAPREJŠNJIH ČASOVNIH KORAKOV ZA SEKVENČNI BECKOV PRIBLIŽEK PRI REŠEVANJU PROBLEMOV INVERZNE TOPLOTNE PREVODNOSTI

Jan Komínek, Michal Pohanka

Brno University of Technology, Faculty of Mechanical Engineering, Technická 2, 616 69 Brno, Czech Republic
kominek@lptap.fme.vutbr.cz

Prejem rokopisa – received: 2014-08-13; sprejem za objavo – accepted for publication: 2015-04-08

doi:10.17222/mit.2014.192

Direct heat-conduction problems are those whose boundary conditions, initial state and material properties are known and the entire temperature field in a model can be computed. In contrast, an inverse problem is defined as the determination of the unknown causes based on the observation of their effects. The inverse heat-conduction method is often used for problems where the boundary conditions cannot be measured directly but are computed from the recorded temperature history inside the model. A very effective method for solving this difficult problem is the sequential Beck approach. To stabilize this inverse problem, a proper regularization parameter must be used. For this method, the regularization parameter is the number of the forward time steps that stabilize the inverse computation. This paper describes two methods for computing the number of the recommended forward time steps for nonlinear heat-conduction models with temperature-dependent material properties. The first method is based on tracking the sensitivity (at the interior point of a measurement) to the Dirac heat-flux pulse on the surface. The second method determines the number of the forward time steps from the residual function computed from the heat fluxes obtained from the inverse computation. The stability and noise (in the results) of several variants of these methods are compared. The results showed that the first method is much less computationally intensive and gives a slightly higher value of the number of forward time steps than the second method.

Keywords: inverse heat-conduction problem, Beck approach, number of forward time steps

Neposredni problemi prevajanja toplote so tisti pri katerih so poznani robni pogoji, začetno stanje in lastnosti materiala ter možnost izračuna temperaturnega polja znotraj modela. Nasprotno pa je inverzni problem definiran kot določanje nepoznanih vzrokov na osnovi opazovanja njihovih vplivov. Metoda inverznega prevajanja toplote se pogosto uporabi pri problemih, kjer se robni pogoji ne morejo neposredno izmeriti, temveč se jih izračuna iz zabeleženega poteka temperature znotraj modela. Zelo učinkovita metoda za reševanje tovrstnega problema je sekvenčni Beckov približek. Za stabilizacijo takšnega inverznega problema se mora uporabiti ustrezen regulirni parameter. Pri tej metodi je regulirni parameter število priporočenih časovnih korakov, ki stabilizirajo inverzni izračun. Članek opisuje dve metodi za izračun števila priporočenih časovnih korakov za nelinearni model prenosa toplote, s temperaturno odvisnimi lastnostmi materiala. Prva metoda temelji na iskanju občutljivosti, na notranji točki merjenja, do Dirac utripa toplotnega toka na površini. Druga metoda določa število vnaprejšnjih časovnih korakov iz preostale funkcije izračunane iz toplotnih tokov, ki so dobljeni z inverznim izračunom. V rezultatih je primerjana stabilnost šuma pri več variantah teh metod. Rezultati so pokazali, da je prva metoda mnogo manj računsko intenzivna in daje rahlo večjo vrednost števila predhodnih časovnih korakov kot druga metoda.

Ključne besede: problem inverzne toplotne prevodnosti, Beckov približek, število vnaprejšnjih časovnih korakov

1 INTRODUCTION

Heat-conduction problems are often solved in engineering applications during simulations. The problem is well known as a direct task. The effect (the temperature field in time) is computed from the causes (the known initial and boundary conditions). Complex direct problems can be solved using many numerical methods such as FDM,¹ FVM,² FEM.³ The situation is opposite for an inverse heat-conduction problem and it is a much more complicated problem. The causes (e.g., the boundary conditions) are determined from the observation of the effects (the temperature record in several points). There are some computational methods dealing with this inverse problem, including the Beck approach,⁴ Tikhonov

regularization⁵ and neural networks.⁶ We focus on the sequential Beck approach in this paper.

The basic idea of the sequential approach is to solve the entire task step by step in time. The measured temperature at an interior point at times $t_n, t_{n+1}, \dots, t_{n+N_f}$ is used to compute the heat flux on the boundary at time t_n , where N_f is the number of forward time steps (the regularization parameter). A computation of N_f temperature fields using a direct task is performed for two different values of constant heat fluxes in each time step. The temperature responses from these two direct tasks are compared to the measured temperature. The new value of the heat flux at time t_n is computed. The choice of an appropriate value for N_f is essential for practical computations. A small value leads to instability and a large

value smoothes sudden changes in the boundary conditions. Thus, the appropriate value of this parameter is essential.

2 IMPACT OF THE NUMBER OF FORWARD TIME STEPS ON THE COMPUTED RESULTS

The main function of parameter N_f is to guarantee the stability of the computation of this difficult problem. The stability increases with an increasing value of N_f . In **Figure 1**, three results for $N_f = 13, 20, 30$ are compared to the correct heat-flux record, which was used to generate the input temperature record for the inverse task. The noise was also added to this temperature record (a standard deviation of $0.05\text{ }^\circ\text{C}$). A large oscillation of the computed heat flux for a low value of N_f is obvious. This is mainly due to the added noise in the input data. The noise reduction in the input data is more effective for larger values of N_f (**Figure 1**). This effect indicates that the use of a large N_f is recommended. Unfortunately, increasing N_f has two effects. First, the computation cost is proportional to N_f . A higher value of N_f results in a longer computational time. Second, a large N_f value smoothes the computed results. Abrupt changes as well as the maximum values of the ideal heat flux (**Figure 1**) are significantly reduced when N_f increases. For $N_f = 30$, the computed maximum heat flux is less than 50 % of the ideal heat flux for this test case.

3 METHODS

The appropriate value of forward time steps is different for each computational model. Two types of methods are described in this article to determine its amount. The first, newly proposed, method is based on the temperature response. The idea is to compare two temperature responses at an interior location (usually a

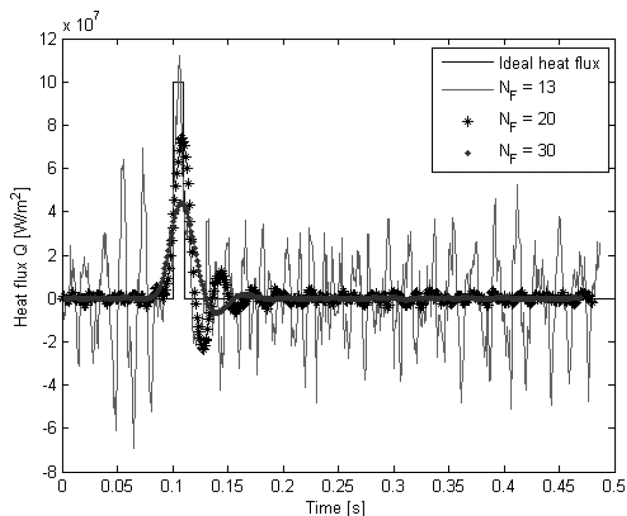


Figure 1: Influence of N_f on the inverse heat-conduction problem
Slika 1: Vpliv N_f na problem inverzne toplotne prevodnosti

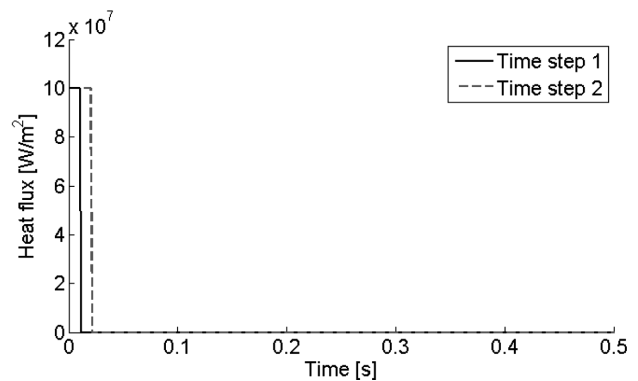


Figure 2: Heat-flux pulses in the subsequent time steps
Slika 2: Sunki toplotnega toka v poznejših časovnih korakih

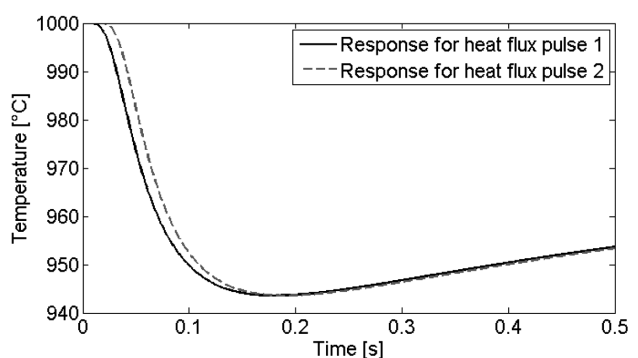


Figure 3: Temperature response
Slika 3: Temperaturni odziv

thermocouple position) to two Dirac pulses of heat flux that are the same but shifted in time by one time step (**Figures 2 and 3**). The first temperature response is computed for the Dirac pulse applied from time step zero to time step one and the second temperature response is computed for the Dirac pulse applied from time step one to time step two. The computed difference between these two temperature responses is shown in **Figure 4**. The computed curve provides an idea of how the information about the changes in the boundary condition is delayed from time step zero to time step two and spread over the time. This curve shows the distribution of the information about the temperature response. This is the information about what happened at the beginning of the

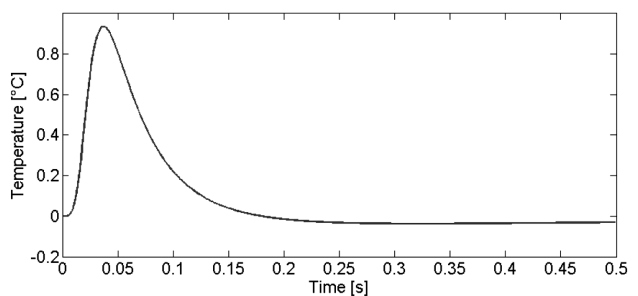


Figure 4: Difference between temperature responses
Slika 4: Razlika med temperaturnimi odzivi

simulation (from time step zero to time step two) at the boundary of the computational model.

For practical computations, it should be noted that both temperature responses are the same except for the time shift, which is one time step. In addition, the temperature response difference $\Delta T_n = T_n - T_{n-1}$ corresponds to the numerical derivation except for the multiplication by constant c (Equation (1)):

$$T_n - T_{n-1} = c \cdot dT = c \cdot \frac{T_n - T_{n-1}}{\Delta t} \quad (1)$$

where $c = \Delta t$.

The shape of the temperature response to the Dirac pulse depends on many parameters. The most important are the material properties (density, thermal conductivity and thermal capacity), the distance of the thermocouple from the boundary, the thermocouple type, the material, and the thermal resistance between the thermocouple and the material.

The number of forward time steps (forward time t , respectively) is taken from the derivation of the temperature response $D(t)$ so that $D(t)$ meets a certain criterion.

For example, t_{Dmax} is the time when $D(t_{max})$ is maximal. $t_{Dmax,p\%,1}$ and $t_{Dmax,p\%,2}$ are the times when the derivation of the temperature response reaches p % of its maximum. An example for $p = 60$ % is shown in **Figure 5**.

The second estimation method for determining the number of forward time steps can be done with a repeated computation of the inverse heat-conduction problem by changing N_f . The sum of the residuals $R = \sum(Q_i' - Q_i)^2$ is evaluated from each inverse task where Q_i is the computed heat flux and Q_i' is the correct heat flux from the test task. An example of how R is dependent on N_f is shown in **Figure 6** and the $N_{f,min}$ value (N_f when R is minimal) can be found here. The value of N_f (slightly larger than $N_{f,min}$) is taken as an estimate for the number of forward time steps. The $N_{f,min}$ value is not used due to the risk that a small shift of the estimated N_f value to the left (to a smaller value) can rapidly increase the R value (**Figure 6**). An analogical application of the

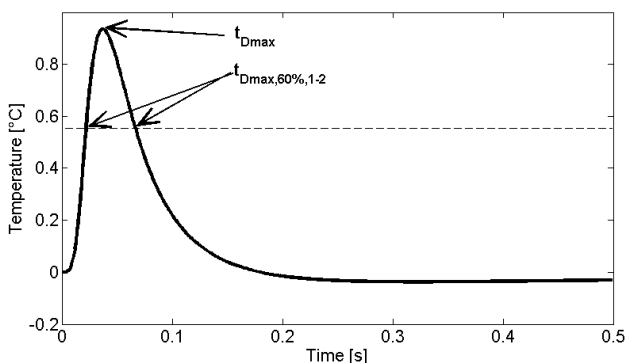


Figure 5: Example of t_{Dmax} and $t_{Dmax,60\%,1-2}$

Slika 5: Primer za t_{Dmax} in $t_{Dmax,60\%,1-2}$

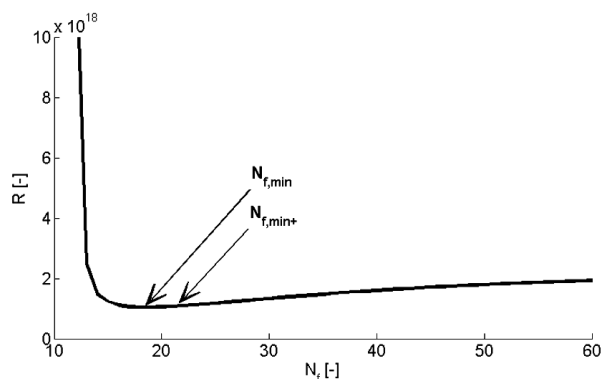


Figure 6: Residual chart for N_f values

Slika 6: Grafikon ostanok za vrednosti N_f

search for the optimum regularization parameter in a Tikhonov digital filter is described by Woodbury.⁷

4 DISCUSSION

The first method described is much less computationally intensive than the second one because the first method needs only one direct computation instead of many inverse (and therefore much more complicated) computations. Each method provides a different value of forward time steps N_f . It is not easy to say which value is better. Generally, this depends on what is more essential for each application. The larger value of N_f smoothes the results but the average values for certain time intervals are correct. A small value of N_f can result in heat fluxes that better fit true values, but the results include more oscillation than would be expected in reality. The choice of the appropriate testing function in the second method also significantly influences the computed value of N_f . Two examples of the testing functions and the obtained N_f value are shown in **Figure 7**.

The comparison of the inverse computations performed with $N_{f,Dmax} = 37$, $N_{f,Dmax,60\%,2} = 65$ (from the first method) and $N_{f,1} = 24$, $N_{f,2} = 18$ (from the second method) is shown in **Figure 8**. The curve for $N_{f,Dmax,60\%,1} = 23$ is not plotted because it is almost the same as that for $N_{f,1} = 24$. These inverse computations

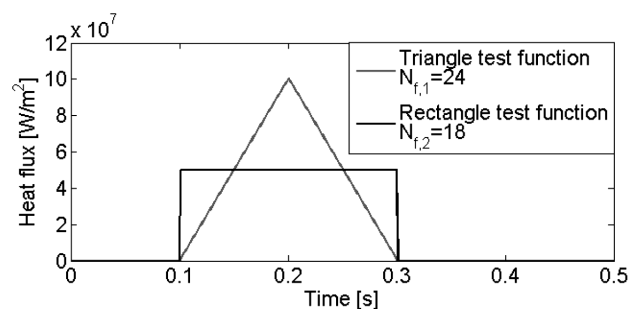


Figure 7: Two examples of testing functions and obtained $N_{f,min}$, using the second method

Slika 7: Dva primera preizkusnih funkcij in dobljen $N_{f,min}$ pri uporabi druge metode

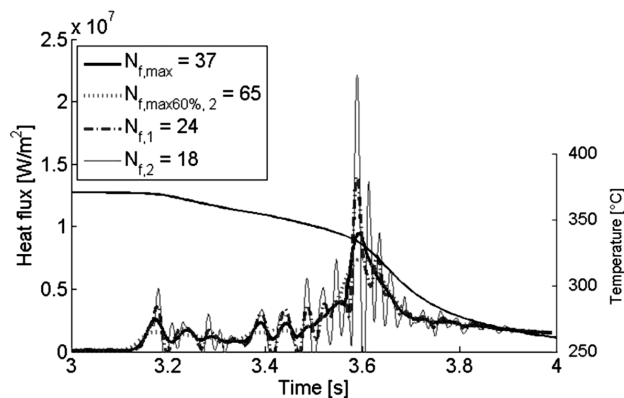


Figure 8: Results of the heat flux for four different values of N_f and the measured temperature

Slika 8: Rezultati toplotnega toka za štiri različne vrednosti N_f in izmerjena temperatura

were made for the 1D inverse heat-conduction problem with thermally dependent material properties. The temperature record from the real measurements was used. Therefore, the correct heat-flux function is unknown.

The heat-conduction problem is described with differential Equation (2):

$$\frac{\partial^2 T}{\partial x^2} = \frac{1}{\alpha} \frac{\partial T}{\partial t} \quad (2)$$

where T is the temperature, t is the time and x is the coordinate. The boundary conditions for (Equation (3)) cooled and insulated surfaces are:⁴

$$-k \frac{\partial T}{\partial x} \Big|_{x=0} = q(t); \quad -k \frac{\partial T}{\partial x} \Big|_{x=L} = 0 \quad (3)$$

The test sample was made from a thick stainless-steel plate ($L = 10$ mm). One side ($x = 0$) of the sample was cooled down by water and the other side ($x = L$) was insulated. A thermocouple was placed under the cooled surface ($x = 2$ mm).

The curves for $N_f = 37$ and $N_f = 24$ (**Figure 8**) appear to be acceptable. The curve for $N_f = 65$ is too smooth. The curve for $N_f = 18$ begins to be unstable and the computed heat flux is less than zero for some points, which is physically impossible in this experiment.

5 CONCLUSION

Two methods for determining the number of forward time steps N_f for the sequential Beck approach were described. The first method (based on the derivation of the temperature response to the Dirac heat-flux pulse) is computationally much less intensive. The choice of $N_f = N_{f,Dmax}$ is acceptable for most applications. For some similar tasks, it may be better to use $N_{f,Dmax,p\%}$ with the same suitable value of p .

The second method, which is computationally very intensive, can be useful when the shape of the heat-flux curve is known and the appropriate testing function can be used. The obtained values of N_f were smaller than those computed using the first method and the computed heat fluxes showed more oscillation.

Acknowledgement

This work is an output of the research and scientific activities of project LO1202, financially supported by the MEYS under programme NPU I.

6 REFERENCES

- ¹ G. D. Smith, Numerical solution of partial differential equations, University Press, Oxford, UK 1978
- ² S. V. Patankar, Numerical Heat Transfer and Fluid Flow, Hemisphere Publishing Corporation, GB 1980
- ³ O. C. Zienkiewicz, R. L. Taylor, The Finite Element Method, Volume I: Basis, Butterworth-Heinemann, Oxford 2000
- ⁴ J. V. Beck, B. Blackwell, R. C. Charles, Inverse Heat Conduction: Ill-posed Problems, Wiley, New York 1985
- ⁵ A. N. Tikhonov, V. Y. Arsenin, Solution of Ill-posed problems, V. H. Winston & Sons, New York 1977
- ⁶ M. Raudenský, J. Horský, J. Krejsa, Usage of neural network for coupled parameter and function specification inverse heat conduction problem, Int. Comm. Heat Mass Transfer, 22 (1995) 5, 661–670, doi:10.1016/0735-1933(95)00052-Z
- ⁷ K. A. Woodbury, J. V. Beck, Estimation metrics and optimal regularization in a Tikhonov digital filter for the inverse heat conduction problem, International Journal of Heat and Mass Transfer, 62 (2013), 31–39, doi:10.1016/j.ijheatmasstransfer.2013.02.052

ENHANCED STABILITY AND ELECTROCHEMICAL PERFORMANCE OF A BaTiO₃/PbO₂ ELECTRODE VIA A LAYER OBTAINED WITH LAYER ELECTRODEPOSITION

IZBOLJŠANA STABILNOST IN ELEKTROKEMIJSKA ZMOGLJIVOST ELEKTRODE BaTiO₃/PbO₂, IZDELANE Z ELEKTRODEPOZICIJO PLAST NA PLAST

Govindan Muthuraman, Kannan Karunakaran, Il Shik Moon

Department of Chemical Engineering, Sunchon National University, #255 Jungangno, Suncheon 540-742, Jeollanam-do, Republic of Korea
ismoon@sunchon.ac.kr

Prejem rokopisa – received: 2014-08-18; sprejem za objavo – accepted for publication: 2015-03-24

doi:10.17222/mit.2014.200

Herein, the electrodeposition of BaTiO₃ and PbO₂ on Ti using the layer-by-layer method under different current densities (*CDs*) and times, was investigated. The weight difference in the deposited BaTiO₃ explains the BaTiO₃ weight decrease by one order with the increasing *CD* from 0.025 A cm⁻² to 0.125 A cm⁻² and also follows the same trend during the PbO₂ deposition. The PbO₂ deposition at different *CDs* demonstrates that the deposited PbO₂ weight increases by one order with the increasing *CD*. Also, cyclic voltammetry results explain the low and moderate deposition *CDs* and the time suitably shows the PbO₂ redox behavior. According to SEM and XRD, a *CD* of 0.05 A cm⁻² affects the formation of crystalline BaTiO₃ and PbO₂ more than higher or lower *CDs*. Finally, the BaTiO₃ and PbO₂ layer-by-layer electrode electrodeposited at a moderate *CD* showed a better stability than the electrode including only PbO₂. The use of BaTiO₃ is promising for the stability of the PbO₂ electrode preparation.

Keywords: BaTiO₃, PbO₂, electrodeposition, layer by layer, electrode stability

Preiskovana je bila elektrodepozicija BaTiO₃ in PbO₂ na Ti, z uporabo metode plast na plast, pri različnih časih in gostotah toka (*CD*). Razlike v teži BaTiO₃ razložijo naraščanje teže BaTiO₃ za red velikosti zaradi naraščanja *CD*, od 0,025 A cm⁻² do 0,125 A cm⁻². Podoben trend je bil opažen tudi pri nanašanju PbO₂. Pri nanašanju PbO₂, različni *CD* kažejo naraščanje teže nanosenega PbO₂ za red velikosti z naraščanjem *CD*. Tudi ciklična voltometrija razloži majhen in srednji *CD* in čas ustrezno kaže redoks vedenje PbO₂. SEM in XRD z 0,05 A cm⁻² vodita nastanek kristaliničnega BaTiO₃ in PbO₂ bolj kot višji in nižji *CD*. Končno se kaže boljša stabilnost elektrode elektronanešenega BaTiO₃ in PbO₂ plast na plast pri zmernih *CD*, kot pa pri PbO₂ elektrodi. Uporaba BaTiO₃ je obetajoča za stabilnost priprave PbO₂ elektrode.

Ključne besede: BaTiO₃, PbO₂, elektro nanašanje, plast na plast, stabilnost elektrode

1 INTRODUCTION

PbO₂ clearly emerges as an attractive material used as an anode for a direct oxidation of organic compounds due to its high oxygen-evolution potential, low price, relative stability under the high positive potentials required, stability at high temperatures and ease of preparation.¹⁻³ Its high overpotential for O₂ evolution allows the application of potentials to about 2.0 V versus a saturated calomel electrode (SCE) in an acidic medium without vigorous O₂ evolution.⁴ The PbO₂ electrodes have some disadvantages, i.e., they corrode at high rates under reducing conditions and in some acids, and they have poor mechanical properties. Its composites with various oxides (e.g., Al₂O₃, RuO₂, and TiO₂) are known⁴⁻⁶ for a high catalytic activity and stability. Among many ways of preparation, such as the sol-gel technology, the plasma-chemical method, etc., the electrochemical synthesis is the most promising method, easy to implement, allowing the technological parameters to be varied smoothly for a better control of the

composition and properties of the resulting composites.⁴⁻⁶

The α - and β -types of PbO₂, applied layer by layer on metal anodes have been widely used in electrolysis.^{7,8} Generally, titanium is not a viable substrate for practical electrodes in electrodepositing non-ferrous metals. Aluminum is relatively cheap and has a good conductivity. The electrode material obtained by electrodepositing lead dioxide on an Al substrate has huge market prospects. A stress-free intermediate α -PbO₂ coating is produced with electrodeposition from an alkaline lead bath⁹ and it plays the role of the binder on the top α -PbO₂ coating, improving the service life of the electrode. A non-conducting ceramic material has also been used as the substrate to achieve a high stability of PbO₂ with the fluorine resin as the co-dopant on the upper layer.¹⁰

In the present investigation, perovskite-type BaTiO₃ is applied to Ti as the lower layer using the hydrothermal electrodeposition method. As the top/upper layer, PbO₂ is to be applied. The effects of the thickness of both layers are controlled with the current density and the deposition

time to achieve the electrode stability and activity. Thus, the main work of this paper deals with the layer-by-layer deposition of BaTiO₃ and PbO₂ and its influence on the PbO₂ electrode stability and electrochemical application as a sandwich-type electrode.

2 EXPERIMENTAL DETAILS

2.1 Electrodeposition

Electrolysis was performed using a DC power supply, BS 32C (0–100 V, 0–50 A) from the Korea Switching Company, Korea, using the constant-current mode (the galvanostatic mode). Before the electrolysis start, the anode was initially immersed in the electrolyte for 1 min to stabilize its surface state. The deposition was performed in two steps: in the first step, BaTiO₃ was formed as the lower coating on a pretreated Ti electrode at 65 °C using a current-density range of 0.025–0.125 A cm⁻² for 15–60 min. The BaTiO₃ deposited electrode was washed after its deposition in hot ammonia water adjusted to pH 11 to minimize the BaCO₃ formation. It was then rinsed in purified Millipore water and cleaned in ethanol with an ultrasonic cleaner for 1 min. Then, β-PbO₂ was deposited as the upper layer using a current-density (*CD*) range of 0.025–0.125 A cm⁻² for 15–60 min in a 0.1 M HNO₃ medium at 65 °C.

2.2 Analysis

Cyclic-voltammetry (CV) measurements were performed using a VersaSTAT3 from Princeton Applied Research, USA. The electrochemical cell was a three-electrode cell with a working electrode, a platinum-plate counter electrode and an Ag/AgCl reference electrode. The working electrode was prepared with the electrodeposition method. Scanning electron microscopy of the prepared PbO₂ electrodes was carried out with Zeiss EVO MA10 to investigate the surface morphology of the films. The XRD patterns of the as-prepared PbO₂ samples were obtained from an X'PERT-PRO X-ray diffractometer with Cu-Kα radiation ($\lambda = 0.1540598$ nm). The electrolysis was done using a DC power supply from KSC, Korea, with an applied *CD* of 0.3 A cm⁻² in 1 M H₂SO₄.

3 RESULTS AND DISCUSSIONS

3.1 Selection of deposition conditions

As the *CD* and time are the key factors to control the deposition, the initial work was done to identify the suitable deposition time and *CD* for the first and second layers of BaTiO₃ and PbO₂, respectively. First, the BaTiO₃ layer was deposited using four different *CD*s of (0.025, 0.05, 0.1, 0.125) A cm⁻² with four different durations such as (15, 30, 45, 60) min, by keeping the PbO₂ (the second layer) deposition parameters (*CD* = 0.05 A cm⁻², 30 min duration) constant. As mentioned in

the experimental section, the BaTiO₃ and PbO₂ depositions were done in different solutions and the obtained results are tabulated in **Table 1**. It is seen from the 1st row and 4th column of **Table 1** that the weight of the deposited BaTiO₃ shows no consistency with different deposition times (15–60 min) within a single *CD* (0.025 A cm⁻²); a similar inconsistency is also shown for the PbO₂ deposition, the 5th column. However, with the increasing *CD* during the BaTiO₃ deposition from 0.025 to 0.125 A cm⁻², shown in the 1st to the 4th rows, the deposited BaTiO₃ weight is reduced by one order from 0.01 to 0.001 (the 5th column).

Table 1: Deposited-electrode weight difference in each step of: 1) BaTiO₃ and 2) PbO₂ at different current densities and times

Tabela 1: Razlika v masi nanešene elektrode za vsako stopnjo: 1) BaTiO₃ in 2) PbO₂ pri različnih gostotah tokov in časih

BaTiO ₃ coating		PbO ₂ coating		Electrode weight difference (g)	
<i>CD</i> [@] (A cm ⁻²)	Time (min)	<i>CD</i> [@] (A cm ⁻²)	Time (min)	BaTiO ₃	PbO ₂
0.025	15	0.05	30	0.0222	0.2837
	30		0.0181	0.2929	
	45		-0.0034	0.3043	
	60		0.024	0.3041	
0.05	15	0.05	30	-0.0027	0.0649
	30		0.0052	0.2681	
	45		0.0055	0.2969	
	60		-0.0087	0.2997	
0.1	15	0.05	30	0.0094	0.0908
	30		0.0054	0.0217	
	45		-0.0089	0.0338	
	60		-0.0076	0.0800	
0.125	15	0.05	30	0.0032	0.0702
	30		-0.0372	*	
	45		0.0629	*	
	60		0.0397	0.0456	
0.025	30	0.025	15	0.0159	-0.0318
			30	0.0091	-0.0133
			45	0.0084	0.1065
			60	0.0167	0.4092
0.025	30	0.05	15	-0.0594	0.2779
			30	0.0105	0.2188
			45	-0.0180	0.0140
			60	-0.0065	0.5551
0.025	30	0.1	15	0.1020	0.1611
			30	-0.0423	0.3547
			45	-0.0137	0.4100
			60	-0.0362	0.2384
0.025	30	0.125	15	*	*
			30	*	*
			45	*	*
			60	*	*

*Dissolution of electrode, [@]*CD* = current density, lower than the original weight

In a similar way, the deposited PbO₂ weight also decreases by one order with the increasing *CD* (the 6th column – from 0.1 to 0.01). At the same time, the results are different if the PbO₂ deposition *CD* is varied at a

fixed CD and time of the BaTiO₃ deposition (5th to 8th rows of **Table 1**) where the weight of BaTiO₃ is maintained constant but the deposited PbO₂ weight is increased by one order with the increasing CD (the 6th column of the 5th to 8th rows in **Table 1**). It is maintained on the basis of the results that the formation of BaTiO₃ on the Ti electrode influenced further deposition of PbO₂, which means that the conductivity was lower when BaTiO₃ completely covered the electrode due to the dielectric properties of BaTiO₃. A similar trend applied to the PbO₂ deposition carried out at a high CD and a fixed, low CD of the BaTiO₃ deposition where a complete dissolution of the deposited film was observed.

Further, through a CV analysis, the electron-transfer behavior of the deposited electrode can be inferred on the basis of PbO₂ redox properties. **Figure 1a** shows the PbO₂ redox response to the effects of various CD s and

times of the BaTiO₃ deposition, where no redox peaks for PbO₂ are observed except for two CD variations in the BaTiO₃ deposition: 0.025 (45 min) A cm⁻² and 0.05 (45 min) A cm⁻². In all the remaining conditions, only a charge transfer like the CV response is observed. In the case of the variation in the PbO₂ deposition, 60 min and 0.025 A cm⁻² or 0.05 A cm⁻², CD only shows redox peaks that resemble PbO₂,¹¹ as shown in **Figure 1b**. Under another two conditions, a CD of 0.1 A cm⁻² over 45 min and 60 min deposition times, the PbO₂ deposition indicates a low oxidation current. All the remaining conditions show a charging current like the CV response without any redox peaks as not enough PbO₂ is exposed on the electrode surface. This is well correlated with the deposited weight of PbO₂ in the 1st, 2nd and 7th rows of the 6th column of **Table 1**, where only the deposited PbO₂ weight is higher than in the other conditions.

3.2 Morphological characterization

SEM images of the BaTiO₃ and PbO₂ deposited at different conditions are depicted in **Figure 2**. The first layer of BaTiO₃ shows no distinctive difference in the SEM image and it looks almost like a needle structure in micrometer size, as shown in **Figure 2a**. Both layers deposited at 0.025 A cm⁻² show a densely deposited PbO₂ layer (**Figure 2b**). There is a defect in the PbO₂

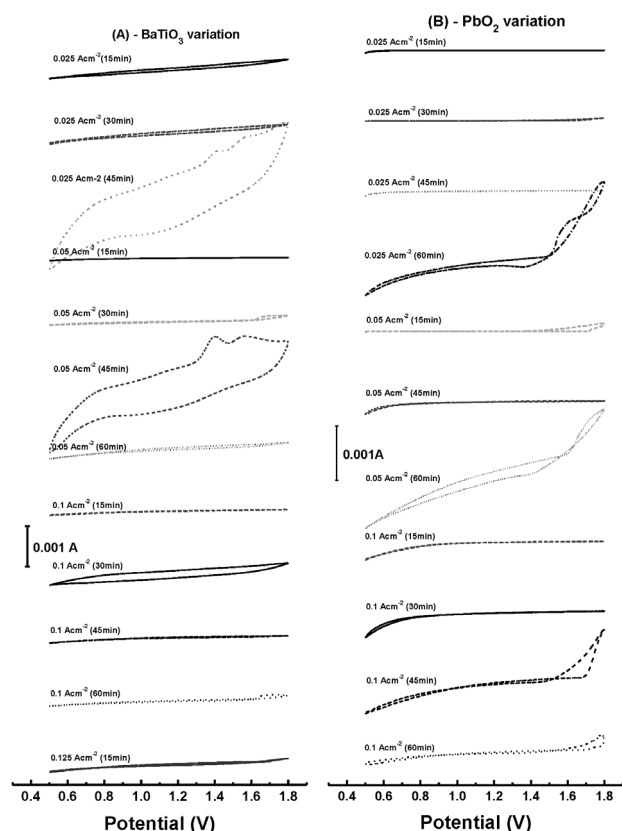


Figure 1: CV results for electrodeposited BaTiO₃/PbO₂ using different current densities and times in a 0.1 M phosphate buffer solution at a scan rate of 20 mV s⁻¹: a) variation in BaTiO₃ deposition current density and time with fixed current density and time (0.05 A cm⁻², 30 min) of PbO₂ deposition, b) variation in PbO₂ deposition current density and time with fixed current density and time (0.025 A cm⁻², 30 min) of BaTiO₃ deposition

Slika 1: Rezultati ciklične voltametrije elektro nanešenega BaTiO₃/PbO₂, pri uporabi različnih gostot tokov in časov, v 0,1 M fosfatni puferški raztopini pri hitrosti skeniranja 20 mV s⁻¹: a) spreminjanje gostote toka in časa nanašanja BaTiO₃ od stalne gostote toka in časa (0,05 A cm⁻², 30 min) pri nanašanju PbO₂, b) spreminjanje gostote toka in časa nanašanja PbO₂ pri stalni gostoti toka in časa (0,025 A cm⁻², 30 min) nanašanja BaTiO₃

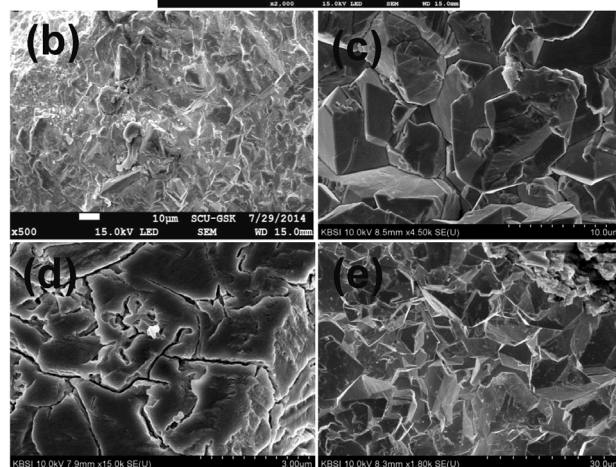
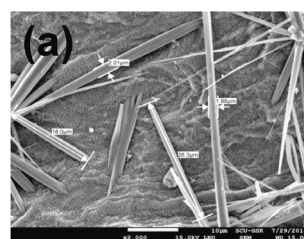


Figure 2: SEM images of BaTiO₃ and PbO₂ electrodes, deposited at different CD s and times: a) BaTiO₃^{0.1(45 min)}, b) BaTiO₃^{0.025(30 min)/PbO₂^{0.025(60 min)}, c) BaTiO₃^{0.025(30 min)/PbO₂^{0.1(60 min)}, d) BaTiO₃^{0.05(45 min)/PbO₂^{0.05(30 min)}, e) BaTiO₃^{0.1(45 min)/PbO₂^{0.05(30 min)}}}}}

Slika 2: SEM-posnetki BaTiO₃ in PbO₂ elektrod, nanešenih pri različnih CD in časih: a) BaTiO₃^{0.1(45 min)}, b) BaTiO₃^{0.025(30 min)/PbO₂^{0.025(60 min)}, c) BaTiO₃^{0.025(30 min)/PbO₂^{0.1(60 min)}, d) BaTiO₃^{0.05(45 min)/PbO₂^{0.05(30 min)}, e) BaTiO₃^{0.1(45 min)/PbO₂^{0.05(30 min)}}}}}

coating if the PbO₂ deposition *CD* increased to 0.1 A cm⁻² (**Figure 2c**). The film cracking is more dominant if both layers were deposited at a *CD* of 0.05 A cm⁻² (**Figure 2d**). The film cracking is more enhanced if the BaTiO₃ layer was deposited at 0.1 A cm⁻² (**Figure 2e**). When both layers were deposited at a low *CD* of 0.025 A cm⁻², there is a smooth layer with smaller particles.

Figure 3a shows the XRD patterns of the BaTiO₃ deposited electrodes using different *CD*s and times with a fixed PbO₂ deposition. With the applied *CD* of 0.05 A cm⁻², the BaTiO₃ peak reflections are less intense at 2θ values of about 31.03, 38.58, 41.88, and 55.47 (VRC# 01-075-0213) along with the Ti reflections. Additionally, BaCO₃ also appeared on the surface, with a 2θ peak at about 23.85 (VRC# 00-044-1487) that might have occurred after the deposition of BaTiO₃ due to high pH.¹² The BaTiO₃ peak intensity increased when the deposition *CD* increased to 0.1 A cm⁻² as shown on curve b in **Figure 3a**. The lowest *CD* (0.025 A cm⁻²) caused a decrease in the crystallinity of BaTiO₃, which turned to the amorphous phase; see a broad peak between 2θ of

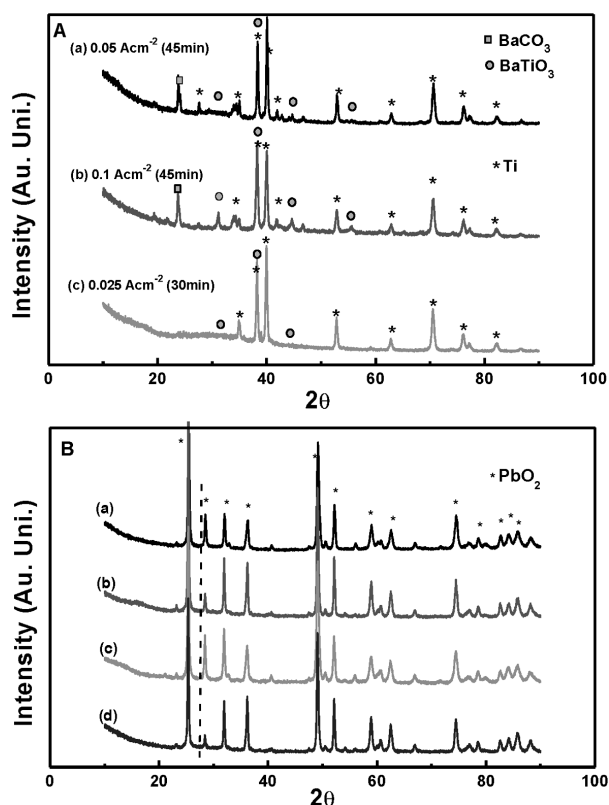


Figure 3: a) XRD patterns of current-density and time variation (mentioned in the figure) of BaTiO₃ deposition, b) XRD patterns of BaTiO₃/PbO₂ prepared at various current densities and times: a) BaTiO₃^{0.025(30 min)}/PbO₂^{0.025(60 min)}, b) BaTiO₃^{0.025(30 min)}/PbO₂^{0.1(60 min)}, c) BaTiO₃^{0.05(45 min)}/PbO₂^{0.05(30 min)}, d) BaTiO₃^{0.1(45 min)}/PbO₂^{0.05(30 min)}

Slika 3: a) Rentgenogram spreminjanja gostote toka in časa pri nanašanju BaTiO₃, b) rentgenogram BaTiO₃/PbO₂ pripravljene pri različnih gostotah toka in časih: a) BaTiO₃^{0.025(30 min)}/PbO₂^{0.025(60 min)}, b) BaTiO₃^{0.025(30 min)}/PbO₂^{0.1(60 min)}, c) BaTiO₃^{0.05(45 min)}/PbO₂^{0.05(30 min)}, d) BaTiO₃^{0.1(45 min)}/PbO₂^{0.05(30 min)}

20–35 on curve c of **Figure 3**. In the case of the PbO₂ deposition, the deposited electrode using various *CD*s and times shows peaks for the PbO₂ formation (VRC# 01-076-0564) as shown in **Figure 3b**. The only difference found is a peak-intensity decrease at a 2θ value of about 28.49 when the PbO₂ is deposited at 0.1 A cm⁻² and 0.05 A cm⁻² (60 min and 30 min) on the top of the BaTiO₃ deposition using the 0.025 A cm⁻² and 0.1 A cm⁻² *CD*s in the 30 min and 45 min durations (**Figure 3b**, curves b and d).

It is evident from the results that the 2θ of 28.49 belongs to the $\alpha(111)$ plane¹³, whose peak intensity is reduced, which means that the β -PbO₂ formation is predominant at this given condition. As seen on curve b in **Figure 3a**, the BaTiO₃ formation is more prominent at the 0.05 A cm⁻² *CD*, which means that the BaTiO₃ concentration increases the β -PbO₂ formation during the PbO₂ deposition. It is well known that the β -PbO₂ formation enhances the catalytic activity tremendously.¹⁴

3.3 Stability analysis

In order to apply the prepared electrodes, the selectively prepared electrodes obtained their stability in 1 M H₂SO₄ due to an enhanced *CD* of 0.3 A cm⁻², as depicted in **Figure 4**. An electrode that was prepared at a *CD* of 0.05 A cm⁻² (45 min) for BaTiO₃ and at 0.05 A cm⁻² (30 min) for the PbO₂ deposition showed a 3.9 V cell voltage up to 110 h (**Figure 4**, curve a); and after the potential sharply increased to 22 V the prepared electrode was decomposed. In the case of the increase in the BaTiO₃ deposition at the *CD* of 0.1 A cm⁻² when the

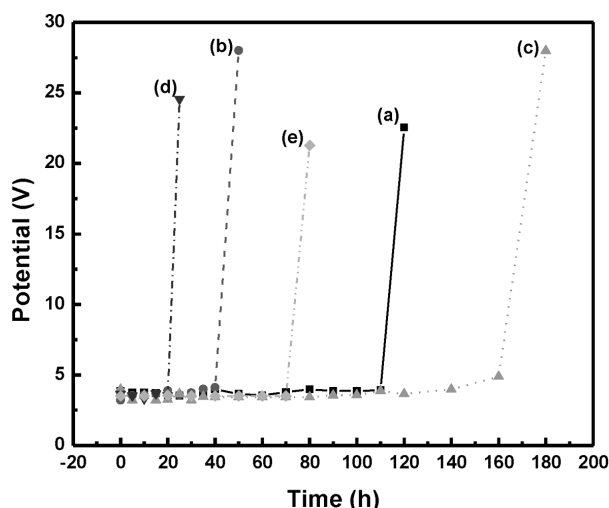


Figure 4: Electrolysis of different electrodes in 1 M H₂SO₄ at accelerated current density of 0.3 A cm⁻²: a) BaTiO₃^{0.05(45 min)}/PbO₂^{0.05(30 min)}, b) BaTiO₃^{0.1(45 min)}/PbO₂^{0.05(30 min)}, c) BaTiO₃^{0.025(30 min)}/PbO₂^{0.025(60 min)}, d) BaTiO₃^{0.025(30 min)}/PbO₂^{0.1(60 min)}, e) PbO₂^{0.025(60 min)}

Slika 4: Elektroliza različnih elektrod v 1 M H₂SO₄ pri pospešeni gostoti toka 0.3 A cm⁻²: a) BaTiO₃^{0.05(45 min)}/PbO₂^{0.05(30 min)}, b) BaTiO₃^{0.1(45 min)}/PbO₂^{0.05(30 min)}, c) BaTiO₃^{0.025(30 min)}/PbO₂^{0.025(60 min)}, d) BaTiO₃^{0.025(30 min)}/PbO₂^{0.1(60 min)}, e) PbO₂^{0.025(60 min)}

other conditions stayed the same, the decomposition of the electrode occurred at around 40 h, which means that the stability was reduced with the increasing *CD* (Figure 4, curve b).

In the case of the lowest *CD* (0.025 A cm⁻²) used for both the BaTiO₃ and PbO₂ depositions for 30 min and 60 min, respectively, the stability increased to 180 h (Figure 4, curve c). By keeping the BaTiO₃ *CD* of 0.025 A cm⁻² and changing the PbO₂ *CD* to 0.1 A cm⁻² over 60 min, the stability of the prepared electrode tremendously decreased to 20 h, as observed in Figure 4, curve d. Finally, only the PbO₂ electrode deposited at the *CD* of 0.025 A cm⁻² in 60 min, showing a stability of 48 h (Figure 4, curve e) explains a high influence of the BaTiO₃ layer on the stability of the PbO₂ electrode.

4 CONCLUSIONS

We successfully investigated an electrodeposition of BaTiO₃ and PbO₂ on Ti using the layer-by-layer method under different conditions. The weight measurement confirms that the BaTiO₃ and PbO₂ formation is optimum at a moderate *CD* of 50 A cm⁻² and a deposition time of 30–45 min. In addition, CV results confirm the same finding through the redox behavior of PbO₂. SEM and XRD results further prove that a moderate *CD* leads to crystalline BaTiO₃ and β-PbO₂ rather than α-PbO₂. The layer-by-layer deposition of BaTiO₃ and PbO₂ makes PbO₂ more stable than it would be if there was only PbO₂. A further application of the selectively prepared electrode is in progress.

Acknowledgements

This work was supported by the National Research Foundation of Korea (NRF), funded by the Korea Government (MEST) (Grant No. 2014R1A2A1A01001974).

5 REFERENCES

¹ C. A. Martinez-Huitle, M. Panizza, Application of PbO₂ Anodes for wastewater Treatment, In: D. V. Zinger (Eds.), *Advances in Chemistry Research: Applied Electrochemistry*, Nova Science Publishers, Inc., New York 2010, 269–300

- ² U. Casellato, S. Cattarin, M. Musiani, Preparation of porous PbO₂ electrodes by electrochemical deposition of composites, *Electrochim. Acta*, 48 (2003) 27, 3991–3998, doi:10.1016/j.electacta.2005.02.126
- ³ A. Shiyun, G. Mengnan, W. Zhang, Q. Wang, Y. Xie, L. Jin, Preparation of Ce-PbO₂ modified electrode and its application in detection of anilines, *Talanta*, 62 (2004) 3, 445–450, doi:10.1016/j.talanta.2003.08.019
- ⁴ G. Li, J. Qu, X. Zhang, J. Ge, Electrochemically assisted photocatalytic degradation of Acid Orange 7 with β-PbO₂ electrodes modified by TiO₂, *Water Res.*, 40 (2006) 2, 213–220, doi:10.1016/j.watres.2005.10.039
- ⁵ S. Cattarin, M. Musiani, V. Palmieri, D. Tonini, EIS study of niobium films sputtered at different target-substrate angles, *Electrochim. Acta*, 52 (2006) 8–9, 1745–1751, doi:10.1016/j.electacta.2005.02.126
- ⁶ U. Casellato, S. Cattarin, P. Guerriero, M. Musiani, Anodic Synthesis of Oxide-Matrix Composites. Composition, Morphology, and Structure of PbO₂-Matrix Composites, *Chem. Mater.*, 9 (1997) 4, 960–966, doi:10.1021/cm960513y
- ⁷ D. Devilliers, M. T. Dinh-Thi, E. Mahe, Q. L. Xuan, Cr(III) oxidation with lead dioxide-based anodes, *Electrochim. Acta*, 48 (2003) 28, 4301–4309, doi:10.1016/j.electacta.2003.07.005
- ⁸ M. Ueda, A. Watanabe, T. Kameyama, Y. Matsumoto, M. Sekimoto, T. Shimamune, Performance characteristics of a new type of lead dioxide-coated titanium anode, *J. Appl. Electrochem.*, 25 (1995), 817–822, doi:10.1007/BF0023389
- ⁹ A. Yoshizawa, T. Nonaka, M. Sekimoto, Y. Nishiki, Preparation of PTFE Composite-Plated Hydrophobic β-PbO₂ Electrodes, *Chem. Lett.*, 8 (1994) 8, 1565, doi:10.1246/cl.1994.1565
- ¹⁰ M. Zhou, Q. Dai, L. Lei, C. Ma, D. Wang, Long Life Modified Lead Dioxide Anode for Organic Wastewater Treatment: Electrochemical Characteristics and Degradation Mechanism, *Environ. Sci. Technol.*, 39 (2005) 1, 363–370, doi:10.1021/es049313a
- ¹¹ T. Chen, H. Huang, H. Ma, D. Kong, Effects of surface morphology of nanostructured PbO₂ thin films on their electrochemical properties, *Electrochim. Acta*, 88 (2013) 15, 79–85, doi:10.1016/j.electacta.2012.10.009
- ¹² V. Sridhar, R. E. Chodelka, J. H. Adair, Preparation and characterization of barium titanate electrolytic capacitors from porous titanium anodes, *J. Am. Ceram. Soc.*, 81 (1998) 9, 2429–2442, doi:10.1111/j.1151-2916.1998.tb02639.x
- ¹³ M. Bervas, M. Perrin, S. Genižes, F. Mattera, Low-cost synthesis and utilization in mini-tubular electrodes of nano PbO₂, *J. Power Sources*, 173 (2007) 1, 570–577, doi:10.1016/j.jpowsour.2007.04.077
- ¹⁴ R. Amadelli, A. Maldotti, A. Molinari, F. I. Danilov, A. B. Velichenko, Influence of the electrode history and effects of the electrolyte composition and temperature on O₂ evolution at β-PbO₂ anodes in acid media, *J. Electroanal. Chem.*, 534 (2002) 1, 1–12, doi:10.1016/S0022-0728(02)01152-X

DEFORMATION BEHAVIOUR OF AMORPHOUS Fe-Ni-W/Ni BILAYER-CONFINED BULK METALLIC GLASSES

OBNAŠANJE DEFORMIRANEGA, AMORFNEGA, NA DVE PLASTI OMEJENEGA KOVINSKEGA STEKLA Fe-Ni-W/Ni

Ho Kuen Lau, Natalie Yip, Shun Hua Chen, Wen Chen, Kang Cheung Chan

Advanced Manufacturing Technology Research Centre, Department of Industrial and Systems Engineering,
Hong Kong Polytechnic University, Hong Kong
kc.chan@polyu.edu.hk

Prejem rokopisa – received: 2014-09-02; sprejem za objavo – accepted for publication: 2015-03-24

doi:10.17222/mit.2014.217

In this study, an amorphous Fe-Ni-W/Ni bilayer was successfully electroplated on a Zr-based bulk metallic glass (BMG), and the deformation behaviour of the bilayer-coating-confined BMG was investigated. The findings show that the macroscopic plasticity of the BMGs was enhanced from 1.3 % to 10.7 %. More importantly, bilayer-confined BMGs have a large plateau of the serrated flow with an insignificant decrement before failure. When characterizing the serrated flows of both uncoated and bilayer-confined BMGs by introducing absolute values of stress raises/drops, smaller amplitudes of stress drops as well as a larger stress-drop frequency during the plastic-deformation stage were found in the bilayer-confined BMGs. The origin of the increased stable plastic flow was discussed, and it is mainly attributed to the enhanced confinement caused by the introduction of the amorphous layer. The findings are significant for enhancing the macroscopic plasticity of the BMGs and for understanding the deformation mechanism of the serrated plastic flow in geometrically confined BMGs.

Keywords: plastic flow, bulk metallic glass, amorphous Fe-Ni-W coating, geometric confinement

V študiji je bilo uspešno elektroplatirano amorfno, dvoplastno steklo Fe-Ni-W/Ni, na masivno kovinsko steklo (BMG) na osnovi Zr. Hkrati je bilo preiskovano obnašanje dvoplastnega BMG pri deformaciji. Ugotovitve kažejo, da se je makroskopska plastičnost BMG povečala z 1,3 % na 10,7 %. Še bolj pomembno je, da ima dvoplasten BMG visok plato nazobljenega dela krivulje z nepomembnim zmanjšanjem pred porušitvijo. Pri karakterizaciji nazobčanega poteka pri obeh; nepokritem in pri dvoplastnem BMG, z vpeljavo absolutne vrednosti narastka in padca napetosti, so bile dobljene manjše amplitude padca napetosti kot tudi večja pogostost padca napetosti med plastično deformacijo dvoplastno omejenega BMG. Razložen je izvor povečanja stabilnega plastičnega toka, ki se ga pripisuje okrepitvi, ki jo povzroči amorfna plast. Ugotovitve so pomembne za povečanje makroskopske plastičnosti BMG in za razumevanje deformacijskega mehanizma nazobčanega plastičnega toka v geometrijsko omejenem BMG.

Ključne besede: plastični tok, masivno kovinsko steklo, amorfna Fe-Ni-W plast, geometrijska omejenost

1 INTRODUCTION

In recent years, due to the extraordinary mechanical properties of bulk metallic glasses (BMGs), such as the high strength and high elastic strain, there has been a growing interest in exploring the application potential of BMGs as structural materials.¹⁻⁶ It is known that plastic deformation occurs mainly in thin shear bands, and a sharp drop in viscosity in deformation zones facilitates a propagation of the existing shear bands, resulting in the final catastrophic failure of BMGs.^{1,7} Macroscopically, the initiation and propagation of shear bands are manifested in serrated plastic flows in the stress-strain curves.⁸⁻¹¹ The serrated flow can be characterised as repeating cycles of elastic loading and unloading where the loading can be classified as elastic deformation and the unloading is caused by an inelastic displacement from a localized shear-band propagation.⁸⁻¹² In order to increase the plasticity of a material, the nucleation of the shear bands must be encouraged and the propagation inhibited to avoid catastrophic failure of the shear bands, i.e., a sudden drop in the load in the flow serrations.¹³

Over the years, geometric confinement has been proven effective in improving the plasticity of BMGs.¹⁴⁻¹⁸ For example, by electroplating a single coating layer of Ni, the plasticity of a nominally "brittle" Fe-based BMG was increased from 0.5 % to 5 %.¹⁶ In 2012, Chen et al.¹⁷ reported an improvement in the plasticity of a Zr-based BMG using a Cu/Ni bilayer coating, in which the soft Cu coating absorbs the loading stress while the hard Ni layer imposes a confining effect. The bilayer coating successfully increased the plasticity of the as-cast Zr-based BMG from 1.3 % to 11.2 %.¹⁷ The disadvantage, however, turns out to be a significant drop in the plastic-flow stress upon reaching a 7 % macroscopic plasticity. Similar phenomena can also be found in single Ni or Cu layer confined BMGs.¹⁷

In a recent work, by applying a Mg/Ti bilayer on a Zr-based BMG, Chu et al.¹⁹ managed to significantly increase its bending plasticity, as compared with the uncoated BMG, the BMGs coated with a single layer of Mg or a single layer of Ti. It was shown that the bilayer is capable of absorbing the deformation by initiating a large number of tiny shear bands, which may provide a

possible way to further suppress the propagation of the shear bands in BMGs in order to achieve a more stable plastic flow.¹⁹ In the present study, an amorphous Fe-Ni-W/Ni bilayer was successfully electroplated on a Zr-based BMG and a more stable plastic flow was achieved.

2 EXPERIMENTAL WORK

As-cast $Zr_{57}Cu_{20}Al_{10}Ni_8Ti_5$ (amount fractions, $x\%$) BMG specimens of a 2-mm diameter were prepared by sucking an arc-melted mixture of high-purity raw materials into a copper mould. The electroplating of an amorphous Fe-Ni-W coating on the BMGs was first carried out using an electrolyte with the composition shown in **Table 1**, which is a modification of the one from²⁰. The pH value of the electrolyte was kept at 8, with the current set at 50 mA for 24 h. The amorphous nature of the as-cast BMG specimens and the Fe-Ni-W coating was confirmed using an X-ray diffractometer (XRD), and the composition of the amorphous Fe-Ni-W coating was examined using an energy-dispersive X-ray spectrometer (EDS).

Table 1: Electrolyte composition for the amorphous Fe-Ni-W layer deposition

Tabela 1: Sestava elektrolita pri nanašanju plasti amorfnega Fe-Ni-W

Component	Concentration/mol L ⁻³
Iron sulphate	0.20
Nickel sulphate	0.05
Sodium tungstate	0.13
Citric acid	0.29

After the Fe-Ni-W layer plating, a nickel layer was electroplated onto the existing Fe-Ni-W layer using Watt's electrolyte, containing nickel sulphate, nickel chloride and boric acid.²¹ The anode and cathode in this

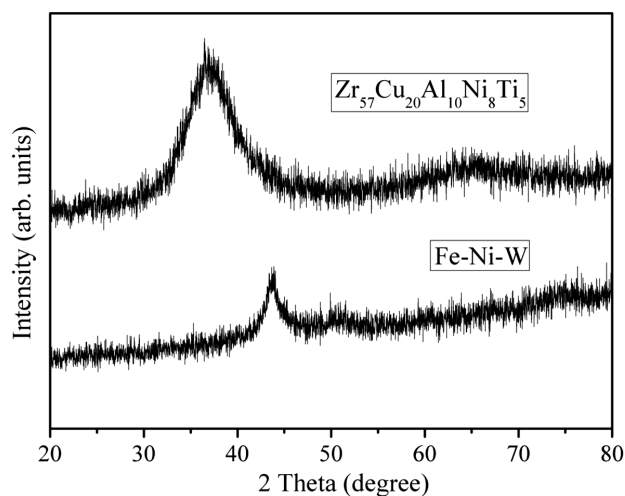


Figure 1: XRD patterns of the $Zr_{57}Cu_{20}Al_{10}Ni_8Ti_5$ BMG and the amorphous Fe-Ni-W coating

Slika 1: Rentgenogram BMG $Zr_{57}Cu_{20}Al_{10}Ni_8Ti_5$ in amorfnega Fe-Ni-W nanosa

step were a pure-nickel sheet and an MG-coated specimen, respectively, and the current was set at 30 mA for 3 h. Both electroplating experiments were carried out at room temperature and the solution was constantly stirred with a magnetic rod to keep the electrolyte homogeneous during the entire electroplating process. The distance between the cathode and anode was kept constant, at about 30 mm. Compressive tests of both uncoated and coated specimens were conducted at room temperature on a MTS 810 materials-testing system at a strain rate of $1 \cdot 10^{-4} s^{-1}$, using an extensometer (model 632.13F-20) to measure the strain. The Vickers-hardness data of the as-cast BMGs and the amorphous Fe-Ni-W coatings were obtained using a VH5N-B hardness tester.

3 RESULTS AND DISCUSSION

Figure 1 shows the XRD patterns of the as-cast BMG specimens and the electroplated Fe-Ni-W coatings. The results show two broad peaks, confirming the amorphous nature of the $Zr_{57}Cu_{20}Al_{10}Ni_8Ti_5$ specimens and the Fe-Ni-W coating. The EDS results show that the composition of the amorphous Fe-Ni-W coating is $Fe_{29.23}Ni_{28.90}W_{41.87}$. A light image of the cross-section of a bilayer-confined BMG is shown in **Figure 2**. The thicknesses of the amorphous Fe-Ni-W layer and the Ni layer were found to be 75.28 μm and 20.39 μm , respectively. It can be seen that the bilayer coating has a good appearance and the two layers are embedded together with no visible microcracks at the interface.

Figure 3 illustrates the compressive stress-strain curves for the uncoated and bilayer-coated BMGs. When compared with the uncoated BMG, although the bilayer-confined BMG has a smaller yield strength, its macroscopic plasticity is enhanced from 1.3 % to 10.7 %. When comparing the results obtained in this experiment with those obtained by Chen et al. using a similar Cu/Ni bilayer-confined BMG¹⁷ both specimens

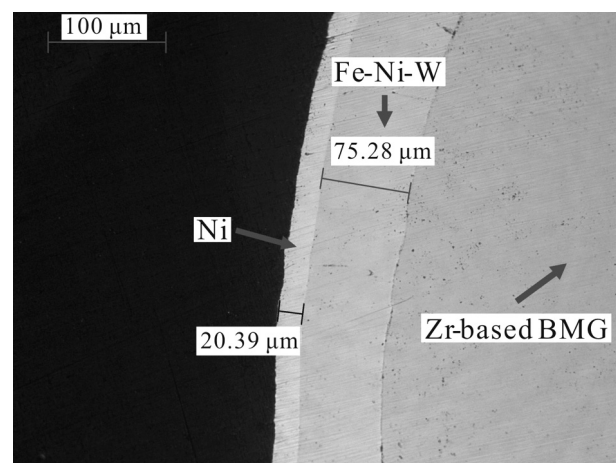


Figure 2: Light image of the amorphous Fe-Ni-W/Ni bilayer-coated BMG

Slika 2: Svetlobni posnetek BMG, pokritega z amorfne dvoplastnim Fe-Ni-W/Ni nanosom

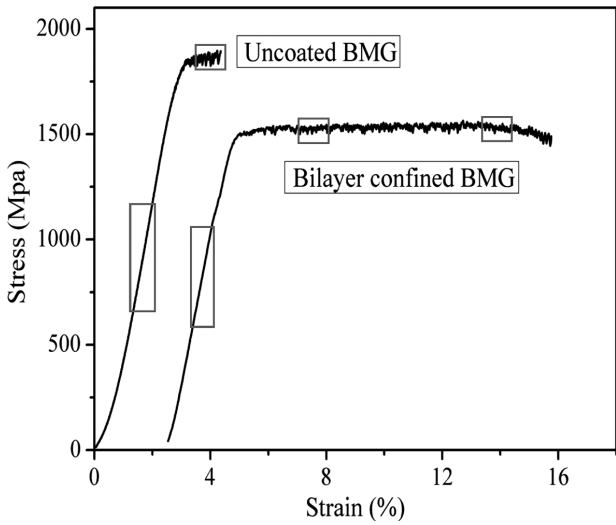


Figure 3: Compressive stress-strain curves for the uncoated and bilayer-coated BMG specimens

Slika 3: Krivulje napetost-raztezek pri tlačnem preizkusu BMG, brez nanosa in z dvoplastnim nanosom

show similar plasticity values, but the current plateau-stress level for the amorphous Fe-Ni-W/Ni coated BMG is notably higher than for the Cu/Ni coated BMG. It is obvious that the amorphous Fe-Ni-W/Ni coated specimen has a much larger plastic-deformation range with a relatively stable plastic flow, and an insignificant decrement in the plastic-flow stresses when compared with the as-cast BMG and the BMGs coated with a single layer of Ni or Cu, or coated with a Cu/Ni bilayer.¹⁷

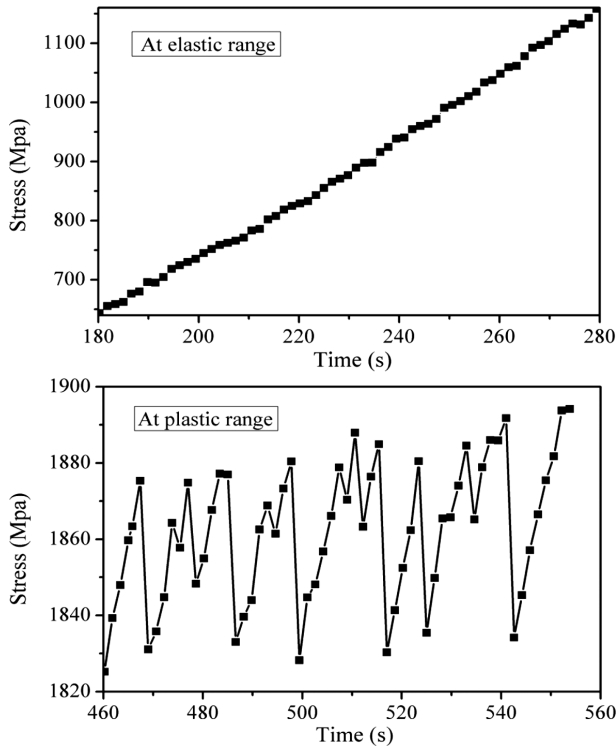


Figure 4: Flow serrations of the uncoated BMG

Slika 4: Nazobčan potek krivulje pri BMG brez nanosa

It is well known that a stress increase during the plastic flow of BMGs is correlated with the arrest of the propagating shear bands. However, when a shear band is initiated and starts to propagate, there is a corresponding displacement burst, which is linked to a stress decrease.²² Repeated stress increases and decreases result in serrations as the plastic flow proceeds. Such successive serrations are recognized as arising from an emission of new shear bands and a propagation of the existing ones.¹⁷ To obtain detailed information on the serrated flow between the uncoated BMG and the bilayer- confined BMGs, five ranges (as indicated by the rectangles in **Figure 3**) of the stress-strain curves were magnified and shown in **Figures 4** and **5**, respectively.

Since the bilayer-confined BMG specimen has a much larger plasticity, two plastic ranges were magnified in **Figure 5**. As shown in **Figures 4** and **5**, during the elastic ranges, the stress increases linearly with time, while during the plastic ranges, serrated flows are clearly

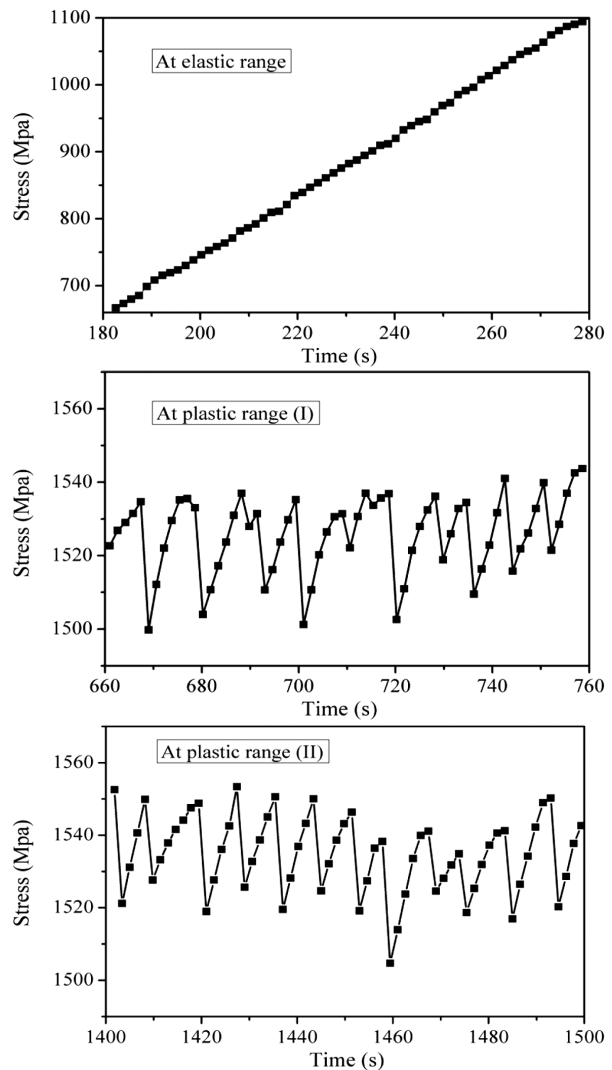


Figure 5: Flow serrations of the bilayer-coated BMG

Slika 5: Nazobčan potek krivulje pri BMG z dvoplastnim nanosom

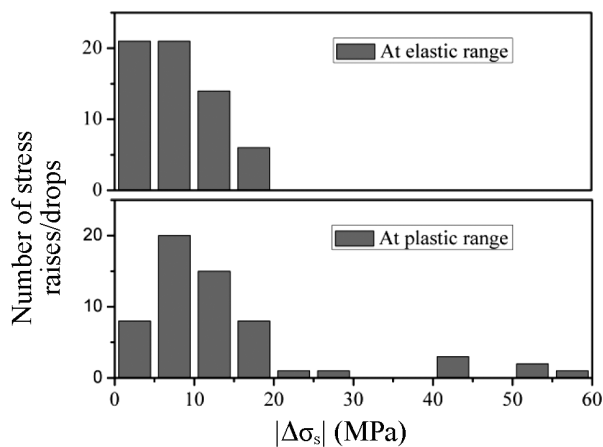


Figure 6: Statistical results of the number of stress loads/drops for the uncoated BMG

Slika 6: Statistični rezultati številnih obremenitev in razbremenitev pri BMG brez nanosa

observed for both kinds of BMG specimens. However, the amplitude of the serrated flow in the bilayer-confined BMGs is much smaller compared to that of the uncoated BMG. The serrated flow of the BMGs is found to be related to the shear-band propagation and termination, dissipating the plastic-deformation energy.^{23,24} A smaller amplitude indicates that the rapid avalanching of the load in a specimen was significantly confined.²⁵

Flow serrations are the result of intermittent sample sliding and the formation of shear bands along the principal shear plane.^{8,17} To characterise the flow serrations, an absolute value of the stress raises/drops

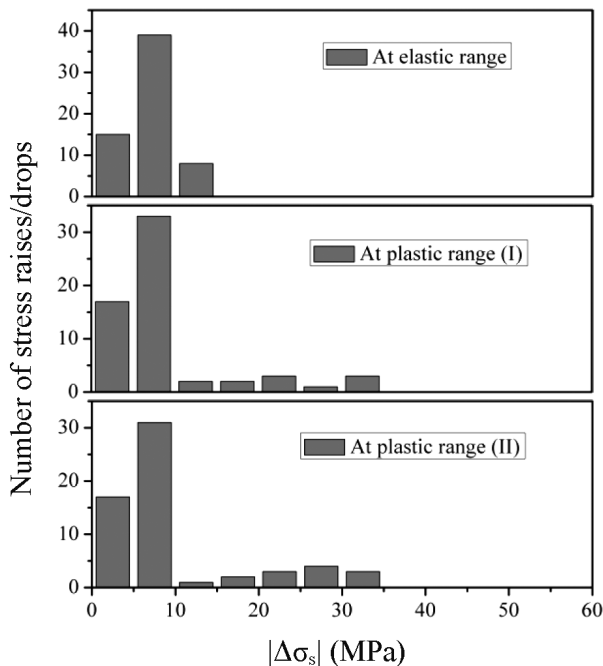


Figure 7: Statistical results of the number of stress loads/drops for the bilayer-confined BMG

Slika 7: Statistični rezultati številnih obremenitev/razbremenitev pri BMG z dvoplastnim nanosom

($|\Delta\sigma_s| = |\sigma_{n+1} - \sigma_n|$, where σ_{n+1} and σ_n are two neighbouring values of the stresses on the stress-strain curves) was introduced. Detailed statistical results of the $|\Delta\sigma_s|$ values of the selected ranges from **Figures 4** and **5** are shown as histograms in **Figures 6** and **7**, respectively. It can be seen that, in the plastic ranges, the uncoated BMG shows a large stress drop of up to 60 MPa (**Figure 6**), while the bilayer-confined BMG has a relatively smaller stress drop, no larger than 35 MPa (**Figure 7**).

The smaller amplitudes of the stress drops indicate that the specimen has a smaller axial displacement during the avalanches⁸ and that it can more easily self-organize to a critical state to obtain enhanced macroscopic plasticity.²⁵ Moreover, the number of the stress drops for the bilayer-confined BMGs is larger than for the uncoated BMG specimen (due to the vibration of the testing machine, only stresses larger than 12 MPa were determined here),²⁵ illustrating the initiation of more shear bands in the bilayer-confined BMGs.

A serrated flow can also be explained as a cycle of elastic-energy accumulation (stress raise) and release (stress drop): a larger serration magnitude corresponds to a higher elastic-energy density. As discussed earlier, the serrations obtained for the bilayer-confined BMG are of a small amplitude and a larger frequency, and their corresponding elastic energies are not dense enough for the shear bands to propagate through the cross-section of the specimen.^{9,10} A large number of small serration flows is a good indicator that the bilayer-confined specimen can release the elastic energy in multiple small bursts rather than releasing all the stored energy in one shear band, thus extending the plastic deformation stage in a more stable manner without a large decrease in the stress.

Several studies have shown that the geometric confinement is able to significantly affect the plastic flow.¹⁴⁻¹⁷ The process of electroplating can cause a residual stress at the interface between the coating and the BMG.²⁶ During the elastic loading, a mismatch in Poisson's ratio of the BMG and the coating leads to a confining stress on the BMG, and the maximum geometrical confining stress after reaching the yield strength can be estimated using formula $\sigma_{max} = \sigma_y \ln(b/a)$,²⁷ where σ_{max} , σ_y , a and b denote the maximum confining stress, the yield strength of the bilayer coating, the inner diameter and the outer diameter of the specimen, respectively.

By replacing part of the Ni coating with an amorphous Fe-Ni-W coating, the large yield strength of a Fe-based BMG enables larger confining stresses on the BMG matrix.²⁸ Upon loading, the shear bands start propagating on the surface of the uncoated BMG and deformation occurs through the primary shear band, leading to a catastrophic failure. When the bilayer coating is in the place, it inhibits the rapid propagation of single shear bands, causing them to branch out instead.¹⁷ The enlargement of the confined stress arrests the propagation of the shear bands, preventing the catastrophic failure from the

avalanches and resulting in a stable plastic flow before the failure.^{16,25}

Recently, many studies have reported that the interface can induce the initiation of more smaller shear bands and the corresponding increased interactions (branching and arresting) between the shear bands that, in turn, increase the plasticity of a coated specimen.^{16,19} Besides the confining effect, the outside nickel layer is also found to be effective at hindering the propagation of the shear bands, dissipating the stored elastic energy in the core BMG.¹⁶ Moreover, since the hardness of the Fe-Ni-W coatings (measured as 647 HV) is much larger than the hardness of the BMG specimen (about 442 HV), the inner Zr-BMG layer may act as the softer phase, initiating the shear bands, and the outer amorphous Fe-Ni-W layer may act as the harder phase, inhibiting the propagation of the shear bands.^{29,30}

The complicated mechanisms for the initiation and propagation of the shear bands (intermittent sliding) in the bilayer-confined BMGs may need further verification; however, the corresponding serrated flow shown in the stress-strain curves, without much decrease in the loads, distinctly illustrates the stable plastic flow in the bilayer-confined BMGs. This provides a feasible route for achieving a stable plastic flow in the BMGs for industrial applications and guidance in understanding the plastic-deformation mechanism in geometrically confined BMGs.

4 CONCLUSIONS

An amorphous Fe-Ni-W/Ni bilayer was successfully applied onto a Zr-based BMG through electroplating. The bilayer-confined BMG exhibits greatly enhanced macroscopic plasticity before failure, without much decrease in the loads during the serrated-flow stage. The statistical results of the flow serrations show that the bilayer-confined BMG has smaller amplitudes and larger frequencies of stress decreases. The enhanced stability of the plastic flow in the bilayer-confined BMGs may be mainly due to the large confining effect caused by the amorphous layer. The present work not only proposes a feasible route to achieve a more stable plastic flow in BMGs but also gives more insight into the plastic-deformation mechanisms of geometrically confined BMGs.

Acknowledgements

The work described in this paper was supported by a grant from the Research Grants Council of the Hong Kong Special Administrative Region, China (Project No. PolyU 511510).

5 REFERENCES

¹ A. R. Yavari, J. J. Lewandowski, J. Eckert, Mechanical properties of bulk metallic glasses, *MRS Bulletin*, 32 (2007) 8, 635–638, doi:10.1557/mrs2007.125

² W. H. Wang, C. Dong, C. H. Shek, Bulk metallic glasses, *Materials Science and Engineering R*, 44 (2004) 2–3, 45–89, doi:10.1016/j.mser.2004.03.001

³ A. L. Greer, Metallic glasses ... on the threshold, *Materials Today*, 12 (2009) 1–2, 14–22, doi:10.1016/S1369-7021(09)70037-9

⁴ S. H. Chen, K. C. Chan, F. F. Wu, L. Xia, Pronounced energy absorption capacity of cellular bulk metallic glasses, *Applied Physics Letters*, 104 (2014) 11, 111907, doi:10.1063/1.4869229

⁵ S. H. Chen, K. C. Chan, L. Xia, Deformation behavior of a Zr-based bulk metallic glass under a complex stress state, *Intermetallics*, 43 (2013), 38–44, doi:10.1016/j.intermet.2013.07.006

⁶ S. H. Chen, K. C. Chan, L. Xia, Deformation behavior of bulk metallic glass structural elements, *Materials Science and Engineering A*, 606 (2014), 196–204, doi:10.1016/j.msea.2014.03.094

⁷ A. S. Argon, Plastic-Deformation in Metallic Glasses, *Acta Metallurgica*, 27 (1979) 1, 47–58, doi:10.1016/0001-6160(79)90055-5

⁸ S. X. Song, H. Bei, J. Wadsworth, T. G. Nieh, Flow serration in a Zr-based bulk metallic glass in compression at low strain rates, *Intermetallics*, 16 (2008) 6, 813–818, doi:10.1016/j.intermet.2008.03.007

⁹ C. N. Kuo, H. M. Chen, X. H. Du, J. C. Huang, Flow serrations and fracture morphologies of Cu-based bulk metallic glasses in energy release perspective, *Intermetallics*, 18 (2010) 8, 1648–1652, doi:10.1016/j.intermet.2010.04.018

¹⁰ J. W. Qiao, Y. Zhang, P. K. Liaw, Serrated flow kinetics in a Zr-based bulk metallic glass, *Intermetallics*, 18 (2010) 11, 2057–2064, doi:10.1016/j.intermet.2010.06.013

¹¹ S. X. Song, T. G. Nieh, Flow serration and shear-band viscosity during inhomogeneous deformation of a Zr-based bulk metallic glass, *Intermetallics*, 17 (2009) 9, 762–767, doi:10.1016/j.intermet.2009.03.005

¹² W. J. Wright, R. Saha, W. D. Nix, Deformation mechanisms of the $Zr_{60}Ti_{10}Ni_{10}Cu_{10}Be_{24}$ bulk metallic glass, *Materials Transactions*, 42 (2001) 4, 642–649, doi:10.2320/matertrans.42.642

¹³ B. A. Sun, S. Pauly, J. Tan, M. Stoica, W. H. Wang, U. Kuhn, J. Eckert, Serrated flow and stick-slip deformation dynamics in the presence of shear-band interactions for a Zr-based metallic glass, *Acta Materialia*, 60 (2012) 10, 4160–4171, doi:10.1016/j.actamat.2012.04.013

¹⁴ H. Q. Li, L. Li, C. Fan, H. Choo, P. K. Liaw, Nanocrystalline coating enhanced ductility in a Zr-based bulk metallic glass, *Journal of Materials Research*, 22 (2007) 2, 508–513, doi:10.1557/Jmr.2007.0060

¹⁵ W. Chen, K. C. Chan, P. Yu, G. Wang, Encapsulated Zr-based bulk metallic glass with large plasticity, *Materials Science and Engineering A*, 528 (2011) 6, 2988–2994, doi:10.1016/j.msea.2010.12.077

¹⁶ W. Chen, K. C. Chan, S. F. Guo, P. Yu, Plasticity improvement of an Fe-based bulk metallic glass by geometric confinement, *Materials Letters*, 65 (2011) 8, 1172–1175, doi:10.1016/j.matlet.2011.01.030

¹⁷ W. Chen, K. C. Chan, S. H. Chen, S. F. Guo, W. H. Li, G. Wang, Plasticity enhancement of a Zr-based bulk metallic glass by an electroplated Cu/Ni bilayered coating, *Materials Science and Engineering A*, 552 (2012), 199–203, doi:10.1016/j.msea.2012.05.031

¹⁸ T. G. Nieh, Y. Yang, J. Lu, C. T. Liu, Effect of surface modifications on shear banding and plasticity in metallic glasses: An overview, *Progress in Natural Science: Materials International*, 22 (2012) 5, 355–363, doi:10.1016/j.pnsc.2012.09.006

¹⁹ J. P. Chu, J. E. Greene, J. S. C. Jang, J. C. Huang, Y. L. Shen, P. K. Liaw, Y. Yokoyama, A. Inoue, T. G. Nieh, Bendable bulk metallic glass: Effects of a thin, adhesive, strong, and ductile coating, *Acta Materialia*, 60 (2012) 6–7, 3226–3238, doi:10.1016/j.actamat.2012.02.037

²⁰ F. J. He, J. Yang, T. X. Lei, C. Y. Gu, Structure and properties of electrodeposited Fe-Ni-W alloys with different levels of tungsten content: A comparative study, *Applied Surface Science*, 253 (2007) 18, 7591–7598, doi:10.1016/j.apsusc.2007.03.068

- ²¹ L. Mirkova, G. Maurin, M. Monev, C. Tsvetkova, Hydrogen coevolution and permeation in nickel electroplating, *Journal of Applied Electrochemistry*, 33 (2003) 1, 93–100, doi:10.1023/A:1022957600970
- ²² H. M. Chen, C. J. Lee, J. C. Huang, T. H. Li, J. S. C. Jang, Flow serration and shear-band propagation in porous Mo particles reinforced Mg-based bulk metallic glass composites, *Intermetallics*, 18 (2010) 6, 1240–1243, doi:10.1016/j.intermet.2010.03.024
- ²³ A. Lemaitre, C. Caroli, Rate-Dependent Avalanche Size in Athermally Sheared Amorphous Solids, *Physical Review Letters*, 103 (2009) 6, 065501, doi:10.1103/PhysRevLett.103.065501
- ²⁴ D. Klaumunzer, R. Maass, F. H. Dalla Torre, J. F. Löffler, Temperature-dependent shear band dynamics in a Zr-based bulk metallic glass, *Applied Physics Letters*, 96 (2010) 6, 061901, doi:10.1063/1.3309686
- ²⁵ G. Wang, K. C. Chan, L. Xia, P. Yu, J. Shen, W. H. Wang, Self-organized intermittent plastic flow in bulk metallic glasses, *Acta Materialia*, 57 (2009) 20, 6146–6155, doi:10.1016/j.actamat.2009.08.040
- ²⁶ S. J. Hearne, J. A. Floro, Mechanisms inducing compressive stress during electrodeposition of Ni, *Journal of Applied Physics*, 97 (2005) 1, 014901, doi:10.1063/1.1819972
- ²⁷ G. Ravichandran, J. Lu, Pressure-dependent flow behavior of $Zr_{41.2}Ti_{13.8}Cu_{12.5}Ni_{10}Be_{22.5}$ bulk metallic glass, *Journal of Materials Research*, 18 (2003) 9, 2039–2049, doi:10.1557/Jmr.2003.0287
- ²⁸ X. J. Gu, S. J. Poon, G. J. Shiflet, Mechanical properties of iron-based bulk metallic glasses, *Journal of Materials Research*, 22 (2007) 2, 344–351, doi:10.1557/Jmr.2007.0036
- ²⁹ X. H. Du, J. C. Huang, K. C. Hsieh, Y. H. Lai, H. M. Chen, J. S. C. Jang, P. K. Liaw, Two-glassy-phase bulk metallic glass with remarkable plasticity, *Applied Physics Letters*, 91 (2007) 13, 131901, doi:10.1063/1.2790380
- ³⁰ S. H. Chen, K. C. Chan, L. Xia, Effect of stress gradient on the deformation behavior of a bulk metallic glass under uniaxial tension, *Materials Science and Engineering A*, 574 (2013), 262–265, doi:10.1016/j.msea.2013.03.035

SYNERGISTIC EFFECT OF ORGANIC- AND CERAMIC-BASED INGREDIENTS ON THE TRIBOLOGICAL CHARACTERISTICS OF BRAKE FRICTION MATERIALS

SINERGISTIČEN VPLIV SESTAVIN Z ORGANSKO IN KERAMIČNO OSNOVO NA TRIBOLOŠKE ZNAČILNOSTI MATERIALOV ZA TORNE ZAVORE

Rukiye Ertan

Uludag University, Faculty of Engineering, Department of Automotive Engineering, Görükle, 16059, Bursa, Turkey
rukiye@uludag.edu.tr

Prejem rokopisa – received: 2014-09-11; sprejem za objavo – accepted for publication: 2015-04-08

doi:10.17222/mit.2014.225

In this study, the composition of a brake friction material was experimentally investigated with respect to the effects of the proportions of organic (cashew dust) and ceramic ($ZrSiO_4$ and Fe_2O_3) based ingredients on the tribological properties. The tribological properties of the friction materials were evaluated using a Chase-type friction tester. The effect of the ingredient proportions on the wear resistance and friction stability were obtained in relation to the test temperature and the number of brakings. A scanning electron microscope was used to study the effect of braking on the sliding surface of the friction material. Results showed that the complementary nature of the organic- and ceramic-based ingredients provided the optimum friction behaviour, such as the coefficient of friction stability and the wear resistance.

Keywords: sliding friction, brakes/clutches, wear testing, electron microscopy

V študiji je bila eksperimentalno preiskovana sestava materiala za torne zavorne obloge, glede na razmerje organskih (prah indijskih oreščkov) in keramičnih sestavin na osnovi $ZrSiO_4$ in Fe_2O_3 ter na tribološke lastnosti. Tribološke lastnosti tornih materialov so bile ocenjene z uporabo preizkuševalca trenja vrste Chase. Vpliv razmerja sestavin na odpornost proti obrabi in stabilnost trenja je bil ugotovljen glede na temperaturo preizkusa in število zaviranja. Vrstični elektronski mikroskop je bil uporabljen za študij učinka zaviranja na torni površini tornega materiala. Rezultati so pokazali, da komplementarna narava sestavin na organski in keramični osnovi, zagotavlja optimalno obnašanje pri trenju kot sta koeficient stabilnega trenja in odpornost na obrabo.

Ključne besede: drsno trenje, zavore/sklopke, preizkušanje obrabe, elektronska mikroskopija

1 INTRODUCTION

In a brake system, the energy input begins as a driver presses the brake pedal, is then mechanically, hydro-pneumatically, electrically or with a hybrid method transmitted to the other components and ends at the disc/drum brakes. This kinetic energy is mostly distributed as the heat resulting from the friction between the brake friction material and the disc/drum interface.¹ Thus, the design and material characteristics of the friction material, the disc/drum material where friction is generated and energy transformation occurs are important for the brake system. Especially brake friction materials are crucial for the stopping distance and noise propensity of a vehicle.^{2,3}

A commercial friction material generally contains more than ten ingredients including metallic-, organic-, ceramic-, polymeric-based powders or fibre materials in a thermoset polymeric matrix. The understanding of the synergistic interaction between the ingredients has largely relied on hands-on experiences and systematic studies of friction materials for the optimum brake performance.⁴ In particular, hard ingredients used as abrasives in brake friction materials, with a relatively high

hardness control the level of the friction force and remove pyrolyzed friction films at the sliding interface.⁵ The amount of abrasive is limited in vehicle brake pads because it does a lot of damage to the disc.⁶ The abrasives used in commercial brake friction materials are generally ceramic-based, in various sizes and forms of oxides and silicates, such as zircon, alumina, quartz, magnesia, etc. The organic ingredients of the friction composites such as resin, cashew dust, aramid pulp, etc., are softer than the ceramic ones and responsible for the fade (a decrease in the braking efficiency or coefficient of friction with an increase in the average temperature of the braking surface) which is an extremely undesirable feature.⁷

From references list, it is seen that only a few studies report about the synergistic effect of the organic- and ceramic-based ingredients in friction materials and their roles in the brake performance.⁸ On the other hand, individual effects of organic- and ceramic-based ingredients were extensively investigated.⁸⁻¹¹ The purpose of the present investigation is to investigate the organic- and ceramic-based ingredients together, with regard to the tribological characteristics of a brake friction material.

2 EXPERIMENTAL WORK

2.1 Material preparation

The brake friction materials used in this study are non-asbestos organic (NAO) materials and the proportions of the ingredients are given in **Table 1**, including the average densities of the finished products. Friction-material specimens were manufactured by mixing, hot pressing, and sintering. The ingredients were weighed and mixed in the given proportions in a plough shear mixer for 10 min. Aramid fibers were added initially, followed by other pulpy materials and finally by powdery materials. The manufacturing parameters were chosen according to the study of Ertan and Yavuz.¹² The mix was moulded at 150 °C under a pressure of 7.5 MPa for 5 min in a steel die. Heat treatment was carried out in a mechanical convection oven at 165 °C for 12 h. The total amount of ZrSiO₄, Fe₂O₃ and cashew dust was not changed and was set as 15 % of mass fractions for all the specimens.

2.2 Friction testing and microstructure analysis

Friction and wear performances were conducted using a Chase-type friction tester (**Figure 1**), according to the national standard of the Society of Automotive Engineers (SAE) J661, determining the friction coefficient, the friction force, the wear loss and the types of wear. Gray cast iron with a 280-mm diameter and a hard-

ness of 210 HB was used as the counterpart. The applied load was exerted on the specimen in the holder with a closed-loop servo system and the maximum hydraulic pressure was 540 N. The speed was held constant at 411 min⁻¹ and controlled by a variable speed drive.

The test procedure consisted of a burnishing step, the fade and recovery tests. The test procedure began with the baseline-I operation of 20 applications. This was followed by the fade-I test at constant speed and load, where the frictional force was recorded continuously at 28 °C intervals while the drum temperature rose to 289 °C. Then, the drum was cooled to 93 °C and the frictional force was recorded continuously at 56 °C intervals during the recovery-I test. This was followed by the baseline-II, fade-II and recovery-II test, similar to the first one, but with the temperatures going up to 345 °C. The wear test, which consisted of 100 applications, was conducted at the end of the testing.

The weight of the pads for each sample was measured before and after the friction test, and the specific wear was determined with the mass method following the standard of TSE 555 (1992)¹³ and calculated with the following Equation (1):

$$\omega = \frac{1}{2\pi R} \times \frac{1}{f_m n} \times \frac{m_1 - m_2}{\rho} \quad (1)$$

where ω is the specific wear rate (cm³/N m), R is the distance between the centre of the specimen and the centre of the drum (m), n is the number of revolutions of

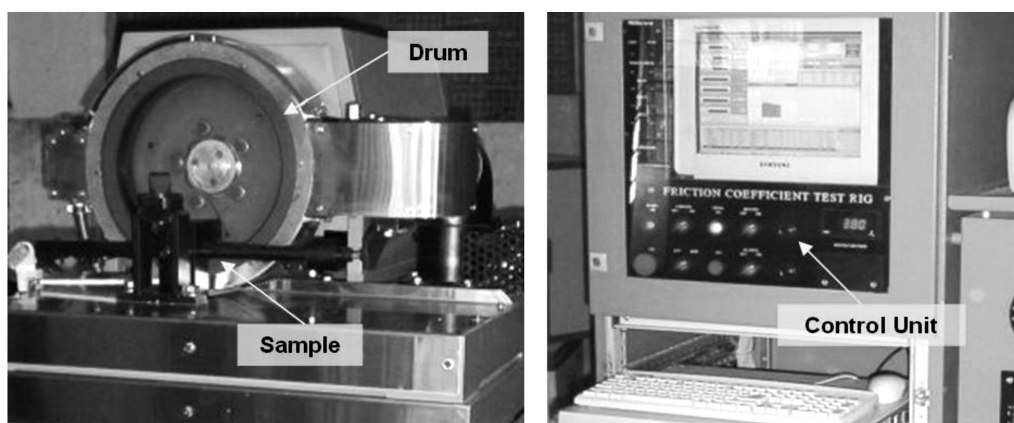


Figure 1: Chase-type friction tester

Slika 1: Preizkuševalna naprava trenja, vrste Chase

Table 1: Ingredients of the friction materials investigated in this work (in mass fractions, w/%)

Tabela 1: Vsebnosti tornih materialov, preiskovanih v tem delu (v masnih deležih, w/%)

Ingredients		A1	A2	A3	A12	A13	A23	A123
Ceramic-based abrasives	ZrSiO ₄	10	3	3	6.5	6.5	3	6
	Fe ₂ O ₃	2	9	2	5.5	2	5.5	4
Organic friction modifiers	Cashew dust	3	3	10	3	6.5	6.5	5
Reinforcements		25	25	25	25	25	25	25
Binders		10	10	10	10	10	10	10
Lubricants		20	20	20	20	20	20	20
Fillers		30	30	30	30	30	30	30
Density (g/cm ³)		2.13	2.11	1.80	2.03	2.01	1.95	2.05

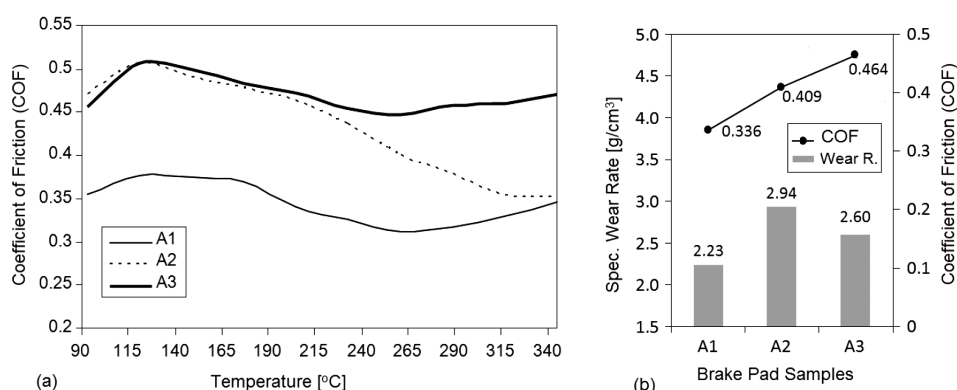


Figure 2: Friction test results for A1, A2 and A3 brake-pad materials: a) *COF* depending on the test temperature (°C), b) the average *COF* at elevated temperatures and specific-wear rates

Slika 2: Rezultati preizkusov trenja A1, A2 in A3 materialov zavorne ploščice: a) *COF* v odvisnosti od temperature preizkusa (°C), b) povprečje *COF* pri povišanih temperaturah in specifične stopnje obrabe

the rotating disk, m_1 and m_2 are the average weights of a specimen before and after the test (g), ρ is the density of the brake lining (g/cm^3) and f_m is the average friction force (N). The densities of the specimens were determined with the Archimedean principle in water, and the density calculations were repeated five times for each specimen after the sintering.

The friction surfaces after the testing were analysed using a scanning electron microscope (Fa. LEO 1455 VP). For all the observations, the samples were carefully cut from an actual-size brake pad in order to avoid any modification of the friction surface, with a sample size of $2 \text{ cm} \times 2 \text{ cm} \times 1 \text{ cm}$.

3 RESULTS AND DISCUSSION

Experimental observations were made to determine the effects of the ceramic and organic constituents on the changes in the *COF* related to the temperature, the average *COF*, the braking number and the specific wear rate. The friction test results for the A1, A2 and A3 specimens are given in **Figure 2**, showing that the *COF* was generally decreased at elevated temperatures. For all the specimens, it is seen that the *COF* continued to increase until 150 °C. The explanation of this behaviour is that the growth of hard particles in the brake material generated a large shear strength and the maximum *COF* at 150 °C.

After this temperature, the *COF* started to decrease. This behaviour can be explained with the destruction of the resin structure and the loss of the local binding properties as well as the formation of the friction film on the surface, called the fade. A compaction of the wear debris generated at the friction interface accounts for the formation of the friction film.^{14,15} After 250 °C the *COF* exhibited a stable change, with the increasing temperature, in the A1 and A3 specimens, but the *COF* stability of the A2 specimen containing a high proportion of Fe_2O_3 was the lowest, especially at elevated temperatures.

The abrasive effect of the Fe_2O_3 powders increased the wear rate (**Figure 2b**) and the wear debris were built at the friction interface and formed a friction film. This friction film reduces the contact between the pad and the disc. This film (with loosened debris, a stable friction level, and low wear rates) can be maintained at various temperatures, as long as it is not destroyed.¹⁶ These results were confirmed with the microstructure analysis given in **Figure 3**. The areas covered with a disconti-

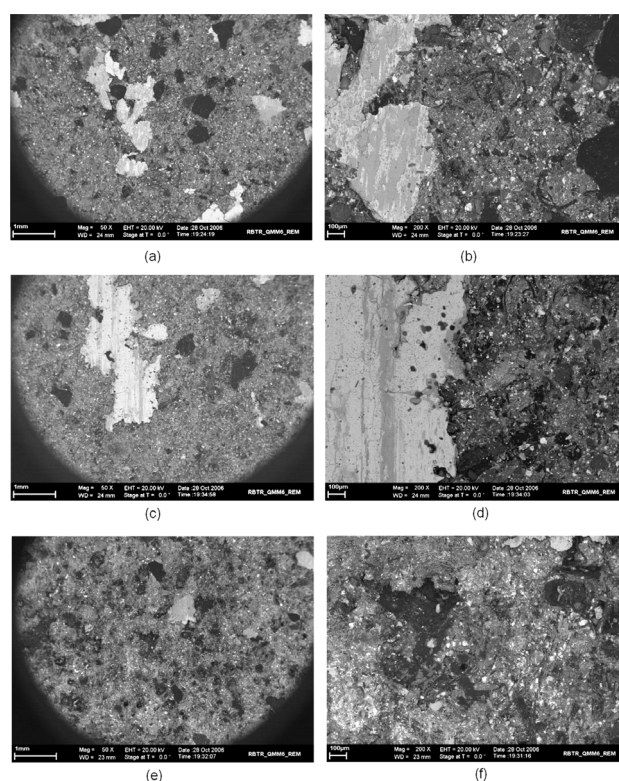


Figure 3: SEM micrographs of the worn surfaces of the brake-pad specimens after the friction test: a) A1-general, b) A1-detailed, c) A2-general, d) A2-detailed, e) A3-general and f) A3-detailed

Slika 3: SEM-posnetki obrabljene površine vzorcev zavornih ploščic po preizkusu trenja: a) A1-splošno, b) A1-podrobno, c) A2-splošno, d) A2-podrobno, e) A3-splošno in f) A3-podrobno

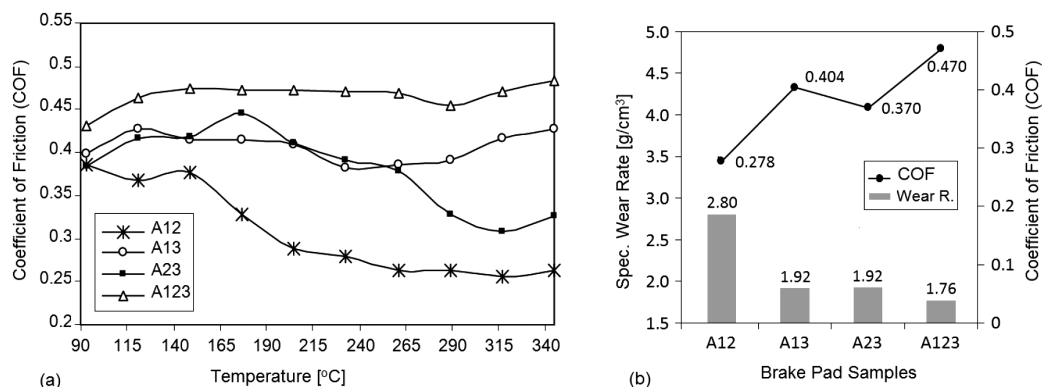


Figure 4: Friction-test results for A12, A13, A23 and A123 brake-pad materials: a) *COF* depending on the test temperature (°C), b) the average *COF* at elevated temperatures and specific wear rates

Slika 4: Rezultati preizkusov trenja A12, A13, A23 in A123 materialov zavornih ploščic: a) *COF* v odvisnosti od temperature preizkusa (°C), b) povprečni *COF* pri povišanih temperaturah in specifične stopnje obrabe

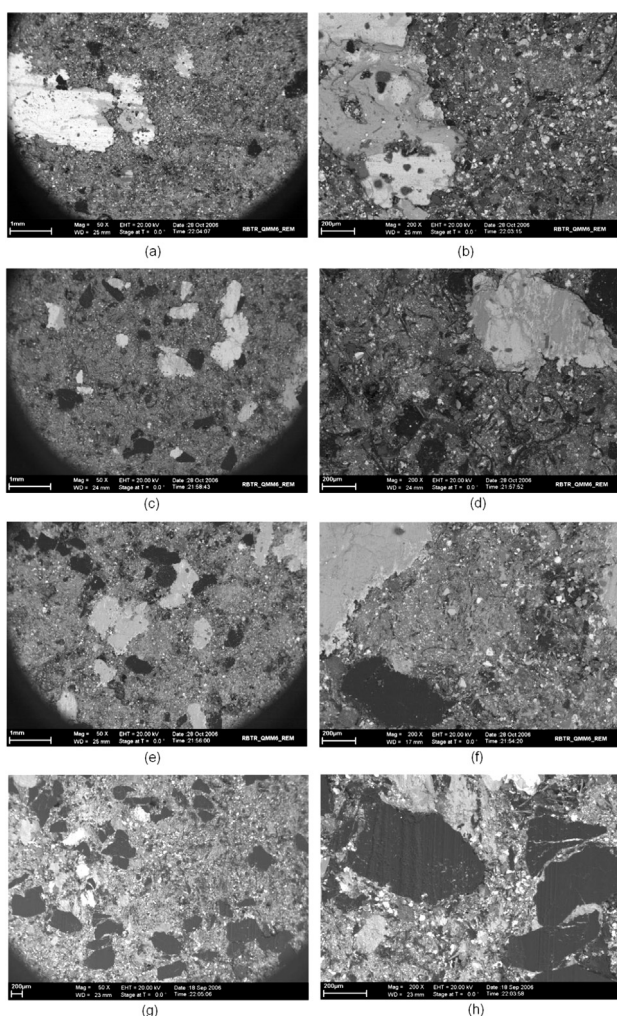


Figure 5: SEM micrographs of the worn surfaces of the composites in the Chase test machine: a) A12-general, b) A12-detailed, c) A13-general, d) A13-detailed, e) A23-general, f) A23-detailed, g) A123-general, h) A123-detailed

Slika 5: SEM-posnetki obrabljene površine kompozitov v Chase preizkuševalni napravi: a) A12-splošno, b) A12-podrobno, c) A13-splošno, d) A13-podrobno, e) A23-splošno, f) A23-podrobno, g) A123-splošno, h) A123-podrobno

nuous friction film on the friction surface are shown in **Figures 3a** and **3b**.

The brake pads containing more Fe_2O_3 powders than ZrSiO_4 and cashew dust show an unstable friction behaviour and a low fade resistance, and the areas covered with the friction film on the friction surface are increased (**Figures 3c** and **3d**). The surface of brake pad A2 is very rough and exhibits large, locally delaminated friction-film regions. Several reasons may explain these differences, some of which are merely physical, such as the particle-size distribution and the hardness.¹⁷

The average *COF* of A3 at elevated temperatures (between the 165–345 °C) was very high (**Figure 2b**). The abrasive proportion in this brake pad was minimum. The SEM images indicate very thin and locally delaminated friction-film regions on the surface of the specimen (**Figures 3e** and **3f**) that do not reduce the contact between the pad and the disc. As shown in **Figure 2b**, sample A3 exhibited a high wear rate. The increase in the wear rate of sample A3 is associated with the temperature sensitivity of the organic-based cashew dust (**Figure 3e**).

When both the ZrSiO_4 and Fe_2O_3 amounts were increased in a mixture (A12), the average *COF* at elevated temperatures (between the 165–345 °C) exhibited the lowest value (**Figure 4b**). The decrease in the *COF* and a high wear rate (**Figure 4**), therefore, appeared due to the low fade resistance and the large friction-film regions at the sliding interface (**Figures 5a** and **5b**). The degradation of the organic particles and the increased abrasive effect caused a decrease in the *COF* at elevated temperatures. When the worn surfaces of A12 were examined, the areas covered with the friction film were larger and thicker than in the cases of the other specimens. The friction-film areas were locally delaminated from each other. These areas decreased the average *COF* and the stability of the friction material because a friction film reduces the contact between the pad and the disc.¹⁸ The abrasive effect of the ceramic particles caused

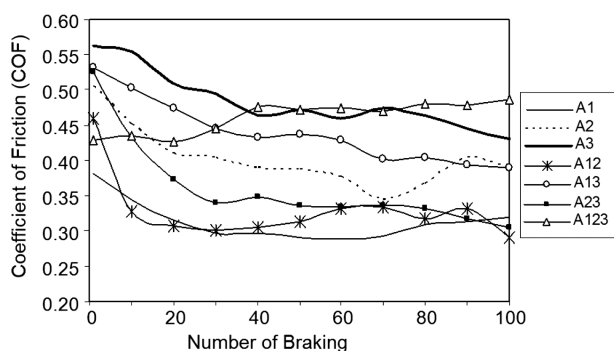


Figure 6: *COF* variations related to the number of brakings for the A1, A2, A3, A12, A13, A23, A123 brake-pad materials

Slika 6: Spreminjanje *COF* glede na število zaviranj pri A1, A2, A3, A12, A13, A23, A123 materialih zavrne ploščice

an increase in the wear rate. Therefore, the maximum wear rate was obtained for sample A12.

The brake pad with a high relative amount of $ZrSiO_4$ and cashew dust (A13) has a stable *COF* at elevated temperatures, but the values are not so high. This result can be explained with the lubricating effect of the cashew dust and the stable friction behaviour of $ZrSiO_4$. The friction-film formation is more homogeneous and locally delaminated than in the case of A12 (Figures 5c and 5d). However, the wear rate is lower than that of A12.

When Figure 5e is examined, it is seen that the areas covered with the friction film increased and the stability decreased with the increasing amounts of Fe_2O_3 and cashew dust. The abrasive effect of Fe_2O_3 decreased the stability and eliminated the cashew-dust lubrication effect. The *COF* exhibited an unsteady change, especially at elevated temperatures, as shown in Figure 4a. It can be observed that large, locally delaminated friction-film regions formed on the surface of sample A23. A low wear rate with the increased amount of Fe_2O_3 and cashew dust is associated with the strong and durable friction film (Figures 5e and 5f).

Sample A123 exhibited the highest fade resistance among the brake-pad samples due to its stable *COF* changing with high values. When the worn surface of this sample is examined, it can be seen that the friction film was barely formed on the friction interface (Figure 5g). The synergistic effect of the ceramic- and organic-based constituents is clearly seen from the wear rate (Figure 4b). The wear rate for this sample is the lowest among the tested samples. This optimum tribological behavior of the A123 brake-pad material can be explained with a combination of the stable friction behavior of $ZrSiO_4$, the aggressive behavior of the high *COF* of Fe_2O_3 and the lubricating effect of the cashew dust.

The *COF* change related to the number of brakings can be seen in Figure 6. From the literature review, it is observed that the number of braking applications has the strongest effect on the friction-interface temperature.¹⁹

Consequently, the *COF* change decreases with the number of brakings. The stability of the *COF* is slightly reduced after the 50th braking. It can be seen that A1, A13 and A123 exhibit high and stable *COFs*, while A3, A12 and A23 exhibit low and unstable *COFs*.

4 CONCLUSION

The friction characteristics of the brake pads including organic (cashew dust) and ceramic ($ZrSiO_4$ and Fe_2O_3) based ingredients in different combinations were examined. The results showed that the organic and ceramic ingredients used as abrasive and friction modifiers have strong synergistic effects providing the average *COF*, the friction stability and the wear resistance. The friction film on the brake-pad material was mainly affected by the proportions of the ceramic-based ingredients. Increasing the cashew-dust proportion increased the average *COF* in the specimens. The wear resistance of a brake pad was decreased with an increase in the ceramic ingredients. On the other hand, an addition of a certain amount of cashew dust greatly improved the wear resistance. This complementary nature of the organic and ceramic ingredients provided the optimum friction behavior. In this study, the best friction behavior was obtained in the brake-pad material with the proportions of the ingredients close to the composition of specimen A123 (6 % $ZrSiO_4$, 4 % Fe_2O_3 and 5 % cashew dust).

Acknowledgements

The author deeply appreciates the Frenetek Automotive and Brake Lining Industry Corporation, where the brake-pad production and the experimental work were carried out.

5 REFERENCES

- D. J. Kim, Y. M. Lee, J. S. Park, C. S. Seok, Thermal stress analysis for a disk brake of railway vehicles with consideration of the pressure distribution on a frictional surface, *Mat. Sci. and Eng. A*, 483–484 (2008), 456–459, doi:10.1016/j.msea.2007.01.170
- S. W. Yoon, M. W. Shin, W. G. Lee, H. Jang, Effect of surface contact conditions on the stick-slip behavior of brake friction material, *Wear*, 294–295 (2012), 305–312, doi:10.1016/j.wear.2012.07.011
- Y. Dai, T. C. Lim, Suppression of brake squeal noise applying finite element brake and pad model enhanced by spectral-based assurance criteria, *App. Acoustics*, 69 (2008) 3, 196–214, doi:10.1016/j.apacoust.2006.09.010
- B. K. Satapathy, J. Bijwe, Composite friction materials based on organic fibres: Sensitivity of friction and wear to operating variables, *Compos Part A: App. Sci. Manuf.*, 37 (2006) 10, 1557–1567, doi:10.1016/j.compositesa.2005.11.002
- Y. C. Kim, M. H. Cho, S. J. Kim, H. Jang, The effect of phenolic resin, potassium titanate, and CNSL on the tribological properties of brake friction material, *Wear*, 264 (2008) 3–4, 204–210, doi:10.1016/j.wear.2007.03.004
- S. S. Kim, H. J. Hwang, M. W. Shin, H. Jang, Friction and vibration of automotive brake pads containing different abrasive particles, *Wear*, 271 (2011) 7–8, 1194–1202, doi:10.1016/j.wear.2011.05.037

- ⁷ S. Zhang, F. Wang, Comparison of friction and wear performances of brake materials containing different amounts of ZrSiO₄ dry sliding against SiCp reinforced Al matrix composites, *Mat. Sci. and Eng. A*, 443 (2007) 1–2, 242–247, doi:10.1016/j.msea.2006.09.054
- ⁸ P. V. Gurunath, J. Bijwe, Friction and wear studies on brake-pad materials based on newly developed resin, *Wear*, 263 (2007) 7–12, 1212–1219, doi:10.1016/j.wear.2006.12.050
- ⁹ A. Patnaik, M. Kumar, B. K. Satapathy, B. S. Tomar, Performance sensitivity of hybrid phenolic composites in friction braking: Effect of ceramic and aramid fibre combination, *Wear*, 269 (2010) 11–12, 891–899, doi:10.1016/j.wear.2010.08.023
- ¹⁰ S. Y. Zhang, S. S. Feng, Friction and wear performances of brake material dry sliding against a composite with a semi-interpenetrating network structure of ceramics and Al-alloy, *Trib. Int.*, 44 (2011) 3, 248–257, doi:10.1016/j.triboint.2010.10.029
- ¹¹ Y. Ma, G. S. Martynková, M. Valášková, V. Matějka, Y. Lu, Effects of ZrSiO₄ in non-metallic brake friction materials on friction performance, *Trib. Int.*, 41 (2008) 3, 166–174, doi:10.1016/j.triboint.2007.07.004
- ¹² R. Ertan, N. Yavuz, An experimental study on the effects of manufacturing parameters on the tribological properties of brake lining materials, *Wear*, 268 (2010) 11–12, 1524–1532, doi:10.1016/j.wear.2010.02.026
- ¹³ *Testing and Examination Methods of Automotive Brake Linings*, TS 555, TSE Press, Ankara 1992, 6–33
- ¹⁴ J. Brecht, W. Hoffrichter, A. Dohle, Mechanisms of Brake Creep Groan, SAE, Technical Paper, paper 973026 (1997), 79–85, doi:10.4271/973026
- ¹⁵ S. J. Kim, M. H. Cho, K. H. Cho, H. Jang, Complementary effects of solid lubricants in the automotive brake lining, *Trib. Int.*, 40 (2007) 1, 15–20, doi:10.1016/j.triboint.2006.01.022
- ¹⁶ M. G. Jacko, P. H. S. Tsang, S. K. Rhee, Wear debris compaction and friction film formation of polymer composites, *Wear*, 133 (1989) 1, 23–38, doi:10.1016/0043-1648(89)90110-5
- ¹⁷ R. Ertan, N. Yavuz, The effects of graphite, coke and ZnS on the tribological and surface characteristics of automotive brake friction materials, *Ind. Lub. and Trib.*, 63 (2011) 4, 245–253, doi:10.1108/00368791111140468
- ¹⁸ A. Méndez, R. Santamaría, M. Granda, R. Menéndez, Preparation and characterisation of pitch-based granular composites to be used in tribological applications, *Wear*, 258 (2005) 11–12, 1706–1716, doi:10.1016/j.wear.2004.11.030
- ¹⁹ H. S. Qi, A. J. Day, Investigation of disc/pad interface temperatures in friction braking, *Wear*, 262 (2007) 5–6, 505–513, doi:10.1016/j.wear.2006.08.027

OPTIMIZATION OF THE PARAMETERS FOR THE SURFACTANT-ADDED EDM OF A Ti-6Al-4V ALLOY USING THE GRA-TAGUCHI METHOD

OPTIMIZACIJA POVRŠINSKO AKTIVNIH MEŠANIH EDM PARAMETROV NA Ti-6Al-4V ZLITINI Z UPORABO GRA-TAGUCHI METODE

Murahari Kolli, Kumar Adepu

Department of Mechanical Engineering, National Institute of Technology, Warangal, Telangana, India
kmhari.nitw@gmail.com

Prejem rokopisa – received: 2014-09-30; sprejem za objavo – accepted for publication: 2015-03-23

doi:10.17222/mit.2014.249

In this research, the Taguchi technique was applied to determine the optimum process parameters for the electrical discharge machining (EDM) of a titanium alloy with an added surfactant. The surfactant added to the dielectric fluid played an important role in the discharge gap, increasing the conductivity and suspending debris particles in the dielectric fluid, reducing abnormal discharge conditions of the machine and improving the overall machining efficiency. The performance characteristics were the material-removal rate (*MRR*) and the surface roughness (*SR*), which were experimentally explored for various input parameters such as the discharge current, the pulse-on time, the pulse-off time and the surfactant concentration in the dielectric fluid. The optimum setting of the parameters was verified through planned and conducted experiments and analysed using the Taguchi technique. Further, a multi-response optimisation was carried out, maximising the *MRR* and minimising the *SR*, using the Grey relational analysis (GRA). It was observed that the pulse-on time, the discharge current, the pulse-off time and the surfactant concentration contribute significantly to the multi-response optimisation. Confirmation test results showed an improvement in the *MRR* by 20.69 % and in the *SR* by 11.09 %. A scanning-electron-microscope (SEM) analysis was conducted to study the recast layer that evolved during the electrical discharge machining process and the topography of surfaces was also observed.

Keywords: surfactant, Ti-6Al-4V alloy, Grey-Taguchi method, material-removal rate, surface roughness, recast-layer thickness

V članku je uporabljena Taguchi metoda za določanje optimalnih parametrov procesa površinsko aktivne elektroerozije (EDM) na titanovi zlitini. Površinsko aktivne snovi, dodane dielektrični tekočini, igrajo pomembno vlogo pri razelektivitveni reži, kar poveča prevodnost in ustavi delce v dielektrični tekočini, zmanjša neobičajne razelektivitve pri obdelavi in na splošno poveča učinkovitost obdelave. Značilnosti zmogljivosti sta hitrost odstranjevanja materiala (*MRR*) in hrapavost površine (*SR*), ki sta bili eksperimentalno uporabljene za različne vhodne parametre, kot je: tok razelektivitve, trajanje impulza, trajanje prekinitve in koncentracija površinsko aktivne snovi v dielektrični tekočini. Optimalna postavitev parametrov je bila preizkušena z načrtovanimi preizkusi in analizirana s Taguchi metodo. Izvršena je bila optimizacija z več odgovori, to je maksimiranje *MRR* in minimiziranje *SR* s pomočjo uporabe Grey relacijske analize (GRA). Ugotovljeno je, da tok razelektivitve, trajanje pulza, čas brez pulza in koncentracija površinsko aktivne snovi, močno prispevajo k optimizaciji. Rezultati potrditvenih preizkusov so pokazali izboljšanje *MRR* za 20,69 % in *SR* za 11,09 %. Z vrstičnim elektronskim mikroskopom (SEM) je bila izvršena analiza (SEM) pretaljenega sloja, ki se je razvil med postopkom elektroerozije, opazovana pa je bila tudi topografija površine.

Ključne besede: površinsko aktivne snovi, Ti-6Al-4V zlitina, Grey-Taguchi metoda, hitrost odstranjevanja materiala, hrapavost, debelina nataljene plasti

1 INTRODUCTION

The usage of and demand for the Ti-6Al-4V alloy is on an increase day by day because of its high strength, low weight ratio, high corrosion resistance, resistance to high temperature and high toughness. This makes it the appropriate alloy for surgery, medicine, aerospace, the automotive industry, chemical plants, pressure vessels and power generation. It is used to manufacture propeller shafts, riggings and other parts of boats. It is also used to create artificial hips, pins for setting the bones and other biological implants due to its excellent biocompatibility. Its application also includes aircraft-turbine components, aircraft structural components, aerospace fasteners and high-performance automotive parts.^{1,2}

Ti-6Al-4V is one of the materials difficult to machine due to its properties. It chemically reacts with almost all

cutting-tool materials. Its low thermal conductivity and low modulus of elasticity reduce the machinability.³ Low cutting speeds, high feed rates, a huge quantity of cutting fluids, sharp tools and a rigid set-up are essential for the conventional machining of Ti-6Al-4V. This makes its conventional machining uneconomical. EDM is one of the advanced manufacturing processes, with which a Ti-6Al-4V alloy can be machined economically and efficiently.⁴

In modern manufacturing industries, EDM is one of the most popular non-conventional machining processes, used to produce dies, moulds or process ceramics, etc. Tough and hard metals that are generally used in the industries, such as aerospace, automotive and surgical applications, can be machined easily using EDM, taking into account various material properties, such as the elec-

trical and thermal conductivity. EDM is a thermoelectric machining process, in which the electrode and the work-piece do not come into direct contact, which eliminates the mechanical residual stresses and chatter or vibration problems during the machining.⁵ In an EDM process, the dielectric fluid plays a vital role, affecting the material-removal rate and the surface integrity of the machined surface. The vital tasks of the working fluid are transporting sediment particles, enhancing the discharge-energy density of the plasma zone and cooling the electrodes.⁶ It has been noticed from a wide literature survey that most of the researchers focused on reducing the surface roughness and increasing the material-removal rate using kerosene, water and water-oil emulsions of different materials. Very few researchers studied the effect of a surfactant added to EDM. A scarce amount of research work was done on the surfactant added to the EDM oil in the conventional EDM of the titanium alloy.

A surfactant is added into the dielectric fluid for a better circulation in the discharge gap and to avoid particle agglomeration (debris and tar). During the machining process, surfactant molecules enter the discharge gap, thereby breaking down the voltage easily, reducing the insulating strength by increasing the discharge gap and passage and ensuring an even discharge distribution during the machining process. As a result, the process becomes more stable, thereby improving the machining efficiency, reducing the surface roughness and increasing the material-removal rate.⁷⁻⁹

A considerable amount of work on EDM of titanium alloy Ti-6Al-4V was reported by the researchers. Chen et al.¹⁰ compared the influences of kerosene and distilled water. It was noticed that the material-removal rate was increased and the relative electrode-wear rate was decreased when distilled water was used as the dielectric, when compared to kerosene. Ho et al.¹¹ investigated the use of a powder-metallurgy (PM) compacted electrode. It was observed that the PM electrode was more alloyed than the solid electrode. The thickness of the recast layer was increased when the PM electrode and positive polarity were used.

Hascalik and Caydas¹² analysed the effects of copper, graphite and aluminum electrodes. The material-removal rate was increased in the case of the graphite electrode and the surface roughness was reduced with the aluminum electrode, compared to other electrodes. Caydas and Hascalik¹³ developed a model of the electrode wear and recast-layer thickness using the response surface methodology. It was observed that the values predicted by the model reasonably matched the experimental values. Fonda et al.¹⁴ studied the effects of the properties of Ti-6Al-4V on EDM. It was observed that the optimum duty factor was 7 % as far as the productivity and quality of an EDMed surface were concerned.

Abdulkareem et al.¹⁵ analysed the effect of cryogenic cooling on the copper-electrode wear and the surface roughness of Ti-6Al-4V. It was observed that the

electrode wear reduced remarkably and the surface finish improved due to cryogenic cooling. Bozdana et al.¹⁶ compared the performance of brass-copper tubular electrodes with copper electrodes. It was observed that the material-removal rate increased with decreased electrode wear when brass electrode was used, as compared to the copper electrode. Khan et al.¹⁷ developed a single-order mathematical model for correlating the parameters and performance characteristics during EDM. It was observed that as the peak current increased, the surface roughness increased. The combination of a high-peak current and long pulse-on time deteriorated the surface roughness. Rahman¹⁸ developed an artificial-intelligence model to predict the optimum parameters. It was found that the developed model was within the limits of tolerable errors with respect to experimental results. Kolli and Kumar¹⁹ investigated the effects of the additives added to the dielectric fluid on the EDM of a titanium alloy. Their experiments were conducted by varying the concentration of the additives and the discharge current to measure their effects on the *MRR*, *SR* and *TWR*. It was observed that the *MRR* increased with an increase in the discharge current and the surfactant concentration.

Multi-response optimisation has become an increasingly important area in the modern manufacturing industry to satisfy the customer's strict requirement for the overall quality improvement in the process and machined components, Jeyapaul et al.²⁰ and Kao et al.²¹ considered the Taguchi method and the grey relational analysis to optimize the multiple-performance characteristics of the EDM of the Ti-6Al-4V alloy. Kerosene was taken as the dielectric fluid and electrolytic copper as the electrode. It was observed that the optimized parameters increased the *MRR* by 12 %, *EWR* by 15 % and *SR* by 19 %, when applying the GRA technique. Tang and Du²² employed the multi-objective optimization technique for the grey EDM of the Ti-6Al-4V alloy. In this study, tap water was used as the dielectric fluid and tungsten copper as the electrode of a 10 mm diameter. The input process parameters included the discharge current, the open-circuit voltage, the lifting time, the pulse-on time and the pulse-off time. The machining performance parameters like the *EWR*, the *MRR* and the *SR* were estimated. The authors concluded that when the multi-optimization technique was included in the Taguchi method it increased the machining performance parameters, i.e., the *MRR* by 2 %, the *EWR* by 59 % and the *SR* by 4 %.

Lin et al.²³ applied the Grey-Taguchi technique to optimise the EDM parameters for a titanium alloy with kerosene as the dielectric fluid. The effects of the process parameters such as the peak current, the pulse-on time, the pulse-off time and the gap voltage on their performance parameters like the electrode depletion (ED), the *MRR* and the overcut were studied. It was observed from the final results that the discharge current

and the pulse-on time were the most significant parameters of the EDM using the Grey-Taguchi method. In addition, it was mentioned that the Grey-Taguchi method is highly suitable for the optimization of the ED, the *MRR* and the overcut.

In this experimental study, the dielectric fluid with an added surfactant used for the electrical discharge machining of a titanium alloy was investigated and the characteristics were optimized with the Grey-Taguchi technique. The process parameters such as the discharge current, the pulse-on time, the pulse-off time and the surfactant concentration were varied. The optimum setting of the parameters was verified through the planned experiments, conducted and analysed with the Taguchi technique. The material-removal rate (*MRR*) and the surface roughness (*SR*) were considered as the performance characteristics. Further study was carried out to observe the influence of the process parameters on the presence of the recast layer on the machined surfaces using SEM and also to observe the topography of surfaces.

2 EXPERIMENTAL SET-UP

The experiments were performed on a Formatics EDM-50 die-sinking machine mounted on a custom-built dielectric-cycling system. The electrode was fed downwards, under the DC servo control, into the workpiece. Surfactant-added (Span 20) spark-erosion 450 EDM oil was used as the dielectric fluid for the machining, used in die-sinking machines for a high machining speed and a good surface finish. The surfactant was added in a certain amount into the dielectric fluid and continuously stirred in order to maintain a uniform distribution. The homogeneously mixed dielectric fluid was pumped into the machining region using side flushing. Surfactant chemical properties are presented in **Table 1**. The experiments were conducted with a reverse-polarity electrode. A electrolytic copper with a diameter of 14 mm and a length of 70 mm was selected as the electrode. A workpiece with a length of 100 mm, a width of 50 mm and a thickness of 5 mm was employed. Each experiment was conducted for 30 min.

Table 1: Surfactant properties

Tabela 1: Lastnosti površinsko aktivnih snovi

Property	Quantity
Chemical formula	C ₁₈ H ₃₄ O ₆
Molecular weight	346.47 (g/mol)
Density	1.032 g/mL at 25 °C (L)
Flash point	> 230 °F (110 °C)
Relative index	n 20/D1.4740 (L)
HLB value	8.6
Water content	< 1.5 (%)
Acid value	4–8
Heavy metal	9.5–10.0 (L/%)
Saponification value	158–170

Prior to the machining, the workpiece and the electrode were cleaned and polished. The workpiece was firmly clamped in the vice and immersed in the dielectric fluid. The die-sinking EDM-machine experimental set-up is shown in **Figure 1** and the titanium-alloy chemical composition and properties are shown in **Tables 2** and **3**. The weight of the workpiece and the electrode tool was measured using a digital weighing balance

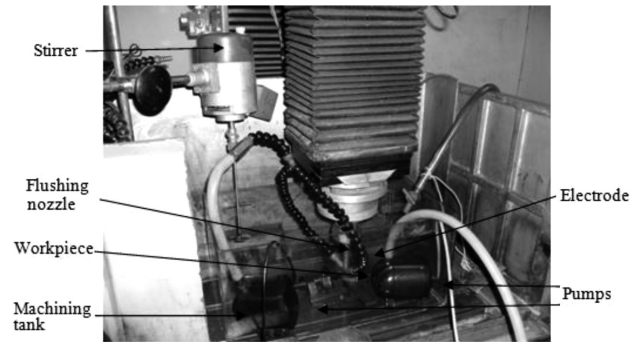


Figure 1: Modified experimental set-up

Slika 1: Spremenjen eksperimentalni sestav

Table 2: Chemical composition of Ti-6Al-4V alloy

Tabela 2: Kemijska sestava Ti-6Al-4V zlitine

Element	C	Al	V	N	O	Fe	H	Ti
%	Max. 0.014	6.07	4.02	0.0036	0.1497	0.03	0.0115	Balance

Table 3: Properties of Ti-6Al-4V alloy

Tabela 3: Lastnosti zlitine Ti-6Al-4V

Property	Values
Hardness (HRC)	32–34
Melting point (°C)	1649–1660
Density (g/cm ³)	4.43
Ultimate tensile strength (MPa)	897–950
Thermal conductivity (W/m K)	6.7–6.9
Specific heat (J/kg K)	560
Mean coefficient of thermal expansion (W/kg K)	8.6 × 10 ⁻⁶
Volume electrical resistivity (Ω cm)	170
Elastic modulus (GPa)	113–114

Table 4: Experimental settings

Tabela 4: Eksperimentalne nastavitve

Working parameters	Description
Workpiece material	Ti-6Al-4V
Size of work piece	100 × 50 × 5 mm
Electrode material	Electrolytic copper
Size of electrode	ϕ 14 × 70 mm
Electrode polarity	+ ve (reverse polarity)
Dielectric fluid	Spark erosion 450 EDM oil + surfactant
Discharge open voltage	110 V
Discharge gap voltage	65 V
Flushing pressure	0.75 MPa
Machining time	30 min

(manufactured by CITIZEN) before and after the machining to calculate the *MRR*. The surface roughness of the machined workpieces was measured using Handysurf equipment. The range of each factor was taken based on the capability of the machine and the data from the literature, and preliminary experiments were conducted to that effect.^{19,24,25} The process parameters and experimental conditions considered are listed in **Tables 4** and **5**, respectively.

Table 5: Process parameters
Tabela 5: Parametri procesa

Symbols	Control factors	Level 1	Level 2	Level 3	Units
A	Discharge current (I_p)	10	15	20	A
B	Pulse-on time (T_{on})	25	45	65	μs
C	Pulse-off time (T_{off})	24	36	48	μs
D	Surfactant concentration (SC)	0.25	0.50	0.75	g/L

2.1 Taguchi method

The Taguchi method is very effective when dealing with responses influenced by many parameters. It is a simple, efficient and systematic approach for determining optimum process parameters. It is a powerful tool for designing experiments, drastically reducing the number of experiments required for modelling and optimising the responses. Also, it saves lot of time and reduces the experimental cost. The Taguchi method is devised for process optimization and identification of the optimum levels of the process parameters for given responses.²⁶⁻²⁸ In Taguchi method, the experimental values of various responses are further transformed to the signal-to-noise (*S/N*) ratio. The response that is to be maximized is called the ‘higher the better’ response and the one that is to be minimized is called the ‘lower the better’ response. The Taguchi method uses the *S/N* ratio to measure the deviation of a response from the mean value. *S/N* ratios for ‘higher the better’ and ‘lower the better’ characteristics are calculated using Equations (1) and (2), respectively:

$$\eta = -10 \lg_{10} \left[\frac{1}{n} \sum_{i=1}^n \frac{1}{y_i^2} \right] \tag{1}$$

$$\eta = -10 \lg_{10} \left[\frac{1}{n} \sum_{i=1}^n y_i^2 \right] \tag{2}$$

where η denotes the *S/N* ratio of experimental values, y_i represents the experimental value of the i^{th} experiment and n is the total number of experiments. In the present study, the Taguchi method was applied to experimental data using the MINITAB 16 software. The number of process parameters considered under this study is four and the level of each factor is three. The degree of freedom of all four factors is eight. Hence, the L_9 (3^4) ortho-

gonal array is selected. Each condition of the experiment was repeated three times in order to reduce the noise/error effects. The quality characteristics of the *MRR* and the *SR* of the titanium alloy, evaluated for all the experimental results are listed in **Table 6**. The optimum element combinations were verified using the statistical analysis of variance (ANOVA).

2.2 Grey relational analysis (GRA)

The Grey relational analysis (GRA) was initially introduced by Dr. Deng in 1982. GRA has uncertain relations between one main factor and multi-input factors in a given system. It is an impact-measurement method of the grey-system theory.²⁹ The Taguchi method, along with GRA, is applied to optimize the EDM process parameters with multi-performance characteristics, which include the following steps:

1. Identifying the performance characteristics and EDM process parameters to be evaluated.
2. Finding out the number of levels for further EDM control parameters.
3. Selecting the suitable OA layout (orthogonal array).
4. Conducting OA-layout experiments.
5. Normalizing the experimental results, i.e., the measured features of the performance characteristics ranging from 0 to 1, usually known as the Grey relational generation.
6. Calculating the Grey relational co-efficient (ξ) based on the experimental results.
7. Obtaining the grey relational grade for selected performance parameters by averaging the corresponding grey relational coefficients.
8. Analysing the experimental results by using the Grey relational grade and statistical ANOVA.
9. Selecting the optimum level of EDM process parameters for maximizing the overall Grey relational grade.
10. Verifying the optimum EDM process parameters through the conformation test.

During the Grey relational generation, the material-removal rate (*MRR*) corresponding to the higher the better (*HB*) criterion can be expressed as:

$$x_i(k) = \frac{y_i(k) - \min y_i(k)}{\max y_i(k) - \min y_i(k)} \tag{3}$$

The surface roughness (*SR*) should follow the smaller the better (*LB*) criterion, which can be expressed as:

$$x_i(k) = \frac{\max y_i(k) - y_i(k)}{\max y_i(k) - \min y_i(k)} \tag{4}$$

However, if a definite target value is to be achieved, the original sequence is normalised in the following form:

$$x_i(k) = 1 - \frac{|y_i(k) - OB|}{\max\{\max y_i(k) - OB, OB - \min y_i(k)\}} \tag{5}$$

where *OB* is the target value.

Alternatively, the original sequence can be simply normalised using the most basic methodology, i.e., the values of the original sequence are divided by the first value of the sequence:

$$x_i(k) = \frac{y_i(k)}{y_i(1)} \tag{6}$$

where $x_i(k)$ is the value after the grey relational generation (data processing), $y_i(k)$ is the original sequence, $\max y_i(k)$ is the largest value of $y_i(k)$ for the k^{th} response, and $\min y_i(k)$ is the smallest value of $y_i(k)$, being the desired value.^{29,30} The ideal sequence of responses is $y_i(k)$ ($k = 1, 2, 3, \dots, m$).

Further, during the data pre-processing, the Grey relational coefficient is calculated to express the relationship between the ideal and actual normalised experimental results. The Grey relational coefficient can be expressed as follows:

$$\xi_i(k) = \frac{\Delta_{\min} + \zeta \Delta_{\max}}{\Delta_{0i}(k) + \zeta \Delta_{\max}} \tag{7}$$

where $\Delta_{0i}(k)$ is the deviation sequence of the reference sequence $x_0(k)$ and the comparability sequence $y_i(k)$.

$\Delta_{0i} = \|x_0(k) - x_i(k)\| = \text{difference of the absolute value between } x_0(k) \text{ and } x_i(k);$

$\zeta = \text{distinguishing coefficient } (0 \sim 1)$

$$\Delta_{\min} = \forall j^{\min} \in i \forall k^{\min} \|x_0(k) - x_i(k)\|$$

$$\Delta_{\max} = \forall j^{\max} \in i \forall k^{\max} \|x_0(k) - x_i(k)\|$$

After obtaining the Grey relational coefficient, its average is calculated to obtain the grey relational grade. The Grey relational grade (γ) is defined as follows:³¹

$$\gamma_i = \frac{1}{n} \sum_{k=1}^n \xi_i(k) \tag{8}$$

The GRA also indicates the degree of influence that the comparability sequence can exert over the reference sequence. Therefore, if a particular comparability sequence is more important than the other comparability sequence for the reference sequence, then the Grey relational grade for that comparability sequence and the reference sequence is higher than the other Grey relational grade.^{31,32} With this technique, both the comparability sequence and the reference sequence are of equal preference.

3 RESULTS AND DISCUSSION

3.1 Effects of the parameters on the MRR

Table 6 shows the values of *MRRs* and their *S/N* ratios. **Table 7** has the corresponding ANOVA results where the contributions of individual parameters are calculated. It can be observed that the discharge current with a contribution of 90.51 %, the pulse-on time with a

contribution of 7.95 % and the surfactant with a contribution of 1.01 % significantly affect the *MRR* at the 95 % confidence interval, but the pulse-off time makes an insignificant contribution to the *MRR*.

Table 6: Experimental layout $L_9(3^4)$ OA and results for *S/N* ratios for *MRRs* and *SRs*

Tabela 6: Eksperimentalna postavitev $L_9(3^4)$ OA in rezultati razmerja *S/N*, *MRR* in *SR*

Ex. no	(A)	(B)	(C)	(D)	<i>MRR</i>	<i>S/N</i> ratio	<i>SR</i>	<i>S/N</i> ratio
1	10	25	24	0.25	1.108	0.893	2.51	-7.958
2	10	45	36	0.50	1.260	2.010	2.75	-8.786
3	10	65	48	0.75	1.461	3.292	3.19	-10.076
4	15	25	36	0.75	1.755	4.887	2.65	-8.464
5	15	45	48	0.25	1.917	5.652	3.57	-11.053
6	15	65	24	0.50	2.216	6.911	3.66	-13.271
7	20	25	48	0.50	2.321	7.315	3.23	-10.184
8	20	45	24	0.75	2.514	8.008	4.22	-12.465
9	20	65	36	0.25	2.530	8.062	4.48	-13.029

Table 7: ANOVA of means for *MRRs*

Tabela 7: ANOVA sredstva za *MRR*

Parameters	Degree of freedom (DF)	Sum of squares (SS)	Mean sum of squares (MSS)	% contribution
A	2	50.835	25.417	90.51
B	2	4.466	2.233	7.95
C	2	0.292	0.146	0.53
D	2	0.571	0.285	1.01
Total	8	56.164		100.00

The main response plot of the *S/N* ratio in **Figure 2** shows that the *MRR* increases with an increase in the discharge current. It indicates that the discharge current is the leading impact factor for the *MRR*. The discharge current mainly influences the discharge density available in the discharge gap. To improve the discharge current, spark energy is increased, which results in a higher discharge density. This eventually heats the workpiece, thus increasing the *MRR* at increased discharge-current conditions.²¹ The pulse-on time controls the pulse duration of the time, for which the current is supplied to the flow per cycle. The pulse-on time increases with an increase in the *MRR*. Due to higher discharge energy on the workpiece, more material is melted and evaporated in the machined zone. During the pulse-off time, no material is removed from the workpiece as there is no current supply to the workpiece and the existing material on the machined surface of the workpiece is removed.³³

Another observation from the present experiment is that an increase in the surfactant concentration increases the *MRR*. The conductivity of the dielectric fluid is increased by adding non-polar surfactant, which results in a shorter bridging time and a higher electrical-discharge efficiency, which finally results in an increase in the *MRR*. An addition of the surfactant to the EDM oil retards the agglomeration of debris, carbon dregs due to electrostatic forces or Van der Waals forces during ma-

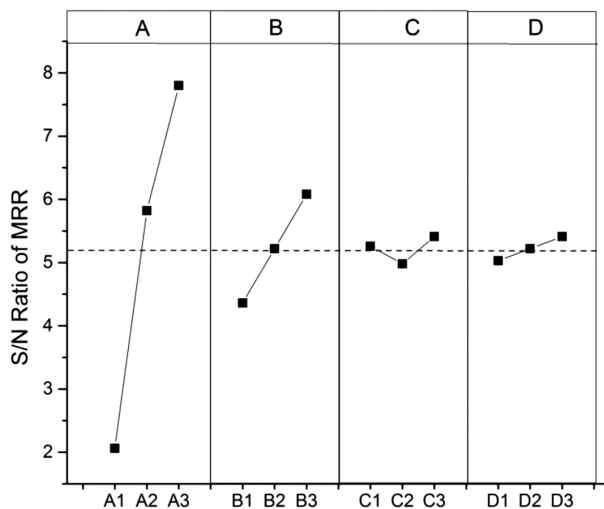


Figure 2: Main-effect plot for MRR
 Slika 2: Diagram glavnega učinka MRR

ching. After that the dielectric-fluid behaviour in the inter-electrode gap is changed, minimizing the bridge effect that leads to a better distribution of discharge energy, resulting in an overall increase in the *MRR*.^{34,35}

3.2 Effects of the parameters on the SR

The average values of the *SR* for each experiment and their respective *S/N* ratio values are presented in **Table 6**. **Figure 3** shows *SR* response curves, representing individual effects of discharge current, pulse-on time, pulse-off time and surfactant concentration. The ANOVA results tabulated in **Table 8** show the contributions of the discharge current (52.89%), the pulse-on time (39.61%) and the concentration of surfactant (6.07%), reducing the *SR* considerably. It is found that the discharge current has a leading impact on the *SR*. It is observed from **Figure 3** that an increase in the *SR* takes place with an increase in the discharge current. The explanation for

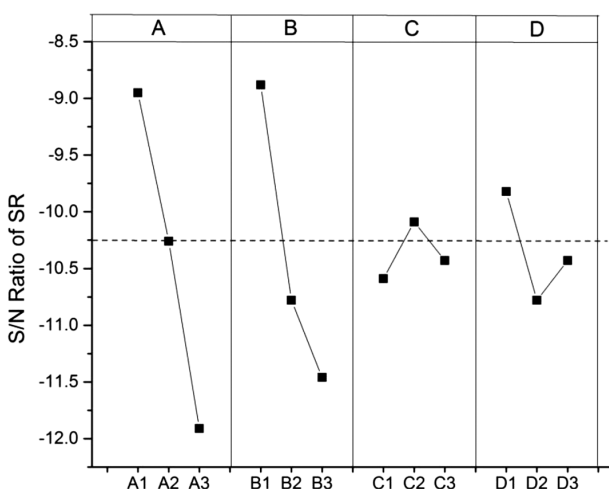


Figure 3: Main-effect plot for SR
 Slika 3: Diagram glavnega učinka SR

this can be that an increase in the discharge current causes a corresponding increase in the spark energy, which results in the formation of deeper and larger craters and which, in turn, results in an increased surface roughness. The *SR* increases with the increasing pulse-on time due to the fact that at a constant supply of current, the increase in the pulse-on time is proportional to the increase in the spark energy; subsequently, the melting boundary becomes wider and deeper and hence there is an increase in the *SR* value.³⁶

Table 8: ANOVA of means for SRs

Tabela 8: ANOVA sredstva za SR

Parameters	Degree of freedom (DF)	Sum of squares (SS)	Mean sum of squares (MSS)	% contribution
A	2	13.138	6.569	52.89
B	2	10.707	5.353	39.61
C	2	0.389	0.194	1.53
D	2	1.500	0.750	6.07
Total	8	23.878		100.00

The pulse-off time is the least important factor and shows the smallest contribution as far as the *SR* is concerned. This is due to the fact that no material is removed from the workpiece as there is no supply of the discharge current. It is observed that the pulse-off time increases with an increase in the *SR*. An increase in the surfactant concentration increases the surface roughness. This may be due to the fact that an increase in the surfactant concentration increases the dielectric conductivity, causing the spark energy to be more concentrated, which results in increased surface roughness. On the other hand, an increase in the surfactant concentration causes an increase in the dielectric conductivity and, at the same time, the dielectric fluid is mixed with the debris and tar particles accumulated in the machining gap.^{35,37,38}

3.3 Multi-response optimisation of the parameter combination for the MRR and the SR based on the GRA

Normalisation of the experimental data using Equations (3) and (4) is performed and considered in the range between 0–1. The normalised data and the deviation sequence for each of the responses are listed in **Table 9**. A higher value of the response indicates a better performance and the higher normalised values that are equal to 1 depict the best performance. Hence, all the experimental values presented in **Table 6** are substituted in Equations (3) and (4) to get the normalised values shown in **Table 9**. Typically, larger values of the *MRR* and smaller values of the *SR* are desirable for any machining operation. Thus, in the present work, the selected criterion for the *MRR* is the larger the better and for the *SR* it is the smaller the better.

These normalised-sequence values (data-processing values) are then substituted in Equation (5) and the Grey

Table 9: Sequence of each performance characteristic after data pre-processing

Tabela 9: Zaporedje vsake lastnosti po predobdelavi podatkov

Number	Deviation sequences	
	MRR (larger the better)	SR (smaller the better)
Ideal sequence	1	1
1	0	1.0000
2	0.1069	0.8782
3	0.2482	0.6548
4	0.4550	0.9289
5	0.5689	0.4619
6	0.7792	0.4162
7	0.8530	0.6345
8	0.9887	0.1320
9	1.0000	0.0000

relational coefficient with the weights of ξ MRR = 0.5 and ξ SR = 0.5 is calculation using Equation (6). The grey relational grade is calculated using Equation (7) and the responses are presented in **Table 10**. Thus, the multi-criteria optimisation problem was transformed into a single equivalent objective function using the Grey-Taguchi relational analysis. The higher the value of the Grey relational grade, the closer to the optimum value is the corresponding factor in the combination. **Table 11** suggests that the highest value of the Grey relational grade was achieved for experiment no. 4. This result indicates that the best combination of the parameters for multiple responses among the nine experiments is $A_2B_1C_2D_2$.

Table 10: Deviation sequences (Grey relational generating)

Tabela 10: Odkloni sekvenc (Grey relacijsko generiranje)

Number	Deviation sequences	
	MRR (Δ_i) 1	SR (Δ_i) 2
Ideal sequence	1	1
1	1	0.0000
2	0.8931	0.1218
3	0.7518	0.3452
4	0.5450	0.0711
5	0.4311	0.5381
6	0.2208	0.5838
7	0.1470	0.3655
8	0.0113	0.8680
9	0.0000	1.0000

A Grey-relational-response graph is shown in **Figure 4** and its ANOVA analysis is shown in **Table 12**. The most significant factors contributing to the multiple responses are the discharge current (33.79 %), the pulse-on time (34.59 %), the pulse-off time (22.28 %) and the surfactant concentration (9.34 %). The results of **Figure 4** indicate that the optimum parameter combination for these multiple responses is obtained for $A_3B_1C_2D_1$.

Table 11: Grey relational coefficient and grade for each performance

Tabela 11: Grey relacijski koeficient in dosežena stopnja za vsako izvajanje

Number	Grey relational coefficient		Grey relational grade	
	MRR	SR	Average value	Rank
1	0.3333	1.0000	0.6667	4
2	0.3589	0.8041	0.5815	6
3	0.3994	0.5916	0.4955	9
4	0.4785	0.8756	0.6770	1
5	0.5370	0.4817	0.5093	8
6	0.6937	0.4614	0.5775	7
7	0.7728	0.5777	0.6753	2
8	0.9780	0.3655	0.6717	3
9	1.0000	0.3333	0.6667	5

Table 12: ANOVA of means for Grey relational analysis

Tabela 12: ANOVA sredstva za Grey relacijsko analizo

Parameters	Degree of freedom (DF)	Sum of squares (SS)	Mean sum of squares (MSS)	% contribution
A	2	3.267	1.633	33.79
B	2	3.343	1.671	34.59
C	2	2.154	1.077	22.28
D	2	0.903	0.451	9.34
Total	8	9.667		100.00

3.4 Confirmation test

Conformation experiments were conducted for the optimum parameter combinations to verify the improvement in the responses. The results of the conformation experiments are compared with the outcome of the initial data and the predicated parameter combination based on the GRA (M. Kolli, A. Kumar¹⁹). **Table 13** shows the results of the conformation experiments using the optimum surfactant-added EDM-process parameters ob-

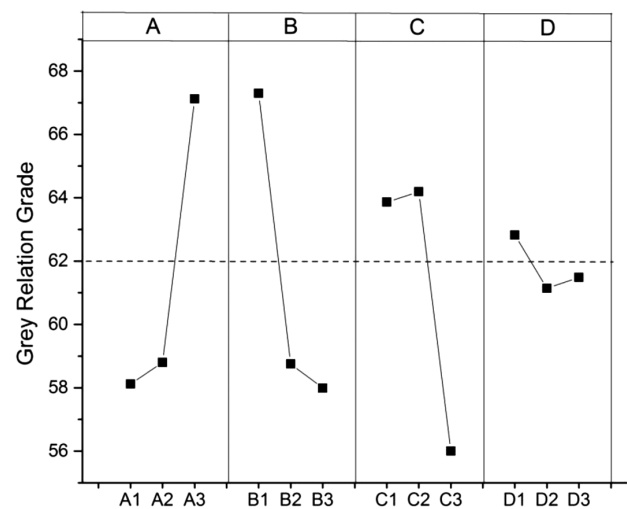


Figure 4: Process-parameter effect on Grey relational grade
Slika 4: Učinek parametrov procesa na Grey relacijski razred

tained using the GRA-Taguchi method, i.e., the initial data with combination $A_2B_1C_2D_3$ and the optimum combination $A_3B_1C_2D_1$. It is observed that the *MRR* increased from 1.755 to 2.213 mm³/min. However, the *SR* was obtained in a considerable range. The corresponding percentage improvements in the *MRR* and the *SR* are 20.69 % and 11.07 %, respectively.

Table 13: Results of the conformation experiment
Tabela 13: Rezultati preizkusa skladnosti

Observed values	Orthogonal array	Optimum combination level of machining parameters	
		Prediction	Experiment
Levels	$A_2B_1C_2D_3$	$A_3B_1C_2D_1$	$A_3B_1C_2D_1$
<i>MRR</i>	1.755	–	2.213
<i>SR</i>	2.65	–	2.98
Grey relational grade	67.70	69.18	70.45

3.5 Recast-layer thickness

The EDM process is very complex due to rapid local heating causing an increase in the local temperatures, exceeding the melting point of the material, where

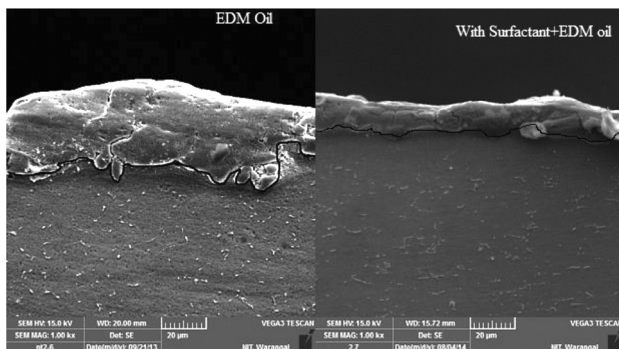


Figure 5: SEM micrographs of cross-sectional view of EDMed recast layer with surfactant and without surfactant: a) without EDM oil, b) with GRA surfactant at optimum conditions

Slika 5: SEM-posnetki prečnega prereza z EDM preoblikovano plastjo s površinsko aktivno snovjo in brez površinsko aktivne snovi: a) brez EDM olja, b) s površinsko aktivno snovjo GRA pri optimalnih pogojih

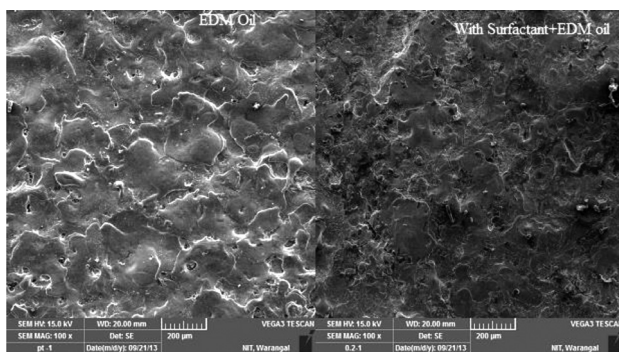


Figure 6: SEM micrographs of the machined samples: a) without surfactant and b) with the optimum GRA surfactant

Slika 6: SEM-posnetka obdelanih vzorcev: a) brez površinsko aktivne snovi in b) z optimalno površinsko aktivno snovjo GRA

melting/vaporization is followed by rapid cooling and also by random attacks of the sparks. This results in surface damage in the form of cracks and generation of high thermal stresses exceeding the fracture strength of the material. It is also observed from **Figure 5** that the *RLT* decreases significantly with the surfactant added to the dielectric fluid. The addition of the surfactant to the dielectric improves its conductivity and lowers its viscosity, resulting in a smoother flow of the dielectric in the inter-electrode gap. As a result, the increase in the dreg-removal rate leads to improved flushing conditions. At the same time, an increase in the surfactant concentration in the dielectric results in a uniform distribution of discharge energy, which lowers the amount of the heat energy penetrating into the work surface and reducing the thickness of the recast layer.

3.6 Surface micrographs

Figure 6 shows SEM micrographs of the machined surfaces with and without the surfactant in the dielectric fluid. It is observed that the EDM process produces complex surfaces covered with globules of debris, large and small melted drops, pocket marks and cracks of various sizes. During the EDM process, some particles were eroded and attached to the material surface and the molten material was expelled randomly from the machining gap. As it can be seen from the figure, the surface structure is uneven. The size of the molten drops depends on the surfactant concentration, which is associated with a low *SR* of the machined sample as shown in **Figure 6b**.

As discharge current is applied to the machining zone, equal-intensity discharge energy strikes the metal surface and a large quantity of the molten and flushed metal is suspended in the electrical-discharge gap, which results in a deterioration of the *SR*. Other reasons for a better surface finish of the machined surface are lower and smaller craters, cracks produced during the machining and generation of fewer micro-cracks because of the intense impulsive forces and stresses due to the equal-discharge energy.³⁶

4 CONCLUSION

This paper presents an effective approach for the optimisation of the surfactant-added EDM of a titanium alloy. The process parameters were the discharge current, the pulse-on time, the pulse-off time and the surfactant concentration; the multi-optimization Grey-Taguchi approach was used. Based on the experimental results of the present study, the following conclusions are drawn:

- The *MRR* at the optimum condition (i.e., $A_3B_3C_3D_3$) increases with the increase in the discharge current (20 A), the pulse-on time (65 μ s) and the surfactant concentration (0.75 g/L). As the pulse-off time increases from 24 to 36 μ s, the *MRR* decreases, while beyond 36 μ s the *MRR* increases.

- The optimum condition for the *SR* was observed at $A_1B_1C_2D_1$ having lower values of the discharge current (10 A), the pulse-on time (25 μ s) and the surfactant concentration (0.25 g/L). It was observed that the *SR* is directly proportional to the discharge current, the pulse-on time and the surfactant concentration.
- The optimum combination of the surfactant-added EDM parameters and their levels for the multi-performance characteristics of the surfactant-added EDM process are $A_3B_1C_2D_1$, the discharge current of 20 A, the pulse-on time of 25 μ s, the pulse-off time of 36 μ s and the surfactant concentration of 0.25 g/L.
- All the process parameters significantly affect the multi-performance characteristics of the surfactant-added EDM process. However, the machining performance of the *MRR* significantly increases from 1.755 mm³/min to 2.213 mm³/min. The percentage contributions of various process parameters like the discharge current, the pulse-on time, the pulse-off time and the surfactant concentration are (33.79, 34.58, 22.28 and 9.34) %, respectively.
- Fewer micro-cracks and even craters on the work-piece surface machined by EDM are formed when a surfactant is added to the dielectric fluid.

5 REFERENCES

- ¹ ASM International, Introduction to Titanium and Titanium alloys, Properties and selection: Nonferrous Alloys and Special Purpose Materials, Vol. 2, ASM Handbook, 1993
- ² E. O. Ezugwu, Z. M. Wang, Titanium alloys and their machinability – a review, Journal of Materials Processing Technology, 68 (1997) 12, 262–274, doi:10.1016/S0924-0136(96)00030-1
- ³ C. H. C. Haron, A. Jawaid, The effect of machining on surface integrity of titanium alloy Ti-6Al-4V, Journal of Materials Processing Technology, 166 (2005) 5, 188–192, doi:10.1016/j.jmatprotec.2004.08.012
- ⁴ B. H. Yan, H. C. Tsai, F. Y. Huang, The effect in EDM of a dielectric of a urea solution in water on modifying the surface of titanium, International Journal of Machine Tools Manufacture, 45 (2005) 6, 194–200, doi:10.1016/j.jmactools.2004.07.006
- ⁵ K. H. Ho, S. T. Newman, State of the art electrical discharge machining (EDM), International Journal of Machine Tools and Manufacture, 43 (2003) 13, 1287–1300, doi:10.1016/S0890-6955(03)00162-7
- ⁶ K. L. Wu, B. H. Yan, J. W. Lee, C. G. Ding, Study on the characteristics of electrical discharge machining using dielectric with surfactant, Journal of Materials Processing Technology, 209 (2009) 8, 3783–3789, doi:10.1016/j.jmatprotec.2008.09.005
- ⁷ A. S. Dukhin, P. J. Goetz, Ionic properties of so-called non-ionic surfactants in non-polar liquids, Dispersion Technology, Inc., New York 2004, 1–21
- ⁸ A. S. Dukhin, P. J. Goetz, Evolution of water-in-oil emulsion controlled by droplet-bulk ion exchange: acoustic, electroacoustic, conductivity and image analysis, Dispersion Technology, Inc., New York 2012, 2, 1–15
- ⁹ Kirk Othmer, Encyclopedia of chemical technology, Wiley, New York, 2004, 1–44
- ¹⁰ S. L. Chen, B. H. Yan, F. Y. Huang, Influence of kerosene and distilled water as dielectrics on the electric discharge machining characteristics of Ti-6Al-4V, Journal of Materials Processing Technology, 87 (1999) 5, 107–111, doi:10.1016/S0924-0136(98)00340-9
- ¹¹ S. K. Ho, D. K. Aspinwall, W. Voice, Use of powder metallurgy (PM) compacted electrodes for electrical discharge surface alloying/modification of Ti-6Al-4V alloy, Journal of Materials Processing Technology, 191 (2007) 4, 123–126, doi:10.1016/j.jmatprotec.2007.03.003
- ¹² A. Hascalik, U. Caydas, A comparative study of surface integrity of Ti-6Al-4V alloy machined by EDM and AECG, Journal of Materials Processing Technology, 190 (2007) 10, 171–180, doi:10.1016/j.jmatprotec.2007.02.048
- ¹³ U. Caydas, A. Hascalik, Modeling and analysis of electrode wear and white layer thickness in die-sinking EDM process through response surface methodology, International Journal of Advance Manufacturing Technology, 38 (2007) 9, 1148–1156, doi:10.1007/s00170-007-1162-1
- ¹⁴ P. Fonda, Z. Wang, K. Yamazaki, Y. Akutsu, A Fundamental study on Ti-6Al-4V's thermal and electrical properties and their relation to EDM productivity, Journal of Materials Processing Technology, 202 (2008) 7, 583–589, doi:10.1016/j.jmatprotec.2007.09.060
- ¹⁵ S. Abdulkareem, A. A. Khan, M. Konnch, Reducing electrode wear ratio using cryogenic cooling during electrical discharge machining, International Journal of Advance Manufacturing Technology, 45 (2009) 6, 1146–1151, doi:10.1007/s00170-009-2060-5
- ¹⁶ A. T. Bozdana, O. Yilmaz, M. A. Okka, I. H. Filz, A comparative study on fast hole EDN of Inconel 718 and Ti-6Al-4V, 5th International conference and exhibition on Design and Production of machines and dies/moulds, Kusadasi, Aydin, Turkey, 2009
- ¹⁷ Md. A. R. Khan, M. M. Rahman, K. Kadirgama, M. A. Maleque, M. Ishak, Prediction of surface roughness of Ti-6Al-4V in electrical discharge machining: a regression model, Journal of Mechanical Engineering and Sciences, 1 (2011) 9, 16–24
- ¹⁸ M. M. Rahman, Modeling of machining parameters of Ti-6Al-4V for electric discharge machining: A neural network approach, Scientific Research and Essays, 7–8 (2012) 10, 881–890, doi:10.5897/SRE10.1116
- ¹⁹ M. Kolli, A. Kumar, Experimental investigation of surfactant mixed dielectric fluid for electric discharge machining of titanium alloy, International Colloquium on Materials, Manufacturing and Metrology, ICMMM 2014, IIT Madras, Chennai, India, 2014
- ²⁰ R. Jeyapaul, P. Shahabudeen, K. Krishnaiah, Quality management research by considering multi-response problems in the Taguchi method – a review, International Journal of Advanced Manufacturing Technology, 26 (2005) 7, 1331–1337, doi:10.1007/s00170-004-2102-y
- ²¹ J. Y. Kao, C. C. Tsao, S. S. Wang, C. Y. Hsu, Optimization of the EDM parameters on machining Ti-6Al-4V with multiple quality characteristics, International Journal of Advanced Manufacturing Technology, 47 (2010) 7, 395–402, doi:10.1007/s00170-009-2208-3
- ²² L. Tang, Y. T. Du, Multi-Objective Optimization of Green Electrical Discharge Machining Ti-6Al-4V in Tap Water via Grey-Taguchi Method, Materials and Manufacturing Processes, 29 (2014) 7, 507–513, doi:10.1080/10426914.2013.840913
- ²³ M. Y. Lin, C. C. Tsao, H. H. Huang, C. Y. Wu, C. Y. Hsu, Use of the grey-Taguchi method to optimize the micro-electrical discharge machining (micro-EDM) of Ti-6Al-4V alloy, International Journal of Computer Integrated Manufacturing, 28 (2015) 6, 569–576, doi:10.1080/0951192X.2014.880946
- ²⁴ M. Kolli, A. Kumar, Parametric optimization of boron carbide powder added electrical discharge machining of titanium alloy, Applied Mechanics and Materials, 592–594 (2014), 678–683, doi:10.4028/www.scientific.net/AMM.592-594.678
- ²⁵ A. M. Nikalje, R. D. Gupta, A. Kumar, Analysis of recast layer and surface machined by Electrical Discharge Machining, International Conference on Recent Advances in Mechanical Engineering, Dr. M.G.R. Educational and Research Institute University, Chennai, India, 2012, 19–20

- ²⁶ P. J. Ross, Taguchi techniques for quality engineering, McGraw-Hill, New York 1998, 24–98
- ²⁷ D. C. Montgomery, Design and analysis of experiments, Wiley, New York 1997, 395–476
- ²⁸ S. Phadke Madhav, Quality engineering using robust design, Prentice Hall, Englewood Cliffs, New Jersey 1989, 41–229
- ²⁹ C. L. Lin, J. L. Lin, T. C. Ko, Optimization of the EDM process based on the orthogonal array with fuzzy logic and grey relational analysis method, International Journal of Advanced Manufacturing Technology, 19 (2002) 7, 271–277, doi:10.1007/s001700200034
- ³⁰ Z. A. Khan, S. Kamaruddin, A. N. Siddique, Feasibility study of use of recycled high density polyethylene and multi response optimization of injection molding parameters using combined grey relational and principal component analysis, Materials & Design, 31 (2010) 7, 2925–2931, doi:10.1016/j.matdes.2009.12.028
- ³¹ Y. Y. Yang, J. R. Shie, C. H. Huang, Optimization of dry machining parameters for high purity graphite in end milling process, Materials and Manufacturing Processes, 21 (2006) 8, 838–845, doi:10.1080/03602550600728257
- ³² G. Pankul, Z. A. Khan, Influence of slab milling process parameters on surface integrity of HSLA: a multi-performance characteristics optimization, International Journal of Advanced Manufacturing Technology, 61 (2012) 12, 859–871, doi:10.1007/s00170-011-3763-y
- ³³ A. M. Nikalje, A. Kumar, K. V. Sai Srinadh, Influence of parameters and optimization of EDM performance measures on MDN 300 steel using Taguchi method, International Journal of Advanced Manufacturing Technology, 69 (2013) 9, 41–49, doi:10.1007/s00170-013-5008-8
- ³⁴ W. Konig, L. Jorres, Aqueous solution of organic compounds as dielectric for EDM sinking, Annals of the CIRP, 36 (1987) 5, 105–109, doi:10.1016/S0007-8506(07)62564-5
- ³⁵ K. L. Wu, B. H. Yan, J. W. Lee, C. G. Ding, Study on the characteristics of electrical discharge machining using dielectric with surfactant, Journal of Materials Processing Technology, 209 (2009), 3783–3789, doi:10.1016/j.jmatprotec.2008.09.005
- ³⁶ A. Hascalik, U. Caydas, A comparative study of surface integrity of Ti–6Al–4V alloy machined by EDM and AECG, Journal of Materials Processing Technology, 190 (2007) 8, 173–180, doi:10.1016/j.jmatprotec.2007.02.048
- ³⁷ R. Ji, Y. Liu, Y. Zhang, X. Li, Research of the rosin in machining fluid for electrical discharge machining, 16th international symposium on electromachining, Shanghai, China, 19–23 April 2010
- ³⁸ Y. Zhang, Y. Liu, R. Ji, B. Cai, Y. Shen, Sinking EDM in water-in-oil emulsion, International Journal of Advanced Manufacturing Technology, 170 (2012) 11, 705–716, doi:10.1007/s00170-012-4210-4

DETERMINATION OF THE CUTTING-TOOL PERFORMANCE OF HIGH-ALLOYED WHITE CAST IRON (Ni-Hard 4) USING THE TAGUCHI METHOD

DOLOČANJE ZMOGLJIVOSTI REZALNIH ORODIJ NA MOČNO LEGIRANEM BELEM LITEM ŽELEZU (Ni-Hard 4) Z UPORABO TAGUCHI METODE

Durmuş Kir¹, Hasan Öktem¹, Mustafa Çöl², Funda Gül Koç², Fehmi Erzincanlı³

¹University of Kocaeli, Hereke Vocational School, Kocaeli, Turkey

²University of Kocaeli, Faculty of Engineering, Metallurgy and Material Engineering, Kocaeli, Turkey

³University of Düzce, Faculty of Engineering, Mechanical Engineering, Düzce, Turkey
hoktem@kocaeli.edu.tr

Prejem rokopisa – received: 2014-10-22; sprejem za objavo – accepted for publication: 2015-04-09

doi:10.17222/mit.2014.270

High-alloyed white-cast-iron materials are commonly used in the manufacturing industry due to their high wear resistance. The aim of this research is to determine the cutting tool and the optimum cutting conditions required for the metal cutting of these materials. In this study, it is proposed to determine the wear and the tool life utilizing the Taguchi optimization method when hard turning the Ni-Hard 4 material, the alloyed cast iron, with cutting tools produced with powder metallurgy (PM) and to improve the performance of the cutting tools. A series of 18 experiments were conducted on a CNC turning machine, using the cutting process parameters such as the cutting speed, the feed and the depth of cut, based on the Taguchi L_9 orthogonal design of experiments. Uncoated cutting tools were utilized to perform these experiments. PM cutting tools with WC grain sizes of 0.8 μm and 1.25 μm were selected for the hard-turning experiments. The flank wear of the cutting tools was examined with SEM. Then, the life of each cutting tool was identified based on the cutting length. The performance of the cutting tools in terms of the wear and the tool life was determined with the Taguchi method based on the obtained data. The results of this study contributed to the hard turning of the Ni-Hard 4 material that is mostly employed in the as-cast condition in the manufacturing industry due to its high hardness. The optimum cutting conditions were determined by means of the Taguchi method.

Keywords: hard turning, cutting tools, wear, Taguchi method

Močno legirano belo lito železo se uporablja v predelovalni industriji zaradi velike odpornosti proti obrabi. Namen raziskave je poiskati rezalno orodje in optimalne pogoje rezanja, potrebne za rezanje teh materialov. V študiji je predlagano, da se določi obraba in zdržljivost orodij, z uporabo Taguchi metode, optimizacija pri struženju materiala Ni-Hard 4 legiranega litega železa z rezalnimi orodji, izdelanimi po postopku metalurgije prahov (PM), da bi izboljšali zmogljivost rezalnega orodja. Serija 18-ih preizkusov, z uporabo procesnih parametrov, kot so: hitrost rezanja, podajanje in globina reza, na podlagi Taguchi L_9 ortogonalne postavitve preizkusa, so bile izvršene na CNC stružnici. Za te eksperimente so bila uporabljena rezalna orodja brez prevleke. Za preizkus težkega struženja so bila izbrana PM rezalna orodja, z velikostjo zrn WC med 0.8 μm in 1.25 μm . Obraba boka rezalnega orodja je bila preiskovana s SEM. Zdržljivost vsakega orodja je bila določena na podlagi dolžine struženja. Rezultati študije se nagibajo k težkem struženju materiala Ni-Hard 4, ki se ga večinoma uporablja v predelovalni industriji v litem stanju, zaradi velike trdote. Optimalni pogoji rezanja so bili določeni s pomočjo Taguchi metode.

Ključne besede: težko struženje, rezalna orodja, obraba, Taguchi metoda

1 INTRODUCTION

In today's industry, customers expect low costs, short machining times and competitiveness, so the developments in the material science have to involve new and flexible manufacturing technologies. Especially, some mechanical parts used in cement, concrete, machine-manufacturing and ceramic industries are very difficult to machine because of their high hardness. Based on modern technologies^{1,2} such as hard turning, milling and drilling, it is possible to cut high-alloyed cast iron materials. High-alloyed cylindrical cast-iron materials can be machined with different methods. Hard turning is preferred for these kinds of materials due a faster, low-cost and high-quality process. The hard-turning process has advantages like short set-up times, short process steps, a better surface quality, a lower wear rate

and a longer tool life. In addition, it is not necessary to use the cutting fluid for alternative metal-cutting methods.³ Several studies⁴⁻⁶ have been performed to investigate and develop the microstructure and mechanical properties of Ni-Hard 4, so far known as the high-alloyed white-cast iron. Its main alloying elements are 7–11 % Cr, 5–7 % Ni and 2.5–3.2 % C. Researchers have studied the wear resistance, heat treatments and the influence of the alloying elements on cast iron.⁴⁻⁶

The tool wear and the tool life are two important problems encountered in the hard-turning processes. There are many investigations, focused on diminishing these problems. Some of them⁷⁻⁹ try to determine the wear rate and the tool life of the AISI 52100, AISI D2 and AISI H11 steel materials during hard turning. Most frequently, experiments were carried out on cubic boron nitride (CBN) tools under various cutting conditions.

Some other researchers¹⁰⁻¹² measured the wear on CBN tools and polycrystalline cubic boron nitride (PCBN) tools after the hard turning of the AISI 52100 steel materials. They examined the performances of the cutting tools with respect to the tool life using mathematical models depending on the Taylor rule. In two group studies, the tool wear was investigated with a light microscope and SEM. Lin et al.¹³ and Khrais and Lin¹⁴ examined the hard turning of the AISI 1040 material by employing uncoated and coated WC-Co tools under wet and dry cutting conditions. They classified the wear mechanisms and types of the WC-Co tools coated with PVD AlTiN and AlCrN with a light microscope. They also determined the effects of the coatings on the wear and tool life at five different cutting speeds and $V_{Bmax} = 0.6$ mm.

Özel et al.¹⁵ and Arsecularatne et al.¹⁶ performed experiments to identify the wear, tool life and material-removal rate when hard turning the AISI D2 steel material with PCBN and ceramic tools under dry conditions. Mathematical models were developed based on the Taylor rule (the formula) to obtain the cutting conditions providing the longest tool life and the largest material-removal rate. Costes et al.¹⁷ investigated the machining of the Inconel 718 material, utilizing CBN cutting tools in wet conditions. According to this study, the adhesion and diffusion are the most dominant mechanisms for the wear in different cutting conditions.

Unlike the studies mentioned above, Thamizhmanii and Hasan¹⁸ and Yiğit et al.¹⁹ reported about experimental results predicting the tool wear and life during the hard turning of gray and spheroidal graphite cast iron with various cutting tools based on the Taguchi optimization method. Several researchers²⁰⁻²³ used the Taguchi method for different materials and cutting tools in the hard-turning process to find the optimum cutting conditions versus the minimum tool wear and to prolong the tool life. Other researchers^{24,25} were focused on the surface roughness, cutting forces and tool wear during the hard turning of high-alloy white cast iron in different cutting conditions, employing CBN inserts. Yücel and Günay²⁶⁻²⁸ conducted investigations on the machinability of the high-alloy white cast-iron material, Ni-Hard 4. They studied the tool wear, tool life, surface roughness and cutting forces during the hard turning with ceramic and CBN tools based on the Taguchi optimization method.

In this study, a total of 18 hard-turning experiments based on the L_9 orthogonal array design were performed on the Ni-Hard 4 material, which has a high wear resistance and which is not supposed to be machinable. The as-cast material was turned on a CNC machine without the cutting fluid. Uncoated cutting tools (WC-Co) with two different grain sizes (0.8 μm and 1.25 μm) were utilized in the hard-turning experiments. After each experiment, each cutting tool was investigated for the wear and specific cutting lengths with a light microscope and SEM. The optimum cutting conditions that provide

the lowest wear rate and the longest tool life were determined with the Taguchi optimization method. Thus, the aim was to develop the cutting performance of the tools for the hard turning of a cast-iron material.

2 TAGUCHI METHOD

The Taguchi method, developed by Dr. Genichi Taguchi, is a technique to determine the optimum combinations of the process conditions widely used in engineering and manufacturing industry. This method is also a powerful tool for improving and designing high-quality systems. Therefore, industries are able to reduce the time of the product development without increasing the costs.³⁰

The Taguchi method is divided into three categories: the system design, the parameter design and the tolerance design. Among these, the parameter design is the most important and used category for improving the performance characteristics without increasing the costs. The Taguchi method solves the problems by integrating the orthogonal array design, the signal to noise (S/N) ratio and the analysis of variance (ANOVA). The orthogonal array is used to create a special design determining the whole parameter space with a small number of experiments. The S/N ratio is employed to analyze the experimental results obtained from the orthogonal array design. The S/N ratio has three performance characteristics, in Equation (1) to (3) to obtain the optimum process conditions: the smaller-the-better (S/N)_{SB}, the larger-the-better (S/N)_{LB} and the nominal-the-best (S/N)_{NB}. ANOVA is applied to identify which process conditions significantly affect the performance characteristics. A confirmation test was conducted to verify the accuracy and efficiency of the desired values achieved for the optimum process conditions:³¹⁻³³

$$S/N_{SB} = \eta = -10 \lg \left[\frac{1}{n} \sum_{i=1}^n y_i^2 \right] \quad (1)$$

$$S/N_{LB} = \eta = -10 \lg \left[\frac{1}{n} \sum_{i=1}^n \frac{1}{y_i^2} \right] \quad (2)$$

$$S/N_{NB} = \eta = 10 \lg \left[\frac{\bar{y}}{s^2 y} \right] \quad (3)$$

where y_i is the observed value from the experiments, \bar{y} is the average of the observed values from the experiments, n is the number of the experiments and $s^2 y$ is the variance of y . The steps required for applying the Taguchi method are illustrated in **Figure 1**.

3 EXPERIMENTAL PROCEDURE

3.1 Materials

Cast irons are called low-alloy cast-iron materials (36-55 HRC) if the amount of carbon is below 4 % or high-alloy cast-iron materials (47-65 HRC) if this

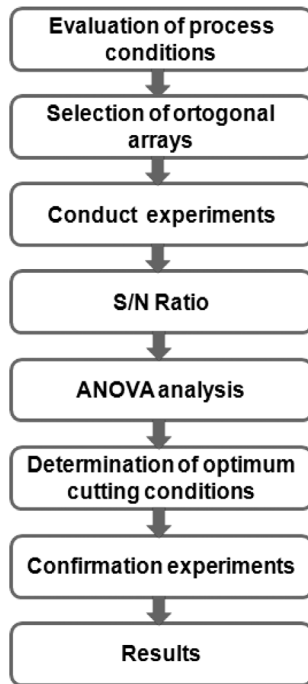


Figure 1: Application of the Taguchi method
Slika 1: Uporaba Taguchi metode

amount is above 4 %.⁴ In this study, the Ni-Hard 4 material, a high-alloy cast iron, is used to perform the turning experiments. It is a commercial name of high-alloy white cast iron, which has a high wear resistance (58-65 HRC). Its microstructure mainly includes M_7C_3 type ($M = Fe, Cr$) carbides and a martensitic matrix (**Figure 2**). It can be used in the as-cast form or after having been hardened and tempered with heat treatments. In this

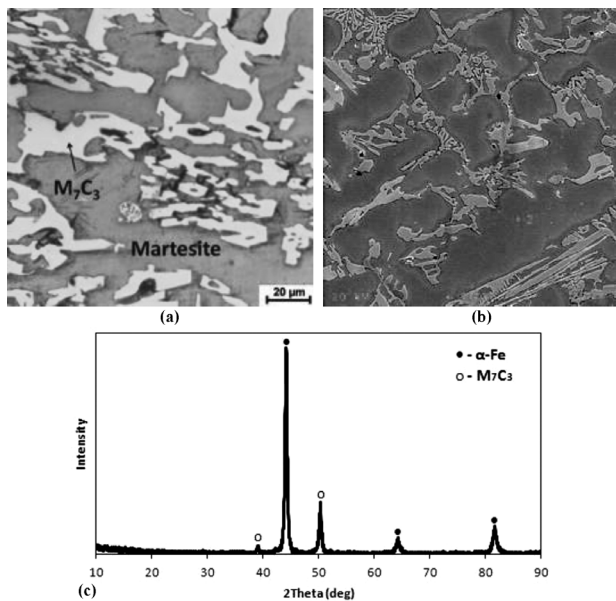


Figure 2: Light and SEM micrographs and XRD analysis of Ni-Hard 4 material

Slika 2: Svetlobni in SEM-posnetek ter XRD analiza materiala Ni-Hard 4

study, the material was used in the as-cast condition. This material is used in the as-cast condition in the cement and machine industries as well as in the mining sector.⁴ The material was melted and alloyed in a high-frequency induction furnace with a neutral pot and poured in a sand mold with a cylindrical form and solidification dimensions of $\varnothing 40 \text{ mm} \times 120 \text{ mm}$. The chemical composition of the cast material is given in **Table 1**.

Table 1: Chemical composition of Ni-Hard 4 alloy (in mass fractions, w/%)

Tabela 1: Kemijska sestava zlitine Ni-Hard 4 (v masnih deležih, w/%)

Elements	ASTM A 532	Ni-Hard 4 (sample)
Carbon (C)	2.6–3.2	2.89
Silicon (Si)	1.8–2	1.43
Chrome (Cr)	7–11	9.22
Nickel (Ni)	4.5–6.5	6.15
Molybdenum (Mo)	0–0.4	1.03
Manganese (Mn)	0.4–0.6	0.91
Phosphor (P)	max. 0.06	0.25
Sulfur (S)	max. 0.10	0.16
Iron (Fe)	Balance	Balance

The cross-section of the machined material was prepared for microstructural examinations. It was etched with the Beraha II solution for about 5 s and then examined with a Zeiss light microscope and a Jeol JSM 6060 SEM as illustrated in **Figures 2a** and **2b**. The components of the microstructure were determined with a RigakuSA HS3 XRD diffractometer. The XRD analysis result is given in **Figure 2c**.

The microstructure of the Ni-Hard 4 material consists of a martensitic matrix and M_7C_3 primary-eutectic carbides (**Table 2**). The primary-carbide rate in the microstructure was estimated to be about 20 %. The hardness of the material was measured as 55 HRC with a Zwick/ZHR instrument.

Table 2: EDX microanalysis results for points 1 and 2, (in mass fractions, w/%)

Tabela 2: Rezultati EDX-mikroanalize za točki 1 in 2 (v masnih deležih, w/%)

Analysis	C	Si	Cr	Fe	Ni	Mo	W
1 – (M_7C_3)	4.3	–	28.7	66.9	–	–	–
2 – (Martensite)	1.6	1.9	4.0	82.7	5.6	1.9	2.1

3.2 Cutting conditions

A series of 18 hard-turning experiments based on the Taguchi L_9 orthogonal array design were carried out on the Ni-Hard 4 material using nine different tools without the cutting fluid. Initially, cutting conditions were selected on the basis of the user experience and tool catalogues. In this study, the speed (n), the chip thickness (h_{ex}) and the feed rate (V_f) were calculated with Equation (4) to (6) utilizing the cutting conditions shown in **Table 3**:

$$n = \frac{1000V_c}{\pi D_c} \tag{4}$$

$$h_{ex} = f_n x \sin K_r \tag{5}$$

$$V_f = f_n x n \tag{6}$$

where;

n = spindle speed, (rev/min)

D_c = workpiece diameter, (mm)

V_c = cutting speed, (m/min)

f_n = feed rate, (mm/rev)

K_r = entering angle, (45°)

h_{ex} = maximum chip thickness, (mm)

a_p = depth of cut, (mm)

Nine experiments were performed for each cutting tool (**Table 3**) and the wear of the cutting tools was examined with a light microscope and SEM. In addition, the performances of the cutting tools were examined in terms of the powder-grain size. In these experiments, a Johnford CNC turning machine, 3500 min^{-1} , 12.5 kW, with a feed rate of 2500 mm/min was employed. **Figure 3** shows four different steps applied during the hard-turning experiments.

Table 3: Hard-turning process parameters

Tabela 3: Parametri procesa trdega struženja

Levels	Cutting conditions		
	V_c (m/min)	f_n (mm/rev)	a_p (mm)
1	100	0.05	0.1
2	150	0.075	0.2
3	200	0.1	0.3

Table 4: Cutting tools for turning experiments

Tabela 4: Rezalna orodja za preizkus struženja

Cutting tools (Uncoated)	Tool code	
	BS 710	BS 610
Grain size (WC)	($0.8 \mu\text{m}$)	($1.25 \mu\text{m}$)

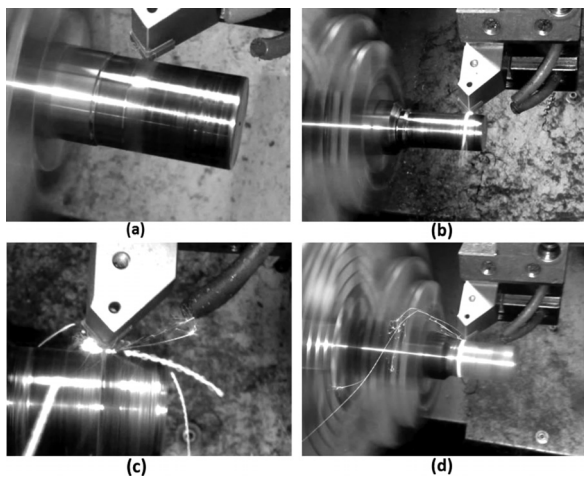


Figure 3: Hard-turning experiments

Slika 3: Preizkusi trdega struženja

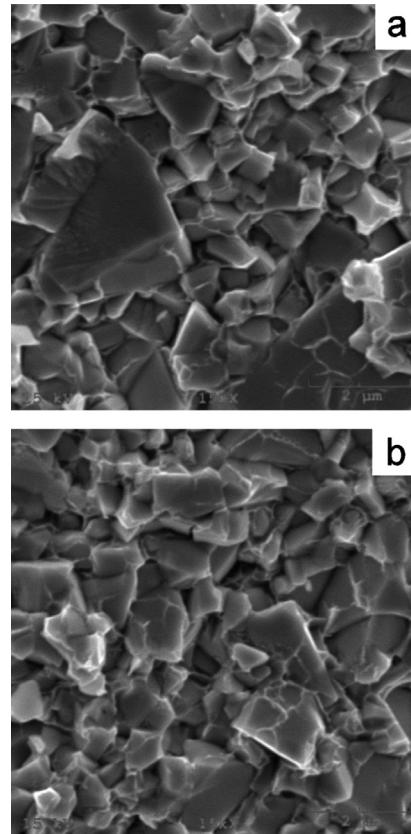


Figure 4: SEM comparison of grain sizes for cutting tools: a) BS 610, b) BS 710

Slika 4: SEM-primerjava velikosti zrn rezalnih orodij: a) BS 610, b) BS 710

The cutting tools given in **Table 4** are hard-metal tools with two different WC grain sizes, sintered with cobalt (Co), (94 % WC and 6 % Co). These tools were broken to observe the grain-size distributions and bonding characteristic between WC and Co. Broken surfaces were examined at a single magnification as shown in **Figures 4a** and **4b**. **Figure 4** shows that the cutting tool with fine grains ($0.8 \mu\text{m}$) is more homogenous than the one with coarse grains ($1.25 \mu\text{m}$). In addition, the porosity rate between the WC grains in **Figure 4a** is higher than the one in **Figure 4b**. Cutting-tool manufacturers usually use a certain amount (5 % – 10 %) of course grains added to fine grains to improve the cutting-tool performance.^{13,14}

3.3 Wear measurement of the cutting tools

The wear was investigated with a light microscope and SEM after each experiment planned with the L_9 orthogonal array design by stopping the CNC turning machine at (250, 500, 750 and 1000) mm. The numerical value of the wear rate was calculated using the CLEMEX program equipped with a light microscope. The wear rate was not allowed to exceed $V_B = 0.6 \text{ mm}$ in accordance with the ISO standards. Moreover, the wear rate for the largest cutting length (1000 mm) and the

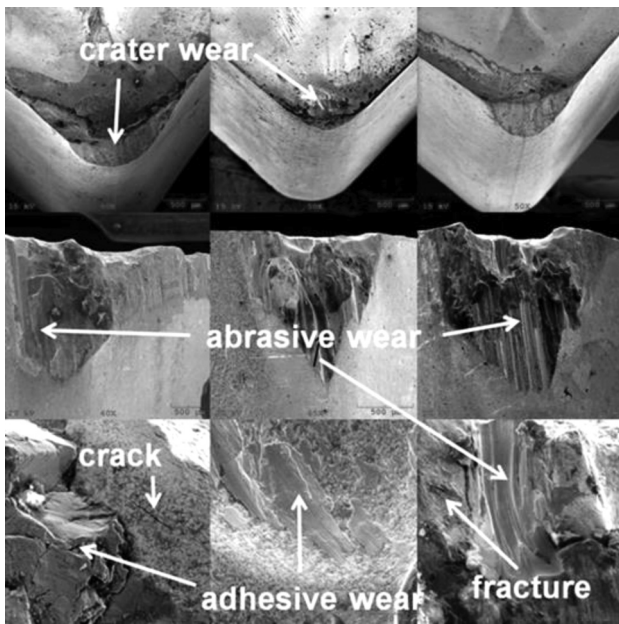


Figure 5: SEM micrographs of wear surfaces (BS 710)
 Slika 5: SEM-posnetki obrabe na površini (BS 710)

shortest tool life were used to determine the optimum cutting conditions with the Taguchi optimization method.

The tool wear at the edges of the BS 610 and BS 710 cutting tools for a depth of cut of (0.1–0.2–0.3) mm, at a cutting speed of 100 m/min and a cutting length of 250 mm is shown in Figures 5 and 6, respectively. The abrasive wear increases as the depth of cut increases. Also, it can be observed that some material is adhered to the cutting edge (the adhesive wear) throughout the hard-turning experiments. In addition, some partial fractures and micro-cracks occurred due to the forces

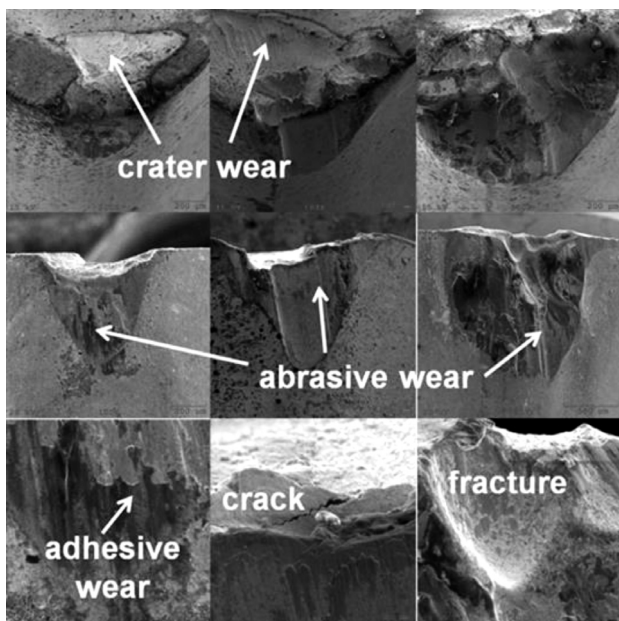


Figure 6: SEM micrographs of wear surfaces (BS 610)
 Slika 6: SEM-posnetki obrabe na površini (BS 610)

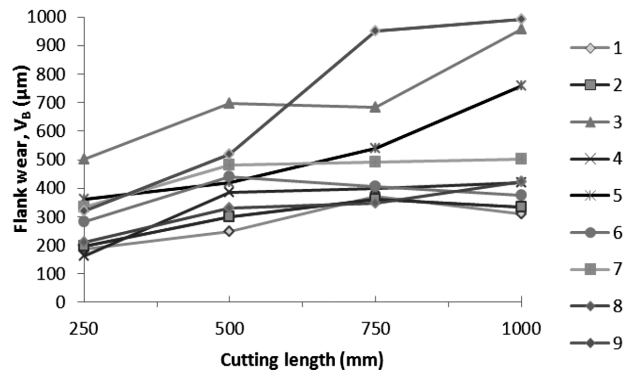


Figure 7: Change in the wear rate versus the cutting length (BS 710)
 Slika 7: Sprememba hitrosti obrabe v odvisnosti od dolžine rezanja (BS 710)

affecting the cutting edge. These failures indicate that the cutting tool was forced considerably during the hard-turning process.

4 ANALYSIS OF EXPERIMENTAL RESULTS AND DISCUSSION

4.1 Wear and tool life

Figure 7 displays the flank-wear values obtained with nine experiments conducted with the BS 710 cutting tool. In Figure 7, the smallest flank wear is obtained for experiment 1 ($V_c = 100$ m/min, $f_n = 0.05$ mm/rev, $a_p = 0.1$ mm) whereas the largest flank wear is observed for experiment 3 ($V_c = 200$ m/min, $f_n = 0.05$ mm/rev, $a_p = 0.3$ mm).

Figure 8 illustrates the flank-wear values obtained with nine experiments conducted with the BS 610 cutting tool. In Figure 8, the smallest flank wear is obtained for experiment 8 ($V_c = 150$ m/min, $f_n = 0.1$ mm/rev, $a_p = 0.1$ mm) whereas the largest flank wear is observed for experiment 3 ($V_c = 200$ m/min, $f_n = 0.05$ mm/rev, $a_p = 0.3$). It can be seen that the flank wear of each type of the cutting tools generally increases with the increasing cutting length. On the other hand, for experiment 1, the

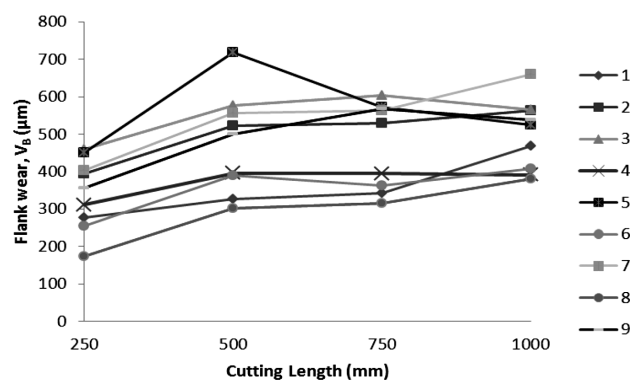


Figure 8: Change in the wear rate versus the cutting length (BS 610)
 Slika 8: Sprememba hitrosti obrabe v odvisnosti od dolžine rezanja (BS 610)

flank wear of the BS 610 cutting tool is greater than that of the BS 710 cutting tool.

4.2 Taguchi analysis

The Taguchi method integrates orthogonal arrays, the S/N ratio and ANOVA to analyze and evaluate numerical results.^{29–32} The hard-turning experiments were performed according to L_9 (3^3) orthogonal arrays. L_9 (3^3) has 9 rows corresponding to the number of hard-turning experiments (8 degrees of freedom) with 8 columns at three levels. The hard-turning experiments based on the Taguchi orthogonal array design were conducted by means of three cutting conditions, namely, the cutting speed (V_c), the feed (f_n) and the depth of cut (a_p). The wear values obtained with the experiments and their S/N ratios calculated with Equation (1) for each of the two cutting tools (BS 710 and BS 610) are given in **Table 5**.

Table 5: S/N ratios for the wear values

Tabela 5: Razmerje S/N pri vrednosti obrabe

Experiment number	Wear results (μm)		S/N ratios (dB)	
	(BS 710)	(BS 610)	(BS 710)	(BS 610)
1	188.2	276.6	-45.49	-48.84
2	197.2	394.1	-45.90	-51.91
3	501.3	459.7	-54.0	-53.25
4	163.7	311.4	-44.28	-49.87
5	361.6	449.4	-51.16	-53.05
6	284.0	255.5	-49.07	-48.15
7	332.5	402.1	-50.44	-52.09
8	211.6	174.5	-46.51	-44.84
9	319.4	355.9	-50.09	-51.03

In order to determine the optimum turning conditions providing the smallest wear value, it is required to calculate the average-response values for the cutting conditions at different levels. For this purpose, an average-response table involving the wear values and their S/N ratios is created in **Table 6**. The values in the average-response table are calculated by averaging the S/N ratios for each cutting condition at different levels for experiments 1 to 9.

Table 6: Average-response table for the wear values

Tabela 6: Tabela povprečnega odgovora pri vrednosti obrabe

Cutting conditions	Parameter levels					
	BS 710			BS 610		
	I	II	III	I	II	III
V_c	-46.74	-47.86	-51.05	-50.26	-49.93	-50.81
f_n	-48.46	-48.17	-49.01	-51.33	-50.36	-49.32
a_p	-47.02	-46.76	-51.87	-47.27	-50.94	-52.80

In this study, the ANOVA was performed using Minitab to identify which three cutting conditions significantly affect the wear.³³ **Table 7** shows the ANOVA results for the wear. In **Table 7**, the statistical significance of three cutting conditions for the wear was evaluated by the F-test. The F -value (tabulated) at the 95 % confi-

dence interval controlling the three cutting conditions is $F_{0.05, 2, 8} = 4.46$. The percentage contributions of the three cutting conditions to the wear for the two cutting tools are given in **Table 6**. As can be seen from this table, the most significant cutting condition is the depth of cut (a_p).

Table 7: ANOVA analysis results

Tabela 7: ANOVA analiza rezultatov

Cutting conditions	Percentage contribution (%)	
	BS 710	BS 610
V_c	35.238	1.56
f_n	1.13	9.1
a_p	62.8	84.7

The optimum cutting conditions providing the smallest wear value were determined by selecting the largest S/N ratios for each cutting condition at three levels as given in **Table 6**. Also, the final confirmation test for the two cutting tools was carried out in the optimum cutting conditions providing the smallest wear value. Each confirmation test was repeated at least three times. The improvement rates were calculated by comparing the results of the confirmation test and the initial values in **Table 8**. Thus, the optimum cutting conditions providing the best cutting-tool performance were determined with the Taguchi analyses without carrying out a high number of hard-turning experiments.

Table 8: Confirmation tests

Tabela 8: Preizkusi za potrditev

Cutting tools	Optimum cutting conditions	Initial values (dB)	Calculated values (dB)	Confirmation tests (dB)	Improvements (%)
BS 710	$V_c(\text{I}), f_n(\text{II}), a_p(\text{II})$	-45.686	-44.565	-44.280	3.2
BS 610	$V_c(\text{II}), f_n(\text{III}), a_p(\text{I})$	-50.554	-45.853	-46.510	8.7

5 CONCLUSIONS

In this study, hard-turning experiments were conducted on the Ni-Hard 4 material utilizing two different cutting tools (BS 610 and BS 710) under dry conditions. The following results were obtained:

- The optimum cutting entering angle is selected as $K_r = 45^\circ$ by trying a few experiments.
- During the hard-turning experiments performed with the BS 610 and BS 710 cutting tools, the wear rate on the cutting edge increases as the cutting length, the cutting depth and the cutting speed increase.
- At a cutting speed of 200 m/min, for experiments 3, 6 and 9, the wear rate of the BS 710 cutting tool is larger than that of BS 610. This situation shows that, in the case of excessive force, WC coarse grains display a better performance than fine grains.
- At a low cutting speed (100 m/min), the BS 710 cutting tool has a better performance than BS 610. For a

longer tool life, hard turning should be performed at a low cutting speed and with fine-grain cutting tools.

- The optimum cutting conditions providing the lowest wear and the longest tool life were determined by means of the Taguchi analyses. Improvements of 3.2 % and 8.7 % were obtained for both cutting tools, respectively.
- According to the ANOVA analyses, the depth of cut (a_p) is the most important turning parameter for both cutting tools.
- Finally, the machinability of the material, which is very difficult to cut and whose cutting conditions are not widely known, were examined experimentally and numerically.
- In future, the cutting forces, the tool wear and the surface texture will be investigated by measuring the cutting forces and surface roughness in turning or milling processes.

Acknowledgements

The authors would like to thank Uğur Yücel at the University of Kocaeli and ARMEKSAN, Machine Part Industry Corporation. This study was supported by the Scientific Research Project Unit of the Kocaeli University (KOU-BAP-2012/72).

6 REFERENCES

- ¹ G. Boothroyd, W. Knight, *Fundamentals of machining and machine tools*, Marcel Dekker Inc., USA 1989, 129–151
- ² M. Akkurt, *Machine Tools, Metal cutting principles and technology*, Birsan Publication, Istanbul 1985, 49–60
- ³ W. König, G. Ackershoff, R. Komanduri, H. K. Tönshoff, *Machining of hard materials*, Annual CIRP, 3 (1984), 417–427
- ⁴ J. M. Radzikowska, *Metallography and microstructures of cast iron*, ASM handbook 9, ASM international, Materials Park, Ohio, USA 2006, 555–588
- ⁵ R. Correa, A. Bedolla-Jacuinde, J. Zuno-Silva, E. Cardoso, I. Mejía, Effect of boron on the sliding wear of directionally solidified high-chromium white irons, *Wear*, 267 (2009), 495–504, doi:10.1016/j.wear.2008.11.009
- ⁶ C. Xiang, L. Yanxiang, Effect of heat treatment on microstructure and mechanical properties of high boron white cast iron, *Materials Science and Engineering A*, 528 (2010), 770–775, doi:10.1016/j.msea.2010.09.092
- ⁷ I. Uçun, K. Aslantaş, Investigation of cutting performance of solid carbide tool in turning hardened AISI 52100 tool steel, 5th International Advanced Technology Symposium, IATS'09, Karabük, Turkey, 2009, 200–255
- ⁸ Y. K. Chou, C. J. Evans, M. M. Barash, Experimental investigations on CBN turning of hardened AISI 52100 steel, *Journal of Materials Processing Technology*, 124 (2002), 274–283, doi:10.1016/S0924-0136(02)00180-2
- ⁹ G. Poulachon, B. P. Bandyopadhyay, I. S. Jawahir, S. Pheulpin, E. Seguin, Wear behavior of CBN tools while turning various hardened steels, *Wear*, 256 (2004), 302–310, doi:10.1016/S0043-1648(03)00414-9
- ¹⁰ G. Poulachon, A. Moisan, I. S. Jawahir, Tool-wear mechanisms in hard turning with polycrystalline cubic boron nitride tools, *Wear*, 250 (2001), 576–586, doi:10.1016/S0043-1648(01)00609-3
- ¹¹ Y. Huang, T. G. Dawson, Tool crater wear depth modeling in CBN hard turning, *Wear*, 258 (2005), 1455–1461, doi:10.1016/j.wear.2004.08.010
- ¹² Y. Huang, S. Y. Liang, Modeling of CBN tool crater wear in finish hard turning, *International Journal of Advanced Manufacturing Technology*, 24 (2004), 632–639, doi:10.1007/s00170-003-1744-5
- ¹³ Y. J. Lin, A. Agrawal, Y. Fang, Wear progressions and tool life enhancement with AlCrN coated inserts in high-speed dry and wet steel lathing, *Wear*, 264 (2008), 226–234, doi:10.1016/j.wear.2007.03.007
- ¹⁴ S. Khrais, Y. J. Lin, Wear mechanisms and tool performance of TiAlN PVD coated inserts during machining of AISI 4140 steel, *Wear*, 262 (2007), 64–69, doi:10.1016/j.wear.2006.03.052
- ¹⁵ T. Özel, Y. Karpat, L. Figueira, J. P. Davim, Modeling of surface finish and tool flank wear in turning of AISI D2 steel with ceramic wiper inserts, *Journal of Materials Processing Technology*, 189 (2007), 192–198, doi:10.1016/j.jmatprotec.2007.01.021
- ¹⁶ J. A. Arsecularatne, L. C. Zhang, C. Montross, P. Mathew, On machining of hardened AISI D2 steel with PCBN tools, *Journal of Materials Processing Technology*, 171 (2006), 244–252, doi:10.1016/j.jmatprotec.2005.06.079
- ¹⁷ J. P. Costes, Y. Guillet, G. Poulachon, M. Dessoly, Tool-life and wear mechanisms of CBN tools in machining of Inconel 718, *International Journal of Machine Tools and Manufacture*, 47 (2007), 1081–1087, doi:10.1016/j.ijmachtools.2006.09.031
- ¹⁸ S. Thamizhmani, S. Hasan, Analyses of roughness, forces and wear in gray cast iron, *Journal of Achievements in Materials and Manufacturing Engineering*, 17 (2006), 401–404
- ¹⁹ R. Yiğit, F. Findik, E. Çelik, Performance of multilayer coated carbide tools when turning cast iron, *Turkish Journal of Engineering and Environmental Sciences*, 33 (2009), 147–157, doi:10.3906/muh-0904-6
- ²⁰ Y. Şahin, Comparison of tool life between ceramic and cubic boron nitride (CBN) cutting tools when machining hardened steels, *Journal of Materials Processing Technology*, 209 (2009), 3478–3489, doi:10.1016/j.jmatprotec.2008.08.016
- ²¹ W. H. Yang, Y. S. Tarng, Design optimization of cutting parameters for turning operations based on the Taguchi method, *Journal of Materials Processing Technology*, 84 (1998), 122–129, doi:10.1016/S0924-0136(98)00079-X
- ²² A. Haşçalık, U. Çaydaş, Optimization of turning parameters for surface roughness and tool life based on the Taguchi method, *International Journal of Advanced Manufacturing Technology*, 38 (2008), 896–903, doi:10.1007/s00170-007-1147-0
- ²³ B. L. Gopalsamy, B. Mondal, S. Ghosh, Optimisation of machining parameters for hard machining: Grey relational theory approach and ANOVA, *International Journal of Advanced Manufacturing Technology*, 45 (2009), 1068–1086, doi:10.1007/s00170-009-2054-3
- ²⁴ J. Zhou, M. Andersson, Effects of lubricant condition and tool wear in hard turning of novel-abrasion-resistance (N-AR) cast iron, *Materials and Manufacturing Processes*, 22 (2007), 865–870, doi:10.1080/10426910701448925
- ²⁵ E. Sayit, K. Aslantaş, A. Çiçek, Tool wear mechanism in interrupted cutting conditions, *Materials and Manufacturing Processes*, 24 (2009), 476–483, doi:10.1080/10426910802714423
- ²⁶ E. Yücel, M. Günay, Modeling of cutting force when turning high-alloyed white cast irons (Ni-Hard 4), 3rd National Metal Cutting Symposium, Ankara, Turkey, 2012, 489–495
- ²⁷ M. Günay, E. Yücel, Application of Taguchi method for determining optimum surface roughness in turning of high-alloy white cast iron, *Measurement*, 46 (2013), 913–919, doi:10.1016/j.measurement.2012.10.013
- ²⁸ E. Yücel, M. Günay, Modelling and optimization of the cutting conditions in hard turning of high alloy white cast iron (Ni-Hard 4), *Journal of Mechanical Engineering Science*, 227 (2013), 2280–2290, doi:10.1177/0954406212471755

- ²⁹ H. Öktem, Optimum process conditions on shrinkage of an injected-molded part of DVD-ROM cover using Taguchi robust method, *International Journal of Advanced Manufacturing Technology*, 61 (2012), 519–528, doi:10.1007/s00170-011-3750-3
- ³⁰ G. Taguchi, *Introduction to quality engineering*, Asian Productivity Organization, Tokyo 1986
- ³¹ G. Taguchi, S. Chowdhury, S. Taguchi, *Robust engineering*, 1st Ed., McGraw-Hill, New York, USA 2000
- ³² W. Yuin, W. Alan, *Taguchi methods for robust design*, 1st Ed., ASME Press, New York 2000
- ³³ *Minitab User Manual, Release 15, Making data analysis easier*, Minitab Corp., McGraw-Hill Companies, Massachusetts, USA 2007

USE OF THE ABI TECHNIQUE TO MEASURE THE MECHANICAL PROPERTIES OF ALUMINIUM ALLOYS: EFFECT OF CHEMICAL COMPOSITION ON THE MECHANICAL PROPERTIES OF THE ALLOYS

UPORABA TEHNIKE ABI ZA MERJENJE MEHANSKIH LASTNOSTI ALUMINIJEVIH ZLITIN: VPLIV KEMIJSKE SESTAVE NA MEHANSKE LASTNOSTI ZLITIN

Maxim Puchnin¹, Oleksandr Trudonoshyn^{1,2}, Olena Prach^{1,2,3}

¹Czech Technical University in Prague, Karlovo náměstí 13, 12135 Prague 2, Czech Republic

²National Technical University of Ukraine "KPI", Polytechnichna str. 35, Build. 9, 03056 Kiev, Ukraine

³Technische Universität Darmstadt, Karolinenplatz 5, 64289 Darmstadt, Germany
maxim.puchnin@fs.cvut.cz

Prejem rokopisa – received: 2014-12-08; sprejem za objavo – accepted for publication: 2015-03-10

doi:10.17222/mit.2014.294

The effects of the chemical composition on the microstructure and mechanical properties were investigated using automated ball-indentation tests, scanning electron microscopy and energy dispersive X-ray analysis. It was observed that the mechanical properties change with the presence of the eutectic and varying excess content of elements. In this work, the automated-ball-indentation (ABI) technique was compared with the standard mechanical tests. The ABI method is based on controlled multiple indentations into a polished surface by a spherical indenter under load. The indentation depth is progressively increased to the maximum, user-specified limit, with intermediate partial unloading. This technique allows to measure the yield strength, stress-strain curve, strength coefficient and strain-hardening exponent. For all these test materials and conditions, the ABI-derived results were in very good agreement with those obtained with the conventional, standard test methods.

Keywords: Al-alloys, microstructure, mechanical properties, ABI tests

Vpliv kemijske sestave na mikrostrukturo in mehanske lastnosti je bil preiskovan z avtomatskim preizkusom vtiskovanja kroglice, z vrstično elektronsko mikroskopijo in z energijsko disperzijsko rentgensko analizo. Opaženo je bilo, da se mehanske lastnosti spreminjajo s prisotnostjo eitektika in s spreminjanjem vsebnosti presežnih elementov. V prispevku je bila preverjena metoda avtomatskega vtiskovanja kroglice (ABI) z običajnimi mehanskimi preizkusi. ABI metoda temelji na kontroliranih večkratnih vtiskih kroglastega vtiskača v polirano površino. Globina vtiskov progresivno narašča do maksimalne, z uporabnikom določene meje, s takojšnjo vmesno razbremenitvijo. Ta tehnika omogoča merjenje meje plastičnosti, krivulje napetost-raztezek, koeficienta trdnosti in eksponenta napetostnega utrjevanja. Za vse pogoje preizkušanja materiala so dobljeni ABI rezultati skladni z rezultati, dobljenimi iz običajnih metod preizkušanja.

Ključne besede: Al-zlitine, mikrostruktura, mehanske lastnosti, ABI preizkusi

1 INTRODUCTION

The growing demand for more fuel-efficient and ecological vehicles to reduce energy consumption and air pollution is a challenge for the automotive and aircraft industries. The characteristic properties of aluminum, high strength-to-weight ratio, good formability, good electrical mass conductivity, unique corrosion behavior and recycling potential make it the essential material for the applications such as fuel-efficient transportation vehicles, building construction, and food packaging.¹

Si in Al-alloys improves the corrosion resistance of the alloys. An addition of Si to composites significantly affects the diffusion of Mg and Si in an Al liquid. Also, when Si is used together with Mg, they create heat-treatable alloys. An extra Si content in Al-Mg₂Si-Si composites leads to an increase of the solidification range. The aspect ratio of the eutectics and the size of primary

particles decrease with the increasing Si content in Al-Mg₂Si composites.^{2,3}

Mg in Al-alloys increases the weldability, improves the corrosion resistance and decreases the weight of alloys. An addition of Mg to aluminium alloys can increase the hardness and strength of the materials.⁴ An extra amount of Mg in the Al-Mg₂Si system moves the eutectic point to a lower Mg₂Si concentration. Several authors⁵⁻⁸ maintain that an excess of Mg in Al-Mg₂Si alloys can promote the formation of primary Mg₂Si. It also shows that increasing the Mg addition decreases the volume fraction of the α -Al matrix and increases the volume fraction of the Al-Mg₂Si eutectic.

Fe is the most common impurity found in Al. Fe reduces the grain size of an alloy, but decreases its hardness and strength, and also increases the brittleness. Mn improves the corrosion resistance and decreases the negative effect of Fe.^{9,10}

Table 1: Nominal composition of alloys, in mass fractions (w%) (Al-bal.)

Tabela 1: Nominalna sestava zlitin, v masnih deležih (w%) (Al-ostalo)

Alloys	Mg	Si	Mn	Fe	Ti	Cu	Zn	Comment
AlMg6Mn (M3)	6.0	0.4	0.6	0.3	0.1	0.1	0.1	Al-1Mg ₂ Si-5Mg
AlMg7SiMn (MS1)	7.0	1.0	0.6	0.02	0.1	0.05	0.05	Al-3Mg ₂ Si-5Mg
AlMg7Si2Mn (MS2)	7.0	2.0	0.6	0.02	0.1	0.05	0.05	Al-6Mg ₂ Si-3Mg
AlMg5Si2Mn (MS9)	5.0	2.0	0.6	0.02	0.1	0.05	0.05	Al-6Mg ₂ Si-1Mg
AlMg7Si3Mn (MS3)	7.0	3.0	0.6	0.02	0.1	0.05	0.05	Al-9Mg ₂ Si-1Mg
AlMg7Si4Mn (MS4)	7.0	4.0	0.6	0.02	0.1	0.05	0.05	Al-10.5Mg ₂ Si-0.5Si
AlMg7Si5Mn (MS5)	7.0	5.0	0.6	0.02	0.1	0.05	0.05	Al-10.5Mg ₂ Si-1.5Si
AlSi7Mg (S1)	0.3	6.9	0.02	0.2	-	0.05	0.05	Al-7Si

The main objective of this paper is to investigate the influence of the chemical composition on the mechanical properties and structures of Al-alloys.

The determination of the mechanical properties of materials with non-conventional techniques has been an

active area of research for a long time. Among some non-destructive methods for determining the mechanical properties of materials, a semi-destructive type of testing, called automated ball indentation (ABI), has been developed. The automated-ball-indentation technique is used to measure material properties when a tensile test cannot be applied: in welded parts with a continuous property variation, in brittle materials with an unstable crack growth during preparation and specimen testing, in samples with a high porosity and in the parts of the present structural use.^{11,12}

2 MATERIALS AND METHODS

The chemical compositions of the evaluated alloys are shown in **Table 1** and **Figure 1**.

All the alloys were prepared in an electric-resistance furnace using graphite crucibles. High-purity Al (A99.997), AlMg50, AlSi25 and AlMn26 were used as master alloys. The melt with a temperature of 720 °C ± 5 °C was being degassed under an argon atmosphere for 10 min.

Hardness was measured using a Brinell-hardness testing machine (EMCOTEST M4C) with a ball diameter of 2.5 mm and a load of 62.5 kg; where the load time was 10 s. Microhardness tests were performed on a polished non-etched specimens using a LECO M-400-G1 microhardness tester, HV0.05 with the standard indentation time.

Tensile tests were performed using a testing machine (INSTRON 5582, USA) according to the EN ISO 6892-1 standard. Tensile samples were also prepared according to this standard.

Indentation tests were performed with a special device (patent CZ 304637 B1), which is capable, due to its design, of continuous recording of the load and indentation depth of the used indenter. The system includes a recording device, an analog-to-data converter, a PC with software, and an Instron 5582 tensile-testing machine as the force-producing mechanism. The maximum load indentation was 2.5 kN and the indenter diameter was 5 mm. Plane-parallel samples were used for the ABI testing.

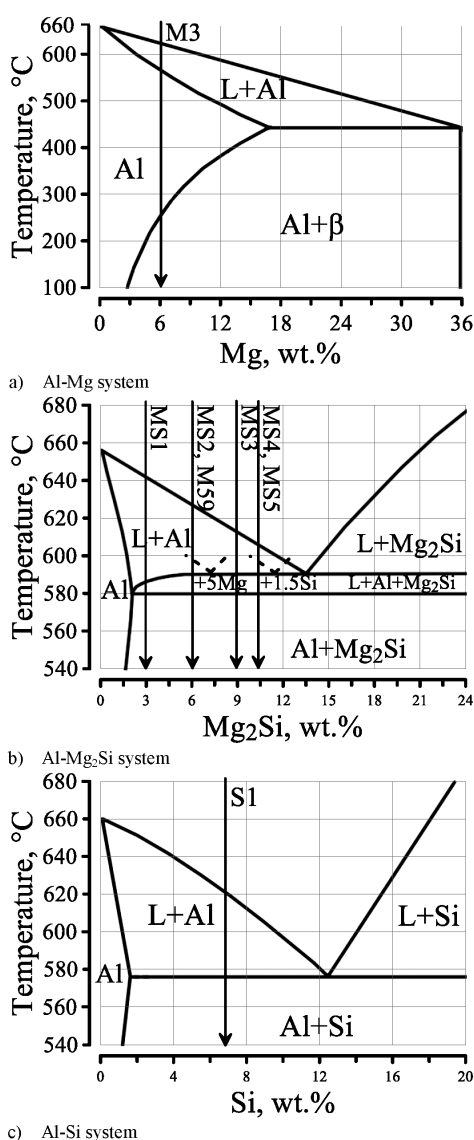


Figure 1: Equilibrium-phase diagrams

Slika 1: Ravnotežni fazni diagrami

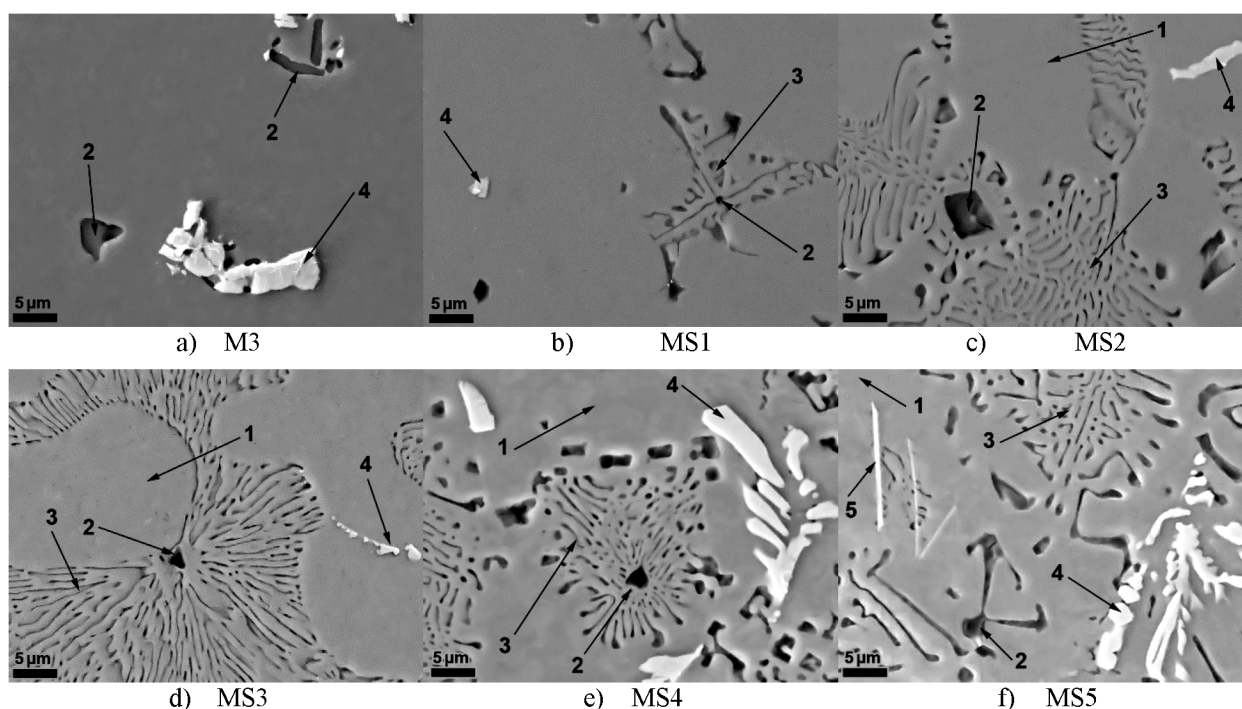


Figure 2: Microstructures of as-cast state of Al-Mg-Si-Mn alloys: a) AlMg6Mn (M3), b) AlMg7SiMn (MS1), c) AlMg7Si2Mn (MS2), d) AlMg7Si3Mn (MS3), e) AlMg7Si4Mn (MS4), f) AlMg7Si5Mn (MS5), (according to the **Table 1**). The names of phases: 1. Matrix of α -Al, 2. Primary Mg_2Si phase, 3. Eutectic of Al- Mg_2Si , 4. α - $Al_{15}(Mn,Fe)_3Si_2$, β - $Al_5(Mn,Fe)Si$, 5. δ - $Al_4Si_2(Mn,Fe)$.

Slika 2: Mikrostruktura zlitin Al-Mg-Si-Mn, v litem stanju: a) AlMg6Mn (M3), b) AlMg7SiMn (MS1), c) AlMg7Si2Mn (MS2), d) AlMg7Si3Mn (MS3), e) AlMg7Si4Mn (MS4), f) AlMg7Si5Mn (MS5), (glede na **Tabelo 1**). Imena faz: 1. Osnovna α -Al, 2. Primarna Mg_2Si faza, 3. Evtetik Al- Mg_2Si , 4. Mn-faza $Al_6(Mn,Fe)$, α - $Al_{15}(Mn,Fe)_3Si_2$, β - $Al_5(Mn,Fe)Si$, 5. Si-Mn faza δ - $Al_4Si_2(Mn,Fe)$

3 RESULTS AND DISCUSSION

3.1 Microstructure investigation

Figure 2 presents the polished microstructures of the samples. The microstructures of all the samples consist of primary Al grains (the light areas) and the (Al)+(Mg₂Si) eutectic (grey). The preferential morphology of α -Al is a globular-rosette morphology and Al grains are surrounded by eutectic colonies. The (Al)+(Mg₂Si) eutectic has a lamellar morphology. Primary Mg_2Si crystals have a regular polyhedral shape and are located in the centers of the eutectic colonies.

3.2 Element distribution in α -Al grains

The α -Al matrix of the Al-Mg-Si-Mn alloys contains Mg, Si and Mn. It is known that the solubility of Mg in Al amounts to 1.4 % and the solubility of Si is 0.4 % at room temperature.¹⁰

In the investigated alloys, the Mg and Si contents in a solid solution change with an alteration of the Mg/Si ratio in the alloys (**Table 2**). The stoichiometric composition of Mg_2Si is 66.7 % of amount fractions of Mg and 33.3 % of amount fractions of Si (the Mg/Si at. ratio is 2.0, and its weight ratio is 1.73:1). The Mg content is considered to be in excess when the ratio is more than 2, and the Si content is in excess when the ratio is less than 2. For all the alloys, the Mn content in the α -Al solid solution is ~0.5 % of mass fractions. The existence of an

insignificant peak of oxygen in the EDX spectrum is explained with the tendency of Al and Mg silicides to

Table 2: Average composition of α -Al solid solution in Al- Mg_2Si alloys measured with EDX

Tabela 2: Povprečna sestava trdne raztopine α -Al v Al- Mg_2Si zlitinah, izmerjena z EDX

Alloy	Mg/Si ratio	Chemical composition (w/%)					
		Mg	Al	Si	Ti	Mn	Fe
MS1 (AC)	7.0	5.8	93.2	0.2	0.2	0.5	<0.1
MS1 (ST)		5.9	93.1	0.2	0.2	0.5	<0.1
MS1 (AA)		5.9	93.2	0.1	0.2	0.5	<0.1
MS2 (AC)	3.5	3.5	95.5	0.2	0.2	0.5	<0.1
MS2 (ST)		3.9	95.1	0.2	0.2	0.5	<0.1
MS2 (AA)		3.7	95.4	0.1	0.2	0.5	<0.1
MS3 (AC)	2.2	2.5	96.3	0.3	0.3	0.5	<0.1
MS3 (ST)		2.4	96.5	0.2	0.3	0.5	<0.1
MS3 (AA)		2.4	96.6	0.2	0.3	0.4	<0.1
MS4 (AC)	1.8	2.1	96.6	0.5	0.3	0.4	<0.1
MS4 (ST)		1.3	97.0	0.8	0.3	0.5	<0.1
MS4 (AA)		1.3	97.0	0.8	0.3	0.5	<0.1
MS5 (AC)	1.4	1.5	96.6	1.1	0.3	0.4	<0.1
MS5 (ST)		0.8	95.8	1.4	0.3	0.5	<0.1
MS5 (AA)		0.8	96.9	1.4	0.3	0.5	<0.1

AC – as cast state, ST – after solution treatment (570 °C, 60 min), AA – after artificial aging (at the point of maximum mechanical properties)

oxidation. The average composition of the α -Al matrix for all the samples is presented in **Table 2**.

The solution treatment increases the concentration of Mg and decreases the concentration of Si (**Table 2**) in the solid solutions in the MS1 and MS2 alloys (the alloys with an excess Mg concentration). The artificial aging leads to a further reduction in the concentration of Si (it is connected with a small amount of Si in the alloys and the tendency of Mg to form the Mg_2Si compound), but the concentration of Mg is back to the initial values.

The situation is different in the MS3, MS4, MS5 alloys. During the solution treatment, taking 60 min, the amount of Mg reduces and the amount of Si increases in these alloys. The increase in the concentration of Si in the solid solution is connected with the dissolution of Mn-containing phases. Aging does not significantly change the chemical composition of α -Al (**Table 2**).

3.3 Mn- and Si-containing phases

Due to a poor solubility, Fe with Si and Al in the Al-Mg-Si alloys constitute acicular-shaped intermetallic inclusions, which reduce the mechanical properties of the alloys. The investigated alloys are additionally doped by 0.6 % Mn to neutralize the negative effect¹³⁻¹⁵ of the Fe-containing phase. As it is shown by other studies, an addition of 0.6 % of mass fraction of Mn in the alloy with a nominal composition of Al-7Mg-3Si improves its mechanical properties. Thus, the tensile strength and yield strength of the alloy with the Mn addition increase on average by 30 %.

Some authors¹³ reported that in the alloy with a nominal composition of Al-7Mg-5Si (w%), the Al- Mg_2Si eutectic and Al-Si eutectic are formed. However, the Al-Si eutectic was not detected in the alloy with a nominal composition of Al-7Mg-5Si-Mn (**Figure 2f**). Therefore, the excess Si with Mn and Fe form several types of the Mn-phase in the submitted alloys.

The morphologies of all the types of the Mn-containing phases observed in the MS-series are shown in **Figure 2**. These phases can be identified as $Al_6(Mn,Fe)$, $\alpha-Al_{15}(Mn,Fe)_3Si_2$, $\beta-Al_5(Mn,Fe)Si$, $\delta-Al_4(Mn,Fe)Si_2$. The first two types are found in the alloys with the ratio of Mg/Si greater than 2 (M3, MS1, MS2, MS3, M59). Phases β and δ are found in the alloys with the ratio of Mg/Si lower than 2 (MS4, MS5). The δ -phase is unstable and it disintegrates during the heat treatment.¹⁵⁻¹⁷

3.4 Eutectic

The EDX spectra of the lamellas excluding Al from the quantification showed a composition very close to the stoichiometry of Mg_2Si . The EDX spectra of interlamellar spacing show high concentrations of Mg and Si. With the increase in Mg and Si, the Al- Mg_2Si eutectic volume fraction grows bigger.¹⁸

With the addition of extra Mg into the Al- Mg_2Si system, the eutectic point moves towards the corner with

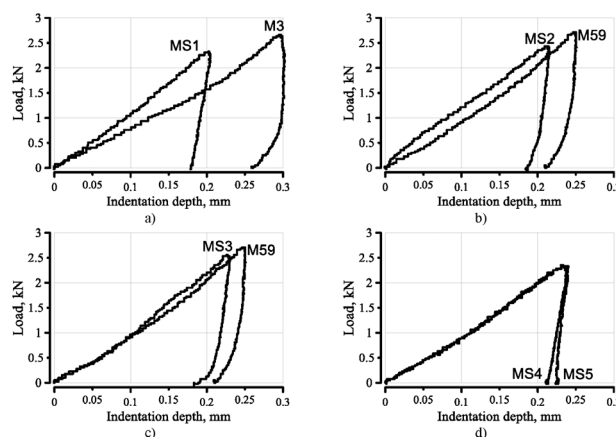


Figure 3: ABI indentation curves

Slika 3: ABI krivulje vtiskovanja

a lower Mg_2Si concentration and the volume of the Al- Mg_2Si eutectic increases.

With the addition of extra Si into the Al- Mg_2Si alloys, the eutectic point moves to a higher Al concentration and the volume of the Al- Mg_2Si eutectic increases. In the AlMg7Si5Mn alloy (with 1.5 % of mass fractions of excess Si and 0.6 % of mass fractions of Mn) the volume fraction of the Al- Mg_2Si eutectic reaches its maximum.

3.5 Reproducibility of the results of classical tests and ABI tests

Figure 3 represents the dependencies of the indentation-depth load, recorded in the ABI study. They show how the material behaves in the research process, which consists of three parts: the load, the holding at the maximum force and the unloading. The growing part of the curve describes the process of loading. This process has elastic and elastic-plastic sections.¹⁹ Then, after the holding at the maximum force for 10 s, the unloading process begins. The waning part of the curve describes the process of unloading. The point where the curve intersects with the x -axis corresponds to the plastic indentation depth (h_p). The difference between the plastic depth and the depth of the maximum load (h_{max}) corresponds to the elastic depth (h_s).

For the results validation, the data obtained with the ABI method were compared with the data obtained with the classical methods (**Table 3**).

The hardness was calculated with Equation (1) and Equation (2)²⁰ was used to determine the tensile strength (R_m):

$$HB = \frac{P}{\pi Dh} \quad (1)$$

$$R_m = c \cdot HB \quad (2)$$

where: HB – Brinell hardness, P – load (kN) (**Figure 3**), D – diameter of indenter (mm), h – indentation depth (mm) (**Figure 3**), c – coefficient of uncertainty for the presented series of alloys with a value of 2.8.²⁰

Table 3: Comparison of the results obtained with classical methods and ABI method**Tabela 3:** Primerjava dobljenih rezultatov s klasičnimi metodami in z ABI metodo

State	Method	S1	M3	M59	MS1	MS2	MS3	MS4	MS5
As-cast state	HB, ABI	72	65.0	82.3	83.6	83.9	89.4	70.0	66.2
	HB*	75	65.0	81.0	84.0	86.8	87.8	71.1	69.0
	$R_{p0.2}$, (MPa), ABI	180.2	145.6	166.4	194.1	134.4	223.9	145.5	124.8
	$R_{p0.2}$, (MPa)*	182.5	130.0	155.5	169.4	155.3	203.5	137.9	123.5
	R_m , (MPa), ABI	201.6	179.5	226.1	229.5	230.5	245.6	192.4	182.0
	R_m , (MPa)*	205.1	180.0	219.9	199.4	223.1	239.8	185.6	163.5
ST 1 h, 570 °C	HB, ABI	–	–	73.0	79.1	70.5	73.1	71.1	78.7
	HB*	–	–	71.0	77.5	69.6	73.2	71.1	75.5
AA (1 h, 570 °C + 1.5 h, 75 °C)	HB, ABI	90.0	–	93.6	83.6	80.9	99.5	100.4	107.3
	HB*	90.0	–	96.1	82.2	79.6	100.7	101.9	113.7
	$R_{p0.2}$, (MPa), ABI	194.1	–	155.4	194.1	145.6	179.2	224.0	233.0
	$R_{p0.2}$, (MPa)*	171.9	–	175.3	174.2	164.2	200.6	227.1	200.8
	R_m , (MPa), ABI	243.0	–	257.1	229.7	222.4	273.1	275.8	294.7
	R_m , (MPa)*	256.9	–	256.3	226.2	222.1	262.4	264.9	280.7

* – Classic methods

The methodology from the reference²⁰, Equations (3) and (4), was used to determine the yield strength ($R_{p0.2}$):

$$R_{p0.2} = c \cdot HM = \frac{c \cdot P}{\pi a^2} \quad (3)$$

$$a = \sqrt{Dh - h^2} \quad (4)$$

where: c – coefficient of uncertainty (2.8), HM – Meyer hardness, a – contact radius (mm).

The differences between the two curves given in the diagrams (**Figure 3**) may be related to the following parameters taken into account in Equation (1):

1. The difference in the value of the load (P), which leads to a change in the indentation depth.
2. The difference in the hardness of the materials (HB).

Figure 3 shows the indentation curves of the alloys with a difference in the amount of one component (Mg, Si, Mg_2Si). The results of the ABI tests are shown in **Table 3**.

The calculation of the standard deviation shows that the hardness value is determined with a sufficiently high accuracy. The average deviation is about 2–3 %. The tensile strength (defined by the HB values) has a good accuracy (its average deviation is 3–5 %).

The values of the average standard deviation of the yield strength are quite high (9–16 %), but in some tests the accuracy is 1 %. This can be explained in the following manner: the load, at which the deformation is detected in the track (0.2 %) is about 100 N and the measurement device determines the load with an accuracy of 24 N – 50 N. This is sufficient for the determination of the total hardness, but it is not enough for the determination of the hardness at the load of $P_{0.2}$. It is planned to increase the accuracy of the determination of this and other parameters.

3.6 Influence of the chemical composition on the mechanical properties

As it can be seen from **Table 3**, the mechanical properties of the cast Al- Mg_2Si alloys do not increase with the growth of the Mg content (**Figure 3b**, alloys MS2 and M59 – alloys with similar values of Mg_2Si and different values of Mg). Similar results of the Mg behavior in Al-alloys were obtained in another study.²¹

An analysis of the literature data^{3,13} showed that the mechanical properties of the Al- Mg_2Si -Si alloys with an increased amount of Si are improved. However, in these works the mechanical properties are given after the heat treatment of the alloys. In the considered series of alloys, extra Si with Mn forms a metastable acicular-shaped δ - $Al_4(Mn,Fe)Si_2$ phase, which deteriorates the properties of the alloys in the as-cast state, and this phase dissolves during the homogenization process.

As can be seen in **Table 3**, the hardness and the tensile strength of the cast Al- Mg_2Si alloys can relate to the size and morphology of the eutectic and primary Mg_2Si phase (M3 and MS1, M59 and MS3 are alloys with similar values of Mg and different values of Mg_2Si). Hence, the mechanical properties grow with the increasing volume fraction of Mg_2Si . Similar results were obtained in a reference study.⁶

4 CONCLUSIONS

The comparison of the results obtained with classical and ABI methods shows the following:

- The differences in the values of the hardness and tensile strength, obtained with different methods, do not exceed 5 % (with the standard error for such measurements of 10 %).

- The error of the yield-strength measurement is greater than 10 % (and varies from 1 % to 16 %). This problem can be solved by increasing the sensitivity of the device at low values of the load.
- The analysis of the results of the hardness and tensile tests shows the following:
- Excess Mg does not have a significant effect on the mechanical properties of the alloys.
- Metastable δ -Al₄(Mn,Fe)Si₂ phases are formed in the alloys with excess Si. This leads to a degradation of the mechanical properties.
- The main strengthening phase in the as-cast state of the studied alloys is the Al-Mg₂Si eutectic.

Acknowledgments

The authors gratefully thank the Visegrad Fund and DAAD for their support in the research. Also, the authors would like to thank doc. Ing. Jirí Cejp, C Sc. and doc. Ing. Jirí Janovec, C Sc. for their help with the tensile tests, and Ing. Jakub Horník, Ph.D., for supervising the present investigations.

This work was supported by the Ministry of Education, Youth and Sport of the Czech Republic, program NPU1, the project with Nos. LO1207 and SGS13/186/OHK2/3T/12 – Research on the influence of surface treatment on the improvement of service life and reliability of exposed water turbine's components.

5 REFERENCES

- I. N. Fridlyander, V. G. Sister, O. E. Grushko, V. V. Berstenev, L. M. Sheveleva, L. A. Ivanova, Aluminium alloys: promising materials in the automotive industry, *Metal Science and Heat Treatment*, 44 (2002) 9–10, 365–370, doi:10.1023/A:1021901715578
- J. Zhang, Y. Q. Wang, B. Yang, Effects of Si content on the microstructure and tensile strength of an in situ Al-Mg₂Si composite, *Journal of Materials Research*, 14 (1999) 1, 68–74, doi:10.1557/JMR.1999.0012
- Y. Wang, H. Liao, Y. Wu, J. Yang, Effect of Si content on microstructure and mechanical properties of Al–Si–Mg alloys, *Materials and Design*, 53 (2014), 634–638, doi:10.1016/j.matdes.2013.07.067
- C. Li, Y. Wu, H. Li, X. Liu, Microstructural formation in hypereutectic Al–Mg₂Si with extra Si, *Journal of Alloys and Compounds*, 477 (2009), 212–216, doi:10.1016/j.jallcom.2008.10.061
- J. Zhang, Z. Fan, Y. Q. Wang, B. L. Zhou, Equilibrium pseudobinary Al-Mg₂Si phase diagram, *Materials Science and Technology*, 17 (2001), 494–496, doi:10.1179/026708301101510311
- F. Yan, S. Ji, Z. Fan, Effect of Excess Mg on the Microstructure and Mechanical Properties of Al-Mg₂Si High Pressure Die Casting Alloys, *Materials Science Forum*, 765 (2013), 64–68, doi:10.4028/www.scientific.net/MSF.765.64
- A. Furihata, K. Matsuda, J. Y. Nakamura, S. Ikeno, Y. Uetani, Age-hardening behavior and HRTEM observation of precipitates in excess Mg type Al-Mg-Si-Ag alloy, *Materials Science Forum*, 519–521 (2006), 507–510, doi:10.4028/www.scientific.net/MSF.519-521.507
- K. Matsuda, T. Yoshida, T. Wada, A. Yoshida, U. Uetani, T. Sato, A. Kamio, S. Ikeno, Precipitation Sequence in Al-Mg-Si Alloys with Excess Magnesium, *J. Japan Inst. Metals*, 62 (1998) 8, 718–726
- J. Gilbert Kaufman, E. L. Rooy, *Aluminum Alloy Castings: Properties, Processes, and Applications*, ASM International, Materials Park, OH 2004
- V. S. Zolotarevsky, N. A. Belov, M. V. Glazoff, *Casting aluminium alloys*, Elsevier, Amsterdam 2007, doi:10.1016/B978-008045370-5.50003-1
- H. Lee, J. H. Lee, G. M. Pharr, A numerical approach to spherical indentation techniques for material property evaluation, *Journal of the Mechanics and Physics of Solids*, 53 (2005), 2037–2069, doi:10.1016/j.jmps.2005.04.007
- K. Sharma, P. K. Singh, V. Bhasin, K. K. Vaze, Application of Automated Ball Indentation for Property Measurement of Degraded Zr_{2.5}Nb, *Journal of Minerals & Materials Characterization & Engineering*, 10 (2011) 7, 661–669, doi:10.4236/jmmce.2011.107051
- E. Georgatis, A. Lekatou, A. E. Karantzalis, H. Petropoulos, S. Katsamakis, A. Poulia, Development of a Cast Al-Mg₂Si-Si In Situ Composite: Microstructure, Heat Treatment, and Mechanical Properties, *Journal of Materials Engineering and Performance*, 22 (2013) 3, 729–741, doi:10.1007/s11665-012-0337-6
- L. C. Doan, K. Nakai, Y. Matsuura, S. Kobayashi, Y. Ohmori, Effects of Excess Mg and Si on the Isothermal Ageing Behaviours in the Al–Mg₂Si Alloys, *Materials Transactions*, 43 (2002) 6, 1371–1380, doi:10.2320/matertrans.43.1371
- Z. Zhihao, M. Yi, C. Jianzhong, Effect of Mn on microstructures and mechanical properties of Al-Mg-Si-Cu-Cr-V alloy, *China Foundry*, 9 (2012) 4, 349–355
- L. Lia, R. Zhoua, D. Lua, Y. Jianga, R. Zhoua, Effect of Cooling Slope and Manganese on the Microstructure of Hypereutectic Al-Si Alloy with 2 % Fe, *Materials Research*, 17 (2014) 2, 511–517, doi:10.1590/S1516-14392013005000198
- C. Phongphisutthinan, H. Tezuka, T. Sato, Semi-Solid Microstructure Control of Wrought Al-Mg-Si Based Alloys with Fe and Mn Additions in Deformation-Semi-Solid-Forming Process, *Materials Transactions*, 52 (2011) 5, 834–841, doi:10.2320/matertrans.L-MZ201119
- S. Otarawanna, C. M. Gourlay, H. I. Laukli, A. K. Dahle, Microstructure Formation in AlSi₄MgMn and AlMg₅Si₂Mn High-Pressure Die Castings, *Metallurgical and Materials Transactions A*, 40A (2009), 1645–1659, doi:10.1007/s11661-009-9841-1
- K. Sharma, V. Bhasin, K. K. Vaze, A. K. Ghosh, Numerical simulation with finite element and artificial neural network of ball indentation for mechanical property estimation, *Sadhana*, 36 (2011) 2, 181–192, doi:10.1007/s12046-011-0019-3
- P. I. Stoev, V. I. Moschenok, Definition of Mechanical Properties of Metals and Alloys on Hardness, *Bulletin of V. N. Karazin Kharkiv National University*, 601 (2003) 2(22), 106–112
- H. Liu, W. J. Song, G. Zhao, C. M. Liu, L. Zuo, Effect of Mg on microstructures and properties of Al-Mg-Si-Cu aluminium alloys for automotive body sheets, *Trans. Nonferrous Met. Soc. China*, 15 (2005) 1, 30–31

Fe-Zn INTERMETALLIC PHASES PREPARED BY DIFFUSION ANNEALING AND SPARK-PLASMA SINTERING

Fe-Zn INTERMETALNE FAZE, PRIPRAVLJENE Z DIFUZIJSKIM ŽARJENJEM IN S SINTRANJEM V ISKREČI PLAZMI

Petr Pokorný¹, Jakub Cinert^{2,3}, Zdeněk Pala²

¹Czech Technical University, Klokner Institute, Solinova 7, 166 08 Prague 6, Czech Republic

²Institute of Plasma Physics, ASCR v.v.i., Za Slovankou 1782/3, 182 00 Prague 8, Czech Republic

³University in Prague, Faculty of Electrical Engineering, Department of Electrotechnology, Prague 6, Czech Republic
cinert@ipp.cas.cz

Prejem rokopisa – received: 2014-12-22; sprejem za objavo – accepted for publication: 2015-03-10

doi:10.17222/mit.2014.309

The feasibility of iron-zinc intermetallic-phase preparation by spark-plasma sintering (SPS) was investigated. The samples were prepared with a combination of powder metallurgy, where the powder was prepared in evacuated quartz tubes, and a sintering process using SPS. Since the Fe-Zn intermetallic phases are mostly used for hot-dip galvanized steels, the knowledge of the properties of individual intermetallic phases is vital for a better understanding and even further optimization of galvanization processes. The main aim of the article is to compare the phase composition of the initial powder with the SPS samples using X-ray diffraction. Furthermore, the hardness and microstructure were investigated as well.

Keywords: Fe-Zn intermetallics, spark-plasma sintering, diffusion annealing, phase composition, hardness

Preučevana je bila izvedljivost priprave železo-cink intermetalnih faz s sintranjem v iskreči plazmi (SPS). Vzorci so bili pripravljene s pomočjo metalurgije prahov, kjer so bili prahovi zaprti v evakuirane kvarčne cevi, ki mu je sledil postopek SPS. Ker se Fe-Zn intermetalne faze večinoma uporablja pri vročem cinkanju jekel, so lastnosti posamezne faze pomembne za boljše razumevanje in celo za optimiranje procesa galvanizacije. Glavni namen članka je primerjava sestave faz s pomočjo rentgenske difrakcije v začetnih prahovih in SPS vzorcih. Preiskovani sta bili tudi trdota in mikrostruktura.

Ključne besede: Fe-Zn intermetalne zlitine, sintranje z iskrečo plazmo, difuzijsko žarjenje, sestava faz, trdota

1 INTRODUCTION

Hot-dip galvanized coating is one of the most common protection surfaces of low-alloy steels as it offers a good corrosion protection under normal atmospheric conditions. During a hot-dip galvanizing process, iron-zinc diffusion coating grows on the surface of galvanized steel. This coating consists of a specific intermetallic formation, in which the iron content decreases¹ towards the galvanized steel giving rise to a sequence² of Fe-Zn intermetallic phases. These new phases are joined with the substrate and with each other by a system of elementary intermetallic bonds.³ Individual phases are different in composition, structure, morphology, thickness and mechanical properties.⁴

Both the composition and the thickness of the coating depend on impurity elements concentrations in the galvanized steel, composition and temperature of the galvanized zinc bath, time of submersion, thickness of galvanized profiles, mechanical and thermal processing of the galvanized steel and the cooling process after the coating deposition.² There is an unevenly thick layer of galvanized zinc, or the so-called η phase representing the substitutional solid solution of iron in zinc, on the surface. The η -phase layer fosters the galvanizing process by facilitating the formation of specific intermetallic galvanized layers. These layers provide a good protection

against the corrosion and an increased resistance to wear because the intermetallic phases are harder than the η phase.²

With respect to the mechanical properties of intermetallic phases, the microhardness and compressive strength^{5,6} have mostly been analysed. According to single-crystal hardness studies,⁷ the highest hardness is achieved by δ and Γ_1 phases. The results of the studies clearly prove that the Γ_1 phase is the hardest phase in the hot-dip galvanized coating. It has also been shown⁶ that the compression strength and hardness decrease with the increasing hardness, hence, the δ and Γ_1 phases are relatively fragile. Both δ and Γ_1 phases do not experience plastic deformation after exceeding the yield stress; instead a brittle fracture occurs.² On the other hand, it is possible to plastically deform the Γ phase up to the elongation of 2.2 %.⁸ For the ζ phase, the elongation is only 0.5 %.⁹ The values of the microhardness and compressive strength for each Fe-Zn intermetallic phase are shown in **Table 1**.

In our contribution, we have striven to analyse the hardness of the δ and Γ phases, i.e., one brittle and one ductile phase, prepared by spark-plasma sintering.¹⁰ The preparation of the powders for individual intermetallic phases is relatively complicated. We took the path of sealing the powder in an evacuated quartz ampoule followed by a diffusion annealing process.^{11,12}

Table 1: Mechanical properties of Fe-Zn intermetallic phases
Tabela 1: Mehanske lastnosti Fe-Zn intermetalnih faz

Phase	Formula	Hardness, HV	Stress-strain condition
η	Zn	52	–
ζ	FeZn ₁₃	208	ductile ($\epsilon = 0.5\%$)
δ	FeZn ₁₀	358	brittle
Γ_1	Fe ₅ Zn ₂₁	505	brittle
Γ	Fe ₃ Zn ₁₀	326	ductile ($\epsilon = 2.2\%$)

2 EXPERIMENTAL PART

The Fe-Zn intermetallics were prepared with the powder-metallurgy technique. First of all, iron powder (iron-powder, Sigma Aldrich, particles size < 150 μm , purity of mass fractions of 100 % Fe) and zinc powder (zinc powder, AlfaAesar, the median particle size of 6–9 μm , purity of mass fractions of 99 % Zn) were mixed under appropriate conditions of the atomic ratio. These mixtures (Γ and δ) were compressed with 50 kN using a Heckert FPZ 100/1DO universal loading machine, into forms with a diameter of 10 mm. The obtained samples were sealed into pre-evacuated quartz ampoules. The sealed samples were diffusion annealed at 50 °C, below their thermal stability, as shown on **Figure 1**. The duration of diffusion annealing was 12 h and the heating rate was 5 °C/min.

After the diffusion annealing, the powder was removed from the quartz tubes and sintered with the rapid SPS technique. Each sample was made from 9 g of the specific phase powder. The temperature rate was 100 °C/min; 100 °C below the maximum sintering temperature, the temperature rate decreased to 50 °C/min. After the maximum temperature of the sintering was achieved, a force of 60 MPa was applied to the samples and the holding time was 5 min. The values measured during the sintering process are in **Figure 2**.

Powder X-ray diffraction (PXRD) was employed to ascertain the phase compositions of the feedstock mate-

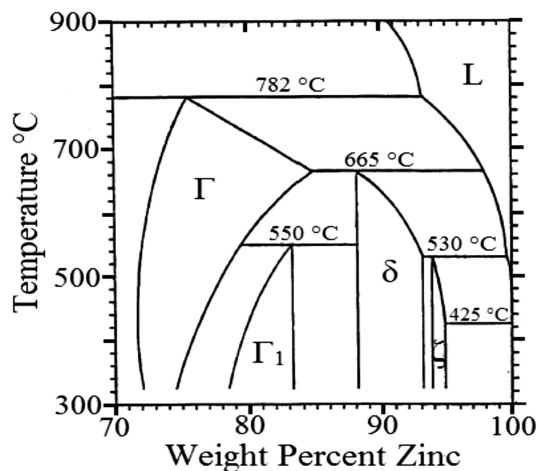


Figure 1: Detail of phase diagram Fe-Zn defining intermetallic phases created by hot-dip galvanizing²
Slika 1: Detajl faznega diagrama Fe-Zn, ki določa intermetalne faze, nastale pri vročem cinkanju²

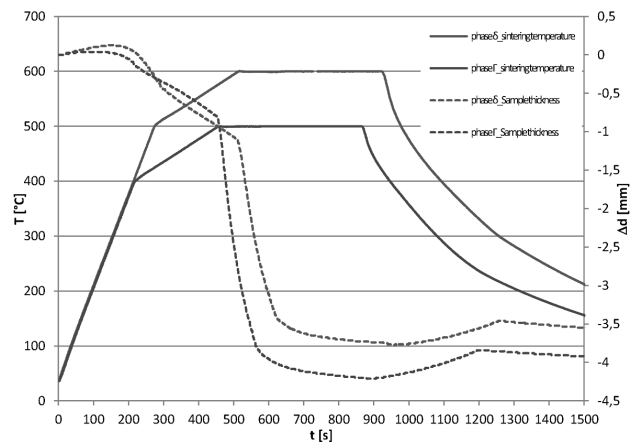


Figure 2: Courses of the temperature (full lines) and changes in the samples' thickness (dotted lines) during SPS of both samples

Slika 2: Potek temperature (polni črti) in spremembe v debelini vzorca (prekinjeni črti) med SPS obeh vzorcev

rials and sintered samples. The samples were mounted onto the x, y, z positioning stage of a D8 Discover diffractometer in the Bragg-Brentano geometry, equipped with a 1D LynxEye detector (Bruker AXS, Germany) and inspected with Cu- $K\alpha$ radiation. After the identification of crystalline phases, the CIFs (crystallographic information files) were taken from the ICSD (the Inorganic Crystal Structure Database) and the COD (the Crystallography Open Database) containing 13 and 2 files for the Fe-Zn systems, respectively. The obtained PXRD patterns were subjected to the Rietveld analysis in the TOPAS 4.2 software. Utmost care was taken to follow the guidelines for measuring and data evaluation.¹³

The microstructures of the sintered samples were observed with a scanning electron microscope, Carl Zeiss SMT, EVO MA 15. Hardness measurements were performed on polished surfaces using Innovatest Nexus with a Vickers indenter with a force of 0.1 kg, i.e., HV0.1, and a dwell time of 10 s according to EN ISO 6507-1. The hardness was tested twelve times in different places across the lengths of the polished surfaces.

3 RESULTS AND DISCUSSION

In **Figure 3**, both the Γ powder after the diffusion annealing and its sintered sample contained only two phases, i.e., zincite (ZnO) and the Γ phase. The Γ phase is bcc with the γ Cu₅Zn₈ brass type and $I\bar{4}3m$ space group. Concerning the stoichiometry, Brandon et al.¹⁴ indicate that it is Fe₃Zn₁₀ (ICSD code 2094), Belins¹⁵ give Fe₁₃Zn₃₉ (ICSD code 150198) and Johansson et al.¹⁶ give Fe₄Zn₉ (ICSD code 103708). Employing the CIFs for all these four stoichiometries, we obtained virtually the same refined lattice parameter of $a = 0.8972$ nm, but the correspondence between the structural model and the measured data was the best for the Fe₁₃Zn₃₉ stoichiometry. The result of the Rietveld refinement of the Γ feedstock powder is in **Figure 4**. When comparing the

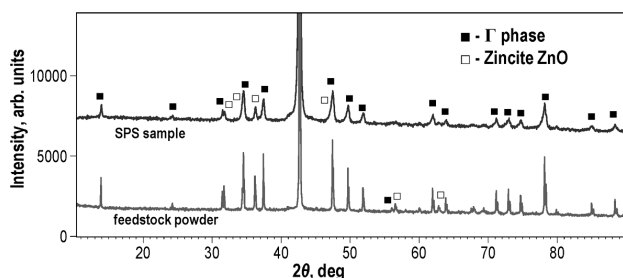


Figure 3: PXRD patterns of Γ feedstock powder and sintered sample. Vertical shift was introduced to make the features of both patterns distinguishable.

Slika 3: Rentgenograma prahu Γ surovca in sintranega vzorca. Vertikalni zamik je izvršen zaradi prikaza obeh diagramov.

diffraction patterns from the viewpoint of profile analysis, the sintered sample exhibited markedly smaller crystallite sizes whose average value was 30 nm, as determined with the Rietveld refinement. This result is mirrored by the broader diffraction profiles of the sintered-sample PXRD pattern. The microstructure of the metallographic specimen of the sintered sample is in **Figure 5**.

For the δ feedstock powder and the sintered sample, the PXRD patterns contain a fairly large number of reflections, which have the same 2θ positions, but are significantly broader for the sintered sample, as seen in **Figure 6**. During the phase identification, the presence of zincite and hexagonal phase of the Fe-Zn system was established in both patterns. There are only two phases with such a structure, one in the ICSD with code 150199¹⁵ and one in the COD with code 2105806.¹⁷ Of these two, the former leads to a better fit; however, the fit was not satisfactory for the lower 2θ range where the used CIFs indicated the presence of more reflections than observed. Since both CIFs are relevant for the so-called δ_{1p} phase, the results of the Rietveld refinement thus indicate that the present phase is δ_{1k} . The microstructure of this sintered sample, which can be seen in **Figure 7**, is notable by a higher intergranular porosity

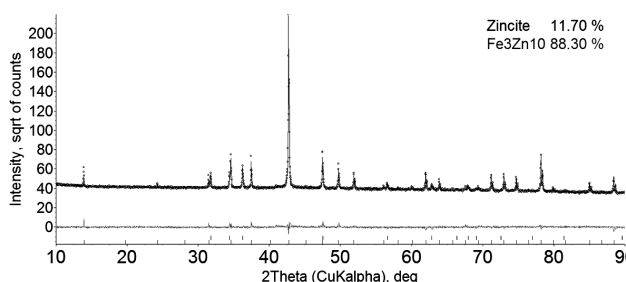


Figure 4: Result of Rietveld refinement of the feedstock powder. Dots are the measured data and the line is the fit. The grey curve at 0 intensity is difference between measured data and fit; $R_{wp} = 3.98$. Information about the quantitative presence of both phases in the top-right corner is in mass fractions (w%).

Slika 4: Rezultati Rietveld udrobnjenja prahu Γ surovca. Izmerjeni podatki so točke, črta so prilegajoči se podatki. Siva krivulja pri intenziteti 0 je razlika med izmerjenimi in prilegajočimi podatki; $R_{wp} = 3,98$. Podatki o kvantitativnem prikazu so v zgornjem desnem kotu v masnih deležih, (w%).

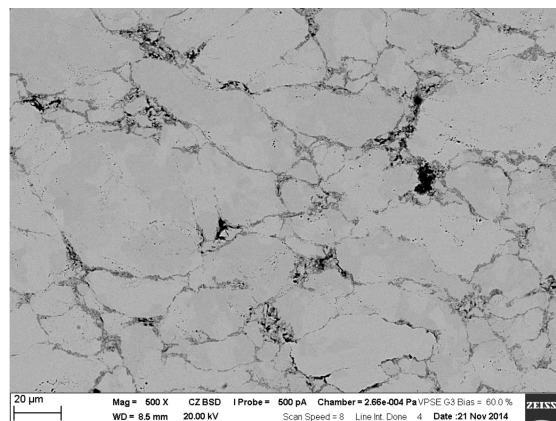


Figure 5: Microstructure of the Γ phase of the spark-plasma-sintered sample

Slika 5: Mikrostruktura faze Γ v vzorcu, sintranem v iskreči plazmi

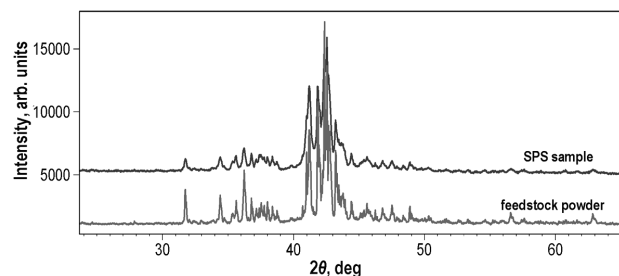


Figure 6: PXRD patterns of the δ feedstock powder and sintered sample. Vertical shift was introduced to make the features of both patterns distinguishable.

Slika 6: Rentgenograma prahu δ surovca in sintranega vzorca. Vertikalni zamik krivulj je izvršen zaradi boljše preglednosti krivulj.

when compared to the Γ phase of the SPS sample. Moreover, while there are clearly visible particles of zincite (dark grey areas) in **Figure 7**, the oxide in the Γ phase of the SPS sample is mostly seen around the Fe-Zn intermetallic grains.

The microhardness results are summarized in **Figure 8** and they, indeed, show that the δ phase is generally about 10 % harder than the Γ phase, as indicated in **Table 1**. The obtained hardness values of the δ phase fall

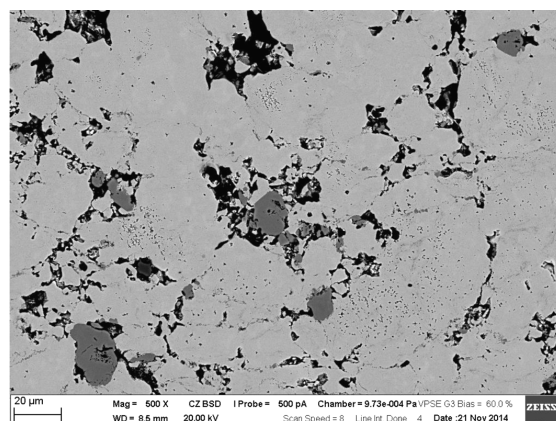


Figure 7: Microstructure of the δ phase of the spark-plasma-sintered sample

Slika 7: Mikrostruktura δ faze vzorca, sintranega v iskreči plazmi

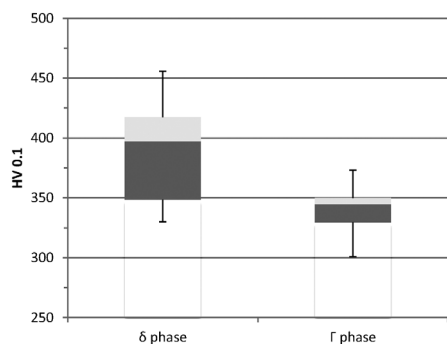


Figure 8: Microhardness results for the sintered-sample polished surfaces

Slika 8: Rezultati meritve mikrotvrdoe polirane površine sintranih vzorcev

within a comparatively broad range from 330 HV to 460 HV, which is probably due to the porosity. However, the values above 400 HV are substantially higher than so far indicated for this phase.

The preparation of the pure Fe-Zn intermetallic phases, from the phase-composition point of view, can facilitate a better understanding of their properties. By using diffusion annealing in the pre-evacuated quartz ampoules and rapid sintering during the SPS process, compact samples with around 10 % of mass fractions of zincite were obtained, with the remaining material being either the δ or Γ phase. However, the zincite phase was already in the material after the diffusion annealing and, hence, the sintering process did not change the phase composition. Moreover, the diffraction-profile analysis shows that a significant grain- or crystallite-size refinement took place during the SPS process. Concerning the presence of zincite and its effect on the hardness, microhardness mapping of the sintered samples' surfaces will be performed in our next study.

4 CONCLUSIONS

By applying diffusion annealing and spark-plasma sintering of Fe-Zn intermetallics, compact samples were obtained. After 5 min of sintering at 500 °C and 600 °C of the Γ or δ Fe-Zn phases, respectively, no change in the phase composition was observed and only the grain-refinement phase took place. The level of zincite, or ZnO, remained the same, at around 10 % of mass fractions. Hence, spark-plasma sintering is a viable way of obtaining a system, where only one Fe-Zn intermetallic is present.

The measured hardness of individual compact samples verifies the fact that the brittle δ phase is generally about 10 % harder than the ductile Γ phase. As for their microstructures, the brittle phase exhibits a higher intergranular porosity.

Acknowledgments

This research has been supported by Czech Science Foundation, Project GA ČR No P105/12/G059 and

Author Z. Pala acknowledges the support of the Czech Science Foundation through project number 14-36566 Genitled Multidisciplinary research centre for advanced materials.

5 REFERENCES

- C. Housecroft, A. G. Sharpe, *Inorganic Chemistry*, 4th Ed., Prentice Hall, 2012, p. 1256
- A. R. Marder, The metallurgy of zinc-coated steel, *Prog. Mater. Sci.*, 45 (2000) 3, 191–271, doi:10.1016/S0079-6425(98)00006-1
- F. A. Cotton, G. Wilkinson, C. A. Murillo, M. Bochmann, *Advanced Inorganic Chemistry*, 6th Ed., Wiley, 1999, p. 1376
- N. N. Greenwood, A. Earnshaw, *Chemistry of the Elements*, 2nd Ed., Butterworth-Heinemann, 1997, p. 1600
- N. L. Okamoto, M. Inomoto, H. Adachi, H. Takebayashi, H. Inui, Micropillar compression deformation of single crystals of the intermetallic compound ζ -FeZn13, *Acta Mater.*, 65 (2014), 229–239, doi:10.1016/j.actamat.2013.10.065
- N. L. Okamoto, D. Kashioka, M. Inomoto, H. Inui, H. Takebayashi, S. Yamaguchi, Compression deformability of Γ and ζ Fe-Zn intermetallics to mitigate detachment of brittle intermetallic coating of galvanized steels, *Scr. Mater.*, 69 (2013) 4, 307–310, doi:10.1016/j.scriptamat.2013.05.003
- G. F. Bastin, F. J. J. van Loo, G. D. Rieck, New compound in the iron-zinc system, *Zeitschrift für Met.*, 65 (1974) 10, 656–660
- X. Hu, T. Watanabe, Relationship between the Crystallographic Structure of Electrodeposited Fe-Zn Alloy Film and its Thermal Equilibrium Diagram, *Mater. Trans.*, 42 (2001) 9, 1969–1976, doi:10.2320/matertrans.42.1969
- X. Hu, G. Zou, S. J. Dong, M. Y. Lee, J. P. Jung, Y. Zhou, Effects of Steel Coatings on Electrode Life in Resistance Spot Welding of Galvanized Steel Sheets, *Mater. Trans.*, 51 (2010) 12, 2236–2242, doi:10.2320/matertrans.M2010239
- Z. A. Munir, U. Anselmi-Tamburini, M. Ohyanagi, The effect of electric field and pressure on the synthesis and consolidation of materials: A review of the spark plasma sintering method, *J. Mater. Sci.*, 41 (2006) 3, 763–777, doi:10.1007/s10853-006-6555-2
- P. R. Munroe, B. Gleeson, The development of Fe-Zn intermetallic compounds in solid Fe/Zn and Fe/Zn-Al diffusion couples during short-term annealing at 400 °C, *Mater. Sci. Eng. A*, 264 (1999) 1–2, 201–209, doi:10.1016/S0921-5093(98)01089-2
- J. Mackowiak, N. R. Short, Metallurgy of galvanized coatings, *Int. Met. Rev.*, 24 (1979) 1, 1–19, doi:10.1179/imtr.1979.24.1.1
- L. B. McCusker, R. B. Von Dreele, D. E. Cox, D. Louër, P. Scardi, Rietveld refinement guidelines, *J. Appl. Crystallogr.*, 32 (1999) 1, 36–50, doi:10.1107/S0021889898009856
- J. K. Brandon, R. Y. Brizard, P. C. Chieh, R. K. McMillan, W. B. Pearson, New refinements of the $\{\gamma\}$ brass type structures Cu5Zn8, Cu5Cd8 and Fe3Zn10, *Acta Crystallogr. Sect. B*, 30 (1974) 6, 1412–1417, doi:10.1107/S0567740874004997
- C. H. E. Belin, R. C. H. Belin, Synthesis and Crystal Structure Determinations in the Γ and δ Phase Domains of the Iron-Zinc System: Electronic and Bonding Analysis of Fe13Zn39 and FeZn10, a Subtle Deviation from the Hume-Rothery Standard?, *J. Solid State Chem.*, 151 (2000) 1, 85–95, doi:10.1006/jssc.2000.8626
- A. Johansson, H. Ljung, S. Westman, X-Ray and Neutron Diffraction Studies on Gamma-Ni, Zn and Gamma-Fe, Zn, *Acta Chem. Scand.*, 22 (1968), 2743–2753, doi:10.3891/acta.chem.scand.22-2743
- N. L. Okamoto, K. Tanaka, A. Yasuhara, H. Inui, Structure refinement of the delta1p phase in the Fe-Zn system by single-crystal X-ray diffraction combined with scanning transmission electron microscopy, *Acta Crystallogr. B Struct. Sci. Cryst. Eng. Mater.*, 70 (2014) 2, 275–282, doi:10.1107/S2052520613034410

HIGH-TEMPERATURE OXIDATION OF SILICIDE-ALUMINIDE LAYER ON THE TiAl6V4 ALLOY PREPARED BY LIQUID-PHASE SILICONIZING

VISOKOTEMPERATURNA OKSIDACIJA PLASTI SILICID-ALUMINID, PRIPRAVLJENE S SILIKONIZIRANJEM S TEKOČO FAZO ZLITINE TiAl6V4

Tomáš František Kubatík

Institute of Plasma Physics AS CR, v.v.i., Za Slovankou 1782/3, 182 00 Prague 8, Czech Republic
kubatik@ipp.cas.cz

Prejem rokopisa – received: 2015-01-02; sprejem za objavo – accepted for publication: 2015-03-26

doi:10.17222/mit.2015.002

The method of coating with silicon from the liquid phase (also called the hot-dip method) was presented by several authors who indicated that this was an effective and inexpensive technique capable of producing Ti-Al-Si layers on titanium and titanium-alloy substrates that are rich in ternary phases. The present study examines the effects of the preparation conditions on the structure and properties of the layers. These layers provide excellent protection from high-temperature oxidation, even at a temperature of 950 °C. It was proved with SEM and X-ray analyses that the original τ_2 ternary phase almost completely decomposed into pure Ti_5Si_4 and TiSi silicides at the temperature of 950 °C. The formed layer, consisting of silicide sub-layers, exhibited superior protective properties in high-temperature applications.

Keywords: TiAl6V4, silicides, high-temperature oxidation, liquid-phase siliconizing

Metodo prekrivanja s silicijem iz tekoče faze (včasih imenovano hot-dip metoda) je predstavilo več avtorjev, ki so potrdili, da je to učinkovita in poceni tehnika, s katero je mogoče izdelati Ti-Al-Si plasti na podlagi iz titana in titanovih zlitin, ki vsebujejo ternarne faze. Predstavljena študija preiskuje vpliv pogojev priprave na strukturo in lastnosti plasti. Te plasti zagotavljajo odlično zaščito pred visokotemperaturno oksidacijo, celo pri temperaturi 950 °C. S SEM in z rentgensko analizo je bilo dokazano, da se prvotna ternarna faza τ_2 , pri temperaturi 950 °C, skoraj v celoti razgradi v čisti Ti_5Si_4 in TiSi silicid. Nastala plast, ki jo sestavlja več podplasti je pokazala odlične zaščitne lastnosti pri visokotemperaturni uporabi.

Ključne besede: TiAl6V4, silicidi, visokotemperaturna oksidacija, silikoniziranje v tekoči fazi

1 INTRODUCTION

Protective layers based on silicide-aluminide phases prepared from the liquid phase were studied by various authors¹⁻⁴ and were shown to exhibit the potential of acting as protective layers where titanium and its alloys are used in high-temperature applications.⁵⁻¹³ The principle of the method is based on the high affinity of silicon and aluminium to titanium. During the immersion of titanium and its alloys in the aluminum melt comprising silicon, a reaction forming a Ti-Al-Si phase at the interface takes place. The temperature of the melt and the silicon content in the melt have effects on the kinetics of the growth of the interface layers as well as on their phase composition. These layers provide an excellent barrier to the diffusion of both oxygen and nitrogen at high temperatures. In high-temperature applications, the layers composed of silicide-aluminide phases cannot be compared with silicides but may offer superior mechanical properties at both high and low temperatures.

The major phase present in these layers, the τ_2 phase, was first described by Brukl et al.¹⁴ as $\text{Ti}(\text{Al}_x\text{Si}_{1-x})_2$ where x is in the range from 0.15 to 0.3, and further characterized by Schubert et al.¹⁵ with the orthorhombic structure and a space group (Cmcm). Layers rich in this

phase exhibit an excellent oxidation resistance. During the course of oxidation, a compact film rich in SiO_2 is formed on the surface of a layer, which substantially mitigates oxygen diffusion. This work is focused on the study of the changes in the phase composition during a high-temperature oxidation of the layers formed by the τ_2 phase.

2 EXPERIMENTAL WORK

The substrate material used in the presented work was the most common titanium alloy, TiAl6V4. Specimens were manufactured as cylinders of 10 mm in diameter and 6 mm in height. They were ground using P180–1200 SiC emery papers. Then they were polished with diamond pastes up to 1 μm . This was followed by degreasing in acetone in an ultrasonic apparatus, rinsing with distilled water, and drying with compressed air. An alloy melt of AlSi20 % of mass fractions was prepared by melting aluminum (99.5 % purity) with silicon (99.99 % purity). To ensure the required homogeneity, the melt was agitated for 30 min and then kept at 650 °C. Then the oxide surface layer was raked off and the TiAl6V4-alloy specimens were immediately introduced.

The melt was agitated again and the specimens were held in the melt for 60 min. At the end of the process, the samples were removed from the bath and air-cooled. The microstructure of the cross-sections of the samples was observed by a scanning electron microscope, EVO MA 15 (Carl Zeiss SMT, Germany, SEM).

The specimens used in the oxidation experiments were treated in 15 % HCl to remove the residues of solidified melt. The specimens were subjected to cyclic oxidation in an electric-resistance furnace at the temperatures of 850 °C and 950 °C for 144 h in air. The results were expressed as weight gains due to oxidation versus oxidation duration. After the oxidation the specimens were mounted in metacrylate resin, ground polished and studied with SEM. A phase analysis was performed with a D8 Discover diffractometer (Bruker, Germany); diffracted Cu-K α radiation was detected with a 1D LynxEye detector.

3 RESULTS AND DISCUSSION

3.1 Microstructure

The temperature applied in the coating process has a significant effect on both the growth rate of the layers and on the layer quality. From previous experiments¹³, the temperature of 650 °C was chosen as the highest temperature for this process. Up to this temperature, the layer is formed only by Ti-Al-Si ternary phases.

The microstructure of the layers prepared by immersion in the AlSi20 melt (with solid silicon) at the temperature of 650 °C for 1 h (**Figure 1**) is compact, non-porous and free from any cracks and fissures. The thickness of the layer reaches approximately 55 μm . The chemical composition across the layer is constant – 11.2 % Al (in amount fractions, $x_i\%$), 55.6 % Si, 31.9 % Ti, and 1.3 % V. This chemical composition corresponds

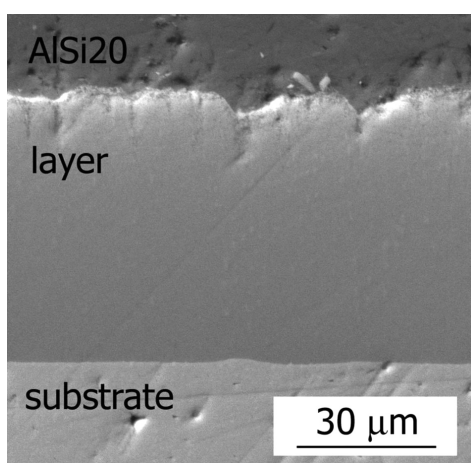


Figure 1: Microstructure of the cross-section of a layer prepared in the AlSi20 melt, at the temperature of 650 °C for 1 h

Slika 1: Mikrostruktura preseka plasti, pripravljene v talini AlSi20, 1 h pri temperaturi 650 °C

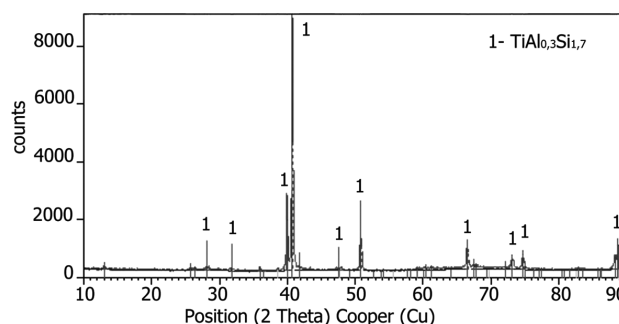


Figure 2: XRD pattern of a cross-section of the layer prepared in the AlSi20 melt

Slika 2: Rentgenogram prečnega preseka plasti, pripravljene v talini AlSi20

to the τ_2 phase that occurs as the main product of the liquid-phase siliconizing process.

According to the phase analysis, the major phase present is $\text{TiAl}_{0.3}\text{Si}_{1.7}$ also known as the τ_2 phase, shown in **Figure 2**. This phase was already identified by the authors who studied the preparation of layers from silicon-rich melts.

3.2 Oxidation resistance

The oxidation resistance of the prepared layer was evaluated with cyclic-oxidation tests. The results of the oxidation at 850 °C are presented in **Figure 3**. The plot represents the weight gains as a function of the oxidation duration. The weight of the scales delaminated from the samples was added to the reported weight. The uncoated samples of titanium and TiAl6V4 alloy were used as the references. The weight gain of the TiAl6V4 alloy (0.0986 g/cm^2 after 144 h) is almost 64 times higher than that of the specimen coated with a protective Ti-Al-Si layer. It is clearly seen that the surface layer provides a considerable protection to the alloy when exposed to the

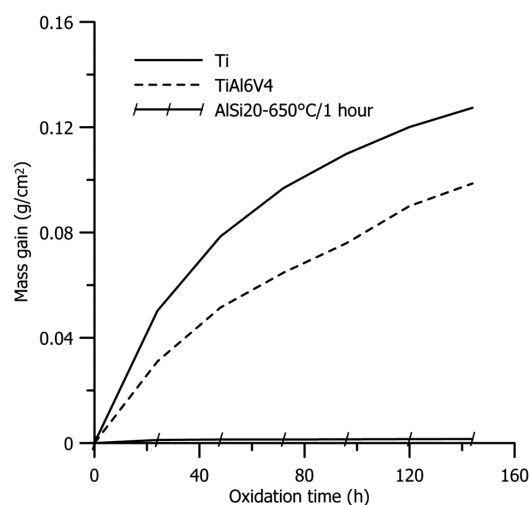


Figure 3: Cyclic-oxidation curves of coated TiAl6V4, uncoated TiAl6V4 and Ti at 850 °C

Slika 3: Krivulje ciklične oksidacije TiAl6V4 s prekritjem, TiAl6V4 brez prekritja in Ti, pri 850 °C

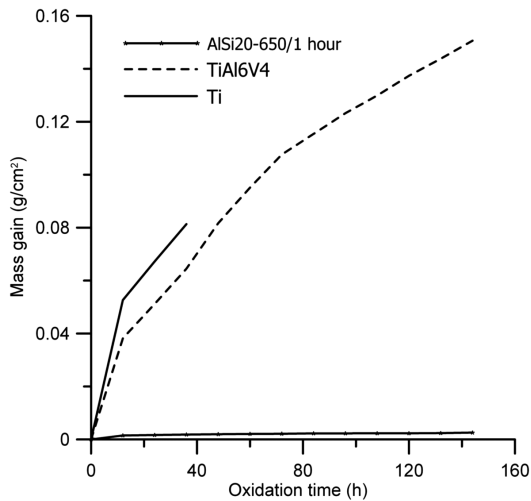


Figure 4: Cyclic-oxidation curves of coated TiAl6V4, uncoated TiAl6V4 and Ti at 950 °C

Slika 4: Krivulje ciklične oksidacije TiAl6V4 s prekritjem, TiAl6V4 brez prekritja in Ti, pri 950 °C

air at high temperatures. The character of the kinetic curve shown in **Figure 3** indicates that the greatest weight gain is reached during the first 24 h. After that, the weight of the tested sample remains almost constant. When taking into account that the testing temperature is much higher than the applicability limits of titanium alloys and the protection Ti-Al-Si layers, it can be stated that the proposed surface treatment provides an excellent protection.

The results of the cyclic oxidation at the temperature of 950 °C are summarized in **Figure 4**. Uncoated titanium exhibited an enormously high oxidation rate at the areas where the oxide scales were peeling off from the surface. In the case of the TiAl6V4-alloy specimens, the weight gains were also high. The oxidation kinetic curve does not exhibit a purely parabolic character, mainly due to a massive delamination of the surface oxide scales. The weight gain after 144 h of oxidation was almost 58 times higher in the case of the TiAl6V4 alloy (0.150 g/cm²) than in the case of the specimen coated with a protective layer (0.00257 g/cm²). The high oxidation resistance of the layers is attributed to the formation of compact silicide sub-layers, as will be discussed below.

3.3 Microstructure and phase analysis of the layers after the oxidation

After performing the oxidation experiments, the changes in the microstructure of the layers were examined with a scanning electron microscope. The microstructure of the cross-section of an as-oxidized layer after the exposure at 850 °C for 144 h is shown in **Figure 5**. It can be seen from the microstructure that the layer structure was subjected to considerable changes. The initially formed layer decomposed into several sub-layers. Chemical microanalysis results and results of the X-ray phase analysis indicate that two new sub-layers were

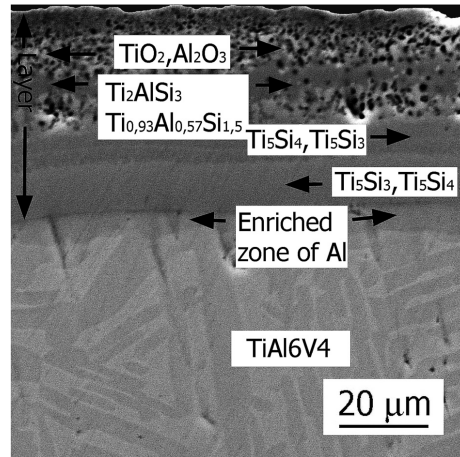


Figure 5: SEM macrograph of the cross-section of the layer prepared in the AlSi20 melt, after the oxidation at 850 °C for 144 h
Slika 5: SEM-posnetek preseka plasti, pripravljene v talini AlSi20, po oksidaciji 144 h na temperaturi 850 °C

formed, constituted by Ti₅Si₄ silicide, probably also containing the TiSi phase, detected with the phase analysis. These layers are followed by an inhomogeneous and porous layer, composed of ternary Ti-Al-Si phases. The SEM-EDS results revealed that the τ₂ phase is present, together with the other ternary phases, more enriched in aluminum. It is suggested that, in analogy to the structure of the layer oxidized at 950 °C, the initially present silicide-aluminide layer decomposes yielding thermodynamically stable silicides, whose subsequent growth acts as the driving force of aluminium diffusion into the substrate and toward the layer surface. This assumption is also supported by the presence of the original Ti-Al-Si phase with a higher aluminum content. This topmost sub-layer hinders the diffusion of aluminum.

The progressive weight gain experienced during the oxidation process indicate that in the early stages the weight gain is minimal, probably owing to the aluminum

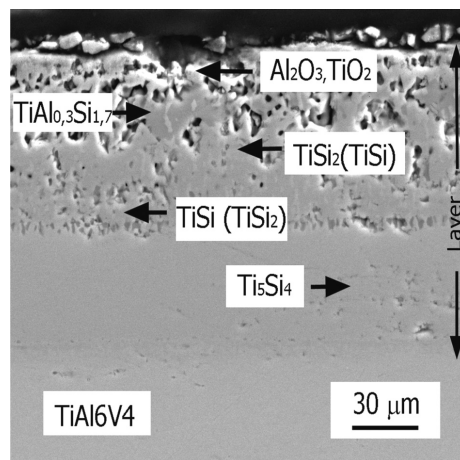


Figure 6: SEM micrograph of the cross-section of the layer prepared in the AlSi20 melt, after the oxidation at 950 °C for 144 h
Slika 6: SEM-posnetek preseka plasti, pripravljene v talini AlSi20, po oksidaciji 144 h na temperaturi 950 °C

diffusion toward the surface and its subsequent oxidation. After that, the oxidation rate is close to the experimental error of the measurement. This may be related to the fact that aluminum cannot diffuse easily within a spongy surface structure. The cross-section of the layer oxidized at 950 °C for 144 h is displayed in **Figure 6**. In this case, there were substantial changes to the layer structure as well. A new layer was formed, composed of several sub-layers. With the chemical microanalysis and X-ray analysis, it can be clearly demonstrated that the original τ_2 phase decomposed yielding silicide sub-layers.

The layer located close to the substrate is constituted by the Ti_5Si_3 silicide, which is more enriched in titanium. This layer is compact and homogeneous, with a thickness of approximately 45 μm . The next layer is a thin intermediate layer composed of nearly pure aluminum (with TiAl determined with the phase analysis). The layer after this one is an inhomogeneous and rather porous layer of TiSi silicide with a thickness of approximately 40 μm . This layer probably also contains particles of $TiSi_2$ silicide that can be observed in the microphotograph, but failed to be precisely detected with the SEM microanalysis. The presence of this silicide was confirmed with the XRD phase analysis. This silicide layer gradually turns into an inhomogeneous layer containing a great number of pores, in which Al and Ti oxides as well as residues of the original Ti-Al-Si phase were detected by means of a semi-quantitative chemical analysis. Most probably, this is related to the spongy surface of the prepared layers, as shown in **Figure 1**. This also makes oxygen diffusion easier and facilitates its oxidation on the layer surface. It can be assumed that at such a high temperature, the original silicide-aluminide phase tends to decompose yielding thermodynamically stable TiSi, Ti_5Si_4 (Ti_5Si_3 has a similar diffraction pattern), and $TiSi_2$ silicides, which were detected as the major constituents with the X-ray phase analysis.

The growth of the silicides causes aluminum to diffuse along the layer/substrate interface and, primarily, to diffuse toward the surface where it is subsequently oxidized. This assumption is also supported by the pre-

sence of a thin aluminum layer between the two silicide sub-layers, detected in the layer structure after the oxidation at both temperatures (850 °C and 950 °C). It can be assumed that the considerable resistance to high-temperature oxidation can be attributed mainly to the presence of the sub-layer constituted by the Ti_5Si_4 silicide. Different chemical compositions of the two sub-layers can be observed, which remain constant across the entire width of the newly formed sub-layers. Vanadium is uniformly distributed across the entire thickness of the layer.

The layers obtained with the oxidation at 850 °C and at 950 °C were subjected to a phase analysis. After the oxidation at the temperature of 850 °C (**Figure 7**), two major phases were detected. They were ternary silicide-aluminide phases having significantly higher aluminum contents than the original τ_2 phase. The minor phases included TiSi and TiAl. It was reported² that the intermetallic phases of TiAl and TiSi were formed due to the reaction of the substrate (Ti-Al alloy) with the ternary phase of Ti-Al-Si in accordance with the following Equation (1):



The achieved results suggest that nuclei of the TiSi phase were formed and continued to grow within the original layer. Due to this process, aluminum was pushed out and allowed to diffuse, producing aluminum-enriched Ti-Al-Si phases.

This assumption was confirmed by the presence of aluminum in the substrate near the layer/substrate interface, by the large quantities of aluminum found on the layer surface and by the presence of the thin intermediate layer at the interface between the silicide sub-layers. At the temperature of 950 °C these changes proceeded more rapidly and caused a nearly complete decomposition of the original layer formed by the τ_2 phase. The phases detected with the X-ray analysis at this high temperature included TiSi, $TiSi_2$, TiO_2 and the silicide-aluminide τ_2 phase as the dominant phase (**Figure 8**).

The minor phases detected were Ti_5Si_4 and Al_2O_3 . These analyses corresponded well with the microanalyses performed with SEM-EDS. Due to the forma-

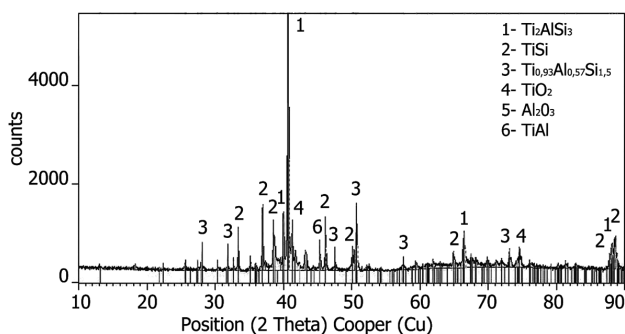


Figure 7: XRD pattern of the cross-section of the layer prepared in the AlSi20 melt, oxidized at 850 °C for 144 h

Slika 7: Rentgenogram prečnega preseka plasti, pripravljene v talini AlSi20, po oksidaciji 144 h na temperaturi 850 °C

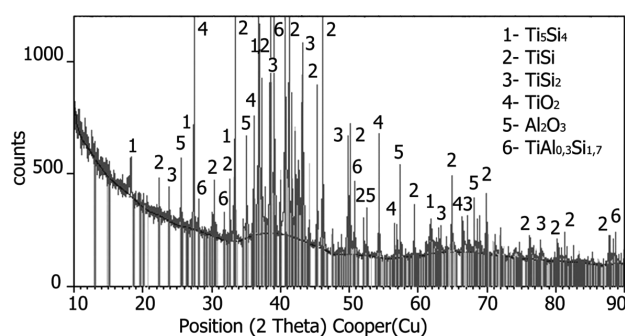


Figure 8: XRD pattern of the cross-section of the layer prepared in the AlSi20 melt, oxidized at 950 °C for 144 h

Slika 8: Rentgenogram prečnega preseka plasti, pripravljene v talini AlSi20, po oksidaciji 144 h na temperaturi 950 °C

tion of the thermodynamically stable TiSi and Ti₅Si₄ (Ti₅Si₃ has a similar diffraction pattern) silicides, the oxidation rates were considerably lower, as can be concluded from the data in **Figure 5**.

4 CONCLUSIONS

The liquid-phase silicon-aluminium coating process can be adopted to produce compact and homogeneous surface layers constituted by the ternary phase TiAl_{0.3}Si_{1.7}. Such layers are prepared from the AlSi₂O melt, at a temperature of 650 °C with the resulting thickness of 55 µm. The layers prepared in the present study provide outstanding protection from cyclic high-temperature oxidation, at both 850 °C and 950 °C in air. In the early stages of the oxidation, there is a gradual increase in the weight gain, but after about 30 h of exposure the weight gains are almost too low to be detected on the specimens used. The analyses of the as-oxidized layers indicate that the original layer decomposes, yielding compact and homogeneous sub-layers constituted solely by the Ti₅Si₃ and TiSi silicides. Due to the formation of these silicide sub-layers, a considerable oxidation resistance is reached, allowing the use of titanium alloys in high-temperature applications. The present study demonstrates that highly resistant protective layers suitable for high-temperature applications can be prepared using a simple and cost-effective technique.

Acknowledgement

The research of the surface-protective layers on TiAl6V4 is financially supported by research project VZ MSM 2579478701.

5 REFERENCES

- ¹ P. Novák, I. Marek, L. Mejzlíková, A. Michalcová, D. Vojtěch, Reactive-Sintering Production of Intermetallics, *Mater. Tehnol.*, 46 (2012) 6, 559–562
- ² H. P. Xiong, W. Mao, Y. H. Xie, W. L. Ma, Y. F. Chen, X. H. Li, J. P. Li, Y. Y. Cheng, Liquid-phase siliconizing by Al-Si alloys at the surface of a TiAl-based alloy and improvement in oxidation resistance, *Acta Materialia*, 52 (2004) 9, 2605–2620, doi:10.1016/j.actamat.2004.02.008
- ³ M. J. Freiría Gándara, Aluminium: The Metal of Choice, *Mater. Tehnol.*, 47 (2013) 3, 261–265
- ⁴ T. Kubatík, M. Jáglová, E. Kalabisová, V. Číhal, Improvement of oxidation resistance of TiAl6V4 alloy by siliconizing from liquid phase using melts with high silicon content, *Journal of Alloys and Compounds*, 509 (2011) 18, 5493–5499, doi:10.1016/j.jallcom.2011.02.068
- ⁵ D. B. Lee, S. W. Woo, High temperature oxidation of Ti-47%Al-1.7%W-3.7%Zr alloys, *Intermetallics*, 13 (2005) 2, 169–177, doi:10.1016/j.intermet.2004.07.043
- ⁶ D. Vojtěch, J. Čížkovský, P. Novák, J. Šerák, T. Fabián, Effect of niobium on the structure and high-temperature oxidation of TiAl-Ti₅Si₃ eutectic alloy, *Intermetallics*, 16 (2008) 7, 896–903, doi:10.1016/j.intermet.2008.04.005
- ⁷ Y. H. Celik, Investigating the Effect of Cutting Parameters on the Hole Quality in Drilling the TiAl6V4 Alloy, *Mater. Tehnol.*, 48 (2014) 5, 653–659
- ⁸ W. Liang, X. G. Zhao, Improving the oxidation resistance of TiAl-based alloy by siliconizing, *Scripta Materialia*, 44 (2001) 7, 1049–1054, doi:10.1016/S1359-6462(01)00675-3
- ⁹ J. D. Majumdar, A. Weisheit, B. L. Mordike, I. Manna, Laser surface alloying of Ti with Si, Al and Si+Al for an improved oxidation resistance, *Materials Science and Engineering A*, 266 (1999) 1–2, 123–134, doi:10.1016/S0921-5093(99)00045-3
- ¹⁰ M. Bassem, H. D. Kessler, D. J. McPherson, The Titanium-Silicon System, *Transactions of American Society for Metals*, 44 (1952), 518–538
- ¹¹ E. A. Loria, Gamma titanium aluminides as prospective structural materials, *Intermetallics*, 8 (2000) 9–11, 1339–1345, doi:10.1016/S0966-9795(00)00073-X
- ¹² K. Funatani, Emerging technology in surface modification of light metals, *Surface and Coatings Technology*, 133–134 (2000), 264–272, doi:10.1016/S0257-8972(00)00940-3
- ¹³ T. Kubatík, E. Kalabisová, Vrstvy Ti-Al-Si na titanu a slitině TiAl6V4, SVUOM, Praha 2010
- ¹⁴ C. Brukl, H. Nowotny, O. Schob, F. Benesovsky, The crystal structure of TiSi, Ti(Al,Si)₂ and Mo(Al,Si)₂, *Monatsh Chem*, 92 (1961), 781–788
- ¹⁵ K. Schubert, H. G. Meissner, A. Raman, W. Rossteutscher, Einige Strukturdaten metallischer Phasen, *Naturwissenschaften*, 51 (1964) 12, 287, doi:10.1007/BF00625465

CHARACTERIZATION AND KINETICS OF PLASMA-PASTE-BORIDED AISI 316 STEEL

KARAKTERIZACIJA IN KINETIKA PLAZMA BORIRANJA S PASTO JEKLA AISI 316

**Redouane Chegroune¹, Mourad Keddami¹, Zahra Nait Abdellah², Sukru Ulker³,
Sukru Taktak³, Ibrahim Gunes³**

¹Laboratoire de Technologie des Matériaux, Faculté G.M. et G.P., USTHB, B.P. 32, 16111 El-Alia, Bab-Ezzouar, Algiers, Algeria

²Département de Chimie, Faculté des sciences Université Mouloud Mammeri, Tizi-Ouzou, 15000, Algeria

³Department of Metallurgical and Materials Engineering, Faculty of Technology, Afyon Kocatepe University, 03200, Afyonkarahisar, Turkey
chegroune_redouane@yahoo.fr, rchegroune@usthb.dz

Prejem rokopisa – received: 2015-01-31; sprejem za objavo – accepted for publication: 2015-03-11

doi:10.17222/mit.2015.031

In this work, AISI 316 steel was plasma-paste borided in a gas mixture of 70 % H₂ – 30 % Ar using a mixture of 30 % SiC + 70 % B₂O₃ as a boron source. The samples were treated at temperatures of (700, 750 and 800) °C for (3, 5 and 7) h. The morphology of the formed boride layers was examined by light microscope and scanning electron microscope coupled to an EDS analyser. The borides present in the boride layer were identified by means of XRD analysis. The boron-activation energy for the AISI 316 steel was found to be equal to 250.8 kJ mol⁻¹. This value for the energy was compared to the literature data. A regression model based on a full factorial design was used to estimate the boride layers' thicknesses as a function of the boriding parameters: time and temperature. A comparison was made between the values of the boride layers' thicknesses estimated from the regression model with those given by an empirical relation. In addition, an iso-thickness diagram was plotted to predict the boride-layer thickness as a function of the processing parameters. This iso-thickness diagram can serve as a simple tool to select the optimum values for the boride layers' thicknesses for a practical utilisation in industry for this kind of steel.

Keywords: plasma paste boriding, kinetics, borides, transition zone, activation energy, regression model

V tem delu je bilo jeklo AISI 316 borirano s plazmo v mešanici plinov 70 % H₂ – 30 % Ar, z uporabo mešanice (30 % SiC + 70 % B₂O₃), kot vir bora. Vzorci so bili obdelani pri treh temperaturah (700, 750 in 800) °C v trajanju (3, 5 in 7) h. Morfologija nastale boridne plasti je bila preiskovana s svetlobnim mikroskopom in z vrstičnim elektronskim mikroskopom, opremljenim z EDS analizatorjem. Boridi v borirani plasti so bili identificirani z rentgensko analizo. Aktivacijska energija bora v jeklu AISI 316 je bila 250,8 kJ mol⁻¹. Ta vrednost je bila primerjana s podatki iz literature. Za določanje debeline borirane plasti v odvisnosti od parametrov boriranja (čas in temperatura), je bil uporabljen regresijski model, ki temelji na upoštevanju faktorjev. Izvršena je bila primerjava debeline borirane plasti, določene z regresijskim modelom in primerjava s tisto, ki je bila določena empirično. Za napovedovanje debeline borirane plasti je bil postavljen diagram enake debeline v odvisnosti od procesnih parametrov. Diagram enake debeline je uporaben kot enostavno orodje pri izbiri optimalne debeline borirane plasti, za praktično uporabo v industriji za to vrsto jekla.

Ključne besede: plazma boriranje s pasto, kinetika, boridi, prehodno področje, aktivacijska energija, regresijski model

1 INTRODUCTION

The boriding process is widely used in industry because of its broad application range.¹ This thermochemical treatment is generally performed in the range 700 °C to 1050 °C. The boriding process results in a metallic boride layer of about 20 µm – 300 µm thickness. The boriding treatment can be carried out in solid, liquid, gaseous or plasma media.²⁻⁵ Due to their relatively small size and very mobile nature, boron atoms can diffuse into the surface material to form hard borides. In the case of ferrous materials, the boriding treatment leads to the formation of either a single layer (Fe₂B) or a double-layer (FeB+Fe₂B) with a definite composition. The boride-layer thickness is determined by the temperature and treatment time. The characteristics of this boride layer depend on the physical state of the boron source used, the boriding temperature, the treatment time, and the chemical composition of the material to be borided.⁶⁻⁹

In order to lower the boriding temperature and the process time, ion-implantation boriding¹⁰, and plasma-assisted boriding¹¹ have been employed. Although the plasma boriding process has an advantage over the powder- or paste-boriding process, the use of expensive gases such as B₂H₆ and BCl₃ for the plasma-boriding process poses a major problem related to their toxicity. To overcome this problem, an alternative was recently proposed by using the plasma paste boriding (PPB) process. This recently developed method uses inert gases such as hydrogen, argon and nitrogen, making it very advantageous.⁵

The objective of this work was to investigate the boriding kinetics of AISI 316 steel by plasma paste boriding. The boron-activation energy for the AISI 316 steel was also estimated basing on our experimental results.

2 MATERIALS AND METHODS

In this study the AISI 316 austenitic steel used for the plasma paste boriding has the following chemical composition given in **Table 1**.

Table 1: Chemical composition of AISI 316 stainless steel (in mass fractions, w/%)

Tabela 1: Kemijska sestava nerjavnega jekla AISI 316 (v masnih deležih, w/%)

C	Cr	Mo	Mn	Si	Ni	P	S	Fe
0.08	16	2	2	0.75	10	0.045	0.03	balance

The samples had a cylindrical shape and were 20 mm in diameter and 5 mm in height. The surfaces of the AISI 316 steel were mechanically polished in sequence with (600, 800, 1200 and 2400) grit wet SiC emery paper, followed by fine polishing with an alumina slurry. The samples were cleaned in alcohol before the plasma paste boriding. In this study, a mixture of powder (30 % SiC + 70 % B₂O₃) constituting a boron source was applied, where silicon carbide (SiC) was used as a catalyst for the B₂O₃ paste. The plasma paste boriding was carried out in a dc plasma system, which is described in detail in the work by Gunes et al.⁵ Argon gas is important for the plasma system. It is used to change the plasma parameters such as the electron temperature and the electron density, which influence the production of active species by inelastic collisions, plasma reactions and plasma surface interactions. During the plasma paste boriding, H₂ gas plays an important role. Borax reacts with active hydrogen (H⁺) in a glow discharge. Atomic boron was produced through the decomposition of the boron hydride (B_xH_y) from the paste, and this atomic boron became the active boron, B⁺, within the molten borax or in the glow discharge. Finally, this active boron B⁺ diffused and reacted with the Fe to form the boride layer. The samples of AISI 316 austenitic steel were plasma paste borided at (700, 750 and 800) °C for (3, 5 and 7) h

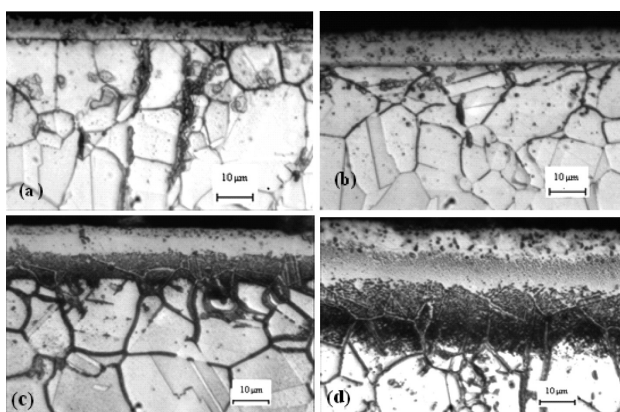


Figure 1: Light micrographs showing the microstructures of boride layers formed on the AISI 316 steel for different boriding parameters: a) 700 °C for 7 h, b) 750 °C for 7 h, c) 800 °C for 3 h, d) 800 °C for 5 h
Slika 1: Svetlobni posnetki mikrostruktur boriranih plasti na AISI 316 jeklu, pri različnih parametrih boriranja: a) 700 °C, 7 h, b) 750 °C, 7 h, c) 800 °C, 3 h, d) 800 °C, 5 h

in a gas mixture of 70 % H₂ – 30 % Ar under a constant pressure of 10 mbar. The temperature of the samples was measured by means of a chromel–alumel thermocouple, placed at the bottom of the treated samples. After the plasma paste boriding process, each borided sample was cleaned in an ultrasonic bath with alcohol. The treated samples were chemically etched using a chemical solution consisting of 20 mL glycerine, 10 mL HNO₃ and 30 mL HCl. The morphology of boride layers was observed using a light microscope (Olympus Vanox AHMTS) and a LEO 1430 VP model Scanning Electron Microscope (SEM). The values of boride layers' thicknesses were taken as averages of at least 10 measurements.

The presence of different borides formed in the boride layer was confirmed by means of an XRD analysis. This analysis was carried out using a Philips X-ray diffractometer with Cu-K_α radiation ($\lambda_{Cu} = 0.154$ nm). The distribution of alloying elements was analysed by energy-dispersive X-ray spectroscopy (EDS) from the surface towards the substrate.

EDS line analyses were performed to determine which element accumulated across the boride layer and the transition zone.

3 RESULTS AND DISCUSSION

3.1 Observation of the morphology of the boride layers

Figure 1 shows the etched cross-sections of boride layers formed on the surfaces of AISI 316 steel at different temperatures and for various treatment times. It reveals the formation of a bilayer configuration composed of FeB and Fe₂B. A transition zone exists in all the optical micrographs due to the accumulation of undissolved elements beneath the boride layer. The morphology of the boride-layer/transition-zone interface exhibited a flat diffusion front due to the effects of the main alloying elements such as Cr, Mo and Ni. This fact can be explained by the reduction of the active boron flux in the diffusion zone by the presence of these elements. It is clear that the thicknesses of the boride layer and the transition zone are affected by the process parameters (time and temperature). For instance, the boride layer's thickness reached a value of 10.4 µm at 750 °C for 7 h, while its corresponding value was 5.11 µm at a temperature of 700 °C during 7 h of treatment. Furthermore, some precipitates (i.e., chromium carbides) were also observed along the austenitic grain boundaries revealed by the chemical etchant composed of 20 mL glycerine, 10 mL HNO₃ and 30 mL HCl.

Figure 2 gives the cross-sectional views of microstructures of borided AISI 316 steel. The FeB and Fe₂B layers are discernable from a difference in contrast. The inner layer Fe₂B is clearer than the outer layer of FeB. The transition zone is also observed on the all SEM images. It is clear that the obtained boride layers are compact and continuous. The smooth morphology of the

boride-layer/transition-zone interface is observed in **Figure 2**.

Figure 3 shows the SEM image (for the EDS analysis) of cross-sections of the boride layer formed on AISI 316 steel at 800 °C for a treatment time of 3 h. The EDS line scan taken perpendicularly from the surface of the borided sample at 800 °C for 3 h showed a qualitative distribution of different elements along the boride layer and the transition zone. It indicates the precipitation of metallic borides inside the boride layer and an accumu-

lation of certain elements (such as Cr, C and Mo) in the transition zone (**Figure 3b**). In particular, molybdenum has a lower tendency to dissolve in the boride layer and tends to concentrate in the diffusion zone.¹² In addition, the boride layer thickness was found to increase with the boriding temperature.

3.2 XRD analysis

Figure 4 gives the XRD pattern recorded at the surface of the borided AISI 316 steel at 800 °C for 3 h of treatment. To confirm the presence of iron and metallic

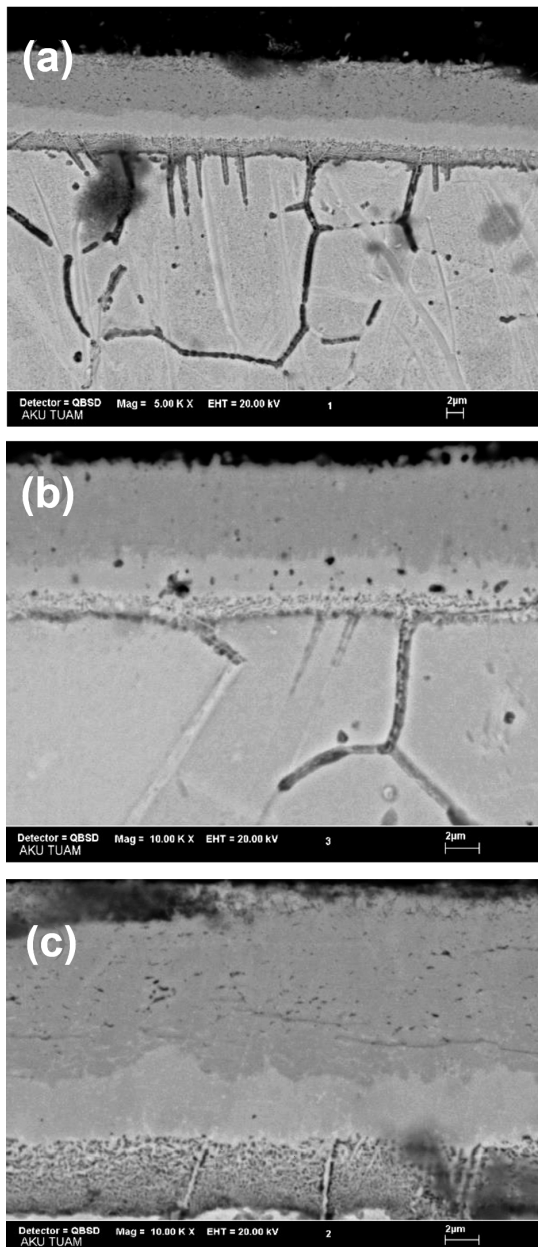


Figure 2: SEM micrographs of the cross-sections of boride layers formed on the AISI 316 steel for different boriding parameters: a) 750 °C for 5 h, b) 750 °C for 7 h, c) 800 °C for 3 h

Slika 2: SEM-posnetki preseka borirane plasti, nastale na AISI 316 jeklu pri različnih parametrih boriranja: a) 750 °C, 5 h, b) 750 °C, 7 h, c) 800 °C, 3 h

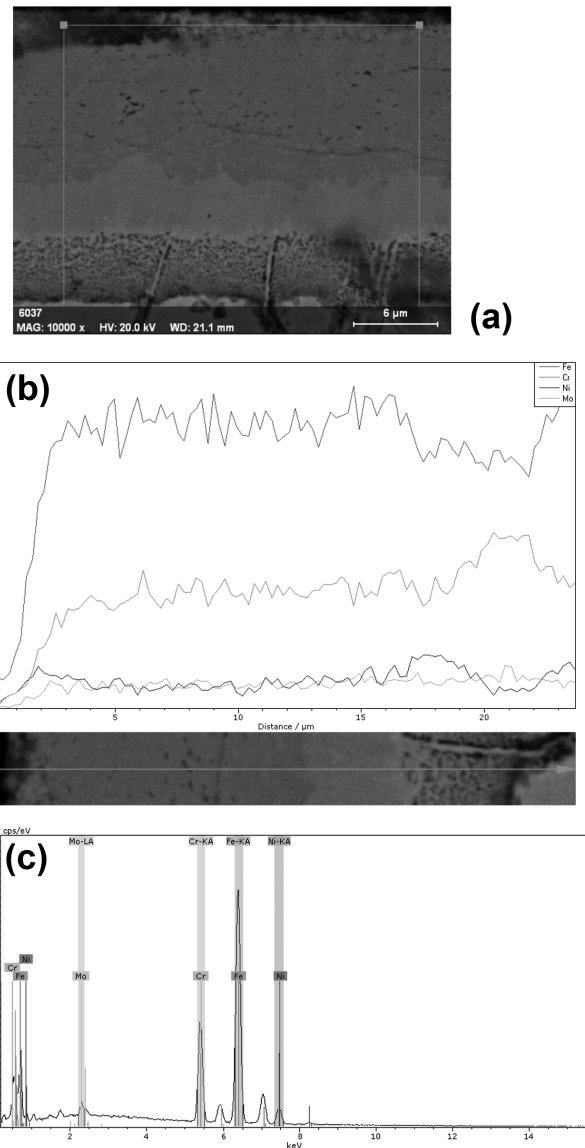


Figure 3: Cross-section of the borided AISI 316 steel at 800 °C for a treatment time of 3 h: a) SEM image of the cross-section of a borided sample for EDS analysis, b) EDS line scan across the borided zone, c) EDS spectrum of the selected zone (**Figure 3a**)

Slika 3: Presek jekla AISI 316, boriranega pri 800 °C, v trajanju 3 h: a) SEM-posnetek preseka borirane plasti za EDS-analizo, b) EDS-linijska analiza skozi borirano področje, c) EDS-spekter v izbranim področju, ki ga kaže **Slika 3a**

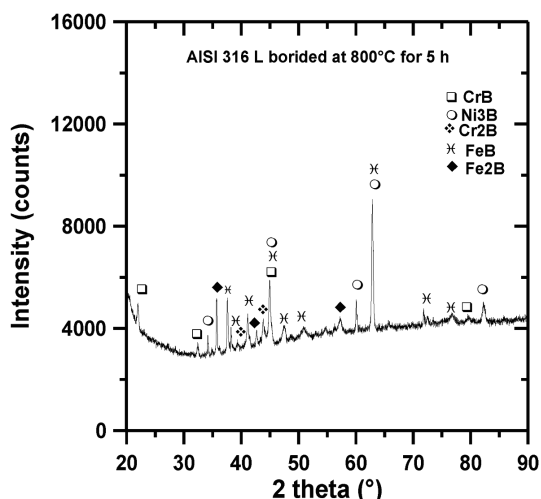


Figure 4: XRD pattern obtained at the surface of borided AISI 316 steel at 800 °C for 3 h of treatment

Slika 4: Rentgenogram, dobljen na površini jekla AISI 316, boriranega 3 h na 800 °C

borides, the corresponding files taken from the JCPDS database¹³ were used.

The iron borides (FeB and Fe₂B) were identified as well as the presence of metallic borides as precipitates within the boride layers such as CrB, Cr₂B and Ni₃B. In addition, Cr and Ni tend to dissolve in the boride layer and form independent metallic borides (CrB, Cr₂B and Ni₃B).

3.3 Estimation of the boron activation energy

The growth kinetics of boride layers is controlled by the boron diffusion into the substrate. The boride-layer thickness varies parabolically¹⁴⁻¹⁷ with the process time given by Equation (1):

$$u = k' \sqrt{t} \tag{1}$$

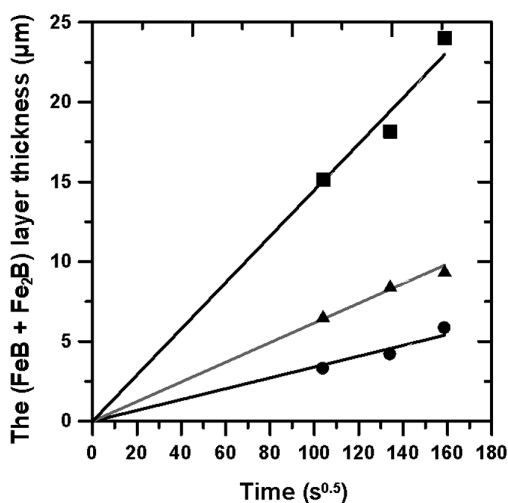


Figure 5: Evolution of the boride layer thickness versus the square root of time for increasing temperatures

Slika 5: Rast debeline borirane plasti pri naraščajoči temperaturi v odvisnosti od kvadratnega korena iz časa

where u is the boride-layer thickness (in μm), k' is a parabolic growth constant (in $\mu\text{m s}^{-1/2}$) at a given temperature, D is the diffusion coefficient of boron in the boride layer, and t is the boriding time. The time dependence of the boride layer thickness for increasing temperatures is given in Figure 5. It is clear that the boride layer varies linearly with the square root of time, which proves that the growth kinetics of the boride layer is governed by the diffusion phenomenon of boron atoms inside the substrate.

The relationship between the parabolic growth constant k' (in $\mu\text{m s}^{-1/2}$) and the boriding temperature T in Kelvin, can be expressed using an Arrhenius-type equation as follows:

$$k' = k \sqrt{D_0 \exp\left(-\frac{Q}{RT}\right)} \tag{2}$$

where D_0 is the diffusion coefficient of boron extrapolated at a value of $1/T = 0$. The Q parameter is the activation energy that indicates the amount of energy (kJ mol^{-1}) required for the reaction to occur, and R is the ideal gas constant ($R = 8.314 \text{ J mol}^{-1} \text{ K}^{-1}$). Taking the natural logarithm of Equation (2), we obtain Equation (3):

$$\ln(k'^2) = \ln(k^2) + \ln(D_0) - \left(\frac{Q}{RT}\right) \tag{3}$$

The activation energy Q can be easily deduced from the slope of the curve relating $\ln(k'^2)$ to the inverse of the temperature. Figure 6 provides the temperature dependence of the natural logarithm of the square of the parabolic growth constant k'^2 .

The reported values for boron-activation energies^{4,18-25} for borided steels are listed in Table 2 together with the value of the boron-activation energy ($250.8 \text{ kJ mol}^{-1}$) estimated from this work. However, these

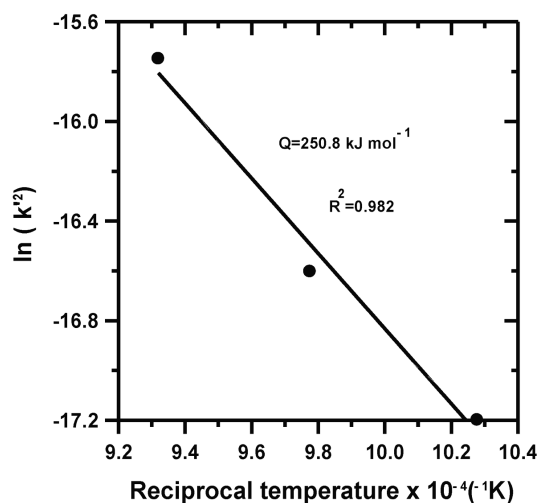


Figure 6: Temperature dependence of the square of the parabolic growth constant

Slika 6: Odvisnost temperature od kvadratnega korena parabolne konstante rasti

values for the boron-activation energies for different steels depended on various factors such as: the boriding method, the chemical composition of the base steel, the nature of the boriding agent, and the mechanism of boron diffusion. For the paste plasma boriding of AISI 316 steel, the high activation energy shown in **Table 2** is ascribed to the formation of FeB, Fe₂B, CrB, Cr₂B and Ni₃B phases in the boride layer. The obtained value of the boron-activation energy (250.8 kJ mol⁻¹) from this work, can also be interpreted as the required barrier to allow boron diffusion inside the steel substrate. Thus, the diffusion phenomenon of boron atoms can occur along the grains boundaries and also in the volume to form the boride layer on the AISI 316 steel.

Table 2: Values of boron-activation energies obtained in the case of borided steels using different methods

Tabela 2: Vrednosti aktivacijske energije bora, dobljene pri boriranju jekel z različnimi metodami

Material	Boriding method	Q (kJ mol ⁻¹)	References
AISI 304	Salt Bath	253.35	18
AISI H13	Salt bath	244.37	18
AISI 4140	Paste	168.5	19
AISI H13	Powder	186.2	20
AISI 1040	Powder	168	21
AISI440C	Powder	340.4	22
AISI 316	Powder	199	23
AISI 51100	Plasma	106	24
AISI 304	Plasma Paste Boriding	123	4
AISI8620	Plasma Paste Boriding	124.7–138.5	25
AISI 316	Plasma Paste boriding	250.8	This work

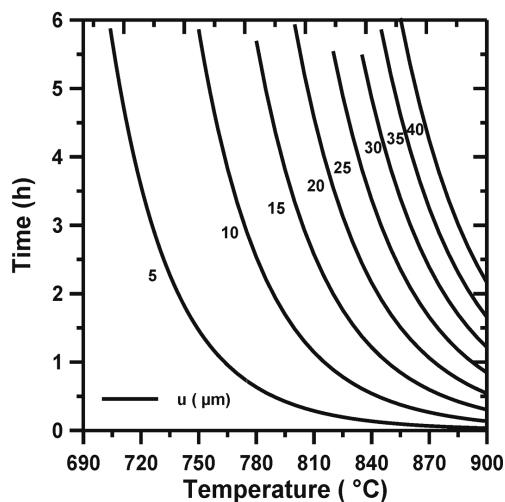


Figure 7: Iso-thickness diagram describing the evolution of the boride-layer thickness as a function of the boriding parameters (time and temperature)

Slika 7: Diagram enakih debelin opisuje razvoj debeline borirane plasti v odvisnosti od parametrov boriranja (čas in temperatura)

3.4 Prediction of the boride-layer thickness with a regression model

A full factorial design with two factors at three levels²⁶ was used to predict the boride-layer thickness as a function of the boriding parameters (time and temperature).

Using this approach, Equation (4) was obtained as follows:

$$u = 761.50 - 2.0856T - 11.763t + 0.015825tT + 0.001435T^2 + 0.108333t^2 \quad (4)$$

where t is the boriding time (h) and T is the temperature in degree Celsius.

Table 3: Comparison between the experimental values of the boride-layer thicknesses and those given by Equation (1) and the regression model (Equation 4) in the temperature range 700–800 °C

Tabela 3: Primerjava eksperimentalnih vrednosti debeline borirane plasti z vrednostmi iz enačbe (1) in iz regresijskega modela (enačba 4), v temperaturnem območju 700–800 °C

T (°C)	Time (h)	Predicted (FeB+Fe ₂ B) Layer thickness (μm) Equation (1)	Predicted (FeB+Fe ₂ B) Layer thickness (μm) Equation (4)	Experimental (FeB+Fe ₂ B) layer thickness (μm)
700	3	3.59	3.34	3.30
700	5	3.92	4.32	4.20
700	7	5.11	5.11	5.84
750	3	5.72	7.15	6.60
750	5	7.63	9.23	8.50
750	7	10.40	10.92	9.45
800	3	15.02	14.20	15.13
800	5	18.51	18.34	18.16
800	7	22.86	21.70	24.00

Table 3 compares between the experimental values of the boride layers' thicknesses and the predicted values using Equations (1) and (4) in the temperature range 700 °C – 800 °C. A good agreement was observed between the simulated values of the boride layers' thicknesses and those obtained experimentally. Equation (1) can be used to plot the iso-thickness diagram shown in **Figure 7**. The iso-thickness diagram can serve as a simple tool to select the optimum value of the boride-layer thickness for a practical use of the plasma paste borided AISI 316 steel in industry. As a rule, thin layers (e.g., 15 μm – 20 μm) are used to protect against adhesive wear (such as chip-less shaping and metal stamping dies and tools), whereas thick layers are recommended to combat abrasive wear (extrusion tooling for plastics with abrasive fillers and pressing tools for the ceramics industry). In the case of low-carbon steels and low-alloy steels, the optimum boride-layer thicknesses are between 50 μm and 250 μm.

4 CONCLUSIONS

In this work AISI 316 steel was plasma paste borided in a gas mixture of 70 % H₂ – 30 % Ar using a mixture of 30 % SiC + 70 % B₂O₃. The boride-layer/transition-

zone interface had a smooth morphology with a boride layer thickness ranging from 3.3 μm to 24 μm .

The boride layer formed on the surface of the AISI 316 was composed of FeB, Fe₂B, CrB, Cr₂B and Ni₃B phases. This result was confirmed by XRD analysis and a transition zone was also visible beneath the boride layer. The boron-activation energy for the AISI 316 steel was estimated to be 250.8 kJ mol⁻¹. This value was interpreted as the required quantity of energy to stimulate the boron diffusion in the preferential direction (0 0 1). This value of the boron-activation energy was comparable to values found in the literature.

In addition, an iso-thickness diagram describing the evolution of the boride-layer thickness as a function of the boriding parameters was proposed. It can serve as a simple tool to select the optimum boride layer thickness according to the practical use of borided AISI 316 steel.

5 REFERENCES

- A. K. Sinha, Boriding (Boronizing) of steels, ASM Handbook, vol. 4, Heat treating, ASM International, 1991, 437–447
- S. Ulker, I. Gunes, S. Taktak, Investigation of tribological behaviour of plasma paste boronized of AISI 8620, 52100 and 440c steels, Indian Journal of Engineering and Materials Sciences, 18 (2011) 5, 370–376
- I. Uslu, H. Comert, M. Ipek, O. Ozdemir, C. Bindal, Evaluation of borides formed on AISI P20 steel, Materials and Design, 28 (2007) 1, 55–61, doi:10.1016/j.matdes.2005.06.013
- J. H. Yoon, Y. K. Jee, S. Y. Lee, Plasma paste boronizing treatment of the stainless steel AISI 304, Surface and Coatings Technology, 112 (1999) 1–3, 71–75, doi:10.1016/S0257-8972(98)00743-9
- I. Gunes, S. Ulker, S. Taktak, Plasma paste boronizing of AISI 8620, 52100 and 440C steels, Materials and Design, 32 (2011) 4, 2380–2386, doi:10.1016/j.matdes.2010.11.031
- C. Bindal, A. H. Ucisik, Characterization of boriding of 0.3% C, 0.02% P plain carbon steel, Vacuum, 82 (2008) 1, 90–94, doi:10.1016/j.vacuum.2007.04.039
- M. Keddama, M. Kulka, N. Makuch, A. Pertek, L. Małdziński, A kinetic model for estimating the boron activation energies in the FeB and Fe₂B layers during the gas-boriding of Armco iron: Effect of boride incubation times, Applied Surface Science, 298 (2014), 155–163, doi:10.1016/j.apsusc.2014.01.151
- S. Sahin, C. Meric, Investigation of the effect of boronizing on cast irons, Materials Research Bulletin, 37 (2002) 5, 971–979, doi:10.1016/S0025-5408(02)00697-9
- I. Campos-Silva, M. Ortiz-Dominguez, M. Keddama, N. Lopez-Perrusquia, A. Carmona-Vargas, M. Elias-Espinosa, Kinetics of the formation of Fe₂B layers in gray cast iron: Effects of boron concentration and boride incubation time, Applied Surface Science, 255 (2009) 22, 9290–9295, doi:10.1016/j.apsusc.2009.07.029
- J. G. Buijnsters, P. Shankar, P. Gopalakrishnan, W. J. P. Van Enkevort, J. J. Schermer, S. S. Ramakrishnan, J. J. Ter Meulen, Diffusion-modified boride interlayers for chemical vapour deposition of low-residual-stress diamond films on steel substrates, Thin Solid Films, 426 (2003) 1–2, 85–93, doi:10.1016/S0040-6090(03)00013-0
- K. A. Khor, L. G. Yu, G. Sundararajan, Formation of hard tungsten boride layer by spark plasma sintering boriding, Thin Solid Films, 478 (2005) 1–2, 232–237, doi:10.1016/j.tsf.2004.07.004
- I. S. Dukarevich, M. V. Mozharov, A. S. Shigarev, Redistribution of elements in boride coatings, Metal Science and Heat Treatment, 15 (1973) 2, 160–162, doi:10.1007/BF00679753
- JCPDS- International Centre for Diffraction Data, PCPDF WIN, Version 202, 1999
- N. Ucar, O. B. Aytar, A. Calik, Temperature behaviour of the boride layer of a low-carbon microalloyed steel, Mater. Tehnol., 46 (2012) 6, 621–625
- X. Tian, Y. L. Yang, S. J. Sun, J. An, Y. Lu, Z. G. Wang, Tensile Properties of Boronized N80 Steel Tube Cooled by Different Methods, Journal of Materials Engineering and Performance, 18 (2009) 2, 162–167, doi:10.1007/s11665-008-9270-0
- L. Xu, X. Wu, H. Wang, Influence of Surface Nano-structured Treatment on Pack Boriding of H13 Steel, J. Mater. Sci. Technol., 23 (2007) 4, 525–528
- B. Bouarour, M. Keddama, O. Allaoui, O. Azouani, Boriding kinetics of C35 steel: Estimation of boron activation energy and the mass gain, Metallurgical Research and Technology, 111 (2014) 2, 67–73, doi:10.1051/metal/2014015
- S. Taktak, A study on the diffusion kinetics of borides on boronized Cr-based steels, Journal of Materials Science, 41 (2006) 22, 7590–7596, doi:10.1007/s10853-006-0847-4
- Z. Nait Abdallah, M. Keddama, A. Elias, Evaluation of the effective diffusion coefficient of boron in the Fe₂B phase in the presence of chemical stresses, International Journal of Materials Research, 104 (2013) 3, 260–265, doi:10.3139/146.110862
- K. Genel, Boriding kinetics of H13 steel, Vacuum, 80 (2006) 5, 451–457, doi:10.1016/j.vacuum.2005.07.013
- I. Uslu, H. Comert, M. Ipek, F. G. Celebi, O. Ozdemir, C. Bindal, A comparison of borides formed on AISI 1040 and AISI P20 steels, Materials and Design, 28 (2007) 28, 1819–1826, doi:10.1016/j.matdes.2006.04.019
- Y. Kayali, I. Günes, S. Ulu, Diffusion kinetics of borided AISI 52100 and AISI 440C steels, Vacuum, 86 (2012) 10, 1428–1434, doi:10.1016/j.vacuum.2012.03.030
- O. Ozdemir, M. A. Omar, M. Usta, S. Zeytin, C. Bindal, A. H. Ucisik, An investigation on boriding kinetics of AISI 316 stainless steel, Vacuum, 83 (2008) 1, 175–179, doi:10.1016/j.vacuum.2008.03.026
- M. Ipek, G. Celebi Efe, I. Ozbek, S. Zeytin, C. Bindal, Investigation of boronizing kinetics of AISI 51100 steel, Journal of Materials Engineering and Performance, 21 (2012) 5, 733–738, doi:10.1007/s11665-012-0192-5
- I. Gunes, S. Taktak, C. Bindal, Y. Yalcin, S. Ulker, Y. Kayali, Investigation of diffusion kinetics of plasma paste borided AISI 8620 steel using a mixture of B₂O₃ paste and B₄C/SiC, Sadhana – Academy Proceedings in Engineering Sciences, 38 (2013) 3, 513–526, doi:10.1007/s12046-013-0136-2
- J. Goupy, Plans d'expériences pour surfaces de réponses, Edition Dunod, Paris 1999, 1–409

INVESTIGATION OF THE ADHESION AND WEAR PROPERTIES OF BORIDED AISI H10 STEEL

PREISKAVA ADHEZIJE IN OBRABNIH LASTNOSTI BORIRANEGA JEKLA AISI H10

Ibrahim Gunes, Melih Ozcatal

Afyon Kocatepe University, Faculty of Technology, Department of Metallurgical and Materials Engineering, 03200 Afyonkarahisar, Turkey
igunes@aku.edu.tr

Prejem rokopisa – received: 2015-02-02; sprejem za objavo – accepted for publication: 2015-03-11

doi:10.17222/mit.2015.032

In the present study the effect of the boriding process on the adhesion and wear properties of AISI H10 steel has been investigated. The boride layer was characterized by light microscopy, X-ray diffraction and the Vickers microhardness. The X-ray diffraction analyses of the boride layers on the surface of the steels revealed the existence of the compounds FeB, Fe₂B, CrB, Cr₂B and MoB. Depending on the chemical composition of the steel, the boride-layer thickness on the surface of the AISI H10 steel was found to be 63.72 μm . The hardness of the boride compounds formed on the surface of the steels ranged from 1648 to 1964 HV_{0.05}, whereas the Vickers hardness value of the untreated steel was 306 HV_{0.05}. The wear tests were carried out in a ball-on-disc arrangement under dry-friction conditions at room temperature with an applied load of 10 N and with a sliding speed of 0.3 m s⁻¹ for a sliding distance of 1000 m. It was observed that the wear rate of the borided and non-borided AISI H10 steels ranged from 3.15 mm³/N m to 62.84 mm³/N m.

Keywords: AISI H10, boriding, microhardness, adhesion, wear rate

V predstavljeni študiji je bil preiskovan vpliv postopka boriranja na adhezijo in obrabne lastnosti jekla AISI H10. Borirana plast je bila karakterizirana s svetlobno mikroskopijo, z rentgensko difrakcijo in z merjenjem mikrotredote po Vickersu. Analiza z rentgensko difrakcijo borirane plasti na površini jekel je odkrila prisotnost spojin: FeB, Fe₂B, CrB, Cr₂B in MoB. Odvisno od kemijske sestave jekla je bila debelina borirane plasti na površini jekla AISI H10 okrog 63,72 μm . Trdota borovih spojin, ki so nastale na površini jekel, je bila med 1648 HV_{0.05} do 1964 HV_{0.05}, medtem ko je bila Vickers trdota neobdelanega jekla 306 HV_{0.05}. Izvršeni so bili preizkusi obrabe z napravo s kroglico na plošči pri pogojih suhega trenja pri sobni temperaturi z uporabljeno obremenitvijo 10 N, s hitrostjo drsenja 0,3 m/s pri dolžini drsenja 1000 m. Hitrost obrabe boriranega in neboriranega jekla AISI H10 je bila v območju od 3,15 mm³/N m do 62,84 mm³/N m.

Ključne besede: AISI H10, boriranje, mikrotredota, adhezija, hitrost obrabe

1 INTRODUCTION

Boriding is a thermochemical treatment in which boron atoms diffuse through the surface of metallic substrates. As boron is an element of relatively small size it diffuses into a variety of metals, including ferrous, non-ferrous and some superalloys.¹⁻⁵ The boriding process provides a high surface hardness as well as good wear properties in terms of adhesion, abrasion, and surface fatigue. The boriding treatment is carried out by heating substrates in the temperature range 973 K –1323 K for a period of time ranging from 0.5 h to 12 h. The boron is supplied to the material surface by a solid, liquid, gaseous or plasma medium.⁶⁻⁹

The wear and friction behaviors of borided steels are broadly dependent on the following surface and boriding conditions: boriding time and temperature, chemical composition, mechanical properties, physical structure, lubricant, surface roughness, etc. As a result of these conditions, the life of machine components may be affected. The efficiency, durability and reliability are improved by reducing the friction and wear rate through certain materials, surface modifications and lubricants.^{10,11}

Boriding is used in numerous applications in industries such as the manufacturing of machine parts for plastics and food processing, packaging and tooling, as well as pumps and hydraulic machine parts, crankshafts, rolls and heavy gears, motor and car construction. The wear behavior of borided steels has been evaluated by a number of investigators.¹²⁻¹⁶ However, there is no information about the friction and wear behaviors of borided AISI H10 steel. The main objective of this study was to investigate the effect of the boriding process on the wear behavior of borided AISI H10 steel. The structural, Daimler-Benz adhesion and tribological properties were investigated using light microscopy, XRD, SEM, EDS, microhardness tests and a ball-on-disc tribotester.

2 EXPERIMENTAL PROCEDURES

2.1 Boriding and characterization

The AISI H10 steel contained $w(\text{C}) = 0.32\%$, $w(\text{Cr}) = 3.15\%$, $w(\text{Mo}) = 2.90\%$, $w(\text{V}) = 0.65\%$ and $w(\text{Mn}) = 0.40\%$. The test specimens were cut into $\varnothing 25\text{ mm} \times 8\text{ mm}$ discs, ground to 1200 G and polished using a diamond solution. The boriding heat treatment was

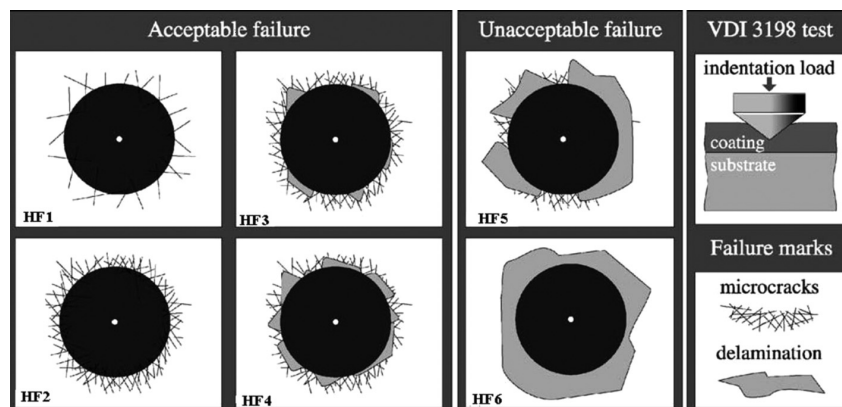


Figure 1: The principle of the VDI 3198 indentation test

Slika 1: Načelo VDI 3198 preizkusa vtiskovanja

carried out in a solid medium containing an Ekabor-II powder mixture placed in an electrical resistance furnace operated at temperatures of 1123 K and 1223 K for 2 h and 6 h under atmospheric pressure. The microstructures of polished and etched cross-sections of the specimens were observed under a Nikon MA100 light microscope. The presence of borides formed in the coating layer was confirmed by means of X-ray diffraction equipment (Shimadzu XRD 6000) using Cu- $K\alpha$ radiation. The hardness measurements of the boride layer on steel and an untreated steel substrate were made on the cross-sections using a Shimadzu HMV-2 Vickers indenter with a 50 g load.

The Daimler-Benz Rockwell-C adhesion test was used to assess the adhesion of the boride layers. This well-known Rockwell-C indentation test is prescribed by the VDI 3198 norm, as a destructive quality test for coated compounds.¹⁷⁻²⁰ The principle of this method is presented in the upper-right-hand part of Figure 1.¹⁸ A load of 1471 N was applied to cause coating damage adjacent to the boundary of the indentation. Three indentations were conducted for each specimen and scanning electron microscopy was employed to evaluate the test.

2.2 Friction and wear

To perform the friction and wear of the borided samples a ball-on-disc test device was used. In the wear tests, WC-Co balls of 8 mm in diameter supplied by H. C. Starck Ceramics GmbH were used. Errors caused by the distortion of the surface were eliminated by using a separate abrasion element (WC-Co ball) for each test. The wear experiments were carried out in a ball-on-disc arrangement under dry-friction conditions at room temperature with an applied load of 10 N and with sliding speeds of 0.3 m s⁻¹ for a sliding distance of 1000 m (track diameter 0.015 m). The wear tests were made with an 8-mm diameter WC-Co ball with a Young's modulus of 598 GPa. The maximum compressive contact pressure in the central point of the contact area was calculated from the Hertzian equation.²¹ According to the

Hertzian equation, the maximum contact pressures of 2824 MPa (for disc $E_d = 325$ GPa and $\nu_d = 0.26$, for ball $E_b = 598$ GPa and $\nu_b = 0.22$) were obtained at a normal load of 10 N. Before and after each wear test, each sample and abrasion element was cleaned with alcohol. After the test, the wear volumes of the samples were quantified by multiplying the cross-sectional areas of the wear by the width of the wear track obtained using a Taylor-Hobson Rugosimeter Surtronic 25 device. The wear rate was calculated with the following Equation (1):

$$W_k = \frac{W_v}{MS} \quad (\text{mm}^3/\text{N m}) \quad (1)$$

where W_k is the wear rate, W_v is the worn volume, M is the applied load and S is the sliding distance. Friction coefficients depending on the sliding distance were obtained through a friction-coefficient program. The surface profiles of the wear tracks on the samples and the surface roughness were measured using a Taylor-Hobson Rugosimeter Surtronic 25. The worn surfaces were investigated using scanning electron microscopy

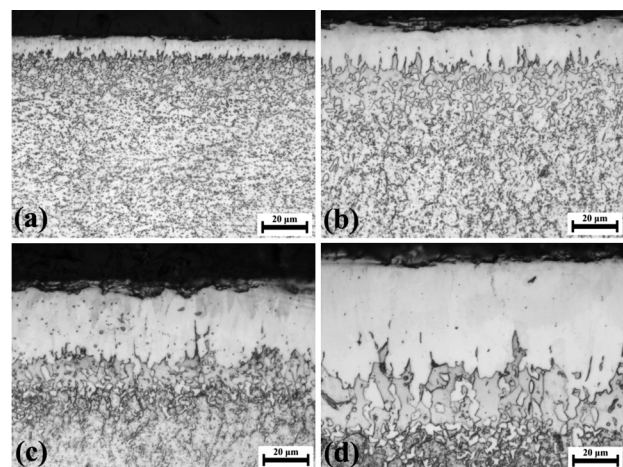


Figure 2: The cross-section of borided AISI H10 steel: a) 1123 K – 2 h, b) 1123 K – 6 h, c) 1223 K – 2 h, d) 1223 K – 6 h

Slika 2: Presek boriranega jekla AISI H10: a) 1123 K – 2 h, b) 1123 K – 6 h, c) 1223 K – 2 h, d) 1223 K – 6 h

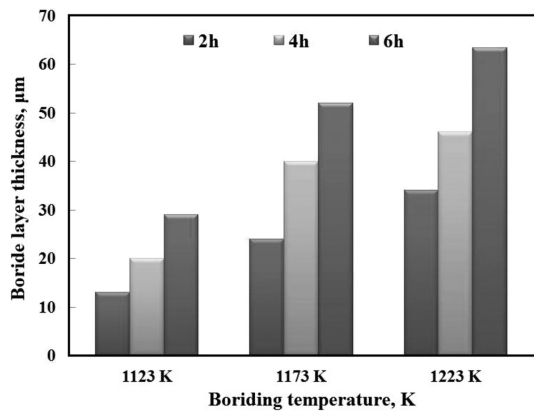


Figure 3: The thickness values of the boride layers with respect to boriding time and temperatures

Slika 3: Vrednosti debeline boriranih plasti glede na čas in temperaturo boriranja

(SEM), energy-dispersive X-ray spectroscopy (EDS) and a Nanovea ST-400 non-contact optical profiler.

3 RESULTS AND DISCUSSION

3.1 Characterization of the boride coatings

The cross-section light micrographs of the borided AISI H10 steel for temperatures of 1123 K and 1223 K for 2 h and 6 h are shown in Figure 2. As can be seen, the borides formed on the AISI H10 substrate have a saw-tooth morphology. It was found that the coating/matrix interface and the matrix could be easily

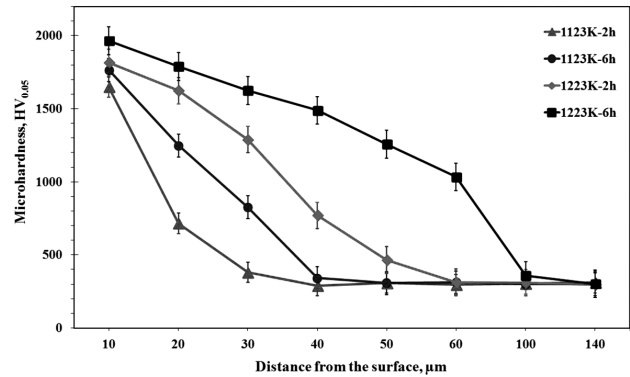


Figure 5: The variation of hardness depth in the borided AISI H10 steel

Slika 5: Spreminjanje trdote v globino pri boriranem jeklu AISI H10

distinguished and the boride layer had a columnar structure. Depending on the boriding time and temperature, the boride-layer thickness on the surface of the AISI H10 steel ranged from 12.86 µm and 63.72 µm (Figure 3).

Figure 4 shows the XRD pattern obtained from the surface of the borided AISI H10 steel at 1123 K and 1223 K for treatment times of 2 h and 6 h. The XRD patterns show that the boride layer consists of borides such as MB and M₂B (M=Metal; Fe, Cr). The XRD results showed that the boride layers formed on the H10 steel contained the FeB, Fe₂B, CrB, Cr₂B and MoB phases (Figures 4a and 4d).

Microhardness measurements were carried out on cross-sections from the surface to the interior along a

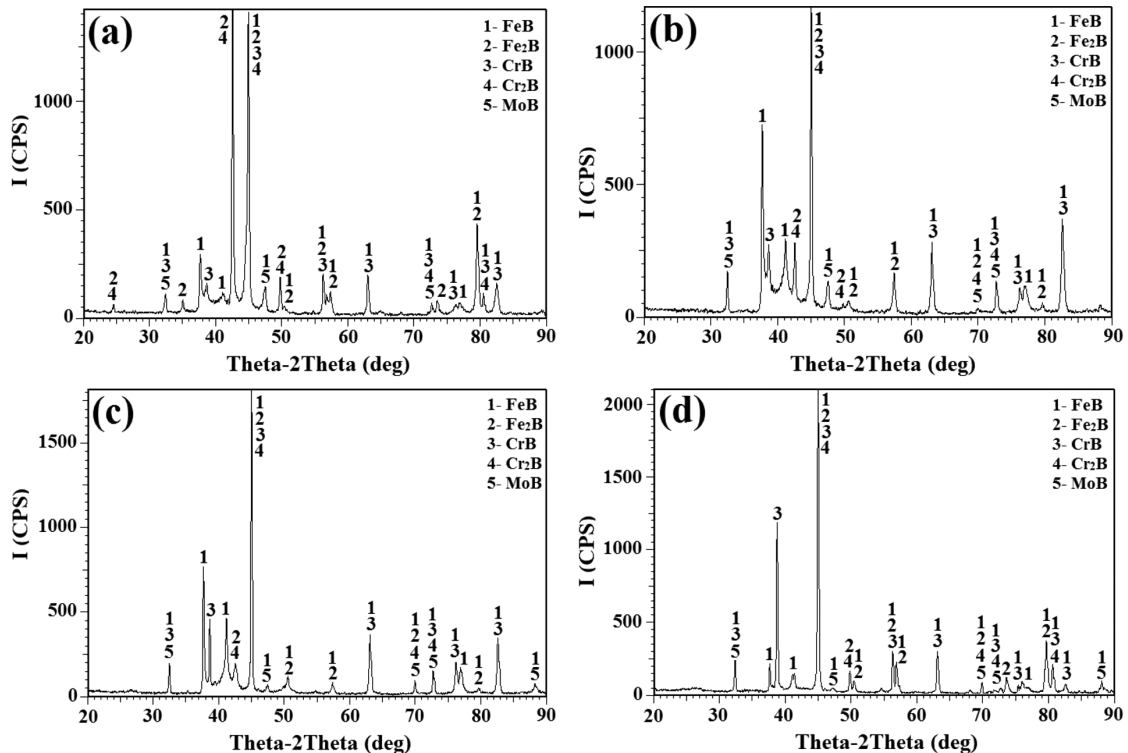


Figure 4: X-ray diffraction patterns of borided AISI H10 steel: a) 1123 K – 2 h, b) 1123 K – 6 h, c) 1223 K – 2 h, d) 1223 K – 6 h

Slika 4: Rentgenska difrakcija boriranega jekla AISI H10: a) 1123 K – 2 h, b) 1123 K – 6 h, c) 1223 K – 2 h, d) 1223 K – 6 h

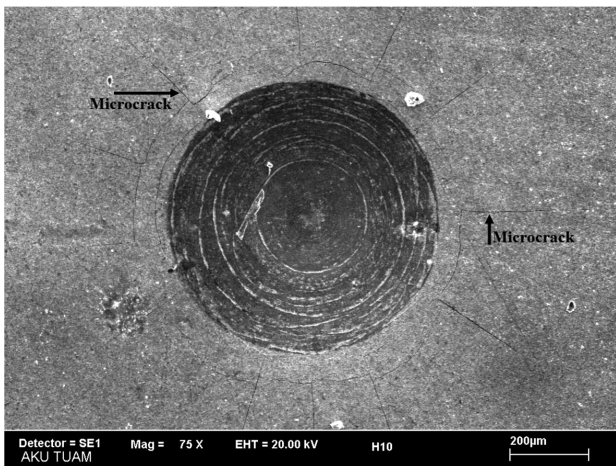


Figure 6: SEM micrograph of VDI adhesion test on AISI H10 steel
Slika 6: SEM-posnetek VDI preizkusa adhezije na jeklu AISI H10

line (Figure 5). The microhardness of the boride layers was measured at 10 different locations at the same distance from the surface and the average value was taken as the hardness.

The boride-layer hardness of the sample borided at 1223 K for 6 h was found to be 1964 HV_{0.05}, the boride-layer hardness of the sample borided at 1223 K for 2 h was 1816 HV_{0.05}, the boride-layer hardness of the sample borided at 1123 K for 6 h was 1765 HV_{0.05}, while the boride-layer hardness of the sample borided at 1123 K for 2 h was 1648 HV_{0.05}. On the other hand, the Vickers hardness values were 306 HV_{0.05}, for the untreated AISI H10 steel. Figure 5 shows that increasing the boriding temperature and treatment time increases the boride-layer hardness. When the hardness of the boride layer is compared with the matrix, the boride-layer hardness is approximately five times greater than that of the matrix.

3.2 Rockwell-C adhesion

A standard Rockwell-C hardness tester was employed in this study. The damage to the boride layer was

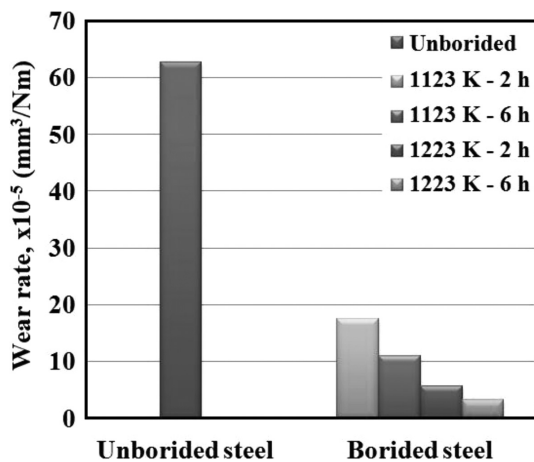


Figure 7: The wear rate of non-borided and borided AISI H10 steel
Slika 7: Hitrost obrabe neboriranega in boriranega jekla AISI H10

compared with the adhesion-strength quality maps HF1–HF6. In general, the adhesion-strength quality HF1–HF4 defines sufficient adhesion, whereas HF5 and HF6 represent insufficient adhesion.¹⁵ SEM micrographs of the indentation craters for the samples borided at 1223 K for 6 h are given in Figure 6. There were radial cracks at the perimeter of the indentation craters without flaking and the adhesion of the boride layer on the sample borided at 1223 K for 6 h was sufficient. The adhesion-strength quality of this boride layer is related to HF1.

3.3 Friction and wear behavior

Table 1 shows the surface-roughness values of the borided and non-borided AISI H10 steel.

The surface roughness of the sample borided at 1123 K for 2 h was found to be 0.34 µm, the boride-layer hardness of the sample borided at 1123 K for 6 h was 0.39 µm, the boride-layer hardness of the sample borided at 1223 K for 2 h was 0.45 µm, while the boride-layer hardness of the sample borided at 1223 K for 6 h was 0.52 µm. On the other hand, the surface-roughness value was 0.09 µm for the untreated AISI H10 steel. Table 1 shows that increasing the boriding temperature and treatment time increases the surface-roughness values. For the AISI H10 steel it was observed that the surface-roughness values increased with the boriding treatment.

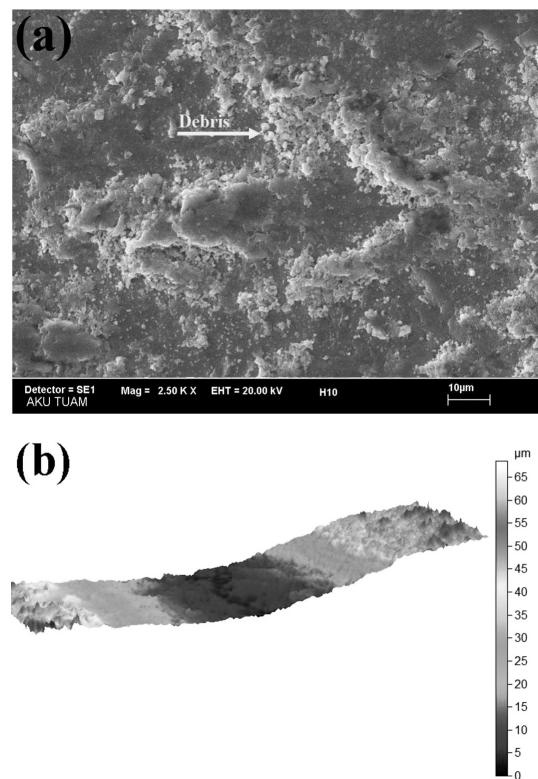


Figure 8: SEM micrograph and cross-sectional surface of the worn-out surfaces of the non-borided AISI H10 steel: a) non-borided, b) cross-sectional surface (CS)

Slika 8: SEM-posnetek in presek obrabljene površine neboriranega jekla AISI H10: a) neborirano, b) presek površine (CS)

Gunes²² and Sahin²³ reported that the surface-roughness values increased with an increase in the boriding temperature.

Table 1: Surface-roughness values of the non-borided and borided AISI H10 steel

Tabela 1: Vrednosti hrapavosti površine neboriranega in boriranega jekla AISI H10

Unborided	Borided			
	1123 K – 2 h	1123 K – 6 h	1223 K – 2 h	1223 K – 6 h
0.09	0.34	0.39	0.45	0.52

Figure 7 shows the wear rate of the non-borided and borided AISI H10 steel. Reductions in the wear rates of the borided steels were observed according to the non-borided steels. Due to the hardness of the FeB and CrB phases, the steel showed more resistance to wear. The lowest wear rate was obtained in the AISI H10 steel borided at 1223 K for 6 h, while the highest wear rate was obtained in the non-borided AISI H10 steel. The wear-test results indicated that the wear resistance of the borided steels increased considerably with the boriding treatment and time. It is well known that the hardness of the boride layer plays an important role in the improvement of the wear resistance. As shown in **Figures 5** and **7**, the relationship between the surface microhardness and the wear resistance of the borided samples also confirms that the wear resistance was improved with the increasing hardness. This is in agreement with reports of previous studies.^{9,23–25} When the wear rate of the borided steel is compared with the non-borided steel, the wear rate of the borided steels is approximately five times lower than that of the non-borided steels.

Table 2: The friction coefficients of the non-borided and borided AISI H10 steel

Tabela 2: Koeficienti trenja neboriranega in boriranega jekla AISI H10

Unborided	Borided			
	1123 K – 2 h	1123 K – 6 h	1223 K – 2 h	1223 K – 6 h
0.64	0.38	0.44	0.48	0.53

The SEM micrographs of the worn surfaces of the non-borided and borided AISI H10 steel are illustrated in **Figures 8** and **9**. **Figure 8a** shows the SEM micrographs of the wear surfaces of the non-borided AISI H10 steel. In **Figure 8a**, the worn surface of the non-borided steel was rougher and coarser wear-debris particles were present. The wear region of the borided steel, debris, delamination wear, surface grooves and cracks on the surface can be observed (**Figure 9**). There were micro-cracks, abrasive particles and small holes on the worn surface of the boride coatings. In the wear region of the borided AISI H10 steel, there were cavities probably formed as a result of layer fatigue (**Figure 9**) and cracks concluded in delaminating wear. **Figure 9** show the wear

surfaces and the cross-sectional surface (CS) of a wear mark obtained from the wear region by analyzing multiple profilometry surface line scans using a Nanovea ST-400 non-contact optical profiler. It was observed that the depth and width of the wear trace on the surfaces of the samples decreased with an increase in the boriding temperature and time (**Figure 9**). **Figure 9** shows the EDS analysis obtained from **Figure 9g**. Fe-based oxide layers formed as a result of the wear test. The spallation

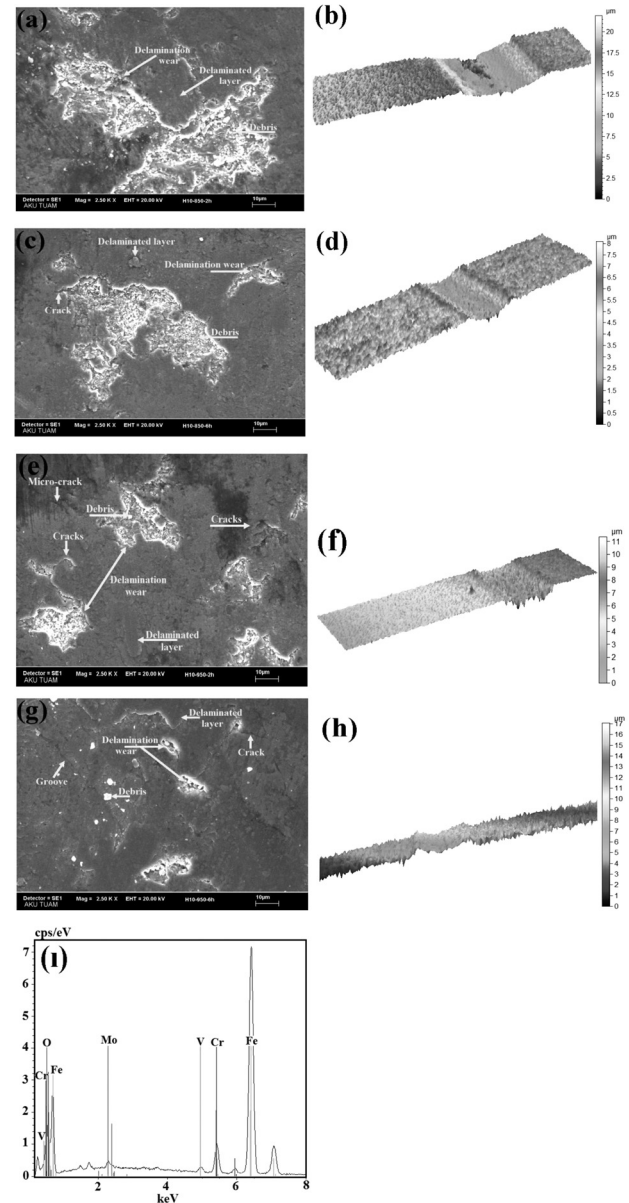


Figure 9: SEM micrographs and cross-sectional surface of the worn-out surfaces of the borided AISI H10 steel: a) 1123 K – 2 h, b) 1123 K – 2 h CS, c) 1123 K – 6 h, d) 1123 K – 6 h CS, e) 1223 K – 2 h, f) 1223 K – 2 h CS, g) 1223 K – 6 h, h) 1223 K – 6 h CS, i) EDS analysis

Slika 9: SEM-posnetki in preseki obrabljene površine boriranega jekla AISI H10: a) 1123 K – 2 h, b) 1123 K – 2 h CS, c) 1123 K – 6 h, d) 1123 K – 6 h CS, e) 1223 K – 2 h, f) 1223 K – 2 h CS, g) 1223 K – 6 h, h) 1223 K – 6 h CS, i) EDS-analiza

of the oxide layers in the sliding direction and their orientation extending along the wear track were identified. When the SEM image of the worn surfaces of the non-borided sample is examined, it can be seen that the wear marks in **Figure 8a** are larger and deeper.

4 CONCLUSIONS

In this study, wear behavior and some of the mechanical properties of the boride layer on the surface of borided AISI H10 steel were investigated. Some of the conclusions can be drawn as follows:

- The boride-layer thickness on the surface of the AISI H10 steel was obtained, depending on the boriding time and temperature, 12.86 μm – 63.72 μm ;
- The multiphase boride coatings that were thermochemically grown on the AISI H10 steel were composed of the FeB, Fe₂B, CrB, Cr₂B and MoB phases;
- The surface hardness of the borided steel was in the range 1648 HV_{0.05} – 1964 HV_{0.05}, while for the untreated the steel substrate it was 306 HV_{0.05};
- The lowest wear rate was obtained in the steel borided at 1223 K for 6 h, while the highest wear rate was obtained for the non-borided steel;
- The wear rate of the borided steel was found to be approximately five times lower the wear rate of the non-borided steel;
- As a result of boriding, the low surface hardness of the AISI H10 steel was improved.

5 REFERENCES

- ¹ M. Hudakova, M. Kusy, V. Sedlicka, P. Grgač, Analysis of the boronized layer on K190PM tool steel, *Mater. Tehnol.*, 41 (2007) 2, 81–84
- ² A. K. Sinha, Boriding (Boronizing) of steels, ASM Handbook, vol. 4, ASM International, 4 (1991), 437–447
- ³ M. Keddama, Simulation of the growth kinetics of FeB and Fe₂B phases on the AISI M2 borided steel: Effect of the paste thickness, *International Journal of Materials Research*, 100 (2009) 6, 901–905, doi:10.3139/146.110915
- ⁴ S. Ulker, I. Gunes, S. Taktak, Investigation of tribological behaviour of plasma paste boronized of AISI 8620, 52100 and 440C steels, *Indian Journal of Engineering and Materials Sciences*, 18 (2011) 5, 370–376
- ⁵ C. Bindal, A. H. Ucisik, Characterization of borides formed on impurity-controlled chromium-based low alloy steels, *Surface and Coatings Technology*, 122 (1999) 2–3, 208–213, doi:10.1016/S0257-8972(99)00294-7
- ⁶ M. Keddama, R. Chegroune, A model for studying the kinetics of the formation of Fe₂B boride layers at the surface of a gray cast iron, *Applied Surface Science*, 256 (2010) 16, 5025, doi:10.1016/j.apsusc.2010.03.048
- ⁷ I. Gunes, Kinetics of borided gear steels, *Sadhana*, 38 (2013) 3, 527–541, doi:10.1007/s12046-013-0138-0
- ⁸ Z. N. Abdellah, M. Keddama, A. Elias, Evaluation of the effective diffusion coefficient of boron in the Fe₂B phase in the presence of chemical stresses, *Inter. Journal of Materials Research*, 104 (2013) 3, 260–265, doi:10.3139/146.110862
- ⁹ I. Gunes, Wear Behaviour of Plasma Paste Boronized of AISI 8620 Steel with Borax and B₂O₃ Paste Mixtures, *Journal of Materials Science and Technology*, 29 (2013) 7, 662–668, doi:10.1016/j.jmst.2013.04.005
- ¹⁰ E. Garcia-Bustos, M. A. Figueroa-Guadarrama, G. A. Rodríguez-Castro, O. A. Gómez-Vargas, E. A. Gallardo-Hernández, I. Campos-Silva, The wear resistance of boride layers measured by the four-ball test, *Surface and Coatings Technology*, 215 (2013), 241–246, doi:10.1016/j.surfcoat.2012.08.090
- ¹¹ T. Leśniewski, S. Krawiec, The effect of ball hardness on four-ball wear test results, *Wear*, 264 (2008) 7–8, 662–670, doi:10.1016/j.wear.2007.06.001
- ¹² I. Gunes, A. Dalar, Effect of sliding speed on friction and wear behaviour of borided gear steels, *Journal of the Balkan Tribological Association*, 19 (2013) 3, 325–339
- ¹³ T. S. Eyre, Effect of boronising on friction and wear of ferrous metals, *Wear*, 34 (1975) 3, 383–397, doi:10.1016/0043-1648(75)90105-2
- ¹⁴ S. Sen, U. Sen, C. Bindal, Tribological properties of oxidised boride coatings grown on AISI 4140 steel, *Materials Letters*, 60 (2006) 29–30, 3481–3486, doi:10.1016/j.matlet.2006.03.036
- ¹⁵ I. Gunes, Tribological behavior and characterization of borided cold-work tool steel, *Mater. Tehnol.*, 48 (2014) 5, 765–769
- ¹⁶ E. Atik, U. Yunker, C. Meriç, The effects of conventional heat treatment and boronizing on abrasive wear and corrosion of SAE 1010, SAE 1040, D2 and 304 steels, *Tribology International*, 36 (2003) 3, 155–161, doi:10.1016/S0301-679X(02)00069-5
- ¹⁷ Verein Deutscher Ingenieure Normen, VDI 3198, VDI-Verlag, Düsseldorf 1991
- ¹⁸ N. Vidakis, A. Antoniadis, N. Bilalis, The VDI 3198 indentation test evaluation of a reliable qualitative control for layered compounds, *Journal of Mater. Science and Technology*, 143–144 (2003), 481–485, doi:10.1016/S0924-0136(03)00300-5
- ¹⁹ S. Taktak, Some mechanical properties of borided AISI H13 and 304 steels, *Materials and Design*, 28 (2007) 6, 1836–1843, doi:10.1016/j.matdes.2006.04.017
- ²⁰ I. Gunes, Y. Kayali, Investigation of mechanical properties of borided Nickel 201 alloy, *Materials and Design*, 53 (2014), 577–580, doi:10.1016/j.matdes.2013.07.001
- ²¹ K. L. Johnson, Contact mechanics, Cambridge University Press, Cambridge 1985
- ²² I. Gunes, Investigation of Tribological Properties and Characterization of Borided AISI 420 and AISI 5120 Steels, *Transactions of the Indian Institute of Metals*, 67 (2014) 3, 359–365, doi:10.1007/s12666-013-0356-5
- ²³ S. Şahin, Effects of boronizing process on the surface roughness and dimensions of AISI 1020, AISI 1040 and AISI 2714, *Journal of Materials Processing Technology*, 209 (2009) 4, 1736–1741, doi:10.1016/j.jmatprotec.2008.04.040
- ²⁴ C. Li, B. Shen, G. Li, C. Yang, Effect of boronizing temperature and time on microstructure and abrasion wear resistance of Cr12Mn2V2 high chromium cast iron, *Surface and Coatings Technology*, 202 (2008) 24, 5882–5886, doi:10.1016/j.surfcoat.2008.06.170
- ²⁵ D. Mu, B. Shen, X. Zhao, Effects of boronizing on mechanical and dry-sliding wear properties of CoCrMo alloy, *Materials and Design*, 31 (2010) 8, 3933–3936, doi:10.1016/j.matdes.2010.03.024

THE EFFECTS OF CUTTING CONDITIONS ON THE CUTTING TORQUE AND TOOL LIFE IN THE TAPPING PROCESS FOR AISI 304 STAINLESS STEEL

VPLIV POGOJEV REZANJA NA MOMENT PRI REZANJU IN ZDRŽLJIVOST NAVOJNEGA VREZNIKA PRI VREZOVANJU NOTRANJIH NAVOJEV V NERJAVNO JEKLO AISI 304

Gultekin Uzun, Ihsan Korkut

Gazi University, Faculty of Technology, Manufacturing Engineering, Ankara, Turkey
uzun.gultekin@gazi.edu.tr

Prejem rokopisa – received: 2015-02-22; sprejem za objavo – accepted for publication: 2015-04-09

doi:10.17222/mit.2015.044

In this study tapping operations were carried out using taps of different diameters and with different cutting parameters on AISI 304 austenitic stainless steel. The cutting performances of the taps were determined according to the cutting torques created during the threading and the depth of cut for each cutting feed (Q). With the aid of the obtained experimental data the solution suggestions to the problems in the threading operations for AISI 304 steel were developed. As a result it was specified that the increasing amount of cutting in each pass directly affected the cutting torque. It was determined that there was a tendency to decrease the cutting torque with the increasing depth of cut for each cutting feed. The best tool-life results for an M5 tap were obtained at a 5-mm Q value, whereas for M6 taps it was at a 3-mm Q value.

Keywords: tapping, AISI 304, machinability

V študiji je bilo izvedeno vrezovanje notranjih navojev z uporabo navojnega vreznika z različnimi premeri in različnimi nivoji vrezovalnih parametrov v avstenitnem jeklu AISI 304. Zmogljivosti vrezovanja navojnih vreznikov so bile določene glede na moment, ki je nastal med vrezovanjem navojev v globino, za vsako hitrost podajanja pri vrezovanju (Q). S pomočjo dobljenih eksperimentalnih podatkov so bili postavljeni predlogi rešitev problemov pri postopku vrezovanja navojev pri jeklu AISI 304. Pokazalo se je, da povečanje vrezovanja pri vsakem prehodu neposredno vpliva na moment pri vrezovanju. Ugotovljeno je, da se zmanjšuje moment vrezovanja s povečanjem globine reza pri vsakem podajanju pri vrezovanju. Najboljša zdržljivost orodja pri M5 vrezniku je bila dosežena pri vrednosti $Q = 5$ mm, pri vrezniku M6 pa pri vrednosti $Q = 3$ mm.

Ključne besede: vrezovanje notranjih navojev, AISI 304, strojna obdelava

1 INTRODUCTION

The need for stainless steels in industry is increasing day by day along with technological developments. Several types of stainless steels are used, especially in the manufacturing of the storage tanks, pressure vessels, heat exchangers and stainless pipes used in the petrochemistry, chemistry and food industries. One of the ways of increasing the strength of stainless steel is to increase the content of the main alloying elements, such as chrome and nickel, and to decrease the carbon content. In recent years, rapid improvements in technology have led to an increase in the expectations from the new methods used in the manufacturing of materials.^{1,2}

The high tensile strength of stainless steels is the main cause of their poor machinability. The distance between the yield and rupture points of stainless steels is more than that of normal carbon steels. Therefore, a higher cutting force is needed for the machining of stainless steels compared to normal carbon steels. The poor machinability of austenitic stainless steels stems from their low heat conductivity and high work-hardening properties.³ In the turning operations of AISI 304 and AISI 316 austenitic stainless steels, TiC/TiCN/TiN-

coated cutting tools lead to lower cutting forces than those for TiC/TiCN/Al₂O₃-coated cutting tools. In a study in the literature, it was specified that the cutting speed did not cause any significant change in the cutting forces, while it affected the surface roughness significantly.⁴ In the turning process for AISI 304 stainless steel, at high cutting speeds exceeding the 150 m/min, the tool wear and the surface-roughness values were decreased with the increasing of the cutting speed.⁵

The cutting tools should provide the suitable cutting parameters required for maximum efficiency. In the threading process, the selection of the correct tap and the necessary parameters (feed, revolution, cooling liquid etc.) are of importance in terms of the threading quality and the economy of production. Incorrect tap selection causes increased costs and time loss. In Germany, in the machine manufacturing industry, the total time spent for threading is equal to 22 % of the total machining time.⁶

The operation steps between the cutting tool and the material during tapping are complicated compared to other cutting tools. The selection of the correct tap and the cutting conditions is a necessity for the efficient use of the tap. In a study, it was emphasized that higher

Table 1: Chemical composition of AISI 304 austenitic stainless steel¹⁴**Tabela 1:** Kemijska sestava avstenitnega nerjavnega jekla AISI 304¹⁴

Chemical composition							
C	Mn	Si	P max	S	Cr	Ni	N
≤0.07 %	≤2.00 %	≤1.00 %	0.045	≤0.015 %	17.50–19.50 %	8.00–10.50 %	≤0.11

forces occurred on the coatings having a lower wear resistance, in contrast with the higher wear-resistant coatings. In the tapping, the TiCN-coated taps exhibited excellent abrasive and adhesive wear resistances.⁷ It was specified that during the tapping of deep holes with small-diameter taps, the reason for frequent tool breakage was the higher torque during threading.⁸ The lowest cutting torque in the tapping operations was obtained under dry-cutting conditions.⁹ It was stated that the cutting liquids containing fluorine formed a lubricant film layer between the tool and workpiece interface, which led to an increase in tool life by preventing build-up-edge formation on the tool and thus the cutting forces could be decreased by about 18 %.¹⁰ The thread precision of CBN-coated taps exhibited improvements in the tapping torque and tool life. The tool life and tapping-torque resistances of CBN-coated taps provided better results compared to conventionally coated taps.¹¹ In some studies, estimation models were also developed to predict the torque occurring during the tapping.^{9–13}

As can be seen from the literature, the tapping of AISI 304 stainless steel is a difficult process owing to its poor machinability. Tapping is a complicated operation and this makes it difficult to solve the problems in this field. There have been limited studies carried out to determine cutting torque, tool life and tool wear regarding the tapping processes.

2 MATERIALS AND METHOD

Tapping a deep hole in the rigid tapping mode may be difficult due to chip sticking on the tool. In such cases, the peck rigid tapping cycle is useful. In this study, the peck rigid tapping operation was carried out using the Tapping cycle (G84). The chip breaking command of

G83 and the depth of cut for each cutting feed (Q) in each pass are entered into G84 and in this way the cutting tool can break the chip during the tapping operation. The sample program used is given as follows:

G84 X25. Y25. Z-20. R5. Q5. F203.64 S255.

At the end:

- The effect of different cutting parameters on the cutting torque,
- The effect of the addition of the Q value to the G84 command on the cutting torque,
- The effects of Q values added to the G84 command on the tool life were determined.
- The materials and equipment that are used in the tests are listed below.

2.1 Experimental method

The chemical composition of the AISI 304 austenitic stainless steel used in the tests is given in **Table 1**.¹⁴

The test samples were prepared as prismatic plates with a size of 100 mm × 80 mm × 15 mm. A mold was designed to fix the test samples to the dynamometer. In the tapping tests, 63 holes were drilled in each sample. The distribution of holes on the upper surface of the samples is given in **Figure 1**. By taking into consideration the hardness distribution around the drilled hole, the symmetrical placing of holes on the piece was done carefully.

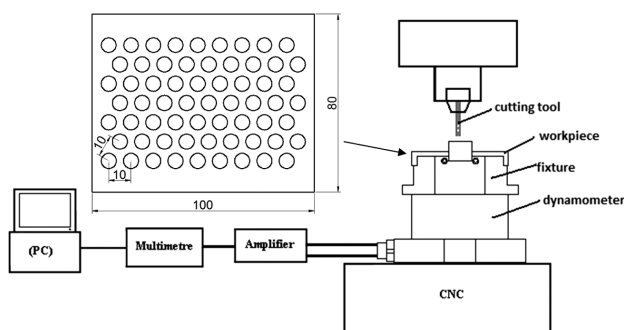
The cutting forces and moments were measured using a KISTLER 9272 A type dynamometer. The dynamometer was fixed to the vertical machining center and thus the three cutting forces (F_x , F_y , F_z) and the moment (M_z) could be measured simultaneously. A fixing die and a workpiece were placed on the dynamometer to perform the cutting tests properly. In the designed system, the force data is taken from the workpiece by direct contact between the workpiece and the dynamometer (**Figure 1**).

The tap types and forms are given in the technical data in **Figure 2**.

Drills with diameters of Ø4.2 and Ø5.0 mm were used for the drilling of the tapping holes. In the tests, for the purpose of preventing the taps experiencing excessive cutting torques, a tapping cap and a safety tap holder were used.

The wear and material adhesions on the cutting tools were examined by using an AM413ZT Polarized Digital Microscope at 50 × magnification (**Figure 3**).

In this study, four different cutting speeds (4-6-8-10 m/min) and four different Q (3-5-8-20 mm) values were used to determine the suitable cutting parameters under

**Figure 1:** Drawings of the samples used in the tests and the experimental setup**Slika 1:** Risba vzorcev, uporabljenih pri preizkusu in eksperimentalni sestavi

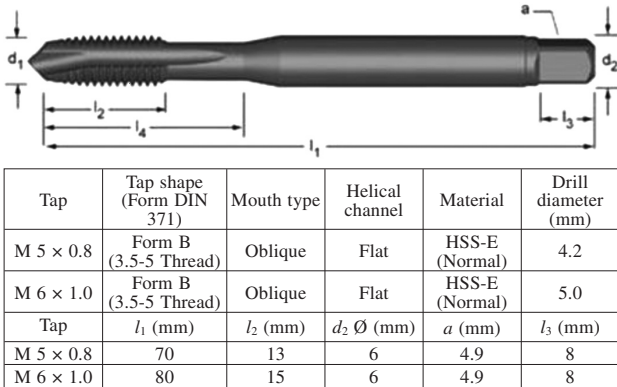


Figure 2: Technical data of M5 and M6 taps
 Slika 2: Tehnični podatki za M5 in M6 navojne svedre

dry-cutting conditions. Taps with different diameters were used to evaluate in detail the effects of the cutting parameters mentioned above on the tapping process. By considering these parameters and studies in the literature, appropriate values in the cutting-tool catalogs were taken into consideration.

2.2 Tapping and measurement of the cutting torque

In the tapping process, a rotating torque (cutting torque) is produced. The most effective factor in the tapping process is rotation torque (Figure 4). There are some factors affecting this, i.e., chip angle, chamfer length, tap form, work piece material, cutting liquid, etc. A wider chip angle decreases the cutting torque, but at the same time decreases the strength of the tap. The main purpose of using the cutting liquid (emulsion, cutting oil, etc.) during tapping is to decrease the friction between the cutting tool and the workpiece. One of the main reasons for heating and cutting torques as a result of friction is the chip squeezing in the tap channels. To prevent this chip squeezing, an appropriate tap form must be selected in accordance with the workpiece and hole type, and in this way the chip in the tap channels is

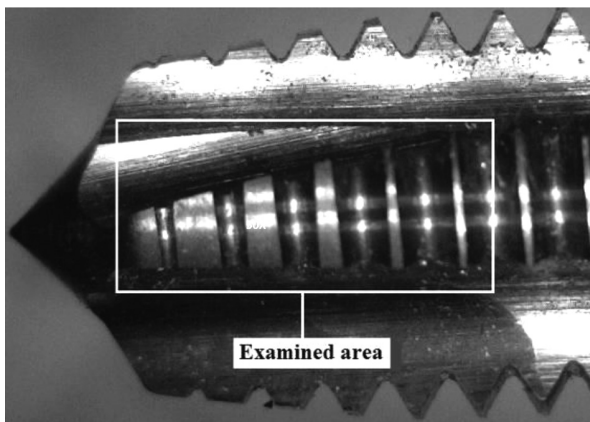


Figure 3: Examined zones of the cutting tools through a digital microscope
 Slika 3: Preiskovana področja rezalnega orodja, prikazana z digitalnim mikroskopom

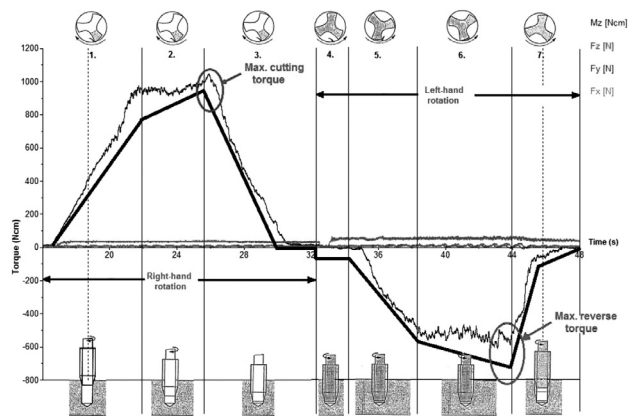


Figure 4: Graphical and experimental measurement of the cutting torque during tapping¹⁶
 Slika 4: Grafični prikaz eksperimentalnih meritev momenta pri vrezovanju notranjih navojev¹⁶

removed. In Figure 4, during the tapping process, graphical and experimental measurements of the torque are shown:

1. zone) beginning of cut to full contact of all chamfer teeth,
2. zone) cutting torque of the tap that is now cutting with all its chamfer teeth,
3. zone) breaking the machine spindle to a stop,
4. zone) beginning reversal of the spindle to contact of the tooth back with the chip root left standing by the next cutting tap tooth,
5. zone) shearing off the chip root,
6. zone) squashing back the chip root remains in place after the shearing off of the chip root (size depending on the chamfer relief angle of the tap and on the rear cutting angle of the tap tooth),
7. zone) sliding friction between tap and workpiece.

3 RESULTS AND DISCUSSION

In this study, the type of tap and cutting parameters were considered as the input, whereas cutting torque (moment) (M_c), which is very important among the cutting forces, was considered as the output. The change of cutting torque (depending on the Q values) that is created during threading under dry-cutting conditions at different cutting speeds with the M5 tap is given in Figure 5.

From Figure 5 it is clear that the increase in the values of Q led to a decrease in the cutting torque. The highest cutting-torque values for all cutting speeds were measured for the Q value of 3 mm. The reason for this is the formation of a discontinuous cutting operation and the insufficient heat in the cutting area for the deformation of the material.³ The second largest cutting-torque values were obtained for the Q value of 5 mm. For the Q value of 8 mm, 4 % and 8 % increases were calculated for the 8 m/min and 10 m/min cutting speeds compared to the Q value of 5 mm. At the cutting speeds of 4 m/min

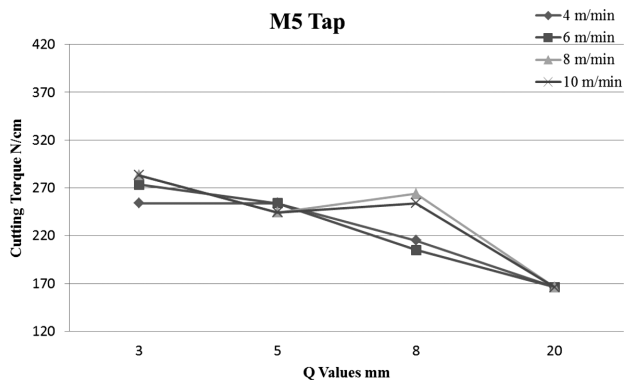


Figure 5: Change of cutting torque (depending on the Q values) at different cutting speeds with the M5 tap

Slika 5: Spreminjanje momenta pri vrezovanju (odvisno od vrednosti Q) pri različnih hitrostih rezanja z navojnim svedrom M5

and 6 m/min, the cutting torque decreased in comparison to that of the Q value of 5 mm. The lowest cutting-torque values were obtained by increasing the Q value to 20 mm. This was attributed to the formation of sufficient heat for cutting in the cutting area due to the lower heat conductivity of the AISI 304 material.^{5,15} The continuous cutting operation provided an easier chip removal. The angular slope at the cutting mouth makes the chip removal easier. In this way, there is no chip accumulation and the tap can make the cutting operation easy. The number of chamfers is 4–5 threads and this decreases the moment distributed to the threads, ending up with a lower cutting moment.^{9,16,17}

The change of cutting torque depending on the Q values that emerged during threading under dry-cutting conditions at different cutting speeds with the M6 tap is given in Figure 6.

For the M6 tap from Figure 6 it is clear that the increase in the values of Q caused a decrease in the cutting torque. When changing the Q values from 3 mm to 5 mm an increase was observed, after which the tendency to decrease continued. The highest cutting-torque values were obtained with a Q value of 5 mm. The reason for this was attributed to an inappropriate cutting speed/feed

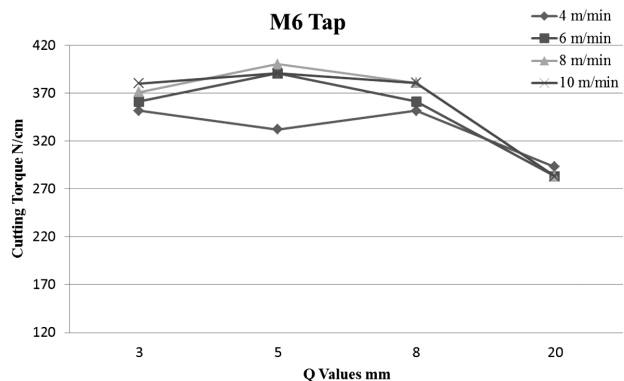


Figure 6: Change of cutting torque (depending on the Q values) at different cutting speeds with the M6 tap

Slika 6: Spreminjanje momenta pri vrezovanju (odvisno od vrednosti Q), pri različnih hitrostih rezanja z navojnim svedrom M6

ratio. In addition, the discontinuous formation of the cutting operation caused insufficient heat for the material deformation.¹¹ The second highest cutting-torque values were seen for the Q values of 3 mm and 8 mm. When Q was 20 mm the lowest cutting-torque values were obtained. This was explained by the formation of sufficient heat for cutting in the cutting area due to the lower heat conductivity of the AISI 304 material.^{3,5,15} The angular slope at the mouth of the cutting tool and the continuous cutting operation made the chip removal easier. Thus, the tap worked easily and there was no chip pile-up. The chamfer of the tap along with 4–5 threads led to a decrease in the moment, which was distributed to the threads and caused the cutting moment to have lower values.^{18,19}

Tool-life tests were carried out at an 8 m/min cutting speed (average speed). Graphics were drawn by calculating the distance of the cutting tool as the cutting-tool life. The distance of the cutting tool was calculated by multiplying the workpiece thickness by the number of threaded holes. Tapping processes were repeated until the breaking of each cutting tool and obtaining the excessive chip build-up-edge.

Figure 7 shows that in the tool-life tests with the M5 tap the shortest tool life came out to be 60 mm at the lowest and highest Q values. The best tool life was determined to be 200 mm for the 5 mm Q value. When the cutting-tool life for the M5 tap is examined, it is seen that the tool life decreases with an increasing Q value.

As seen from Figure 8 the chip build-up-edge values on the cutting tools are the most important factor affecting the tool life.^{11,13,18} In stainless steels, higher ductility makes the machinability difficult. In tapping, the material build-up-edge to the cutting mouths causes squeezing. As a result of these squeezes there are breakages in the cutting tools (Figure 8d).

When Figure 7 is examined for the M6 tap, the effect of Q value is clearly seen. The longest tool life for a 3 mm Q value was 255 mm. The tool life decreased with

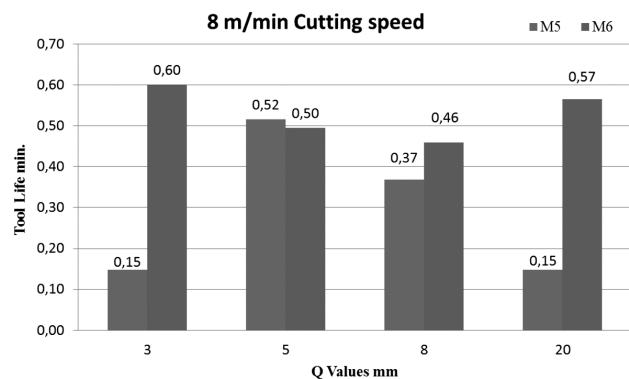


Figure 7: Change of tool life for M5 and M6 taps depending on the Q values

Slika 7: Spreminjanje zdržljivosti M5 in M6 navojnega svedra v odvisnosti od vrednosti Q

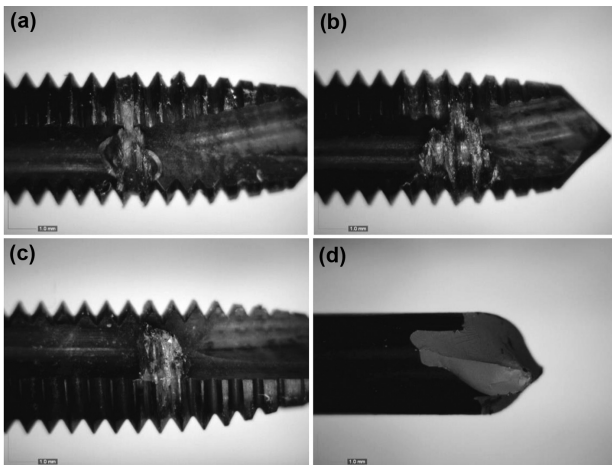


Figure 8: Tool-life (distance of cutting tool) images for M5 at 8 m/min cutting speed, depending on the Q values of: a) 3 mm, b) 5 mm, c) 8 mm, d) 20 mm

Slika 8: Posnetki zdržljivosti orodij (razdalja rezanja orodja) za M5, pri hitrosti rezanja 8 m/min, v odvisnosti od vrednosti Q : a) 3 mm, b) 5 mm, c) 8 mm, d) 20 mm

an increasing Q value. The second best tool life (240 mm) was obtained for a 20 mm Q value.

From **Figure 9** it is clear that all of the cutting tools were broken due to tool squeezing. The main reason for the breaking of the tools was the build-up-edge of the chip. The ductile structure of the AISI 304 material provides the build-up-edge formation at the cutting mouths of the taps. The filling of cutting mouths makes the cutting operation difficult and causes breakage of the cutting tool.^{11,13}

When **Figure 7** was examined for the M5 and M6 taps, it was seen that the best tool-life results were obtained with the M6 taps. The effect of Q value was seen clearly for both the cutting tools. The best tool-life results for the M5 tap were obtained for a 5 mm Q value, and for a 3 mm Q with M6. The best results from the point of view of cutting torques were not obtained at these values mentioned above, but this did not affect the tool life significantly. As a result, in threading with small-scale taps under suitable conditions, it can be said that the Q value can be used.

4 CONCLUSION

The results obtained from this study are summarized as below:

- The cutting-torque values for each of the depth of cut and cutting feed (Q) values have been determined. This was the case for both cutters. A high cutting torque was obtained with the lowest and highest Q values.
- The most important factor affecting the tool life was the build-up-edge formation on the tools. In the tapping operation, the build-up-edge chips on the cutting mouths caused squeezing, which resulted in breakages of the cutting tools.

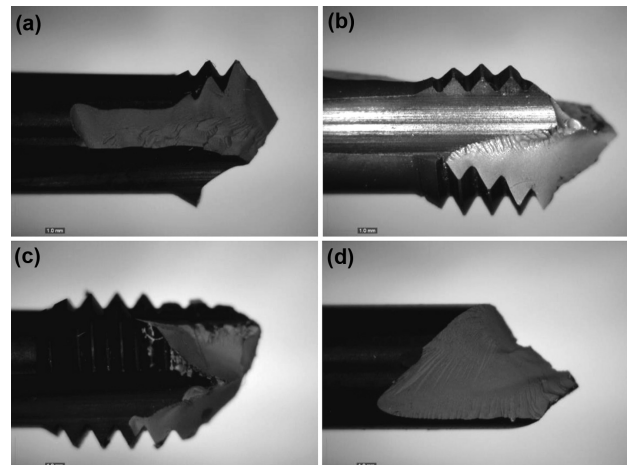


Figure 9: Tool-life (distance of cutting tool) images for M6 at 8 m/min cutting speed, depending on the Q values of: a) 3 mm, b) 5 mm, c) 8 mm, d) 20 mm

Slika 9: Posnetki zdržljivosti orodij (razdalja rezanja orodja) za M6, pri hitrosti rezanja 8 m/min, v odvisnosti od vrednosti Q : a) 3 mm, b) 5 mm, c) 8 mm, d) 20 mm

- Tapping operations were carried out using the M5 and M6 taps on the AISI 304 austenitic stainless steel. It was specified that an increase of the depth of cut for each cutting feed (Q) directly affected the cutting torque. The Q value affecting the tool life was determined.

5 REFERENCES

- ¹ N. Kahraman, B. Gülenç, H. Akça, Mechanical properties of welding of weldment on low carbon steel welded to austenitic stainless steel by arc welding method, *Jour. Fac. Eng. Arch. Gazi Univ.*, 17 (2002) 2, 75–85
- ² H. E. Yeyen, I. Korkut, Y. Turgut, I. Çiftçi, The effects of cutting speed and feed rate on cutting forces and surface roughness in machining of AISI 303 austenitic stainless steel, 5th International Advanced Technologies Symposium, Karabük, Turkey, 2009, 1284–1288
- ³ B. Mills, A. H. Redford, *Machinability of Engineering Materials*, 1st ed., Springer, Netherlands 1983, 107–108, doi:10.1007/978-94-009-6631-4
- ⁴ I. Çiftçi, Machining of austenitic stainless steels using CVD multi-layer coated cemented carbide tools, *Tribology International*, 39 (2006) 6, 565–569, doi:10.1016/j.triboint.2005.05.005
- ⁵ I. Korkut, M. Kasap, I. Çiftçi, U. Seker, Determination of optimum cutting parameters during machining of AISI 304 austenitic stainless steel, *Materials and Design*, 25 (2004) 4, 303–305, doi:10.1016/j.matdes.2003.10.011
- ⁶ <http://www.guhring.com.tr/article/archive/1/kilavuz.html>
- ⁷ A. E. Reiter, B. Brunner, M. Ante, J. Rechberger, Investigation of several PVD coatings for blind hole tapping in austenitic stainless steel, *Surface & Coatings Technology*, 200 (2006), 5532–5541, doi:10.1016/j.surfcoat.2005.07.100
- ⁸ K. Kuo, Experimental investigation of ultrasonic vibration-assisted tapping, *Journal of Materials Processing Technology*, 192 (2007), 306–311, doi:10.1016/j.jmatprotec.2007.04.033
- ⁹ T. Cao, J. W. Sutherland, Investigation of thread tapping load characteristics through mechanistics modeling and experimentation, *International Journal of Machine Tools & Manufacture*, 42 (2002) 14, 1527–1538, doi:10.1016/S0890-6955(02)00108-6

- ¹⁰ S. C. Veldhuis, G. K. Dosbaeva, G. Benga, Application of ultra-thin fluorine-content lubricating films to reduce tool/workpiece adhesive interaction during thread-cutting operations, *International Journal of Machine Tools and Manufacture*, 47 (2007) 3–4, 521–528, doi:10.1016/j.ijmachtools.2006.06.003
- ¹¹ M. Jin, S. Watanabe, S. Miyake, M. Murakawa, Trial fabrication and cutting performance of c-BN-coated taps, *Surface and Coatings Technology*, 133 (2000), 443–447, doi:10.1016/S0257-8972(00)00926-9
- ¹² E. J. A. Armarego, M. N. P. Chen, Predictive cutting models for the forces and torque in machine tapping with straight flute taps, *Cirp Annals-Manufacturing Technology*, 51 (2002) 1, 75–78, doi:10.1016/S0007-8506(07)61469-3
- ¹³ A. P. S. Dogra, S. G. Kapoor, R. E. Devor, Mechanistic model for tapping process with emphasis on process faults and hole geometry, *Journal of Manufacturing Science and Engineering-Transactions Of The ASME*, 124 (2002) 1, 18–25, doi:10.1115/1.1430237
- ¹⁴ <http://www.azimtic.com/hizmetlerimiz.html>
- ¹⁵ B. Balcı, AISI 304 Östenitik paslanmaz çelik malzemenin işlenmesinde yüzey pürüzlülüğünün incelenmesi, *Bilim Uzmanlığı Tezi*, Karabük Üniversitesi Fen Bilimleri Enstitüsü Makine Eğitimi, Karabük 2008
- ¹⁶ G. Uzun, I. Korkut, The effect of cryogenic treatment on tapping, *The International Journal of Advanced Manufacturing Technology*, 67 (2013) 1–4, 857–864, doi:10.1007/s00170-012-4529-x
- ¹⁷ G. Uzun, I. Korkut, Kılavuz ile vida açma işlemine kesme yönteminin ve kesme parametrelerinin etkileri, 3. Ulusal Talaşlı İmalat Sempozyumu, Ankara, Türkiye 2012
- ¹⁸ Y. Kayir, The effect of hole diameter on cutting forces for tapping on an AA5083 alloy, *Jour. Fac. Eng. Arch. Gazi Univ.*, 25 (2010) 4, 671–679
- ¹⁹ M. Günay, Investigation of the effects on screw thread of infeed angle during external threading, *Gazi University Journal of Science*, 24 (2011) 1, 153–160

CHEMICAL SYNTHESIS AND DENSIFICATION BEHAVIOR OF Ag/ZnO METAL-MATRIX COMPOSITES

OBNAŠANJE Ag/ZnO KOMPOZITA S KOVINSKO OSNOVO PRI KEMIJSKI SINTEZI IN ZGOŠČEVANJU

Mohammad Ardestani

Islamic Azad University, Science and Research Branch, Department of Materials Engineering, Tehran, Iran
ardestani80@gmail.com

Prejem rokopisa – received: 2014-09-24; sprejem za objavo – accepted for publication: 2015-04-07

doi:10.17222/mit.2014.243

In this research, the chemical synthesis and densification behavior of Ag/ZnO metal-matrix composites were investigated. The initial precipitates were obtained by adding ammonium carbonate solution to silver and zinc nitrate solutions. The precipitates consisted of silver and zinc carbonates. The thermal behavior of the precipitates was studied using thermogravimetric analysis (TGA) and differential scanning calorimetry (DSC). The TGA curve showed three distinguishable mass-loss stages, related to the evaporation of physically adsorbed water and also the decomposition of silver and zinc carbonates into silver and zinc oxides, respectively. The mass-loss stages were associated with three endothermic reactions. According to the thermal-analysis results, the precipitates were calcined at 600 °C. The compressibility behavior of the synthesized Ag/ZnO powders was evaluated using the Heckel, Panelli and Ge models. The compaction data of the powders was best fitted to the Heckel equation. The synthesized powders were sintered at 930 °C. The results showed that by increasing the cold-compaction magnitude prior to sintering, the sinterability of the powders was enhanced. The microstructural evaluation of the synthesized composites carried out with a scanning electron microscope (SEM) confirmed a fine and homogenous dispersion of ZnO within the silver matrix.

Keywords: Ag/ZnO composites, densification, thermal analysis, sintering

V raziskavi je bilo preiskovano obnašanje Ag/ZnO kompozita na kovinski osnovi pri kemijski sintezi in zgoščevanju. Začetni izločki so bili dobljeni z dodatkom raztopine srebrovega in cinkovega karbonata v raztopino amonijevega nitrata. Izločki so bili sestavljeni iz srebrovega in cinkovega karbonata. Toplotno obnašanje izločkov je bilo posneto s termogravimetrično analizo (TGA) in z diferenčno vrstično kalorimetrijo (DSC). TGA krivulja je pokazala stopnje občutne izgube mase, ki so bile povezane z uplinjanjem fizično adsorbirane vode in tudi z razgradnjo srebrovega in cinkovega karbonata v srebro in v cinkov oksid. Stopnje izgube mase so bile povezane s tremi endotermnimi reakcijami. Na podlagi rezultatov termoanalize so bili izločki kalcinirani pri 600 °C. Stisljivost sintetiziranega Ag/ZnO prahu je bila določena z uporabo Heckel, Panelli in Ge modelov. Podatki za kompaktiranje prahov so se najbolje ujemali s Heckel enačbo. Sintetizirani prahovi so bili sintrani pri 930 °C. Rezultati so pokazali, da povečevanje obsega zgoščevanja pred sintranjem pospešuje sposobnost prahu za sintranje. Ocena mikrostrukture sintetiziranega kompozita z vrstično elektronsko mikroskopijo (SEM) je potrdila drobno in homogeno razporeditev ZnO v osnovi iz srebra.

Ključne besede: Ag/ZnO kompoziti, zgoščevanje, termična analiza, sintranje

1 INTRODUCTION

Silver-matrix particle-reinforced composites are used in several types of electrical contacts with different applications such as starting switches, oil- and air-circuit breakers, relays and thermostat controls. The properties of the contact depend on the characteristics and volume fraction of the reinforcement(s). Various non-refractory and refractory metals and hard materials like iron, tungsten, molybdenum, tungsten carbide and zinc oxide are used as the reinforcement for this group of metal-matrix composites. Silver-matrix composites are made with the melt-cast method or manufactured with powder-metallurgy (P/M) processes.¹ The conventional P/M method, applied as the manufacturing process includes cold compaction and sintering of silver and reinforcing constituent powder blends.^{1,2}

The magnitude of the cold-compaction pressure and sintering temperature significantly affects the final sintering density and other physical properties of the powder

compacts. Recently, it has been shown that a fine and homogenous dispersion of the reinforcement within the matrix phase leads to the desired electrical advantages like the arc stability and also a reduction of the arc-erosion rate of a contact.³ Different methods like mechanical milling^{4,5}, mechanochemical⁶ and chemical precipitation⁷ were applied to synthesize the particle-reinforced silver-matrix composites with a fine dispersion of the reinforcing phase.

In this research, a synthesis of Ag/ZnO powders via the chemical-precipitation process was investigated. Also, the effect of the cold-compaction pressure magnitude prior to the sintering on the solid-state sinterability of the synthesized powders was studied. Furthermore, the compressibility behavior of the synthesized powders was evaluated using the Heckel, Panelli-Ambrosio and Ge models:^{8,9}

$$\ln \left(\frac{1}{1-D} \right) = KP + B_1 \quad (\text{Heckel equation}) \quad (1)$$

$$\ln\left(\frac{1}{1-D}\right) = \sqrt{KP} + B_2 \quad (\text{Panelli-Ambrosio equation}) \quad (2)$$

$$\lg\left[\ln\left(\frac{1}{1-D}\right)\right] = K \ln P + B_3 \quad (\text{Ge equation}) \quad (3)$$

where D is the relative density, P is the cold pressure and B_1 , B_2 and B_3 are the constants.

2 EXPERIMENTAL WORK

Silver and zinc nitrate were used as the precursors. In order to synthesize the 8 % of mass fractions of Ag, ZnO powders, silver and zinc nitrate solutions were made in distilled water separately. A 0.5 molar solution of ammonium carbonate was added to the prepared solutions drop by drop. Subsequently, the prepared solutions containing the precipitates were mixed and the prepared mixture was stirred vigorously for 3 h at 50 °C. In order to determine the appropriate calcination temperature of the obtained precipitates, the thermal behavior of the precipitates was investigated using simultaneous thermal analysis (STA) up to 800 °C with a heating rate of 10 °C/min in air atmosphere. On the basis of the STA result, the precipitates were calcined at 600 °C for 2 h. The calcined powders were characterized with the X-ray diffraction (XRD) technique. The calcined powders were cold compacted with (100, 200 and 300) MPa in a 10 mm diameter cylindrical die and sintered at 930 °C for 2 h in air atmosphere. The microstructures of the powders and the sintered composites were evaluated with scanning electron microscopy (SEM).

3 RESULTS AND DISCUSSION

Figure 1 shows the microstructure of the initial precipitates. According to this figure, the particles have cylindrical and polygonal shapes. One of the advantages of the applied precipitation process was the use of chemical precursors that did not contain sodium. This agent was used due to the agglomeration of the synthe-

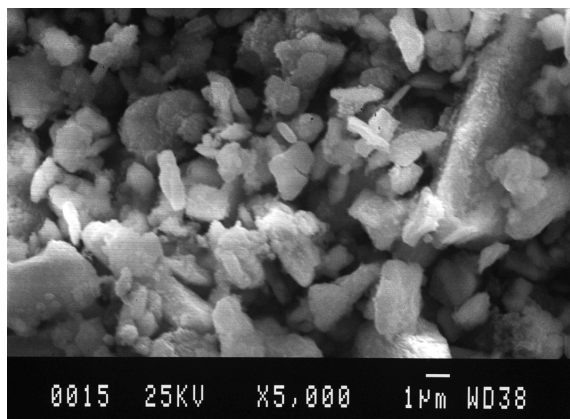


Figure 1: SEM image of the initial precipitates
Slika 1: SEM-posnetek začetnih izločkov

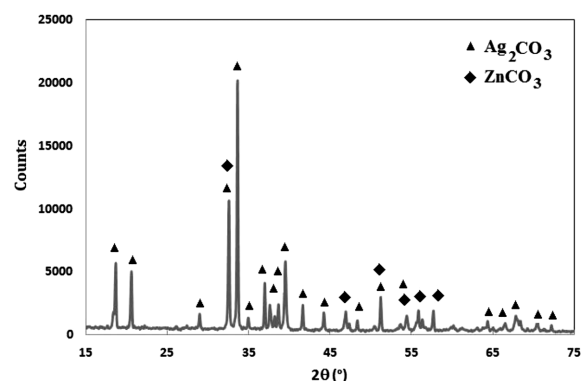


Figure 2: XRD pattern of the initial precipitates
Slika 2: Rentgenogram začetnih izločkov

sized precipitates. However, in order to decrease the agglomeration degree of the particles, the synthesized compounds should be washed for several times, which is a time consuming process. The XRD pattern of the precipitates is shown in **Figure 2**. According to the XRD pattern, the precipitates consisted of silver and zinc carbonates.

The TGA, DTG and DSC curves of the initial precipitates are shown in **Figures 3a** and **3b**. According to the TG and DTG curves, the mass loss of the precipitates occurred up to 600 °C and above this temperature no detectable mass change is seen in the TGA curve. This

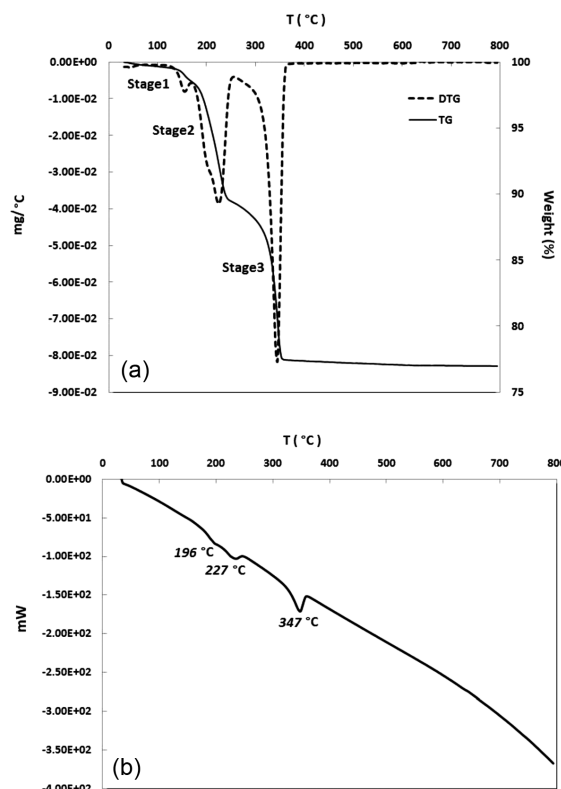


Figure 3: a) TGA and DTG curves of the initial precipitates, b) DSC curve of the initial precipitates

Slika 3: a) TGA- in DTG-krivulji začetnih izločkov, b) DSC-krivulja začetnih izločkov

observation shows that the volatile constituents, such as carbon dioxide, evaporated completely due to the heating of the initial precipitates at 600 °C. Also, according to the DSC curve, the decomposition of the precipitates was due to three endothermic reactions at (197, 226 and 346) °C. So, the appropriate calcination temperature of the initial precipitates was 600 °C.

The XRD pattern of the calcined precipitates is shown in **Figure 4**. This pattern confirms the formation of Ag and ZnO during the calcination that was due to the decomposition of silver and zinc carbonates, respectively. The SEM image of the calcined powders is shown in **Figure 5**. As it is observed, the particles were agglomerated due to calcination at 600 °C. Furthermore, it seems that the heat treatment of the initial precipitates and also the evaporation of the volatile compounds led to considerable microstructural changes of the precipitates during the calcination.

The result of the XRD analysis is in good agreement with the theoretical weight-loss measurements of the precipitates during the calcination that can be calculated using the thermogravimetric curve. According to the TGA curve, the total weight loss during the calcination is 24 %. The theoretical weight loss of the sample can be calculated considering the XRD analysis of the initial and calcined precipitates as shown below:

$$\text{Ag}_2\text{CO}_3, \text{ZnCO}_3 \rightarrow \text{Ag}, \text{ZnO}$$

$$\% \text{ total weight loss} = \frac{2m_{\text{Ag}} + m_{\text{ZnO}}}{m_{\text{Ag}_2\text{CO}_3} + m_{\text{ZnCO}_3}} \approx 74 \% \quad (4)$$

$$100 - 74 = 26 \% \text{ (theoretical weight loss)}$$

where m is the molar weight of the constituent.

The difference between the theoretical calculations and experimental data (2 %) may be due to the evaporation of the physically adsorbed water during the first weight-loss stage of the sample. According to the TGA curve, the weight loss of the precipitates during the first stage is 1.5 %, which is too close to the difference value. The second stage of the weight loss in the TGA curve corresponds to the decomposition of zinc carbonate to

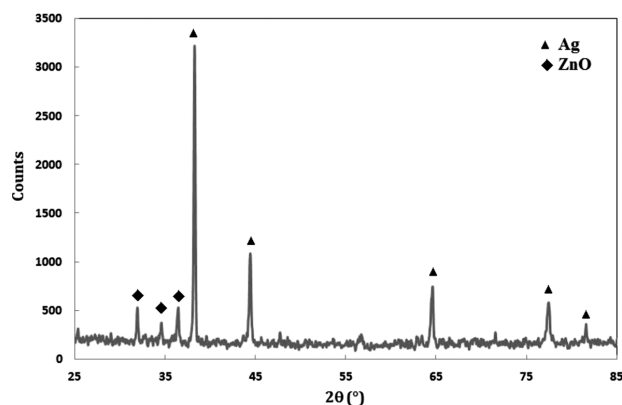


Figure 4: XRD pattern of the calcined precipitates
Slika 4: Rentgenogram kalciniranih izločkov

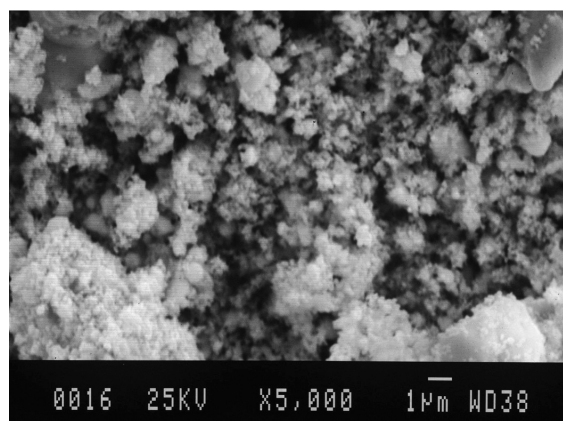
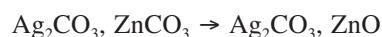


Figure 5: SEM image of the calcined powder. The powder particles are agglomerated.

Slika 5: SEM-posnetek kalciniranega prahu. Delci prahu so aglomerirani.

zinc oxide. The corresponding weight loss of the sample during the second stage is about 10.5 %, which is in good agreement with the theoretical calculation:



$$\% \text{ weight loss of the second stage} = \frac{2m_{\text{Ag}_2\text{CO}_3} + m_{\text{ZnO}}}{m_{\text{Ag}_2\text{CO}_3} + m_{\text{ZnCO}_3}} \approx 12 \% \quad (5)$$

The third weight-loss stage in the TGA curve corresponds to the decomposition of silver carbonate to silver.

The cold-compressibility behavior of the synthesized powders was investigated using the Heckel, Panelli-Ambrosio and Ge models. Three plots were drawn: a plot was drawn with $\ln(1/(1-D))$ along the y-axis and \sqrt{P} along the x-axis (the Panelli-Ambrosio model – **Figure 6**); a plot was drawn with $\ln(1/(1-D))$ along the y-axis and P along the x-axis (the Heckel model – **Figure 7**); and a plot was drawn with $\lg(\ln(1/(1-D)))$ along the y-axis and $\lg P$ along the x-axis (the Ge model – **Figure 8**). Based on the R^2 values, it can be declared that the compaction data of the

Panelli-Ambrosio Model

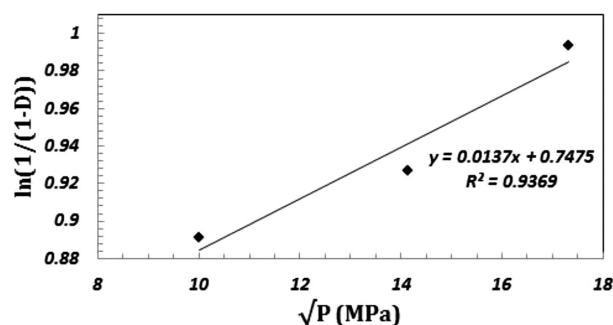


Figure 6: $\ln(1/(1-D))$ versus the square root of uniaxial-pressure compaction magnitude \sqrt{P} (the Panelli-Ambrosio equation)

Slika 6: Odvisnost $\ln(1/(1-D))$ od kvadratnega korena nihanja tlaka pri enoosnem stiskanju \sqrt{P} (enačba Panelli-Ambrosio)

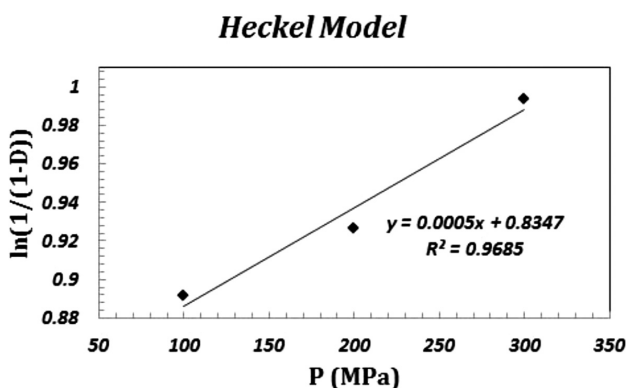


Figure 7: $\ln(1/(1-D))$ versus uniaxial-pressure compaction magnitude (P) (the Heckel equation)

Slika 7: Odvisnost $\ln(1/(1-D))$ od nihanja enoosnega tlaka pri stiskanju (P) (enačba Heckel)

synthesized powders was best fitted to the Heckel equation.

As mentioned before, the synthesized powders were sintered at 930 °C, which is below the melting points of silver and zinc oxide. In other words, the powder compacts were sintered in the solid state. As it is known, during the solid-state sintering, the main mechanism for the densification and elimination of microstructural porosities is the diffusion of atoms. However, it can be declared that in the case of powder blends, the constituent with a relatively low melting point has a larger effect on the overall densification, which is due to the relatively low activation energy for the diffusion of atoms. So, in the case of the Ag/ZnO powders, the dominant mechanism for the consolidation of the powder compacts is the diffusion of silver atoms during the sintering process. It is worthy to note that the melting points of zinc oxide and silver are 961.8 °C and 1975 °C, respectively.

Figure 9 shows the relative green and sintered densities versus the cold compaction prior to the sintering. On the basis of the obtained results, the samples that were cold compacted at 300 MPa had the highest final

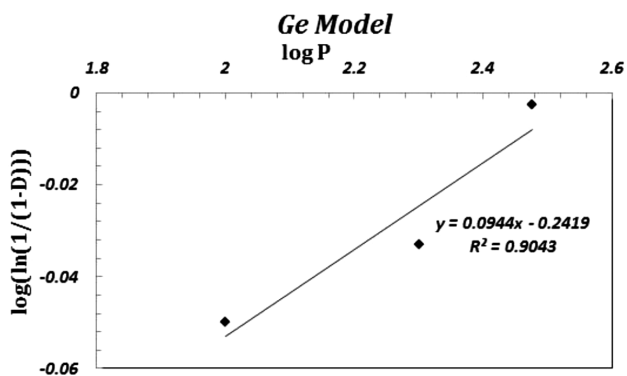


Figure 8: $\lg(\ln(1/(1-D)))$ versus uniaxial-pressure compaction magnitude ($\lg P$) (the Ge equation)

Slika 8: Odvisnost $\lg(\ln(1/(1-D)))$ od nihanja enoosnega tlaka pri stiskanju ($\lg P$) (enačba Ge)

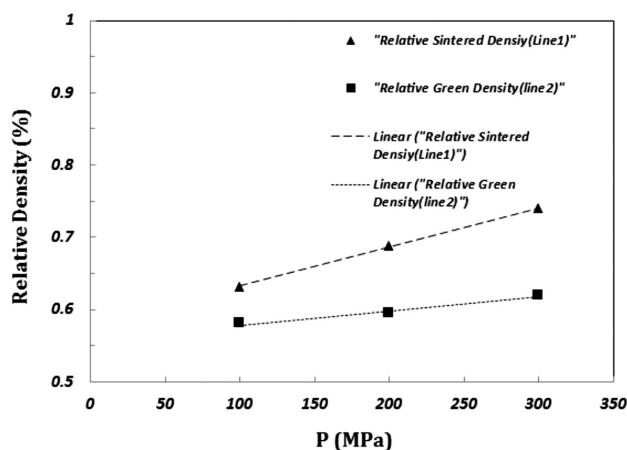


Figure 9: Green and sintered relative densities of the powders versus the magnitude of cold compaction prior to sintering

Slika 9: Zelene in sintrane gostote prahov v odvisnosti od hladnega stiskanja pred sintranjem

sintered relative density among the specimens. According to Figure 9, by increasing the cold-compaction pressure, the difference between the green- and final sintered-density values of the powder compacts was increased. However, the slope of line (1) is higher than that of line (2) in Figure 9. This observation implies that the cold-compaction pressure has a significant effect on the densification of the powder compacts during the solid-state sintering.

The difference between the relative sintered- and green-density values at each compression is shown in Figure 10. It seems that there is a logarithmic relationship between the difference value and the cold-compaction pressure. The value of correlation coefficient R^2 for the corresponding logarithmic curve is very close to unity. Based on the derived equation ($y = 0.0622 \ln x - 0.2447$), it can be concluded that if the cold-compaction pressure of the powders is below 38 MPa, no detectable densification will occur during the solid-state sintering ($y = 0$). More investigations should be done in this regard.

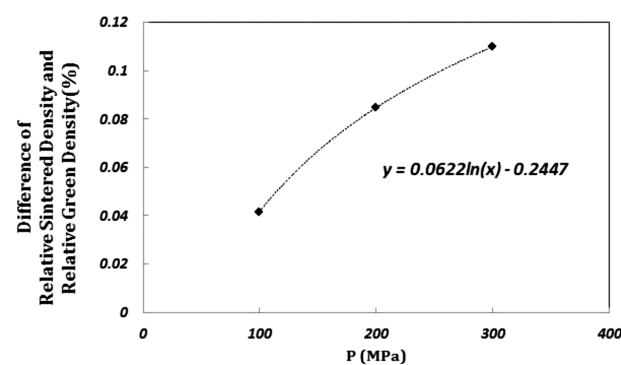


Figure 10: Difference between the relative sintered- and green-density values at each compression

Slika 10: Razlika vrednosti relativne sintrane in zelene gostote pri vsakem stiskanju

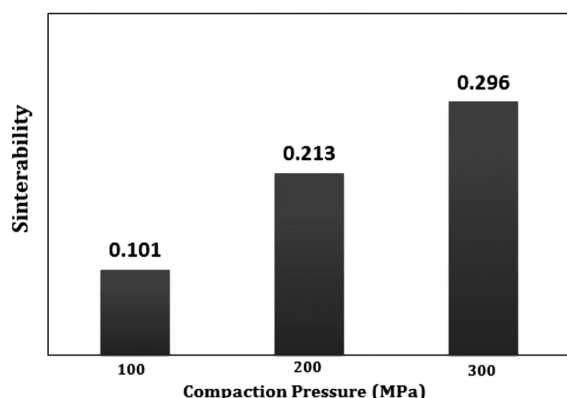


Figure 11: Sinterability (ϕ) of the powder compacts at different cold-compaction pressures

Slika 11: Sposobnost sintranja (ϕ) vzorcev, stisnjenih pri različnih tlakih v hladnem

The sinterability (ϕ) of the synthesized powders is determined with the following Equation⁹:

$$\phi = (d_s - d_g) / (d_{th} - d_g) \quad (6)$$

where d_{th} , d_g and d_s are the theoretical, green and sintered densities, respectively.

Figure 11 shows the sinterability of the powder compacts at different cold-compaction pressures. As it is observed, by increasing the cold-compaction pressure prior to sintering, the sinterability of the powder com-

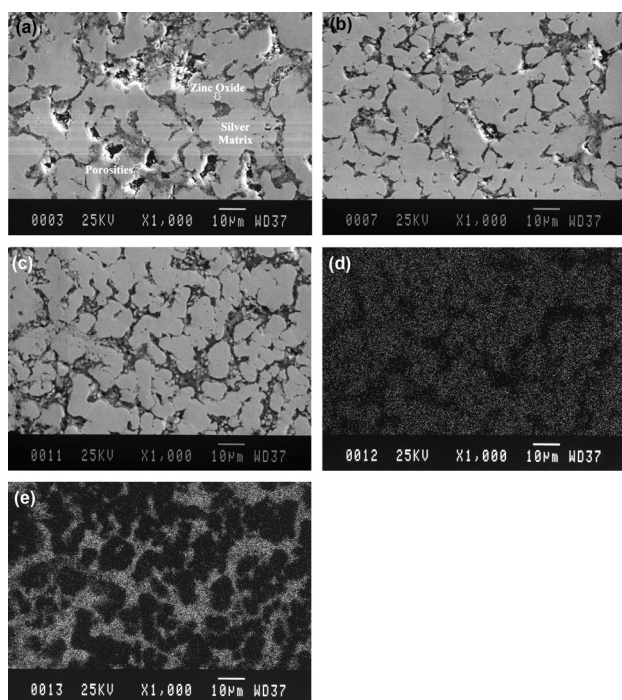


Figure 12: SEM images of the sintered composites cold compacted at: a) 100 MPa, b) 200 MPa and c) 300 MPa prior to sintering, d) silver map analysis of **Figure 12c**, e) zinc map analysis of **Figure 12c**

Slika 12: SEM-posnetki sintranih kompozitov, ki so bili hladno stisnjeni pri: a) 100 MPa, b) 200 MPa in c) 300 MPa pred sintranjem, d) analiza razporeditve srebra na **Sliki 12c**, e) analiza razporeditve cinka na **Sliki 12c**

pacts was enhanced. So, it can be concluded that the magnitude of the cold-compaction pressure has a significant influence on the atomic diffusion during sintering. By increasing the cold-compaction pressure of the powder compacts, the plastic deformation of the powder particles led to an increase in the dislocation density within the microstructures of the particles.

Increasing the number of dislocations, which are one of the main diffusion paths for the diffusion of atoms, may facilitate atomic diffusion during the solid-state sintering. However, the annealing of the cold-worked powder particles during the solid-state sintering process leads to the annihilation of dislocations within the microstructures of the particles. So, it can be concluded that the positive effect of dislocations on the atomic diffusion is more important at the initial stage of the sintering process than at the intermediate or final stages.

SEM micrographs of the synthesized composites are shown in **Figure 12**. These figures also show an elemental-map analysis of the composites that were cold compacted at 300 MPa prior to the sintering. The microstructures of the composites consist of the silver matrix, the zinc-oxide reinforcement and also porosities (**Figures 12a to 12c**). **Figures 12d** and **12e** show the silver and zinc map analyses of **Figure 12c**. The white regions in **Figures 12d** and **12e** are the silver and zinc oxide regions, respectively. It can be stated that the porosities mainly exist at the interface of silver and zinc oxide. However, by increasing the cold-compaction pressure, the size and volume fraction of the porosities were reduced. According to **Figure 12**, the samples that were cold compacted at 200 MPa and 300 MPa prior to the sintering contain silver regions within the bulk of the ZnO reinforcements. This fine dispersion of the constituents within the microstructures of the sintered specimens enhances the homogeneity of the synthesized composites.

4 CONCLUSION

In this study, Ag/ZnO composites were synthesized via a chemical precipitation process. Silver and zinc carbonates were used as the precursors. The initial precipitates contained silver and zinc carbonates. The calcination of the precipitates at 600 °C occurred due to the decomposition of the carbonates and the formation of desired powder constituents, i.e., silver and zinc oxide. The compressibility-behavior investigations confirmed that the most accurate model for describing the compressibility behavior of the synthesized powders was the Heckel equation. Furthermore, the results showed that by increasing the cold-compaction pressure prior to sintering, the density of the synthesized composites was increased.

5 REFERENCES

- ¹ ASM Handbook, Powder Metal Technologies and Applications, Vol. 7, ASM International, 1998
- ² E. Lassner, W. Schubert, Tungsten: Properties, Chemistry, Technology of the Element, Alloys and Chemical Compounds, Kluwer Academic Publishers, New York 1999, doi:10.1007/978-1-4615-4907-9
- ³ W. G. Chen, Z. Y. Kang, H. F. Shen, B. J. Ding, Arc Erosion Behavior of a Nanocomposite W-Cu Electrical Contact Material, *Rare Metals*, 25 (2006) 1, 37–42, doi:10.1016/S1001-0521(06)60011-9
- ⁴ F. A. Costa, A. G. P. Silva, F. A. Filho, U. U. Gomes, Solid state sintering of a W–25 wt% Ag powder prepared by high energy milling, *International Journal of Refractory Metals and Hard Materials*, 26 (2008), 318–323, doi:10.1016/j.ijrmhm.2007.08.003
- ⁵ E. R. Rangel, E. R. Garcia, J. M. Hernandez, E. T. Rojas, Alumina-based composites reinforced with silver particles, *Advances in Materials*, 2 (2013) 6, 62–65, doi:10.11648/j.am.20130206.11
- ⁶ P. B. Joshi, V. J. Rao, B. R. Rehani, A. Pratap, Comparison of properties of silver-tin oxide electrical contact materials through different processing routes, *Indian Journal of Engineering and Materials Science*, 15 (2008), 236–240
- ⁷ F. S. Jazi, N. Parvin, M. R. Rabiei, M. R. Tahriri, Z. M. Shabestari, A. R. Azadmehr, The effect of the synthesis route on the grain size and morphology of ZnO/Ag nanocomposite, *Journal of Ceramic Processing Research*, 13 (2012) 5, 523–526
- ⁸ M. Ardestani, Compaction and solid state sintering behavior of Cu-20wt. % ZnO powders, *Kovove Materialy – Metallic Materials*, 51 (2013), 367–371, doi:10.4149/km_2013_6_367
- ⁹ D. Jeyasimman, K. Sivaprasad, S. Sivasankaran, R. Narayanasamy, Fabrication and consolidation behavior of Al 6061 nanocomposite powders reinforced by multi-walled carbon nanotubes, *Powder Technology*, 258 (2014), 189–197, doi:10.1016/j.powtec.2014.03.039

INCREASING MICRO-PURITY AND DETERMINING THE EFFECTS OF THE PRODUCTION WITH AND WITHOUT VACUUM REFINING ON THE QUALITATIVE PARAMETERS OF FORGED-STEEL PIECES WITH A HIGH ALUMINIUM CONTENT

POVEČANJE MIKROČISTOČE IN DOLOČITEV UČINKA PROIZVODNJE, Z IN BREZ, VAKUUMSKEGA RAFINIRANJA NA KVALITATIVNE PARAMETRE KOVANEGA JEKLA Z VISOKO VSEBNOSTJO ALUMINIJA

Vladislav Kurka, Jaroslav Pindor, Jana Kosňovská, Zdeněk Adolf

Material and metallurgical research, Ltd, Pohranicni 693/31, 703 00 Ostrava-Vítkovice, Czech Republic, Vysoká škola báňská – Technical University of Ostrava, 17. listopadu 15/2172, 708 33 Ostrava-Poruba, Czech Republic
vladislav.kurka@mmvyzkum.cz, jaroslav.pindor@mmvyzkum.cz, jana.kosnovska@mmvyzkum.cz, zdenek.adolf@vsb.cz

Prejem rokopisa – received:; sprejem za objavo – accepted for publication:

doi:10.17222/mit.xxx

The quality production technology for the W.Nr. 1.8504 steel was developed. The aim of the work was to achieve the required internal micro-purity and determine the effects of different production technologies on the qualitative parameters of forged-steel pieces. Firstly, polygonal ingots weighing 1600 kg were produced, using the metallurgical units, in a controlled-atmosphere induction-melting furnace (IM) without vacuum treatment, and in a vacuum and pressurized induction-melting furnace (VPIM) with vacuum treatment. The ingots were subsequently reshaped by open-die forging into bars with a rectangular cross-section. The effect of the ingot-production technology was evaluated by comparing the forged-steel pieces in terms of their purity, macrostructure and microstructure.

Keywords: vacuum, inclusion, aluminium, steel

Izvršen je bil razvoj kakovostne proizvodne tehnologije jekla W.Nr. 1.8504. Namen je bil doseči zeleno notranjo mikročistočo in ugotoviti vpliv različnih tehnologij proizvodnje na kvalitativne parametre odkovkov. Najprej so bili izdelani poligonálni kovani ingoti z maso 1600 kg, z uporabo naslednjih metalurških agregatov: v indukcijski talilni peči s kontrolirano atmosfero (IF) brez vakuumskega rafiniranja in v vakuumski ter indukcijski talilni peči (VPIM) s povišanim tlakom in z vakuumskim rafiniranjem. Nato so bili ingoti s prostim kovanjem preoblikovani v palice s pravokotnim prerezom. Vpliv tehnologije proizvodnje ingotov je bil ocenjen s primerjavo odkovkov z vidika čistosti, makro in mikrostrukture.

Ključne besede: vakuum, vključki, aluminij, jeklo

1 INTRODUCTION

Aluminium is primarily used in steel as a deoxidising agent as well as an alloying element. In a melt, aluminium occurs in the dissolved form, in a solid solution as aluminium metal, aluminium oxide Al_2O_3 and, in an interaction with nitrogen, also as aluminium nitride AlN .¹ An increased aluminium content in steel reduces its formability due to the mechanical effect of its precipitates, and alternatively also due to its local ferrite affecting the structural state. An increased concentration of strongly ferrite generating aluminium may occur in the vicinity of dissolved AlN particles. AlN is separated in steel in the form of acicular crystals, usually on the grain borders. The quality of W.Nr.1.8504 (hereinafter referred to as the "steel") is, with regard to its chemical composition, intended for surface nitration. Nitration is a saturation of the steel surface with nitrogen that creates hard nitrides with the alloying elements Al, Cr, Ti and V. **Figure 1** shows an example of a nitrated steel layer. The process of nitration takes place at temperatures of 500 °C – 540 °C for about 50 h², when the nitrated steel layer

achieves a 0.3 mm thickness in 30 h, and a 0.5 mm thickness in 50 h. The process depends on the temperature, pressure, chemical composition of the steel and atmospheric composition.

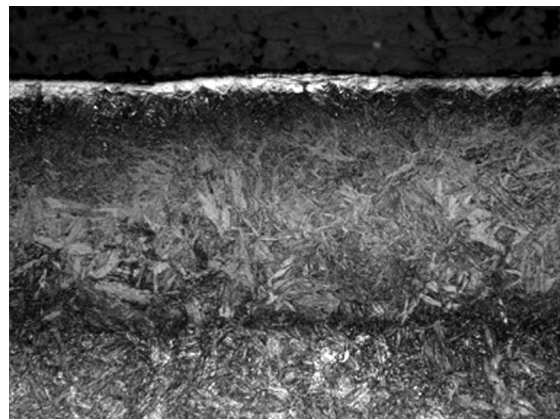


Figure 1: Example of a nitrated steel layer²
Slika 1: Primer nitrirane plasti na jeklu²

Nitrogen is thus an element that creates AlN nitrides with Al in steel, which are very hard and non-malleable. On the steel surface, it creates a hard, abrasion-resistant area. AlN nitrides inside the steel are non-malleable inclusions that impair the micro-purity of the steel. This work is concerned with the elimination of AlN inclusions from the WNr. 1.8504 quality steel with a high Al mass content of 0.8 % – 1.1 %. The chemical composition of the steel according to the standard³ and the chemical compositions of the monitored and evaluated melts and forged pieces are shown in **Table 2**.

An important step in the elimination of the AlN-type inclusions with a high aluminium content from steel is the reduction of the nitrogen content to the minimum level.

1.1 Nitrogen in steel

Nitrogen in steel not only reacts with iron but also with other dissolved elements, forming a wide variety of compounds. These are dominated by nitrides, but carbonitrides, oxynitrides, cyanonitrides, complex binary nitrides and other phases of variable compositions can occur as well. Their existence depends on a number of factors, such as the composition of the steel, the melting method, the temperature, the pressure, the thermal treatment, etc.⁴ In our case, aluminium nitrides form under the liquidus temperature and re-dissolve in the steel at temperatures of 900 °C – 1100 °C, where the dissolution rate is a function of the material temperature and structure.⁵ Increased frequency and size of, for example, the AlN particles may lead to the generation of inter-crystalline steel fractures. The effects of the elements on the solubility of nitrogen in molten iron at a temperature

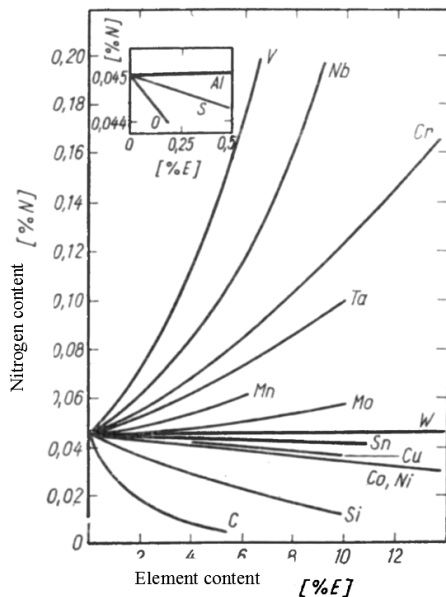


Figure 2: Effects of elements on the solubility of nitrogen in molten iron at a temperature of 1600 °C and a pressure of 100 kPa⁴

Slika 2: Vpliv elementov na topnost dušika v staljenem železu pri 1600°C in tlaku 100 kPa⁴

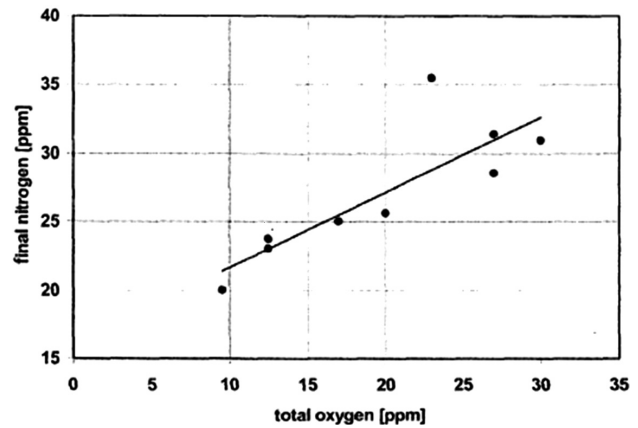


Figure 3: Nitrogen removal by tank degassing as a function of the total oxygen content⁶

Slika 3: Zmanjšanje vsebnosti dušika pri odstranjevanju plina v korni, kot funkcija skupne vsebnosti kisika⁶

of 1600 °C and a nitrogen pressure of 100 kPa are presented in **Figure 2**.⁴

Surface-active elements such as sulphur and oxygen hinder the removal of nitrogen from the molten steel during vacuuming (nitrogen diffusion in argon bubbles during bubbling) and from the vacuum above the steel surface. If reducing the nitrogen content, e.g., to a required value below 40 ppm, very low values of sulphur and oxygen need to be ensured at the same time. See **Figures 3** and **4** for a graphic illustration of this dependence.⁶

2 SOLUBILITY OF NITROGEN IN STEEL

The solubility of nitrogen in steel and the effects of individual elements are described in detail in a previous paper.⁷ The transition of nitrogen in steel is governed by Sievert's law, which presupposes its atomic dissolution. The dependence of the nitrogen content in an iron melt at pressure is described with relationship (1):

$$[\%N]_{Fe} = \frac{K_N}{f_N} \cdot \sqrt{\{P_{N_2}\}_{rel.}} \quad (1)$$

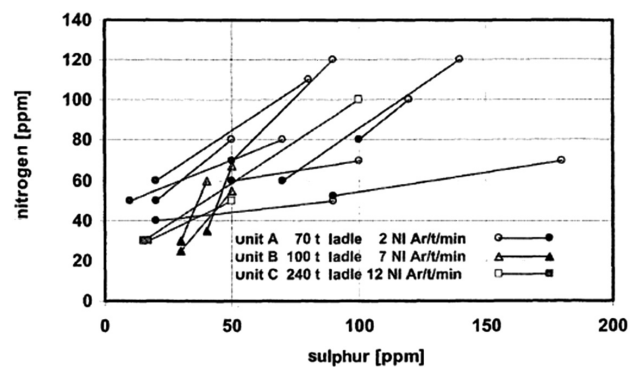


Figure 4: Nitrogen removal by tank degassing as a function of sulphur content⁶

Slika 4: Zmanjšanje vsebnosti dušika pri odstranjevanju plina v korni, kot funkcija skupne vsebnosti žvepla⁶

where:

K_N is the equilibrium constant of the dissolution process (% mass) maximum,

f_N is the nitrogen activity coefficient in iron melt¹,

$\{p_{N_2}\}_{rel.}$ is the relative partial nitrogen pressure above iron melt.¹

The equilibrium constant K_N expresses the nitrogen solubility in iron under standard conditions, i.e., its maximum content under a pressure of 0.1 MPa $\{p_{N_2}\}_{rel.} = 1$ a $f_N = 1$. The temperature dependence of nitrogen solubility is expressed with equation (2):

$$\lg K_N = -\frac{188}{T} - 1.246 = \lg[\%N]_{Fe} \quad (2)$$

and the adequate dependence of the reaction-free enthalpy on the temperature is expressed with relationship (3):

$$\Delta G^0 = 3600 + 23.86T \quad (J) \quad (3)$$

As it is clear from equation (2), the solubility of nitrogen at a temperature of 1600 °C is 450 ppm, but it drops significantly when the melt solidifies. It slightly increases in iron γ , and then drops in iron α to approximately 15 ppm at 600 °C.

The nitrogen solubility in steel is significantly affected by the presence of alloying elements, particularly in highly alloyed corrosion-resistant steels. The effect of alloying elements is manifested in the value of active coefficient f_N :

$$\lg f_N = \sum e_N^X [\%N]_{Fe} \quad (4)$$

This effect can be expressed by means of interaction coefficients $e_{N(1873K)}^X$. The temperature dependence of the interaction coefficients expressing the effects of elements on the nitrogen activity was described by Chipman and, according to the author⁸, it is expressed with relation (5):

$$e_{N(T,K)}^X = \left(\frac{3280}{T} - 0.75 \right) \cdot e_{N(1873K)}^X \quad (5)$$

Therefore, the dependence of the nitrogen solubility on the temperature can be expressed with equations (6) and (7):

$$\lg[\%N]_{steel} = \lg K_N - \lg f_N + \frac{1}{2} \lg \{p_{N_2}\}_{rel.} \quad (6)$$

$$\lg[\%N]_{steel} = \left(-\frac{188}{T} - 1.246 \right) - \sum \left(\frac{3280}{T} - 0.75 \right) \cdot e_{N(1873K)}^X + \frac{1}{2} \lg \{p_{N_2}\}_{rel.} \quad (7)$$

An improvement of the calculation is, especially for highly alloyed steels (e.g. CrNi steels) conditioned not only by the knowledge of the first values of the interaction coefficients but also of the second values and the cross-interaction coefficients, see equation (8):

$$\lg[\%N]_{steel} = \lg[\%N]_{Fe} - \sum e_N^X \cdot [\%X^2] - \sum e_N^{X,Y} \cdot [\%X][\%Y] \quad (8)$$

For significantly corrosion-resistant steel alloys, these values are quoted by, e.g., Buzek in its paper⁸, see **Table 1**.

Table 1: Values of interaction coefficients 1, 2, and cross-interaction coefficients⁸

Tabela 1: Vrednosti interakcijskih koeficientov 1., 2. in navzkrižnih⁸

X (% mass)	$e_{N(1873K)}^X$	$r_{N(1873K)}^X$	$r_{N(1873K)}^{X,Y}$
Cr	-0.0468	+0.00034	–
Nb	-0.0667	+0.00019	+0.00136 (Cr-Nb)
Mo	-0.0106	–	+0.00002 (Cr-Mo)
Ni	+0.0107	–	-0.00041 (Cr-Ni)
Si	+0.047	–	-0.00149 (Cr-Si)

1.3 Elimination of AlN from WNr.1.8504 quality steel

Elimination of the AlN inclusions from steel commenced with the evaluation of standardly produced steel with production-technology adjustments. The objective of the work was a reduction of the nitrogen content and thus the occurrence of AlN in the final product. In MMR, ingots were produced in an atmospheric induction-melting furnace (hereinafter referred to as the IF) with a nominal batch weight of 1750 kg, and in a vacuum and pressurized induction-melting furnace (hereinafter referred to as the VPIM), in which vacuum degassing (VD) at a pressure of 40 Pa (a), or vacuum oxygen decarburisation (VOD) can be carried out by means of an oxygen-argon nozzle.

One polygonal ingot for forging, V2A, was produced from each melt, weighing approximately 1650 kg. With every melt, the ingot was filled from the bottom through the casting system. The ingots were forged by open-die forging into bars of the following dimensions: 140–160 × 90–110 mm.

The melts were produced and found as follows:

Melt 1 – Production of the melt in the IF with casting on an atmospheric casting bed under a protective argon atmosphere.

Melt 2 – Production of the melt in the VPIM, vacuum refined with VD, with casting on an atmospheric casting bed under a protective argon atmosphere.

Melt 3 – Production of the melt in the VPIM, vacuum refined with VD, with casting under a protective argon atmosphere in a cofferdam.

The chemical compositions of the melts and the forged pieces of the evaluated melts are listed in **Table 2**. All the melts and forged pieces featured the required standardised chemical composition. The content of nitrogen in the forged piece from Melt 1 was 132 ppm. This amount was reduced to the value of 108 ppm, through the VD process, in the pieces forged from Melts 2 and 3.

Table 2: Chemical compositions of standardised³ WNr. 1.8504, the melts and forged pieces (% mass)**Tabela 2:** Kemijska sestava normiranega³ jekla WNr. 1.8504, taline in odkovkov (% mase)

1.8504		C	Si	Mn	P	S	Cr	Al _{diss.}	Al _{bound}	Al _{total}	N
Standard	min	0.30	0.15	0.60	–	–	1.20	–	–	0.800	–
	max	0.37	0.35	0.90	0.035	0.035	1.50	–	–	1.100	–
Melt 1	melt	0.33	0.30	0.81	0.017	0.006	1.39	–	–	1.20	–
	forged piece	0.33	0.30	0.82	0.012	0.007	1.42	1.08	0.02	1.10	0.0132
Melt 2	melt	0.33	0.27	0.70	0.015	0.007	1.44	–	–	1.11	–
	forged piece	0.34	0.26	0.73	0.011	0.008	1.45	1.07	0.02	1.09	0.0108
Melt 3	melt	0.35	0.24	0.76	0.018	0.007	1.47	–	–	0.97	–
	forged piece	0.35	0.23	0.77	0.010	0.007	1.48	0.94	0.02	0.96	0.0108

Elements of C, S, N were determined with the thermochemical method using equipment LECO CS 230 and LECO TCH 600. Metal samples were melted in an induction (for C and S) or resistor (for N) furnace in a gas stream. The gas was analysed for the absorption of infrared radiation (for SO₂ and CO₂) and the change in the thermal conductivity was measured (for N₂). Elements Si, Mn, P, S, Cr were determined with an X-ray spectrometry apparatus, ARL ADVANT'X IntelliPower THERMOFISHER SCIENTIFIC. The method of sequential X-ray fluorescence spectrometry is based on the excitation of characteristic X-rays of the elements present in a sample using an X-ray lamp. The Al element was determined on Optima 3000SC PERKIN ELMER. The analysed sample was dissolved in acids and transferred into the solution, and then it was measured using optical emission spectrometry with inductively bounded plasma.

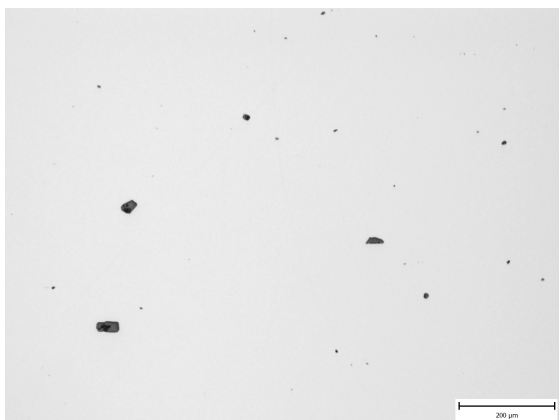
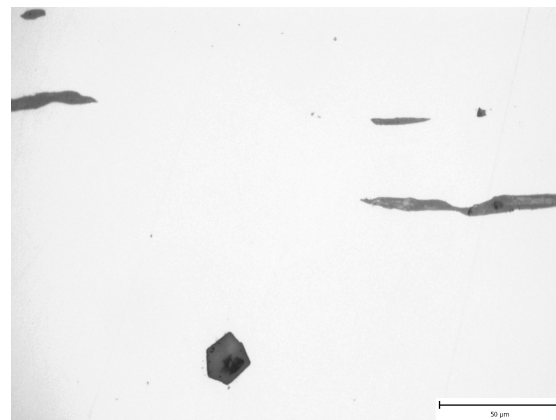
The pieces forged from all the melts were subjected to non-destructive ultrasound testing according to SEP 1921/84 Group 3, Class C/c. All the forged pieces fully conformed to the evaluation.

The work further presents an evaluation of the micro-purity of the pieces forged from Melts 1 to 3, according to ASTM E45-10, method A. This method classifies the inclusions by their shape and light reflectivity only, so their chemical composition plays no role. For the above reason, a spectral microanalysis was also

performed with a scanning electron microscope JEOL JSM-5510, equipped with an energy-dispersive analyser from Oxford Instruments, with which the chemical compositions of the inclusions were determined. Last but not least, the work presents an evaluation of the forged pieces' macrostructures.

1.4 Micro-purity of the pieces forged from Melt 1 in the IF

First of all, micro-purity was evaluated on the pieces forged from Melt 1 in the IF. Very coarse inclusions, spot D (oxidic inclusions), were observed in the specimens that often exceeded the allowed limit of 12 µm, specified in the classification of these inclusions. The biggest inclusion achieved the size of 49 µm; the spot-D (oxidic) inclusions were not quite standard, i.e., globular. They featured a rather sharp-edged shape with a variable size. Then there was a smaller quantity of specimens with the inclusions arranged in lines, often in combination with sulphides that were, using the relevant standard etalon, evaluated as the B type – line Al₂O₃. A very low number of slightly shaped A-type inclusions were then observed in some places, exceeding the thickness of 6 µm that is specified for the coarse A-type inclusions. Examples of non-metallic inclusions are shown in **Figures 5** and **6**; see **Figures 7** and **8** for the chemical compositions of the most frequent inclusions.

**Figure 5:** Non-metallic inclusions in the piece forged from Melt 1; magnified 65x**Slika 5:** Nekovinski vključki v odkovku iz taline 1. Povečava 65 x**Figure 6:** Non-metallic inclusions in the piece forged from Melt 1; magnified 330x**Slika 6:** Nekovinski vključki v odkovku iz taline 1. Povečava 65

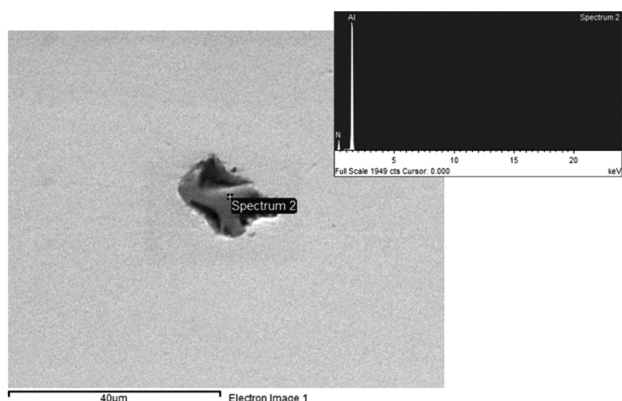


Figure 7: EDX spectrum of non-metallic AlN particles in the piece forged from Melt 1

Slika 7: EDX spekter nekovinskih delcev AlN, v odkovku iz 1. taljenja

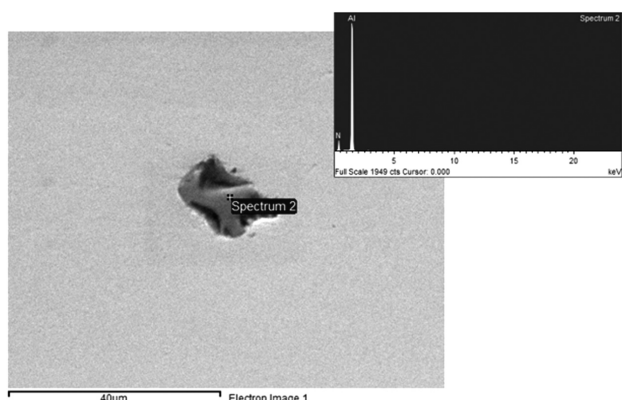


Figure 8: EDX spectrum of non-metallic Al₂O₃ particles in the piece forged from Melt 1

Slika 8: EDX spekter nekovinskih delcev Al₂O₃, v odkovku iz 1. taljenja

Table 3 shows the results of the micro-purity evaluation; the table also includes the largest inclusion found in the tested metal specimens.

1.5 Micro-purity of the pieces forged from Melt 2 in the VPIM through the VD process and casting under Ar atmosphere

During the examination of the polished state, most often non-metallic inclusions of D- and A-type complexes were observed in the tested chains, as shown in **Figures 9** and **10**. Oval inclusion particles were often locally dispersed in the metallic matrix in the forged pieces, sometimes achieving a diameter of 48 μm. The results of the micro-purity evaluation of Melt 2 are shown in **Table 3**.

Locally occurring complex non-metallic particles on the tested specimen surfaces were classified into groups with the closest shape similarity. The majority of the tested inclusions were observed to be globular particles (D type) or elongated sulphides (A type). Small-scale tiny lines of B-type inclusions were observed in the forged-piece matrix as well.

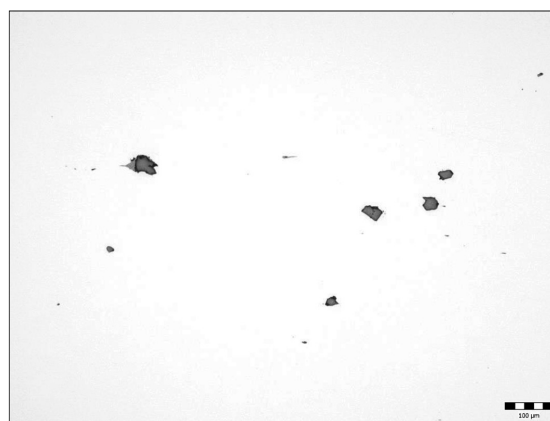


Figure 9: Non-metallic inclusions in the piece forged from Melt 2; magnified 65x

Slika 9: Nekovinski vključki v odkovku iz taline 2. Povečava 65x



Figure 10: Non-metallic inclusions in the piece forged from Melt 2; magnified 330x

Slika 10: Nekovinski vključki v odkovku iz taline 2. Ppovečava 330x

The microanalysis detected the chemical compositions of the most frequent inclusions of the AlN type, as shown in **Figure 11**, the MnS type, as shown in **Figure 12**, or the complex AlN-MnS type inclusions, as shown in **Figure 13**.

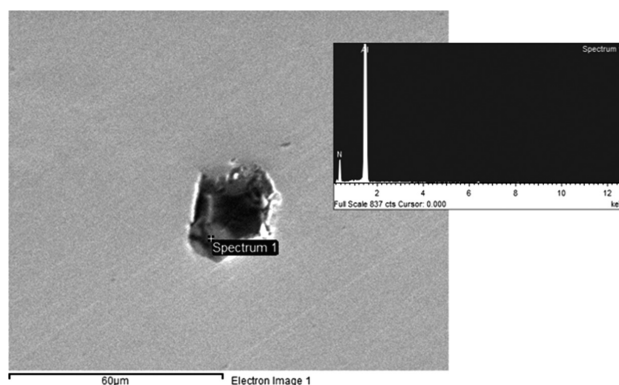


Figure 11: EDX spectrum of non-metallic AlN particles in the piece forged from Melt 2

Slika 11: EDX spekter nekovinskih delcev AlN, v odkovku iz taline 2

1.6 Micro-purity of the piece forged from Melt 3 in VPIM through the VD process and casting in the cofferdam under Ar

As in the previous cases, the presence of a high amount of coarse inclusions was detected in this forged piece; due to their shape, these inclusions were classified as D-type inclusions (oxidic inclusions). Their size significantly exceeded the admissible diameter of up to 12 μm specified for the D-type inclusions. The occurrence of these inclusions was frequent and they achieved the size of up to 50 μm; however, their shape was not typically globular but rather angular, as shown in **Figures 14** and **15**. The occurrence of oxidic inclusions in a line arrangement was less frequent.

Besides the oxidic inclusions, A-type inclusions were observed in the specimen, or complexes of these inclusions, the occurrence of which was relatively frequent. The results of the non-metallic inclusion evaluation are listed in **Table 3**. The microanalysis revealed that, unlike in Melt 2, AlN-type inclusions were the most frequent in Melt 3, as shown in **Figures 16**, **17** and **18**.

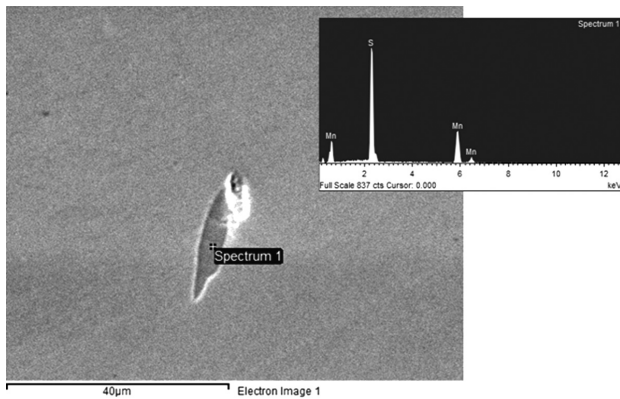


Figure 12: EDX spectrum of non-metallic MnS particles in the piece forged from Melt 2

Slika 12: EDX spekter nekovinskih delcev MnS, v odkovku iz taline 2

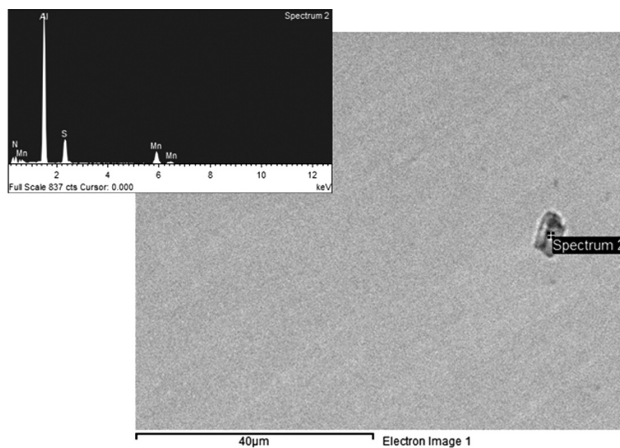


Figure 13: EDX spectrum of non-metallic AlN-MnS particles in the piece forged from Melt 2

Slika 13: EDX spekter nekovinskih delcev AlN-MnS, v odkovku iz taline 2



Figure 15: Non-metallic inclusions in the forged piece in Melt 3; magnified 330 times

Slika 15: Nekovinski vključki v odkovku iz taline 3. Povečava 330x



Figure 14: Non-metallic inclusions in the piece forged from Melt 3; magnified 65x

Slika 14: Nekovinski vključki v odkovku iz taline 3. Povečava 65 x

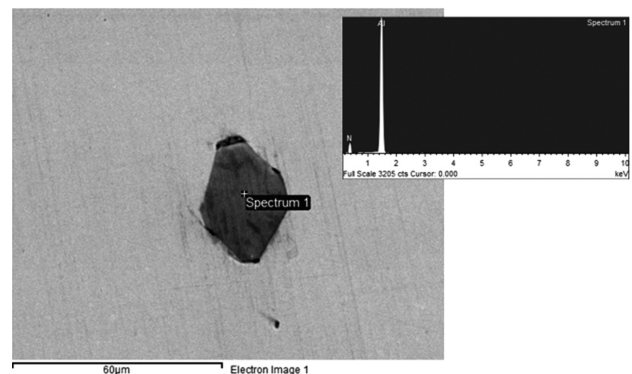


Figure 16: EDX spectrum of non-metallic AlN particles in the piece forged from Melt 3

Slika 16: EDX spekter nekovinskih delcev AlN, v odkovku iz taline 3

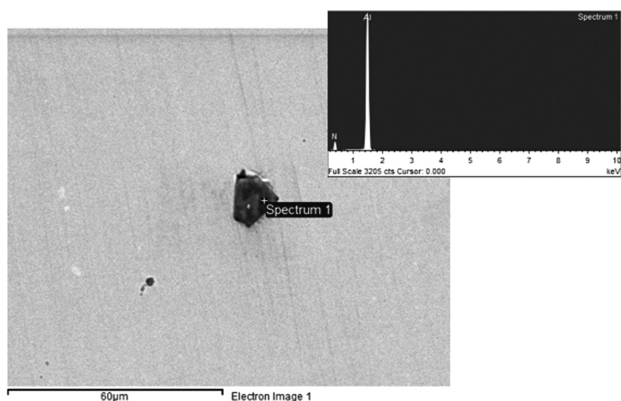


Figure 17: EDX spectrum of non-metallic AlN particles in the piece forged from Melt 3

Slika 17: EDX spekter nekovinskih delcev AlN, v odkovku iz taline 3

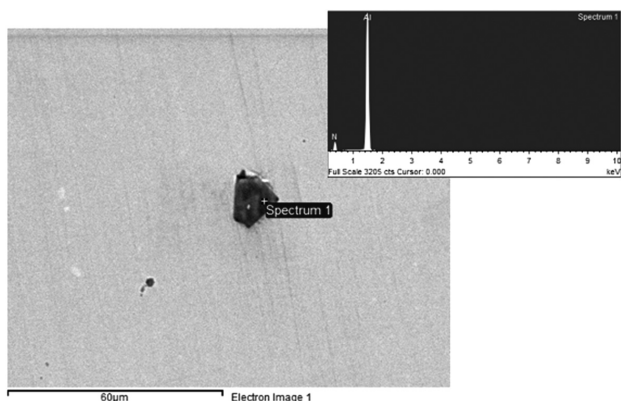


Figure 18: EDX spectrum of non-metallic AlN particles in the piece forged from Melt 3

Slika 18: EDX spekter nekovinskih delcev AlN, v odkovku iz taline 3

1.7 Macrostructure evaluation

The macrostructures of the forged pieces were revealed by etching in 10 % HNO₃. Unequally distributed insignificant segregations of a darker contrast were revealed in the specimen of the piece forged from Melt 1, as shown in **Figure 19**. More or less uniform macrostructures of the surfaces were observed for the specimens forged from Melts 2 and 3, as shown in **Figures 20** and **21**.

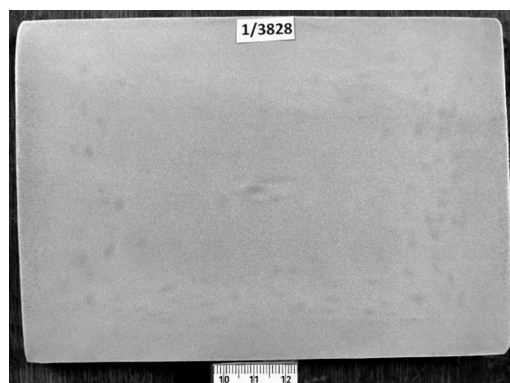


Figure 19: Macrostructure of the piece forged from Melt 1

Slika 19: Makrostruktura odkovkov iz taline 1

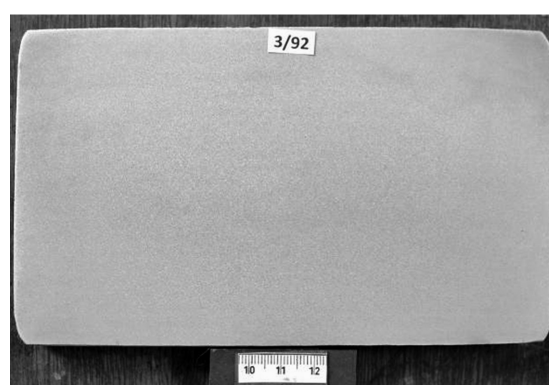


Figure 20: Macrostructure of the piece forged from Melt 2

Slika 20: Makrostruktura odkovkov iz taline 2

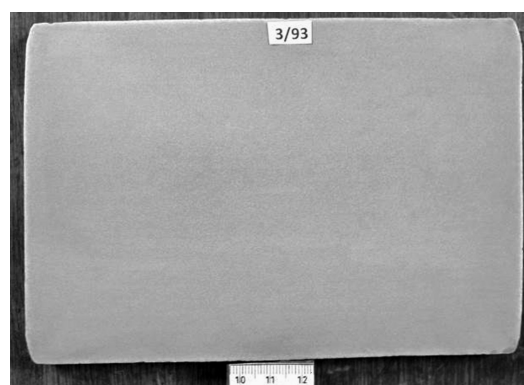


Figure 21: Macrostructure of the piece forged from Melt 3

Slika 21: Makrostruktura odkovkov iz taline 3

Table 3: Micro-purity evaluation according to the ASTM E45-10 standard, method A, and the largest D-type inclusions found in the pieces forged from Melts 1 to 3

Tabela 3: Vrednotenje mikročistoče po standardu ASTM E45-10, metoda A in največji najdeni vključki vrste D v vzorcih iz odkovkov iz taline 1 do 3

Specimen	Maximum contamination, method A								Maximum dimension of D-type inclusion µm
	Type A sulphides		Type B aluminates		Type C silicates		Type D oxides		
	Fine	Coarse	Fine	Coarse	Fine	Coarse	Fine	Coarse	
Melt 1	1	1	2	2			2	2	49
Melt 2	2	2	2	1	–	–	2	2	48
Melt 3	2	1	2	–	–	–	2	2	50

2 CONCLUSION

The objective of the presented work was to increase the inner purity of a WNr. 1.8504 high-quality forged piece. For this reason, three production technologies (melts) were evaluated in this work.

As the performed analysis of the chemical compositions and non-destructive ultrasound tests indicate, the atmospheric induction furnace and the vacuum and pressurized induction-melting furnace with casting outside and inside the cofferdam are suitable for the production of this material.

However, from the macrostructural point of view, the production of melt in the atmospheric induction-melting furnace proved to be unsuitable.

With respect to the micro-purity determined with the microanalysis of the detected particles and nitrogen content in the forged pieces, none of the three technologies can be applied to achieve a reduced content of mostly AlN inclusions. The production technology for Melt 3 in the VPIM, with the VD process and the casting in the cofferdam under a protective argon atmosphere, eliminated the portion of oxidic and complex inclusions but not the AlN inclusions.

The experiments showed that vacuum degassing (VD) helps to reduce the Al content. The content of nitrogen was reduced by 24 ppm, from 132 ppm (the steel made in the IF) to 108 ppm (the steel made in the VPIM). Based on this fact, the authors are preparing another experiment that will eliminate the nitrogen content using vacuum oxygen decarburization (VOD) because the melt is mixed better with VOD than with

VD. VOD includes a more efficient degassing process because, generally, a high oxygen content in a melt decreases the solubility of nitrogen. For this process, a newly manufactured oxygen-argon nozzle will be used.

Acknowledgement

This paper was created within Project No. LO1203 "Regional Materials Science and Technology Centre – Feasibility Program" funded by the Ministry of Education, Youth and Sports of the Czech Republic.

3 REFERENCES

- ¹ J. Šenberger, Z. Bůžek, A. Záděra, K. Stránský, V. Kafka, *Metalurgie oceli na odlitky*, VUTIUM, Brno 2008, 311
- ² Introduction to Metallography [online], PACE Technologies [cited 2014-09-24], available at <http://www.metallographic.com/Technical/Metallography-Intro.html>
- ³ *Stahlschlüssel 2007*, Verlag Stahlschlüssel Wegst GmbH., ver. 5.01.0000, Marbach 2007
- ⁴ T. Myslivec. *Fyzikálně chemické základy ocelářství*, SNTL – Nakladatelství technické webliteratury, Prague 1971, 448
- ⁵ J. Višek, *Hodnocení růstu zrna uhlíkových a nízkolegovaných nástrojových ocelí v závislosti na přítomnosti AlN* [online] [cited 2014-09-24], available at <http://stc.fs.cvut.cz/pdf/VisekJaroslav-338820.pdf>
- ⁶ G. Stolte, *Secondary Metallurgy*, Verlag Stahleisen GmbH, Germany 2002, 217
- ⁷ V. Kurka, Z. Adolf, J. Pindor, *Producing Steel with High Nitrogen Content in Induction Melting Furnaces*, European Oxygen Steel-making Conference, Třinec, 2014
- ⁸ Z. Buzek, *Basic thermodynamic calculations in the steel industry*, *Hutnické aktuality*, 29 (1988) 7